The University Of Sheffield.

In Vitro Damage Quantification of Medical Device Material Interaction with Endothelial Cells

Rasmus Merlin Ferdinand Wagner

A thesis submitted in partial fulfilment of the requirements for the degree of

Doctor of Philosophy

The University of Sheffield

Faculty of Engineering

Department of Mechanical Engineering

Submission Date

January 2022

Abstract

Cardiovascular medical devices are used to treat a number of life-threatening diseases. However, the intervention can have severe complications, such as thrombosis and stent migration, which can be linked to mechanical interaction between blood vessel and medical device. Being located at the surface of blood vessels, the endothelial cells are both at the interface of the frictional interaction and responsible for suppressing factors leading to some of the complications. Therefore, a damaged endothelium can have severe implications. The interaction between medical devices and blood vessels has still not been understood to a satisfactory degree. This work aimed to study the influence of load (normal force) and material choice on friction, to quantify damage to the monolayer, and lays a foundation for meaningful experiments to find more suitable materials causing less, or less severe, complications in the future.

The tribological methodology developed in the context of this work overcomes issues with previous studies and constitutes a way of testing how much friction and damage different probe materials generate under more physiologically-relevant conditions by deploying a soft substrate populated with an endothelial monolayer. A way has been developed to account for a well-known issue in low-friction experiments due to misalignments in the set-up. Furthermore, a new way of quantifying the extent of the induced damage in terms of live, dead and removed cells has been deployed. A key feature of the methodology is that it works without expensive microtribometers and achieves extremely low pressures in the two digit kPa range with a standard tribometer (UMT2 by Bruker), making it adaptable by other research institutions without much cost. This set-up could be used, however, to achieve higher pressures too, either by choosing a harder substrate, or by simply increasing the normal load. The results quantify the damage induced by three different probe materials (glass, stent-grade stainless steel and PTFE) due to friction and indentation and show differences between the materials. These data are analysed and discussed in depth to explain the apparent mechanisms at a cell level.

As a conclusion, friction was successfully measured and damage assessed on endothelial cell monolayers which can be employed without great costs and quickly yield results that could have significant implications. Even after only testing glass, stainless steel and PTFE in this work, it became clear that there are materials in some medical devices - which are in contact with the endothelium - that induce severe damage. As such, techniques and tools developed in the context of this work could be used to test existing materials and to develop new ones that could reduce the risk of complications for many people.

Acknowledgements

As this time of being a PhD student comes to an end, there are people I would like to thank as they have supported me in this exciting time. Firstly, I want to thank my two supervisors, Cecile Perrault and Roger Lewis, who have provided me with guidance throughout this work. Apart from contributing with their expertise in their respective areas, they always let me explore and were approachable when I needed advice. After spending four years of working in academia, I can say with confidence that I was very lucky to have two exceptional supervisors that cared so much about me and my project. Further, I would like to thank my examination committee, Professor Matt Carré and Professor Alison Dunn for examining this work.

I would also like to thank my two previous supervisors, Jaan Unger and Alberto Marzo who have introduced me to Sheffield and encouraged me to do a PhD. Without them, I would not have started this journey. I am also grateful for the people in the lab who have supported me, especially Julie and those who have taught me the ways with cells, Luke and Dhanak.

I also want to thank my friends, those which I have known since years and those which I met on this journey. Please forgive that I cannot mention all of you. Especially I want to thank Julian, Tim and Anton for the fun times. Dave and Tom for the coffees in the kitchen and the talks about leaf layers, ultrasound and endothelial layers which always made for interesting discussions and a great break.

Special thanks go to my family. To my parents, who have always supported me and my siblings, letting us explore and be a bit crazy. To my sister and my brother who I know I can always count on. To my uncle Andreas and to my grandparents who all have invested so much time in me.

Finally, I want to thank my partner Abbie for being at my side in this challenging and often stressful time. For always taking my corner with all her heart, cheering me up when experiments did not work out and rejoicing the moments of success, I am very grateful.

Contents

Glossary

Actin Fibres made from actin are part of the cytoskeleton and are responsible for heping the cell in moving around and exert forces on the ECM

Aliquot A smaller portion of a larger batch

Apoptosis Controlled cell death prompted by internal or external signals

Arterial Relating to or concerning the arteries

Artery A blood vessel carrying (usually oxygen-rich) blood from the heart to the organs

Balloon angioplasty Cardiovascular medical intervention during which attempts are made to revascularise a blocked blood vessel

Blood vessel Organic tube for transporting blood within the body

CO_2 **C**arbon **D**i**O**xide: gas commonly found in the atmosphere, which is also used for cell culture

CAD **C**omputer **A**ided **D**esign: Computer based methods to generate two or three dimensional digital engineering models and drawings

Catheter A flexible tube used to deliver or aspirate fluids to or from organs or insert other medical devices into the body, usually through arteries

Cell culture hood A shielded desk, similar to a reverse fume cupboard, generating a laminar flow outwards to provide a sterile environment for cell culture

Cell membrane Protective layer made from a lipid bilayer surrounding the cell and containing the cytoplasm with all cell organelles

CFD **C**omputational **F**luid **D**ynamics: Computer-simulated prediction of fluid flow

CMD **C**ardiovascular **M**edical **D**evice: A device used for cardiovascular intervention, such as a stent, catheter or stent retriever

CNC **C**omputerised **N**umerical **C**ontrol: A way of operating a machine to follow previously defined instructions or coordinates by means of computerised control, for example to machine a part in a certain way

Confluent What percentage of the surface area is covered with cells

Cytoplasm All contents in a mammalian cell, except for the nucleus

Cytoskeleton The structures within a cell helping it to withstand external loads or move

DH$_2$O **D**eionised **H$_2$O**: purified water suitable for cell culture, that is free from most ions

DAPI 4′,6-**di**a**m**idino-2-**p**heny**l**indole: A fluorescent blue dye staining for DNA, incapable of penetrating healthy cell membranes

DMSO **Dim**ethyl **S**ulf**o**xide: A chemical used to prevent crystallisation while freezing cells

DNA **D**eoxyribo**n**ucleic **A**cid: A molecule containing the instructions for functioning and reproduction of a cell, typically stored in the nucleus

EC **E**ndothelial **C**ell: Cells making up the inner lining of arteries and veins

ECM **E**xtra**c**ellular **M**atrix: The matrix surrounding cells

Endothelium The monolayer lining blood vessels made up of endothelial cells

Endovascular aneurism repair Reparation of an aneurism with a graft reducing stress on the aneurism wall in an attempt to reduce the risk of aneurism rupture

Ex vivo Latin for out of the living, meaning an experiment conducted on biological tissue directly extracted from a living object

FA **F**orm**a**ldehyde: A chemical used to fix cells, binding intracellular proteins together and preserving them

FBS **F**etal **B**ovine **S**erum: Blood serum gained from the blood of calves used for cell culture

Fibronectin A protein found in the ECM used in vitro to help cells to attach to a substrate

Fluorescence Emission of electromagnetic radiation of a specific wavelength, usually on the spectrum of visible light, caused by excitation of atoms

Fluorescent Having fluorescence properties

Glycocalyx A protective structure of carbohydrate chains on the blood-facing side of endothelial cells

Hemocytometer A device made from glass providing a defined volume in which cells can be counted, allowing the of total cell concentration

Hoechst A fluorescent blue dye, similar to DAPI, but capable of penetrating a healthy cell membrane

HUVEC **H**uman **U**mbilical **V**ein **E**ndothelial **C**ell: Cells forming the inner lining of the umbilical vein

Immunocytochemistry Techniques used to evaluate the presence of antigens or proteins, like DNA by means of an (often fluorescent) antibody and a microscope

IMS **I**ndustrial **M**ethylated **S**pirit: Denatured alcohol used for sterilisation

In silico Latin for in silicium i.e. in a computer chip, referring to experiments or studies conducted in a simulation, such as Monte-Carlo, or CFD studies

In vitro Latin for in the glass, referring to experiments or studies conducted with biological material, such as cells, in laboratory conditions

In vivo Latin for in the living, meaning an experiment conducted in a living object

Incubator An insulated box, shielding the contents from the environment and providing a defined temperature, humidity and CO_2 concentration

Intervention A medical intervention is an action, such as vascular surgery, in response to a disease or injury, with the intention to either prevent said disease, or change the medical outcome of the patient

LN_2 **L**iquid **N**itrogen : liquid (diatomic) form of nitrogen, a gas commonly found in the atmosphere, used for long term cell storage

Medium Medium for cell culture contains nutrients and growth factors needed to grow and keep cells *in vitro*. It may also contain antibiotics and antimycotics used to prevent bacterial or fungal infection of the cell culture vessel

MG63 Immortalised cell line derived from fibroblasts

Model In the context of this work, models are studies conducted on a substitute for living tissue, for example hydrogels

Monolayer A layer of cells that is only one cell thick, i.e. without any cells on top of each other

Necrosis Uncontrolled cell death caused by irreversible injury to a cell

Nucleus The cell organelle responsible for controlling all processes in the cell and storage of genetic information in form of DNA

P/S **P**enicillin/**S**treptomycin: Mix of antibiotic and antifungal chemicals

PBS **P**hosphate **B**uffered **S**aline: Phosphate-based buffer solution

PDMS **P**oly**di****m**ethyl**s**iloxane: A relatively soft polymer made from an elastomer base and a curing agent

Percutaneous coronary intervention Procedure attempting the revascularisation of the percutaneous arteries in the heart

Phalloidin A fluorescent red dye that binds to the actin fibres of the cytoskeleton, staining them red under a fluorescence microscope

Physiopathology The science of altered body functions in disease, combining pathology and physiology

PI **P**ropidium **I**odide: Chemical used for staining DNA red

PS **P**oly**s**tyrene: Plastic often used for cell culture vessels

PTFE **P**oly**t**etra**f**luoro**e**thylene: A plastic generally associated with low friction, sometimes used for applications in medical devices

Stent A mesh structure used to keep a vessel open after baloon angioplasty

Stent retriever Mesh structure used to retrieve blood clots from a blocked blood vessel

Triton-X100 A strong surfactant used in cell culture applications to degrade the cell membrane

Trypan Blue A blue dye used to stain apoptotic or necrotic cells in a dark blue colour while leaving healthy cells transparent

Trypsin A protein capable of decomposing the ECM, causing cells to roll up and detach, used during trypsinisation

Trypsinisation The process of submerging an attached cell culture in trypsin to detach it in order to determine cell concentration or density

Tunica externa The outermost layer of blood vessels

Tunica interna The innermost layer of blood vessels

Tunica media The mid-layer of blood vessels

UMT 2 **U**niversal **M**echanical **T**ester Version **2**: Second generation of a modular, CNC universal tribological testing unit

Vascular Relating to or concerning the blood vessels

Vein A blood vessel carrying (usually oxygen-depleted) blood from the organs to the heart

Veinal Relating to or concerning the veins

Symbols

Sign	Description	Unit
t	time	s
x	horizontal stage position	mm
z	vertical stage position	mm
A	area	mm^2
V	volume	mL
v	velocity	$\mathrm{m\,s}^{-1}$
a	acceleration	$\mathrm{m\,s}^{-2}$
v_T	tangential velocity	$\mathrm{m\,s}^{-1}$
F	force	N
F_N	normal force	N
F_T	tangential force	N
F_F	friction force	N
$F_{Fs,adj}$	slope-adjusted static friction force	N
$F_{Fd,adj}$	slope-adjusted dynamic friction force	N
$F_{Fd,level}$	zero-slope dynamic friction force	N
F_H	hemodynamic force	N
F_{Adh}	adhesion force	N
ρ	cell nuclei density	$\mathrm{nuclei}/\mathrm{mm}^2$
ρ_B	blue nuclei density	$\mathrm{nuclei}/\mathrm{mm}^2$
ρ_R	red nuclei density	$\mathrm{nuclei}/\mathrm{mm}^2$
P_B	relative blue nuclei density	–
P_R	relative red nuclei density	–
σ	normal pressure / stress	$\mathrm{N\,mm}^{-2}$
τ	tangential stress	$\mathrm{N\,mm}^{-2}$
μ	friction coefficient	–
μ_s	static friction coefficient	–
μ_d	dynamic friction coefficient	–

List of Figures

List of Tables

Chapter 1

Introduction

1.1 The Problem

Cardiovascular medical devices (CMDs), such as catheters, stents and stent retrievers all touch the vessel wall during their application and operation, which causes mechanical interaction to happen at the interface between endothelial cells (ECs) and medical device. While stents are stationary, catheters and stent retrievers move relative to the vessel surface during their operation. Hence, for both groups of devices, friction plays a role, with dynamic friction being more important in catheters and stent retrievers, while static friction plays a major role in stents. This is the case because catheters and stent retrievers are intended to move through vessels, whereas stents are supposed to be stay at a fixed location after deployment. Stents that do not apply enough static friction between stent struts and vessel wall migrate due to blood flow and can cause problems.

Furthermore, all of the aforementioned interventions come with a risk of complications, some of which can be linked to mechanical trauma or damage to the endothelium. Damage caused by frictional interaction is called "wear" and can be investigated with tribological methods. As cell monolayers are not a standard material in tribology, specific methods need to be developed to make wear visible and to quantify it in this context.

1.2 Aims and Objectives

The aim of this work was to mimic the frictional interaction between blood vessels and medical devices in an *in vitro* environment to explore the relationship between material and load parameters as an input and friction and damage as an output.

The first objective was to develop a methodology that can be used to tribologically test a blood vessel surrogate (henceforth also called "sample") under laboratory conditions as

close to the real situation as possible. The second objective was to establish an analysis protocol to quantify the frictionally-induced damage to the sample. The third objective and overall goal was to quantify damage of the blood vessel surrogate against different materials and under different load conditions.

1.3 Novelty and Impact

The main novelty of this work is the ability to assess damage caused by tribological interaction in a quantitative way at extremely low loads and compatible with cellular analysis methods (i.e. optical and fluorescence microscopy). While most studies on cultured cells were looking at the cells attached to a hard substrate - which is a problem because it does not reflect the real situation and causes unrealistically high pressures in the cells - here, a custom sample structure was developed. As there are not many studies of this kind, solutions for damage quantification were scarce. Multiple approaches for differentiating visually between damaged and healthy cells were assessed. With this, a distinction between live and dead cells was possible under the microscope, but the overall damage had to be quantified, which required multiple programs for data conditioning and analysis. This workflow was then applied in order to, for the first time, compare damage caused by different materials and under different loads.

The frictional results of this work can be used for advanced simulations of interventions and the methodology could be applied to more materials to study and optimise friction in a cardiovascular application. The wear results may be useful to indicate the relation of material properties to physiopathology (linking physiological changes and disease).

1.4 Overview of the Thesis

Chapter 2 of this work looks at the medical context of CMDs and how it is related to tribology. This includes understanding how those devices work, what complications they bring and how these can be linked to friction and wear. Different approaches available to experimentally investigate cardiovascular biotribology are discussed and the current state of the field is assessed. Finally, opportunities for improvement based on what was learned from the medical background are explored.

Chapter 3 details materials and methods used throughout this work. Some of the methods are standard practice for cell culture, others were developed in the context of this work. In the case of novel methodologies and analysis approaches developed in the scope of this

work, Chapter 3 also contains the derivation. The methodologies are then applied to investigate the damage caused to an endothelial layer by different materials under a variety of loads in Chapter 4. This chapter also investigates how the newly developed methodology fares against other approaches. Chapter 5 contains experiments conducted on cells under a simplified (indentation) load condition. Those results are discussed and put into the context of medical applications in Chapter 6. Finally, the main conclusions and ways to build upon this work are laid out in Chapter 7. In the appendix, the code for the programs developed in this work and a cell attachment study conducted to determine the optimal way of attaching the relevant cell type to the substrate as well as additional figures can be found.

1.5 Research Outputs

Publications

R. M. F. Wagner, R. Maiti, M. J. Carré, C. M. Perrault, P. C. Evans, and R. Lewis. "Biotribology of Vascular Devices: A Review of Tissue/Device Friction Research". *Biotribology*, vol. 25. p. 100169, Mar-2021.

R. Maiti, **R. M. F. Wagner**, Noe A. Martinez Sanchez, Alejandro Ramirez-Reivich, Peter Ellison, Cecile Perrault, Matt J. Carre, Rob Dwyer-Joyce, Anne Neville, Roger Lewis. "From Macroscopic to Microscopic: Experimental and Computational Methods to Investigate Bio-tribology". *IFMBE Proceedings*, 2020, vol. 69, pp. 213–216.

Posters and Presentations

iT-CDT Showcase: "Mini project 2: Building of an apparatus for the *in-situ* observation of friction tests on endothelial cells", Poster Presentation, March 2018, Sheffield, UK

TriboUK: "Mini project 2: Building of an apparatus for the *in-situ* observation of friction tests on endothelial cells", Poster Presentation, March 2018, Sheffield, UK, won the prize for the best poster

iT-CDT Sponsor Day: "Cell Tribology for Improved Stent Performance", Oral Presentation, January 2019, Leeds, UK

INSIGNEO Showcase 2019: "Investigation on friction between cardiovascular medical devices and arterial tissue", Poster Presentation, May 2019, Sheffield, UK

Chapter 2

Background and Context

This section explains the medical background of biotribology in cardiovascular applications.

2.1 Physiology of the Cardiovascular System

2.1.1 Blood Vessels

Arteries are comprised of three layers where the tunica externa is the outermost layer of the blood vessel (see Figure 2.1). The tunica externa consists of collagen fibres and scattered elastic fibres. It is responsible for connecting the vessel with the surrounding tissue. The tunica media is the middle layer which contains smooth muscle cells, generally orientated in a concentric pattern, that enables contraction or dilation of the vessel as required. The tunica media is separated from the tunica externa by a band of elastic fibres and connected to the tunica interna by collagen fibres. The tunica interna is the innermost layer. It consists of a thick layer of elastic fibres on the outer perimeter, connective tissue and an endothelial cell monolayer on the inside [1]. The endothelial layer plays an important role in tribological interaction with a medical device as it is in direct contact with the medical device surface.

2.1.2 The Endothelium

The endothelial layer is the interface between tissue and blood and permits the exchange of cells, oxygen and other molecules between these entities whilst containing and controlling blood flow. It is composed of a uniform monolayer of endothelial cells, which senses a number of flow characteristics (shear stress magnitude, directionality, frequency) and converts this information into biochemical responses [2][3][4]. For example, the endothelial

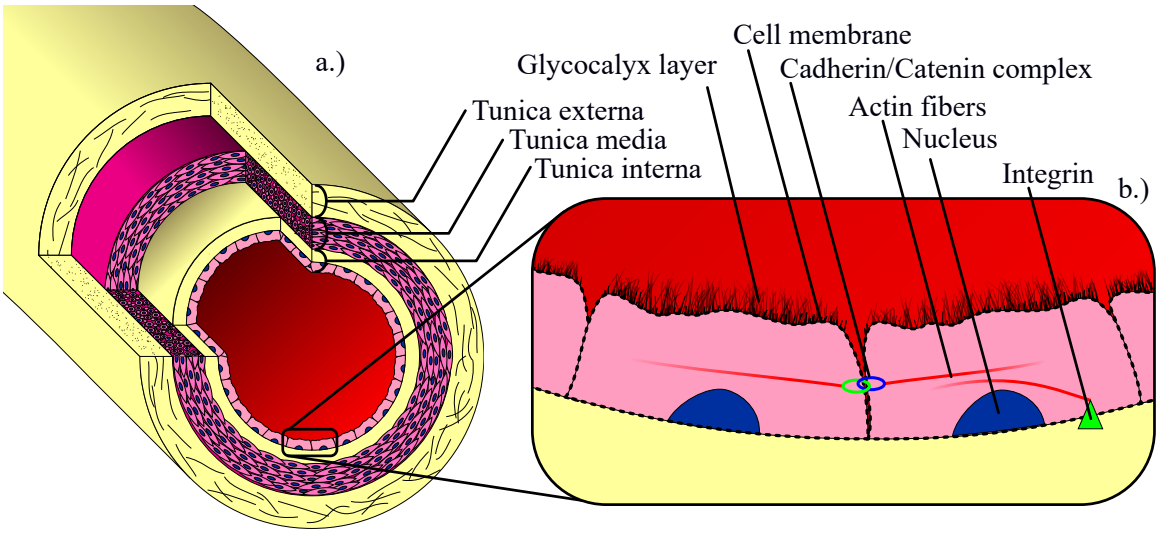

Figure 2.1: Cross-section view of blood vessel (a) and endothelial cell structure (b). Not to scale.

layer can manipulate the vascular tone of blood vessels by releasing contracting and relaxing factors, depending on the flow's intensity. This vascular tone defines the resistance of blood vessel to flow [5], and regulates overall blood flow and supply to organs. This ability to control blood flow is one of the attributes that make the endothelium a critical component for the proper functioning of the cardiovascular machinery.

Stenting affects this machinery and may lead to a damaged endothelium. A successful stenting procedure is one where the blockage is removed and the hence the vessel is revascularised and at the same time no acute or long term implications for the patient occur.

The endothelium also plays a key role in maintaining blood flow by controlling blood fluidity. The surface of a healthy endothelial layer is both antithrombotic (limits the ability of blood to clot) and anti-inflammatory (limits the response of the body to an injury, infection or death of tissue usually accompanied by local pain, heat, redness and swelling). These properties are achieved by the emission of molecules that regulate blood coagulation and platelet functions [6]. When the endothelium becomes diseased or damaged, it shifts towards the emission of procoagulant and prothrombotic molecules [7]. Thus, a diseased endothelium develops blood-clot-promoting features instead of its usual blood-clot-inhibiting features. Therefore, an endothelium that is damaged during procedures involving catheters or stents creates an environment where blood clots could be more likely to form. In the context of stenting, an impaired re-endothelialisation can lead to stent thrombosis [8].

2.1.3 The Endothelial Cell

The endothelial layer consists of endothelial cells arranged in a monolayer. An endothelial cell is shown schematically in Figure 2.1 b.

The cellular membrane is vital to the proper function of cells, as it protects the contents of the cell. The cell membrane is made of a phospholipid bilayer. This forms an effective barrier for water and solutes [1]. Specialised components can be integrated into the cell membrane, such as receptors for adhesion to specific ligands, or gate proteins for active/-passive migration of molecules. The membrane also connects to the cytoskeleton to give the cell its structural integrity and allow it to withstand external forces.

In the cell membrane, apart from the phospholipid bilayer, relevant components to biotribology include the family of cell adhesion molecules (CAMs), specifically cadherins [9] (anchors between cells) and integrins (anchors to the extracellular matrix (ECM)). Both Cadherin/catenin [10] and Integrin [11] complexes can connect to actin fibres. Actin fibres are part of the cytoskeleton; the framework of the cell. The cytoskeleton is not only responsible for structural integrity, but it can also be manipulated to allow the cell to migrate by rearranging actin fibres. Integrins act as a receptor mediating mechanical and chemical signals [12][11][2]. Apart from cadherin and integrin, cell adhesion molecules (CAMs) also include selectins and immunoglobulins [13]. Selectins allow tethering of leukocytes to the endothelium, which is necessary to allow leukocyte migration to the relevant site [6]. Adhesion is an important friction mechanism capable of damage and high friction. As the CAM's purpose is adhesion, and they are the direct interface of the cell to the surrounding environment, they could play a major role in frictional interaction and should be considered when investigating vascular tribology. Any bond or stimulus created by a contacting medical device will affect friction forces and damage inflicted to the cell.

Together, the ECs form the endothelium; a specialised, complex structure not only containing blood flow, but also responsible for the recruitment of leukocytes. Recruitment occurs via secretion of signals that enable leukocytes' adhesion and migration through the endothelial layer [14][6].

The surface of endothelial cells in contact with blood is covered with a fur-like structure called the glycocalyx. The glycocalyx consists of carbohydrates and may be imagined as hairs protruding from cells (compare electron microscope image of Reitsma et al. [15] shown in Figure 2.2). The carbohydrates connect to the membrane with proteoglycans and glycoproteins [15].

Glycocalyx serve a variety of purposes, such as: determining vascular permeability, influencing blood cell-vessel wall interactions, harbouring endothelial cells adhesion molecules, and decreasing the adhesion of leukocytes [15]. The glycocalyx are also responsible for

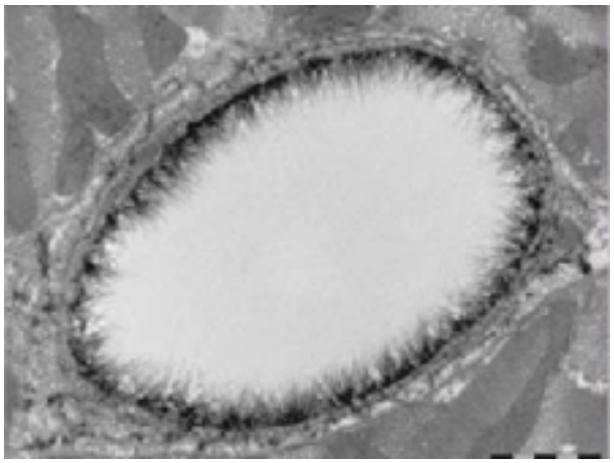

Figure 2.2: Electron microscopic image of glycocalyx (adapted from Reitsma et al. [15]).

shear-sensing and nitric oxide regulation, as well as being anti-coagulant. If the glycocalyx are disrupted, this leads to increased platelet adhesion [16]. Tribological relevance of the glycocalyx has been proposed before, when Chen et al. investigated glycocalyx influence on friction [17] and in a recent study by Lin at al. [18]. Just like CAMs, glycocalyx are in direct contact with the interacting medical device. As such, they should be regarded when studying frictional interaction on a microscopic level and interpreting vascular biotribological data.

2.2 Tribology and Endothelial Cells: Friction Induced Effects on Cell Health and Behaviour

The nucleus and the cytoskeleton may be affected by tribological interaction, without being involved in the frictional contact. The process of cells sensing and reacting to external loads is called mechanotransduction. The sensors are called mechanotransductors which regulate genes that in turn affect cell behaviour. Little is known about the specifics of how endothelial cells behave under frictional load. However, studies were conducted to investigate the effects of indentation, substrate deformation, strain and (fluid) shear stress on endothelial cells, which are the main effects occurring during a frictional experiment. These studies can serve as a reference point for what to expect from a tribological interaction. Studies where cells were tested individually to assess their mechanical failure parameters could prove useful when putting results into context.

The nucleus acts as the main memory and control unit of the cell by storing DNA (the cells gene material) and controlling processes, such as protein synthesis and reproduction. In all cells, these functions are crucial for performing the intended tasks of the respective

cell. The nucleus is suspected to interact bi-directionally with the cytoskeleton [19]. Tension on the cell can induce a reaction of the nucleus, such as gene expression or DNA damage [20]. Endothelial cells are designed to withstand (hemodynamic) shear stress and high (blood) pressures; in fact, endothelial cells thrive under the influence of high unidirectional shear stress. Shear stress is sensed by a number of mechanoreceptors, including VEGFR2/VE-cadherin/Pecam-1-complex, integrins, the glycocalyx and primary cilia. These receptors regulate many biological responses through signalling pathways including Krüppel-like factor 2, nuclear factor erythroid 2-related factor, nitric oxide and MAPK phosphatase-1. In general, high unidirectional shear stress on endothelial cells leads to a protective phenotype promoting quiescence and a healthy endothelium. Healthy shear stresses are between 1 Pa-2 Pa in arteries and 0.1 Pa-0.6 Pa in veins [21]. A low and/or oscillating shear stress can cause the endothelial cells to become pro-inflammatory, apoptotic, more proliferative, pro-thrombotic or unable to regulate vascular tone [22]. *In vivo*, these mechanisms are responsible for vascular remodelling via smooth muscle cells which are sensitive to stretch and ECs which are sensitive to stretch and shear stress [23]. However, stresses could exceed a healthy threshold during frictional interaction. Normal and shear forces affect EC cytoskeleton modelling and signalling pathways and therefore may induce functional and structural changes [24] which can result in disease. Further studies indicating that friction affects endothelial behaviour include Pitenis et al., who have shown that friction can induce inflammation (on epithelial cells) [25], and Dawson et al. who concluded that coated and uncoated catheters alike affect flow mediated dilatation [26]. Considering these studies and the close connection between a healthy shear stress and a functioning endothelium, it should be explored if and how frictional interaction directly interferes with healthy gene expressions and signalling pathways causing ECs to malfunction, linking device friction to physiopathology (connection between physiology and disease).

The cytoskeleton consists of actin fibres, microtubules and intermediate filaments. It can be imagined as a network of ropes and pipes going from one location at the cell membrane to another, enabling the cell to apply forces on the cell membrane. The cytoskeleton can be remodelled in reaction to changes in the environment.

Actin fibres are the main contributors for cell contraction. They can be imagined as ropes going from one location at the cell membrane to another. Myosin motors can move on the actin fibres to allow for cell motility. In quiescent endothelial cells, actin fibres are responsible for structural support [27][28]. When exposed to shear stress, endothelial cells remodel their actin fibres to align with the direction of shear stress to resist the external load [29][30][31]. Therefore the cytoskeleton acts as a bridge between the extracellular and the intracellular domains [32]. Hence, when the cell experiences friction induced shear stress,

the external forces must be equal to the internal forces; the cytoskeleton takes the main load. If the cytoskeleton fails under that load or cannot adjust quickly enough to the change in environment, this could cause the cell to tear apart and be destroyed. Mechanical failure for compressive loads of individual cells has been assessed by Peeters et al. who report cell bursting to occur at a load of $8.7\ \mu N \pm 2.5\ \mu N$, at a strain of $72\ \% \pm 4\ \%$ [33].

When it comes to studying the effects of tribological interactions on endothelial cells, the cytoskeleton and the nucleus should be considered as interacting units. The cytoskeleton transmits forces to the nucleus at a much faster pace than would be expected for biochemical messengers [34][35]. The nucleus then reacts to the sensed change of environment with cytoskeleton remodelling and gene expressions. This might cause ECs to dysfunction, leading to complications.

The purpose of this review section is to present biotribology research relevant to all endovascular medical devices such as stent retrievers and other mechanical thrombectomy devices (devices used to remove blood clots blocking arteries) and more advanced devices like HARP, a snake-like robot that can be inserted into blood vessels [36]. The review will however, focus on research carried out on stents and catheters, as they are the most established and common devices. Stents are thin-walled pipe-shaped mesh structures whose function is to keep a vessel open (using mechanical pressure). Catheters for vascular applications are polymeric tubes of varying flexibility deployed in the body to achieve multiple functions: to deliver stents or stent retrievers to a location or to remove or inject fluids like medication or blood. Despite the obvious physical interaction with blood vessels, the tribology between vascular medical devices and the human body is poorly understood up to this date.

2.3 Motivation for Cell Friction Experiments

Both stents and catheters, the two most common vascular medical devices, inevitably interact with blood vessels as part of their function in the body. This section shall give a general insight into where this frictional interaction takes place exactly and how it is relevant for the complication-free application of the respective devices by considering them from an engineering point of view.

2.3.1 Tribology in Stent Applications

Stents are mesh structures used to keep open a vessel that has been blocked. They are used, for example, during percutaneous coronary intervention, where a blood vessel in the heart is obstructed and needs to be revascularized. The stent is delivered with a catheter to the

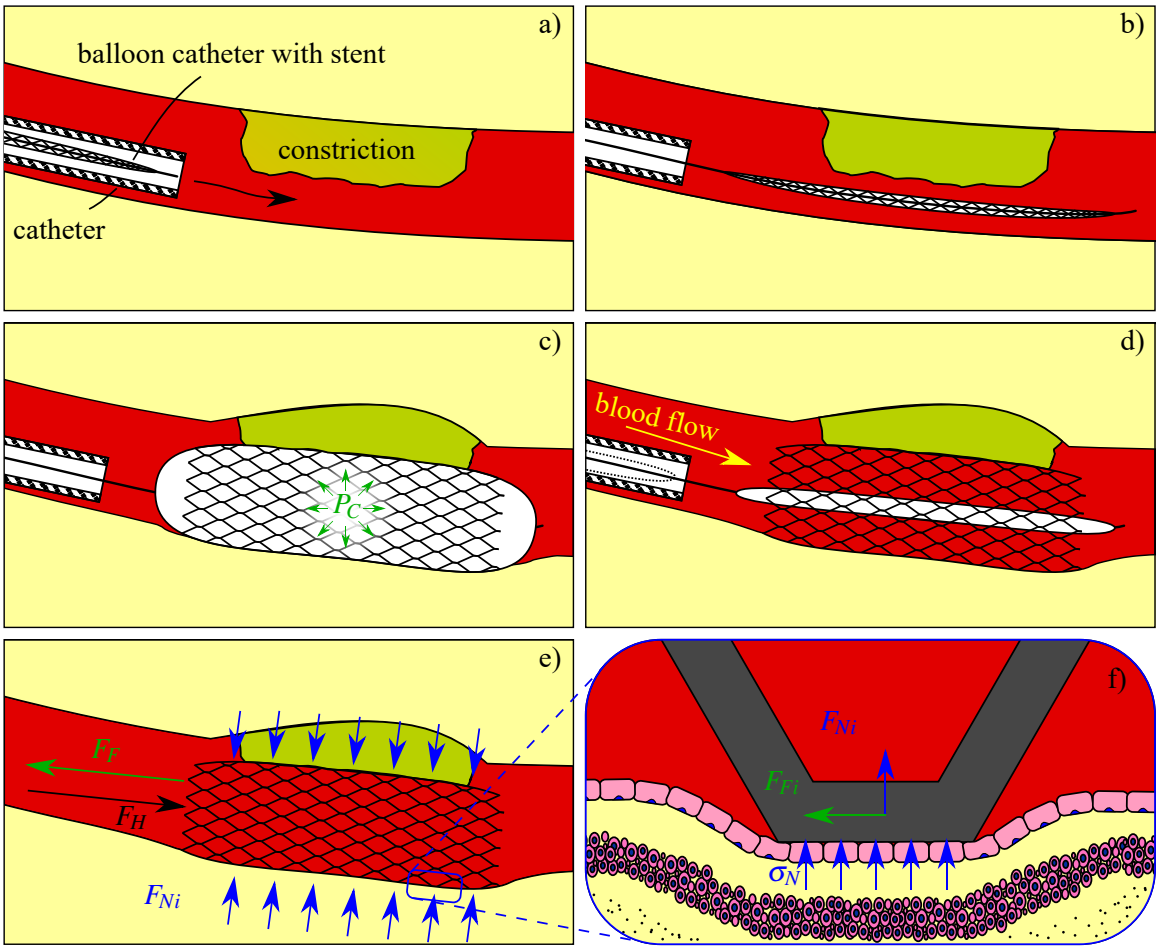

Figure 2.3: Stenting process. a) Delivery of catheter and balloon catheter with stent to constricted vessel. b) Positioning of balloon catheter and stent along constriction. c) Inflation of balloon with pressure P_C, widening the stent and restoring vessel volume. d) Retraction of balloon catheter into the catheter and restoration of blood flow. Blood flow direction marked in yellow. e) Forces acting on deployed stent: Normal forces F_{Ni} between vessel wall and stent struts, friction force F_F, which keeps the stent in place, hemodynamic force F_H exerted by the blood flow on stent. f) Detail view of a single stent strut pressing against the endothelial layer with normal pressure σ_N, resulting in normal force F_{Ni} and friction force $F_F i$.

site of obstruction where it is expanded using a balloon catheter, as seen in Figure 1, with balloon pressure P_C between 8 and 20 atm [37]. Then, the balloon catheter is deflated and flow is restored; the vessel is revascularized. The catheter and balloon catheter are then removed, whilst the stent stays in place ensuring the vessel stays open.

Tribology is relevant during both the deployment and the deployed phase. In the deployment phase, it is important not to cause excessive damage to the tissue, as this may necessitate further intervention. The possible friction related complications caused by stent intervention are covered later.

When the stent is deployed, the possibility of stent migration presents a major complication. It means that the stent is being “washed” downstream under the hemodynamic force

exerted on it by the blood flow, causing it to migrate away from its original deployment site. Stent migration can be attributed to an unfavourable ratio of friction to hemodynamic force. Considering this from an engineering point of view (force diagram, Figure 1 e), only a few forces are exerted on the stent: the hemodynamic force $F_H(t)$, normal forces F_{Ni}, and friction force F_F. $F_H(t)$ is caused by blood flow, making it highly time dependent due to the cardiac cycle. Normal force F_{Ni} is the contact force the vessel wall exerts on the ith stent strut due to the contact pressure σ_N and is related to it by the surface integral of the normal pressure σ_N over the apparent contacting surface $A_{Contact,i}$:

$$F_{Ni} = \oiint^{A_{Contact,i}} \sigma_N \mathrm{d}A \tag{2.1}$$

This interaction causes a friction force which is determined by the static friction coefficient μ_S. The static and not the dynamic friction coefficient should be considered because the stent is not supposed to move. Using Amonton's law on the infinitesimally small area dA, the friction force for the ith strut is:

$$F_{Fi} = \oiint^{A_{Contact,i}} \mu_s \sigma_N \ \mathrm{d}A \tag{2.2}$$

Together, those partial friction forces exerted on the stent, which has n struts, make up the total friction force acting on the stent F_F:

$$F_F = \sum_{i=1}^{n} F_{Fi} = \sum_{i=1}^{n} \oiint^{A_{Contact,i}} \mu_s \sigma_N \ \mathrm{d}A \tag{2.3}$$

Returning to the force diagram, the only forces acting along the vessel direction are F_H and F_F which act against each other. When the maximum hemodynamic force exceeds the friction force, the stent can be flushed away and migrate, hence the condition to avoid stent migration is: $F_{H,max} \leq F_F$ and with Equation 2.1

$$F_{H,max} \leq F_F = \sum_{i=1}^{n} \oiint^{A_{Contact,i}} \mu_s \sigma_N \ \mathrm{d}A \tag{2.4}$$

From this equation, there are several ways to decrease likelihood of stent migration. The first is to increase the normal pressure. This has been done for many years and is known as stent oversizing. It means that the stent is chosen to be bigger than the vessel and hence a larger normal pressure can be achieved. However, this comes with the disadvantage of

possibly damaging the artery as bigger oversizing means more strain to the vessel. Other options to decrease the likelihood of stent migration are to decrease the hemodynamic force by making the stent more streamlined or to increase the contact area, either by adding more struts or by increasing the individual struts contact area. Finally, the friction coefficient could be increased, and this is where tribology comes into play. As stents are inflated very slowly (over $\approx$ 30 s, [38][39]) and hereafter supposed to be static, they can be assumed to be in a permanent state of boundary lubrication. While theoretically blood is an available lubricant and should be considered as such, in practice it probably cannot provide sufficient lubrication during stent application. This is due to the high contact pressure and the low speeds in conjunction with blood's relatively low viscosity. Therefore, chemical and physical properties of the materials are the major factors driving the interaction. Since cells possess the ability to adhere strongly via adherens junctions and ECM molecules [10][11], chemical bonds may play important roles governing the friction between stent and vessel wall. Furthermore, since the glycocalyx consist of long carbohydrate chains, Van der Waals forces and electrostatic effects may occur. This may contribute to the adhesion force F_{Adh} occurring over the real contact area $A_{Contact,real}$ (i.e: actual contact area on a microscopic level where surface asperities interact). Through interfacial shear stress τ:

$$F_{Adh} = \oiint^{A_{Contact,real}} \tau \, dA \tag{2.5}$$

and through F_{Adh}, the static friction coefficient is influenced.

2.3.2 Friction and Wear Implications in Stents

In vascular applications, most commonly, stents are folded around a balloon catheter which is then inflated inside the stenosed (constricted) vessel to revascularize it (re-establish flow). Other designs include self-expanding stents made from advanced materials like shape memory alloys. During catheter or stent deployment, these devices induce friction and radial forces, causing damage to the blood vessel in two ways: 1) the arterial wall can be overstretched and thus injured; 2) the endothelium can be damaged or removed due to friction [40]. Overstretching is caused by too high pressures while the friction damage to the endothelium is a tribological problem.

Damaged endothelium is known to be a leading cause of failure by restenosis (a reconstriction). Restenosis can necessitate a new revascularisation procedure or cause late stent thrombosis [41]. The reason for this is that the natural reaction of the body to the damage is very similar to wound healing, including steps of blood clotting, inflammation,

and recruitment of new cells by proliferation [42]. Marx et al. reviewed the restenosis progress under consideration of smooth muscle cell (SMC) proliferation (multiplication) [43]. Normally, SMCs are kept in a quiescent state where they do not divide or migrate. This is important because uncontrolled growth would decrease the blood vessels lumen. However, they can be activated to switch into a proliferative and migrative mode to repair the vessel after injury. Although this is meant to be a recovery mechanism, it can be disadvantageous as, in a stented artery, this can cause restenosis. The factors that lead to the activation include growth factors, cytokines (proteins involved in cell signalling) and reduced inhibitory factors. Under normal circumstances, the healthy endothelium protects from circulating growth factors by acting like a barrier and producing factors that inhibit SMC proliferation and migration. To counter the harmful proliferation of SMCs, drug-eluting stents can be delivered using medications that inhibits intimal proliferation [43]. Cornelissen et al. reviewed the harm caused by stenting and state that the re-endothelised tissue is often still incomplete or dysfunctional, which promotes in-stent thrombosis and restenosis [44]. Therefore, damage and de-endothelisation caused by tribological interactions must be studied with the aim to minimise or avoid damage to the endothelium. Biotribology can help to understand the underlying friction mechanisms. This knowledge could be used to prevent the root cause of restenosis: the destruction of the endothelium.

After the stent has been deployed, natural deformation of the vessel due to the cardiac cycle can also cause rubbing and friction between the stent and the arterial wall. This might cause further damage or irritate the endothelial cell layer. The endothelium tries to repair itself and, in the process, can cover the stent struts [45]. As the new endothelial cells may be damaged, this can lead to the formation of stent thrombi [46]. Once the endothelium is damaged, the aforementioned chain of events leading to restenosis can be activated. Furthermore, an inflamed cell layer can cause atherosclerosis [47].

A damaged endothelial layer causes restenosis and in-stent thrombosis. These two diseases can be minimised by reducing the damage caused to the endothelial layer when the stent surface is interacting with it, both in the deployment and the deployed phase. Tribology could help to assess and minimise the wear damage caused to the endothelial layer due to the understanding of the underlying friction mechanisms these studies provide. Tribological studies will also help to develop materials that, in turn, produce less invasive stents.

Another complication connected with stents is migration. Migration happens after a stent is deployed if the hemodynamic force of the pulsating blood is higher than the friction force between the stent and the vessel wall. Understanding and optimising friction could help to develop stents that have less risk of migrating for the reasons laid out in Section 2.3.

2.3.3 Tribology in Catheter Applications

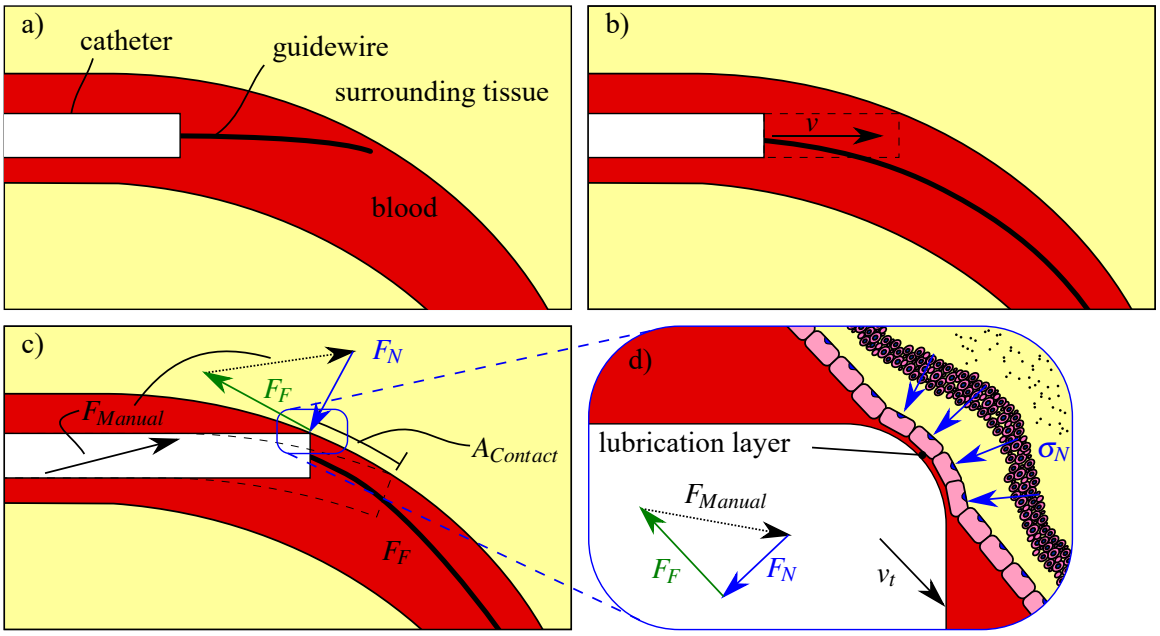

Figure 2.4: Cross-section view of insertion of a catheter into a blood vessel. a) advancing guidewire into vessel b) Movement of catheter through artery with speed v (initial contact of catheter and artery marked by dotted catheter outline). c) Catheter inserted further (final position marked by dotted catheter outline) causing contact and consequent friction at contact area $A_{Contact}$. Forces F_N and F_F determine manual force F_{Manual} required for insertion of catheter. d) Detailed view of contact between catheter and artery. Normal pressure between endothelial cells and catheter σ_N under tangential speed v_t with formation of lubrication layer.

Catheters are tubes usually made from a soft polymer which are inserted into vessels, for example to deliver drugs or medical devices, such as stents. During vascular surgery, guidewires are inserted and advanced through the vessels to guide the catheter to the correct position in the body. This interaction can cause damage to the vessel wall which may cause complications during the intervention. Contrary to a stent's stationary application in the body, the application of guidewires and catheters is of a dynamic nature. They move through the body, touching the vessel walls under relative motion. This is schematically shown in Figure 2.4. After advancing the guidewire into the vessel (Figure 2.4 a), the catheter is pushed into the vessel, guided by the guidewire (Figure 2.4 b) and as the vessel goes around the corner, the catheter touches it along contact area $A_{Contact}$ as shown in Figure 2.4 c. Like the stent, the catheter experiences a normal pressure σ_N from the vessel wall, resulting in a normal force F_N and a friction force F_F through the respective surface integrals; but in this case, there is only one contact area (Equation 2.1, i=1). Hemodynamic effects are neglected in this drawing. Contact forces can be expected in the range of 0 N to more than 1.5 N, with forces bigger than 1 N considered critical [48].

F_{Manual} is the force applied by the person carrying out the insertion operation. This force is determined by the forces F_N and F_F. Hence, a higher friction force causes a higher resistance. This resistance could be reduced through the application of friction and lubrication knowledge. In addition to hindering the intervention, the contact between endothelial layer and catheter means risk of damage to the endothelial cells (wear). This could be prevented by using advanced materials.

As catheters are supposed to move relative to the vessel surface most of the time, lubrication will play a more important role for these medical devices than with stents. Good lubrication may make the procedure easier by enabling lower friction. It may also improve safety by reducing the likelihood of complications, as good lubrication is generally associated with wear reduction. Lubrication regimes are described by the Stribeck Curve which connects friction with sliding speed, lubricant viscosity and normal load. While deployed, stent friction takes place in the boundary lubrication regime (mostly direct contact of surfaces) due to low speeds; catheters could be pushed into mixed (still surface contact but thin film lubrication is present) or even hydrodynamic (full separation of surfaces by lubricant film) lubrication during movement. Soft tissue contact mechanics govern the interaction between the soft vessel surface and the harder medical device material. Models to describe the contact include: the fundamental Hertzian contact theory [49], the JKR model [50], the Winkler foundation model [51] and the Derjaguin Muller Toporov model [52]. Modelling the contact could prove essential to determine pressures and understand the interaction better.

2.3.4 Friction and Wear Implications for Catheters

When a catheter is inserted into a blood vessel, it inevitably touches the vessel walls and could damage the endothelium in the process. This can disrupt the critical functions of the endothelium and could therefore lead to complications like restenosis. An enhanced catheter surface could reduce the risk of injury during insertion. Furthermore, a low-friction catheter might make the procedure simpler and therefore safer overall [53][54]. Certain catheters, such as intravenous catheters, can stay at the same location after insertion. However, when the patient moves, the catheter may interact with the vessel, resulting in irritation. A recent study from Takahashi et al. investigated the effectiveness of reducing mechanical interaction between intravenous catheters and vessels, in order to reduce catheter failure at peripheral intravenous applications. This study shows that reducing interaction could help to lower the risk of catheter failure [55]. Interaction between current catheter materials and blood vessels can cause problems, which can be mitigated by avoiding this

interaction. However, the method outlined by Takahashi et al. required scanning and analysis of vein diameters, a procedure for which there may not always be time. An alternative approach would be to develop materials which even when contacting the artery would not cause major damage. This would eliminate the necessity for expensive and time-consuming scanning procedures and hence make the intervention cheaper, quicker, and more accessible.

2.3.5 Conclusions

Some of the complications caused by vascular medical devices which inherently interact with the blood vessels are of a tribological nature. This becomes obvious when looking at these complications in the context of the very basic concept of tribology: friction, lubrication and wear. The problem of stent migration and difficult catheter deployment can be traced back to an insufficient and an excessive (static) friction coefficient, respectively. Blood can be considered as lubricant in vascular tribological interactions, yet its role has not been explored sufficiently. The serious implications of restenosis are ultimately caused by damage or wear of the arterial wall, making tribological studies necessary.

Therefore, in conclusion, it is important to source and develop methods that allow for the study of vascular biotribological interaction. A deeper understanding on both macro and microscale could then allow for quicker development and discovery of new, promising and less invasive materials, coatings or surface treatments, ultimately making the intervention with stents and catheters less invasive and safer.

2.4 Approaches for Investigating Cardiovascular Medical Devices

Friction studies on the interaction of medical devices with tissue have been conducted using a wide range of techniques, with varying complexity and realism in terms of their emulation of the real system. Tribological experiments can generally be categorised into five major categories of increasing complexity. Each of these categories has advantages and disadvantages. More complex studies usually promise to have a greater significance and more representable results at the cost of reproducibility and financial and time commitments. The five categories in order of increasing complexity are models (using artificial materials as surrogate for biological tissue), *in vitro* (in a petri dish), *ex vivo* (tissue extracted from an animal), *in vivo* (in a living animal) and medical studies. Furthermore, *in silico* (on a silicon chip, computer) models can help to simulate interactions without requiring physical

resources apart from a computer. This section divides experiments into categories based on the environment of the testing apparatus: models, *ex vivo*, *in vitro*, *in vivo* and *ex vivo*, and *in silico*.

2.4.1 Models

Experiments conducted simulating the vessel tissue with a supplement such as a hydrogel, but without biological components, are called models in the context of this review. By simplifying the system that they mimic, models provide more control over the variables. Hence, experiments of this type tend to be more reproducible than the more complex ones and are better at evaluating the influence of specific components. Instead of starting with a complex system and then simplifying it until the experiment is controllable and reproducible, this type of experiment can be seen as a starting point for a different approach where complexity is added as needed. A downside of these experiments is that it can prove difficult to find materials that match the exact behaviour of biological tissue. Also, because realistic behaviour needs to be verified, experiments involving real tissue are inevitable. One of the biggest disadvantages of these experiments is that cell damage and behaviour cannot be investigated. However, models can be used to gain initial insights as they are cheap and quick to set-up. Ho et al. investigated uncoated and poly(MPC-co-BMA) coated PU catheters regarding friction against an AFM tip and surface roughness under wet and dry conditions. While no significant difference could be observed under dry conditions, significantly decreased surface roughness and friction forces were observed under wet conditions [56].

2.4.2 *in vitro*

Classically, in *in vitro* experiments, cells are cultured on polystyrene or glass. This type of experiment has the advantage of using biological components in a controllable environment, hence they are closer to reality than models. However, the mechanical parameters of the substrate (polystyrene or glass) do not match the ones of the real tissue, which leads to pressures that are unrealistically high. To avoid this disadvantage, alternative, soft materials can be used as a substrate, such as hydrogels. The hydrogel approach allows an approximation of *in vivo* mechanical parameters of the ECM and thus lower, more realistic pressures occur than when cells are seeded on polystyrene or glass. Those studies allow for the examination of cell damage depending on the normal pressure, as it can be estimated using Hertzian contact theory or simulations. A disadvantage of most *in vitro* experiments is that they usually do not include the use of the natural lubricant in blood vessels that is blood

itself. It is known that blood is a complex suspension of cells in a liquid and has viscoelastic properties [57]. Given the major influence of the lubricants properties in tribological systems, especially in (elasto)hydrodynamic lubrication [58], it may be worth investigating further the blood's influence on vascular tribological systems to replicate the real situation. *In vitro* experiments allow researchers to investigate which parts of the cells react to friction and could possibly be exploited to fine tune friction coefficients. In 2010, Chen et al. investigated the influence of the glycocalyx on human umbilical vein endothelial cells (HUVECs) [17]. Cells were treated with TGF-β1 to increase the glycocalyx by 148 % or heparinase I to decrease the glycocalyx by 57 %. They found that heparinase I treated cells experience higher frictional stress than non-treated cells, which, in turn, experience higher frictional stress than TGF-β1 treated cells. This study suggests that glycocalyx play an important role in reducing friction. While they draw the connection to friction between red blood cells squeezing through capillaries, the glycocalyx could influence friction between medical device and artery. This study is a good example of how *in vitro* experiments can be used to investigate tribological effects of different cell parts. Pitenis et al. demonstrated the potential of *in vitro* experiments to study the biochemical reaction of cells to friction, as they detected inflammatory markers after conducting tribology on epithelial cells *in vitro* [25]. Marshall et al. developed a spherically capped hydrogel probe that allows the application of load independent contact pressures for low deformations [59]. While this probe shape is not suitable for all materials, this technique may be used for some catheter materials. A lot of research has been conducted on the friction between corneal epithelial cells and hydrogel materials to improve the interaction between the human eye and contact lenses. Established techniques of this research field [60][25][61] could be applied to vascular biotribology.

2.4.3 *ex vivo*

Ex vivo experiments are carried out on tissue that is removed from the animal and then mounted onto a tribometer allowing a precise measurement of normal and friction forces under realistic parameters. These experiments are a compromise between being close to the real tribological system while still allowing the measurement of friction and normal forces which proves difficult in *in vivo* experiments. After the experiment, the sample can be examined for cell damage. The main disadvantage of this type of experiment is that removing the substrate from the body causes relaxation due to the lack of blood pressure. Hence, the material behaviour may differ from when before the substrate is removed from the body.

Takashima et al. used an universal tester to determine friction coefficients between a porcine aorta and a steel ball [54]. The universal tester allows changes in the initial angle between the aorta surface and the horizontal plane. The study suggests that static and dynamic friction coefficient depend on this angle.

2.4.4 *in vivo*

In vivo studies are carried out by inserting a medical device into a living being and examining cell damage by removing the affected tissue after the experiment. A limitation of this approach is the difficulty to measure the exact normal and friction forces. Pull-out forces can be measured to obtain values for the friction component, but the normal component is difficult to measure. Capron et al. investigated the damage a balloon catheter causes to the artery during so called "soft" (inflating the balloon with 0.05 mL of water) and "hard" (0.09 mL-0.11 mL inflation) friction, quantifying the severity of the interaction in ml injected into the balloon catheter rather than in normal pressure [62]. It was found that "hard" friction removes the whole endothelium while "soft" friction can leave parts intact. As established earlier, a dysfunctional endothelium can cause problems in the form of thrombosis or stenosis. While the approach of quantification in the form of measuring added volume is pragmatic, reporting the pressure in the catheter would allow for more comparable results.

2.4.5 *in silico*

In silico studies have been conducted to estimate friction between cells and medical devices. This approach yields the opportunity to simulate the interaction between blood vessel and materials used for medical devices with no physical testing. Rather, a computer model/simulation is built and verified using a given data set. Then parameters for different materials can be inputted to the model and results can be obtained much quicker than with physical testing. Advanced models also include the influence of blood as lubricant. These models could possibly be developed further to estimate cell damage. Simulations rely on being verified by experiments and the availability of the mechanical properties of the material of interest. If this data exists, simulations present a quick way of predicting the experiments outcome without needing anything but a computer. Vad et al. approached the evaluation of the friction coefficient between a stent graft and a PDMS tube and developed a computer model to simulate the contact, finding that oversizing can increase the friction coefficient and hence reduce the risk of stent graft migration [63]. Prokopovich and Perni investigated the friction coefficient of catheters against sheep artery and vein tissue using a JKR theory

based model they developed that predicts the friction force between tissue and biomaterials based on the material parameters and asperity density. They reported that the predicted forces agree with earlier obtained experimental values [64]. They then developed the model further so that it could account for different asperity shapes and the presence of blood as a lubricant [65]. Prokopovich and Perni's simulated results matched well with experimental data and they found that friction between catheter and vessel is mainly dominated by adhesion effects. While experiments simulated *in silico* are not able to reflect the real world interaction perfectly due to its complexity, they have a lot of potential and could be used to highlight promising materials that could then be tested in the real world using *in vitro*, *ex vivo*, or *in vivo* experiments.

2.5 State of the Art *in vitro* Cell Friction Experiments

This section gives an overview over the results of past vascular biotribology studies and their relevant context, as well as recommendations for future studies.

2.5.1 Biotribology for Catheters

For tribology on catheters, two factors should be considered. First, damage caused by frictional interaction between the surfaces on a cellular level should be avoided. Secondly, the friction coefficient should be as low as possible to allow for a quicker and gentler intervention. Classically in tribology, low friction and low damage are linked and it has been shown that lower friction catheters cause less damage in rabbit arteries [66]. Higher frictional forces have been reported to cause inconvenience to the patients during the deployment of the catheter [54].

During deployment, catheters can interact with cells by dragging or removing them from the surface. Dellimore et al. [67] observed high complications with high morbidity (such as mechanical traumata) following the mechanical interaction of urinary catheter and urethra. A review by Dellimore et al. [68] has shown that transcatheter cardiovascular intervention often results in complications that can be linked to mechanical interaction between vessel wall and catheter. Those complications include vascular trauma, haemorrhage and arterial spasm. The prevalence of those complications can be reduced by passive catheter design strategies including surface topography and material design to reduce friction. This study has shown that while some procedures, such as percutaneous coronary intervention, were very mature (i.e. plateauing or decrease of complication prevalence) at the time of the review. Other types of vascular intervention, such as transcatheter aortic valve implantation

and endovascular aneurism repair, still yielded potential for improvement. Lowering friction of catheters has been investigated regarding polymerization [53], hydrogel coatings [69], and polymer coating materials [66][56]. Ho et al. also suggest a further investigation into the contact between endothelial cells and polymers with a focus on cellular adhesion molecules and damage caused to the cells [56], which is supported by the simulations of Prokopovich et al. suggesting that adhesion plays a major role in the interaction [64]. Niemczyk et al. investigated friction of chitosan coated catheters and compared them to commercially available coated ones using an *in vitro* system. They found that (chemically modified) chitosan coatings act as lubricous coatings - frictionally comparable to hydrogel coatings - while coming with additional advantages as they are biodegradable and antimicrobial [70].

Weiss et al. simulated catheter-vein contact to investigate thrombophlebitis (sterile inflammation with formation of a blood clot) [71], a common complication with intravenous therapy [72]. Hydrophilic-coated catheters were reported to cause less trauma than uncoated catheters and were preferred by patients according to Stensballe et al. [73]. Additionally, a recent study by Lin et al. revealed that a hydrophilic coating reduced wear to the glycocalyx [74]. The findings of Weiss et al. [71], Stensballe et al. [73] and Lin et al. [74] are particularly interesting considering the recent studies of Pitenis et al. who found that friction can promote inflammatory gene expressions [25] as an anti-inflammatory phenotype is one of the key features of ECs. As mentioned earlier, shear stress is sensed by ECs through a number of mechanoreceptors and an inappropriate shear stress can cause endothelial cell dysfunction which can lead to more severe complications which, hitherto, seems to affect catheter physiopathology. Even modern, hydrophilic coated catheters, while coming with the advantages of increased patient comfort and reduced spasm incidence, were not found to positively influence endothelial dysfunction and radial occlusion. This suggests that the current reduce in friction alone is not enough and more in-depth understanding is required to tackle the latter two complications [75].

Dellimore et al. [76] investigated Attenuated Total Internal Reflection Fourier Transform Infrared (ATR-FTIR) spectroscopy for quantification of catheter-induced tissue damage *in vivo* using an *ex vivo* set up on porcine aortic tissue. They found clear changes in the resulting FTIR spectra; Most notably damage to the outermost layer of the aorta changed the spectrum significantly, making ATR-FTIR a promising tool for future wear assessment of catheter induced damage. Furthermore, they recorded the friction coefficient during the controlled tissue damage testing and found that friction of catheters on aorta is a function of wear. The friction coefficient they measured was between 0.05 and 0.25, decreasing with consecutive sliding (representing different complexities of catheter intervention) of the catheter, which was attributed to increasing wear [76].

Much work has been done to improve catheters making them safer to use and more comfortable for the patient. Future experiments to improve catheters should be carried out with the aim to be comparable, meaning that the severity of the frictional interaction should be quantified in reproducible parameters, for example by mentioning the normal pressure and relative speed between the surfaces, the frictional force and the geometry of the probe. The interaction between current catheter materials and the human body is not sufficiently understood and optimised up to this point and investigating it further could yield great potential.

2.5.2 Biotribology for Stents

This section reviews the insights we have gained into the tribology of stents. When discussing biotribology for stents, two phases should be considered, deployment and stationery. During the deployment phase, damage to the endothelium occurs due to interaction of vessel wall and stent, which can be so severe that the endothelium is entirely removed from that region. This is wear damage. Hence, in this phase, the wear aspect of tribology is the focus and is linked to in-stent thrombosis and restenosis as established earlier. The second phase is the deployed stage of the stent. While wear in form of constant irritation due to blood vessel interaction must be considered again, the friction aspect takes a significant role in this phase. This is because stent migration in its core is a (static) friction related problem. Both phases must be considered when conducting tribological experiments on stents.

During the deployment phase, wear plays a major role while the coefficient of friction is secondary. Hence, experiments that focus on cell damage/tissue damage and biological reaction are important. Franke et al. used a special apparatus to assess endothelial cell reaction on stenting *in vitro*. In their experiment, a stent mounted on a balloon catheter was pressed in between two surfaces that were cultured with endothelial cells. The balloon catheter was inflated with a pressure of 9 bar. Afterwards, the stent was removed. Nitric oxide, prostacyclin and lactate dehydrogenase were measured. A significant decrease of nitric oxide, which is responsible for down regulation of platelet aggregation, was found [77]. As increased platelet aggregation promotes thrombosis, this makes sense considering in-stent thrombosis is a common complication with stents. Dunn et al. conducted tests with a glass pin on bovine aortic endothelial cells. They drew a connection between damage to the endothelial layer caused by stent deployment and stent migration under the influence of pulsatile blood flow. Dunn et al. also found that pressures around 5 kPa were required to cause significant cell damage [78].

In the deployed phase, there could still be damage or irritation caused by long term interaction between stent and vessel wall. This is supported by a study conducted by Pitenis et al. focusing on biochemical responses during the interaction between hydrogel and epithelial cells which increased the expression of pro-inflammatory genes [25]. Although epithelial cells were used rather than the inner lining endothelial cells, this shows that friction can cause inflammation. Similar experiments must be conducted on endothelial cells and if endothelial cells also show signs of inflammation as a reaction to friction, it should be investigated what causes the inflammation and if advanced materials could reduce it. However, as quantitative knowledge about the interaction in this phase (pressure and relative speeds) is very scarce, it has been difficult to study tribology of deployed stents up to now. Hence, before conducting such experiments, it is crucial to find reliable values for the required mechanical parameters, for example, by means of finite element simulations.

However, during this stage, the CoF plays a major role. Chen et al. studied the friction between aortic stent grafts against porcine aorta, PDMS and PVA cryogels. They reported an average friction coefficient of 0.0328 to 0.0540 for a material pairing of porcine aorta/stent graft sheath [79]. McGee et al. researched the effect of calcification on tissue-stent interaction. They found that calcification significantly increased the coefficient of friction from 0.09 ± 0.05 up to 0.350 ± 0.015 [80].

Dean et al. investigated friction on smooth muscle cells using Lateral Force Microscopy. They report a friction coefficient of 0.06 [81]. All of these friction coefficients are very low and increasing the friction coefficient would likely lead to a decreased likelihood of the stent migrating. According to Liffman et al., the force exerted on the stent-graft by the blood flow may exceed the force needed to displace it [82]. Certain frictional interactions, hooks and barbs and stent-graft oversizing are used to keep stent-grafts in position [63]. Furthermore, reliable values for the friction coefficient are required for advanced finite element modelling of stents and stent grafts [63][83]. Hence, in the context of stents, the effect of friction coefficient and damage caused must be studied very carefully. Generally, in tribology, a higher friction coefficient is associated with higher damage. On the other hand, a low friction coefficient could promote stent migration which is undesirable. Therefore, in-depth studies of the underlying friction mechanisms are necessary to find out if there is an inherent parity between damage and CoF and if not, how a sufficiently high CoF can be obtained while reducing the damage caused to the endothelial layer.

2.6 Conclusions and Room for Improvement of Current Approaches

Conclusively, it can be said that vascular intervention with stents and catheters can cause significant damage on a tissue level, which can lead to severe diseases such as thrombosis and atherosclerosis. Furthermore, it can interfere with a healthy endothelium's cell mechanics and cause endothelial dysfunction. To avoid these diseases, mechanisms between endothelial cells and medical devices must be exploited to develop better materials for the future. It can also be used to improve numerical simulations of interventions. Studies have been carried out to investigate cell damage and friction coefficient, but few have quantified the damage in a comparable way and studied the contact interactions in-depth.

Many studies use a glass bead as probe, but to obtain real contact conditions and to assess friction and wear more meaningfully, it is necessary to use real material pairings. Chemical interaction between the two surfaces appears even more important considering the finding of Prokopovich et al. that adhesion is the driving factor in friction between catheters and arteries [64]. Therefore, more research should be carried out regarding cell reaction on mechanical interaction and friction using real medical device materials such as stainless steel, Nitinol and different polymers.

When studying medical device materials, *in silico* models, as well as *in vitro*, *ex vivo* and finally *in vivo* experiments may be utilised to better understand the interaction. Simulations like the one of Prokopovich [64], that would ideally be able to simulate cell damage, could be carried out to scout for suitable materials. Materials that are deemed to be promising could be used as probe materials in *in vitro* studies on cultured monolayers to examine their compatibility under friction. *In vitro* studies should evaluate cell viability, inflammatory markers and coefficient of friction and parameters may need to be adjusted for different applications (stents, catheters). Results need to be compared and verified with *ex vivo* and finally *in vivo* studies.

This work focuses on *in vitro* experiments to investigate cell damage on a monolayer level. The main issue with these experiments is the special load regime. Due to the mechanical parameters of the tissue (which is very soft in terms of general engineering terms) under the endothelial layer, the loads applied to the endothelium must be considered very carefully. In many studies, cells are cultured on standard cell culture grade polystyrene (PS) or glass. While it is a well-established material for cell culture, using such a hard substrate (in cell dimensions) can introduce great, unrealistic loads. This is not only an issue when assessing the damage to the endothelium, but also when measuring friction. If the monolayer is breached completely, it is possible that the substrate underneath is in direct contact

with the countersurface. At this point, the measured interface is not cells against countersurface material, but rather substrate against countersurface material with cells acting as a lubricant.

Some studies have made efforts to address this issue in different ways. The applied normal force could be reduced to microscopic levels and thus it could be ensured that only the monolayer is tested. Another way to lower the pressures in the contact is to change the countersurface geometry. As one of the most common geometries used in tribology are spheres, the radius of those can be chosen larger, which also reduces the pressure. An example for the use of these two approaches in conjunction is the study of Dunn et al. who tested endothelial monolayers against a borosilicate glass probe of radius 7.78 mm under normal loads of 0.4 mN-1.2 mN [78]. However, to achieve such low loads, a special microtribometer is required, which may be cost-prohibitive. Furthermore, not every set-up (like the one used here) allows the installation of such large spheres, and if only a sphere cap is to be used, this requires manufacturing of the geometry, which again, could be cost-prohibitive. Another option which was developed by Marshall et al. is to use hydrogel membrane probes to achieve very low pressures [59]. This option is affordable, capable of applying very low pressures and most research facilities should posess the equipment required to manufacture these probes. However, it is limited to hydrogel materials. Finally, a softer substrate could be chosen, similar to the *in vivo* situation. Not many studies have chosen this approach for tribological experiments. However, soft substrates with attached cells are at the core of microfluidic experiments. Chen at al. used cells cultured on hydrogels to investigate the damage caused to the glycocalyx [17]. In this work, a different approach was chosen and soft substrates were manufactured with a polydimethylsiloxane polymer. They were then made inhabitable for cells and cultured. This allowed cell against probe interactions to be achieved with low pressures at a lower cost than the other options.

Apart from the implementation of such low loads, when analysing the raw data, two issues became apparent. Firstly, the sample surfaces were not flat. Secondly, the samples were not aligned perfectly with the force sensor. Both resulted in the sample surface being on a slight slope compared to the X and Z axes of movement. This caused problems because reaction forces that should only act in the Z (normal) direction exhibited components in the X (friction) direction. For most applications this effect is negligible, however, for the experiments conducted in this work, the implications are relevant due the very low friction coefficients occuring. When researching this, it became apparent that this issue must be adressed for all very-low-friction experiments [84][85][86]. The general solution to account for it is to conduct a reciprocating experiment, including at least one forward and one backward measurement. As theoretically (assuming a sufficiently stiff substrate, probe,

force sensor and tribometer), on the way backwards the slope is of the same magnitude, but of opposite direction, as it is on the way forwards for any given position, the slope can be accounted for by averaging the two (or more) measurements. Burris et al. approached this by sliding over the sample twice, forwards and reverse, to calculate an average friction coefficient for which the influence of the slope effectively cancels out [84].

While it is a very elegant approach, it was not suitable for the experiments conducted here for several reasons. Firstly, as only one slide is tested, no data for the opposite direction is available. Secondly, with soft substrate (or probes), the substrate cannot be assumed to be infinitely stiff and therefore, the position of the probe on the sample (and with it the slope) may differ for forwards and backwards direction at the same stage position. Thirdly, with cells, the substrate surface, and with it the interface, may change considerably from forwards to backwards slide due to damage caused to the monolayer. For this reason, a mechanical model was developed to account for most of the slope while only requiring one test in one direction.

2.7 Aims and Objectives

This work aimed to study the frictional interaction between the endothelial cells of blood vessels and medical devices under a range of loads and for different materials. For this, an *in vitro* approach was chosen and friction and damage were measured.

A methodology had to be developed that would mimic a vessel as closely as possible *in vitro*. The second objective was to develop methods to analyse and quantify the damage the friction experiment caused to the sample. Finally, the damage of the blood vessel surrogate against different materials and under different load conditions was quantified.

Chapter 3

Materials and Methods

3.1 Introduction

The methodologies used in this work which were required to quantify and analyse damage and friction are described in this chapter. Standard cell culture procedures are described in Appendix D. This chapter states the protocols for the procedures and, for novel ones, the derivation.

As most of this *in vitro* work revolves around the sample, in the next sections, the whole experimental process is based on the lifecycle of a sample. For context, Section 3.2 explains what the purpose of a sample is and what requirements it has to fulfill. Section 3.3 gives an overview of the lifecycle of a sample, showing the individual protocols working together to make a sample that fulfills said requirements, conduct tribological testing on it, collect wear and friction data and finally analyse this data. Sections 3.4 and 3.5 describe how soft substrate samples were created and made compatible for cell culture. Section 3.6 details the cell lines used and Section D.1 contains the protocols for media preparation. Section D.2 deals with protocols used to conduct cell culture, including seeding and growing cells on a substrate. Tribological testing protocols for friction and indentation testing are presented in Section 3.9 and staining and imaging methods in Sections 3.10.3, 3.10.4 and 3.10.5. Finally, custom data analysis tools, developed in the context of this work are described and their derivation explained in Sections 3.11 and 3.12.

3.2 The Purpose of a Sample

In the experiment set-up, the sample is the part which replicates the blood vessel. As such, the sample should reflect surface and mechanical properties as closely as possible. The anatomy of a blood vessel has been described in Section 2.1 and is shown in Figure 2.1.

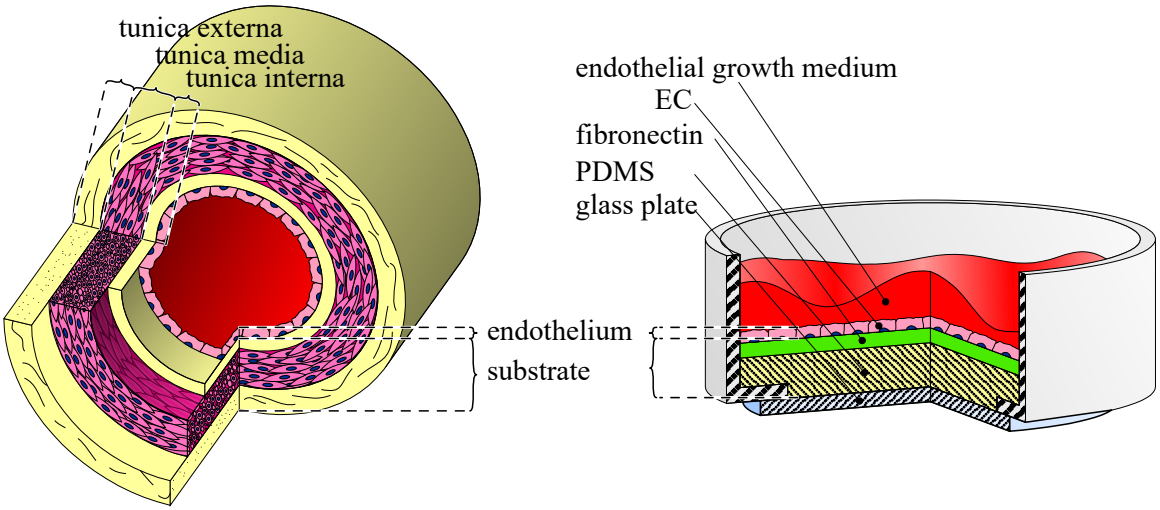

Figure 3.1: Schematic showing the anatomy of an artery against the structure of a sample used for *in vitro* experiments in this work. The endothelium is made up from endothelial cell in both cases, while the underlying tissue in the real artery is represented by a soft polydimethylsiloxane *in vitro*.

The surface properties are defined by the endothelial layer, as long as it is not destroyed. The mechanical properties are defined mainly by everything that lies below since the endothelial layer is thin.

In many previous studies, cells were seeded and tested on either PS or glass substrates. Those materials have Young's moduli of 3.25 GPa and 63 GPa, respectively, while arteries and veins have a Youngs modulus of around 125 kPa [87]. This leads to unrealistically high pressures for the cells which are trapped between two significantly stiffer materials. The sample design proposed in this work attempts overcoming of this issue by using NuSil GEL-8100 polydimethylsiloxane (PDMS) (a soft polymer) to emulate tunica externa and tunica media in a more realistic way than previous studies have with PS or glass. This soft polymer is henceforth referred to as PDMS. The substrate of the samples used in this work has a Young's modulus of around 73.3 kPa [88], so it is softer than blood vessels, however, its mechanical properties are much closer to the real physiological ones than the ones of PS or glass. On the polymer surface, HUVECs were cultured to obtain realistic surface parameters. To allow HUVECs to attach, the polymer had to be coated with fibronectin, a protein they are familiar with. Fibronectin was determined the best protein for this job in the context of this work [89]. A qualitative cell adhesion experiment, which is attached in Appendix B, on NuSil GEL-8100 and another, much stiffer type of PDMS was conducted to confirm this. In Figure 3.1, the sample design and and how it compares to a real blood vessel are shown.

3.3 The Lifecycle of a Sample

A sample in the context of this work refers to a Petri dish which contains a soft substrate with cells seeded on it used for tribological testing. Samples underwent several stages during their creation as mentioned in the introduction of this chapter. The sequence of these stages, from preparation of the substrate over cell culture, to testing and imaging, can be seen as the lifecycle of a sample. This is shown in a timeline in Figure 3.2. Each of these stages is described in a respective section of this chapter.

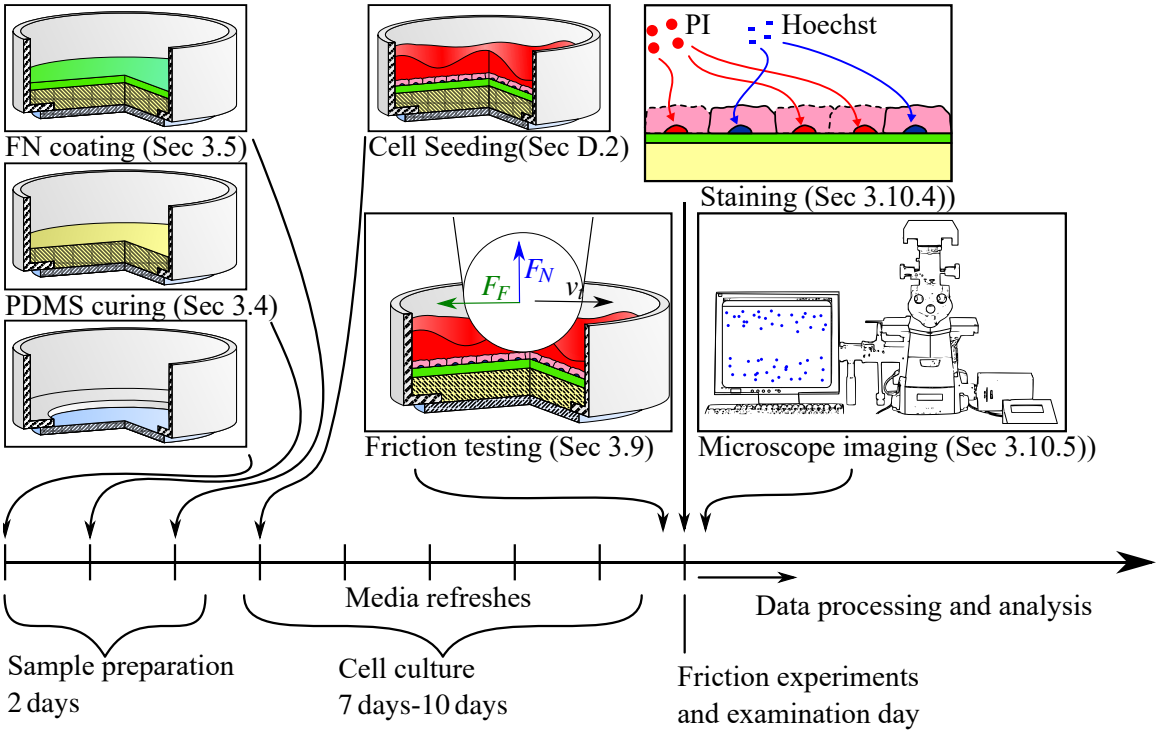

Figure 3.2: The lifecycle of a sample from fabrication to data collection on a timeline. Sample preparation (generating a soft substrate and making it inhabitable for cells) is followed by cell seeding and culture. Once a full monolayer had developed, the sample was subjected to frictional testing and, after staining, examined under the fluorescence microscope.

First, the PDMS was prepared and 2 g was filled into each Petri dish. The PDMS was cured to crosslink the polymer chains. This caused the PDMS to turn into a soft substrate, hence representing the first step towards generating a more realistic *in vitro* surrogate of the *in vivo* anatomy. This is subject to Section 3.4. PDMS is widely used in microbiology to manufacture microfluidic devices. PDMS is highly elastic with some viscoelastic properties [90][91]. Cell attachment on PDMS varies with cell type, however in general, attachment on PDMS is difficult because PDMS possesses a variety of aversive qualities (strong hydrophobicity, absorption of small hydrophobic molecules [92][93][94][95], leaching of oligomers into water [92][93][96] and its ability to release silicon into the media [92]); the

soft substrate had to be coated to make it compatible. For this, fibronectin (an ECM protein) was applied to the PDMS as described per Section 3.5. Cells can attach easily to this type of protein. Once the fibronectin was on the substrate, the sample was washed and was therefore ready to provide an inhabitable environment for HUVEC. HUVEC were seeded with a density of 10000 cells/cm^2. This meant that, immediately after seeding, the cells populating the substrate were sparsely distributed. Hence, media refreshes were conducted until a confluent (95 %-100 %) monolayer was established (after 7 days-10 days of cell culture and 3 to 4 media changes). Cell seeding and culture methods are described in Section D.2. Once a full monolayer could be seen under the light microscope, the samples were tested in the Universal Mechanical Tester Version 2 (UMT 2) (Section 3.9). Immediately after testing, the sample could be either fixed and prepared for storage, or stained in order to visually distinguish between live and dead cells. After staining, the sample was transferred to the fluorescence microscope where it was imaged. Staining and imaging methods are laid out in Section 3.10. Friction and damage data was saved and later examined, conditioned and analysed using a specially derived set of software, which is presented in Sections 3.11 and 3.12.

The protocols presented in this chapter present the final methodology used for the main results. Some experiments presented later in Chapter 4 only used a subset of these techniques, while others applied slight variations. Wherever there are diversions from the methodology specified in this chapter, those diversions are stated.

All reagents were purchased from Sigma-Aldrich (UK), unless stated otherwise. Cell culture medium for HUVECs (catalog #: C-22010) was purchased from Promocell and prepared as per Section D.1.

3.4 PDMS Curing

Standard 35 mm Petri dishes with a glass bottom (CELLView™, Greiner Bio One, Item No. 627860) were selected to hold the sample as the glass bottom allowed a clearer view of the cells than a regular PS dish would. Regular cell culture dishes were also tested, but provided a worse image quality. This was observed in experiments and can be explained by PDMS having a refractive index of 1.43 [97] which is closer to that of glass (1.5144) than to that of PS (1.6) [98]. If certain parts of the cells are to be stained (such as the cytoskeleton), the glass bottom dishes proved to be the optically better option. As a substrate, soft PDMS was prepared as per the protocol of Yoshie et al. [88]. For this, GEL-8100 from NuSil, which consists of two parts A and B, was mixed with 1 % additional crosslinker (Sylgard 184 curing agent from DOWSIL). This substrate has a Youngs modulus of 73.32 kPa $\pm$ 2.96 kPa

[88]. After mixing the three ingredients thoroughly, the mix was transferred into a desiccator to remove residual air in the PDMS. The desiccator which was used is shown in Figure 3.3a. Desiccating helps to make the substrate more transparent by removing bubbles and ensuring a uniform substrate. The low pressure within the desiccator causes the bubbles to expand, which increases their buoyancy hence they possess a stronger tendency to float up and burst. This effect can be seen in the time-lapse in Figure 3.3b. After about 30 s, the bubbles have expanded enough to cause the majority of them to float upwards. After around 80 s, all the bubbles are afloat and the PDMS underneath is free from bubbles. The time it takes for bubbles to float upwards depends on the viscosity of the liquid. In this particular case, a viscous PDMS (Sylgard 184) was used, therefore, it took a relatively long time for the bubbles to float and burst.

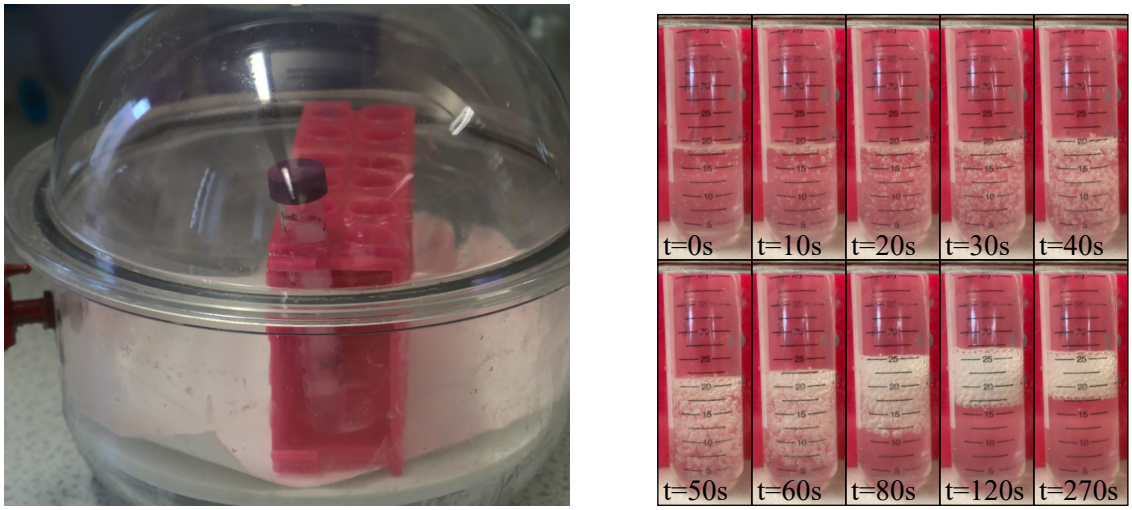

(a) Desiccator **(b)** Desiccating process

Figure 3.3: (a) Desiccator containing a tube holder with a standard 15 mL tube. **(b)** Time-lapse of desiccating process.

Each dish was filled with 2 g of PDMS, which is equivalent to approximately 2 mL. Given the area of one Petri dish is 8.8 cm^2, the approximate height of PDMS is 2.27 mm. The filled Petri dishes were desiccated again, in order to remove air bubbles that might have been created when aspirating and transferring the PDMS.

When friction testing on cells was conducted later, it became apparent that the PDMS sample surface was curved and it could not be perfectly aligned which showed up during testing as the vertical stage position diverged. These divergences were very small, however, they were visible in the data and had an effect on the results. To tackle the level, or misalignment issue, when curing, the samples were kept on a flat glass plate which was levelled with a digital spirit level. The same spirit level was used before tests to ensure the samples were

mounted level, too. This helped, however, it could not completely eradicate the problem because even the digital spirit level is only accurate to a certain degree. Additionally, there may be slight misalignments within the friction testing machine. The second issue could not be tackled. This is because the meniscus geometry can originate from a combination of the physical properties (surface tension and surface free energy) of the liquid, and from surface warping during the curing process, both of which cannot be negated. During the raw data analysis, it was clear that the surface always followed a meniscus shape as can be seen in Figure 3.4. This was evident from the position of the stage in normal direction. This happens because the PDMS is a liquid before it is cured and is hence governed by the laws of gravity and surface tension, which force it to form a meniscus. When the PDMS is cured and solidifies, it stays in that shape. Looking at Figure 3.4, the extent of this may seem limited to the outer parts of the PDMS, where the soft polymer meets the PS. However, the influence is measureable and significant in the centre too. This is shown later in Figure 3.16. A way to generate flatter samples in the future could be to cure the PDMS in the dishes against a flat countersurface, or to use pre-cured PDMS sheets. However, as these approaches could not be tested and assessed within the scope of this work due to time limitations, a method to analyse the data was developed, which allowed to account for the influence of the meniscus and any residual misalignment. This is described in Section 3.11.

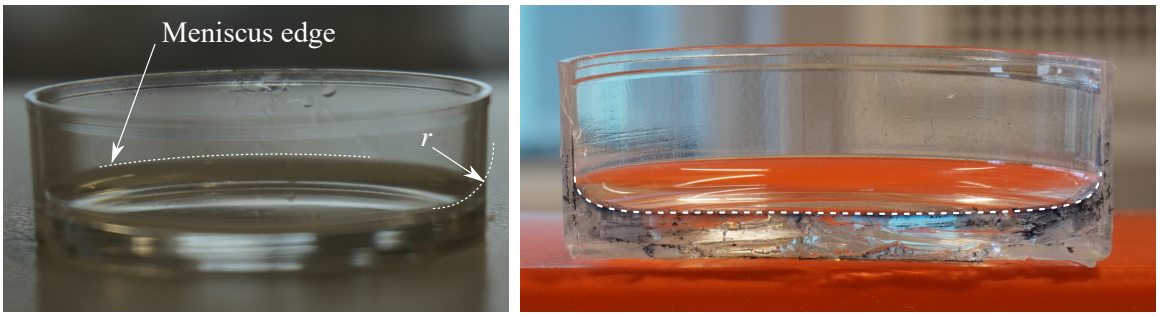

Figure 3.4: Meniscus on a soft PDMS sample. An arc of radius r is annotated where the curvature seems the most visible. The meniscus edge at the interface between PDMS, PS and air is highlighted. In the image on the right, the sample was cut in half with a scalpel and coloured with a lab marker. The surface slope is approximated with a white, dotted line.

The PDMS was cured at 65°C for 8 h in a temperature controlled oven on the flat, levelled glass plate. At first, the PDMS was cured at 100°C for 2 h-3 h, according to the manufacturers standard instructions, however, as the dishes are partly made out of PS which melted under these conditions, the temperature had to be lowered. The curing temperature was increased in accordance with NuSil's specification sheet to 65°C. NuSil's recommendation for the curing time at this temperature is 90 min. The curing time was set higher to 8 h in order to ensure thorough curing of the polymer without repercussions because the

product is stable at up to 240°C. According to standard lab protocol, after curing, the dishes were filled with 70 % industrial methylated spirit (IMS) for sterilisation, transported into the cell culture hood (a sterile environment used for cell culture and experiments), where the IMS was aspirated and the PDMS rinsed 3 times with phosphate buffered saline (PBS).

3.5 Fibronectin Coating

To make the substrate more accommodating for cells, the PDMS substrate was coated with a $1\,\mu g/cm^2$ ($1\,\mu g/cm^2$-$5\,\mu g/cm^2$ is recommended by Merck for endothelial cells) of fibronectin (catalog #: F1141). The amount of fibronectin needed for a standard 35 mm dish of $8.8\,cm^2$ surface area is hence $1\,\mu g/cm^2 \times 8.8\,cm^2 = 8.8\,\mu g$.

The fibronectin must be diluted in a solution to coat the dish. PDMS is hydrophobic before fibronectin coating, and therefore an appropriate amount of volume to cover the whole surface is needed. For 35 mm glass bottom Petri dishes, a working volume of 3.5 mL per dish was found to be sufficient to cover the whole Petri dish surface. The total amount of fibronectin was diluted in the appropriate volume of PBS. The solution was gently mixed with a pipette and each dish filled with 3.5 mL solution containing 8.8 µg fibronectin. The dishes were left in the cell culture hood at room temperature overnight. When the coating process of the substrate was finished, the sample was washed 3 times with PBS.

3.6 Cell Lines

All animal bodies are made from cells. Every cell is intended to serve a specific purpose (including differentiation into a specific cell type) and therefore shows individual properties and behaviour. For example, a neuron (a brain cell) fulfills completely different tasks than a smooth muscle cell. This is immediately obvious from the shape of those cells: a neuron has multiple elongated extensions connecting it to other cells, allowing it to transmit information [99], while a smooth muscle cell is elongated and can carry radial loads, in the case of blood vessels [100]. They also have very different needs and properties. Neurons are capable of transmitting great amounts of information, but require multiple layers of protection: the brain is swimming in fluid and shielded from mechanical stresses by the skull. On the other hand, smooth muscle cells contain much actin and myosin which are responsible for contraction [101] and can hence carry external loads.

Each specific cell type also requires a certain type and concentration of nutrients and prefers an environment to live on, or in. These requirements must be met *in vitro* by choosing the correct cell culture medium and substrate. If the cells are not “happy” with medium

or substrate, they will not attach or not behave as they should; they may die. *In vivo*, the cells demands should be fulfilled naturally through normal bodily functions and collaboration with other cells. However, when this is not the case, this can lead to disease. In the following sections, the cell lines used in this work are described.

3.6.1 MG63

MG63 is a readily available, immortalised cell line derived from fibroblasts in bones used for initial tests in this work due to its resilience and fast proliferation (spread across the sample surface due to reproduction) [102].

3.6.2 Human Umbilical Vein Endothelial Cells (HUVEC)

HUVEC are found in the endothelium of the umbilical vein. They are used to represent the endothelial layer in this work. HUVEC share many properties with the vascular EC types found at the specific locations where interactions with medical devices happen (i.e. the coronary artery, the internal carotid artery or a vein in the arm), however, it is not exactly the same cell type. Therefore, there may be slight differences [103], for example in shape or size [104], release of vasoactive substances or their interaction with white blood cells [105]. HUVEC have, however, similar properties as the cells found in the aforementioned locations and in addition to that, they are readily available and were found to be relatively easy to culture in this work as they are quite resilient. HUVECs (catalog # C-12253) were purchased from Promocell.

3.7 Probe Manufacturing

Now that the sample was seeded with cells, it had to be tested against a material. The object which the sample was tested against is being referred to as probe. For materials, glass, stainless steel and polytetrafluoroethylene (PTFE) were selected. Glass was chosen because it was used in previous studies and hence will make this work more comparable to other people's work. Stainless steel was chosen because it is one of the most common stent materials. PTFE was chosen because it is generally associated with low-friction and low-wear interactions and shows significantly different surface parameters to the other two materials, such as high hydrophobicity and poor wettability. Ball bearings were acquired from Atlas Ball & Bearing Co., UK to be used for probe manufacturing.

For the geometry, a sphere was chosen. A sphere generally represents a good starting point for any tribological experiment because it is a defined and reproducible geometry. In

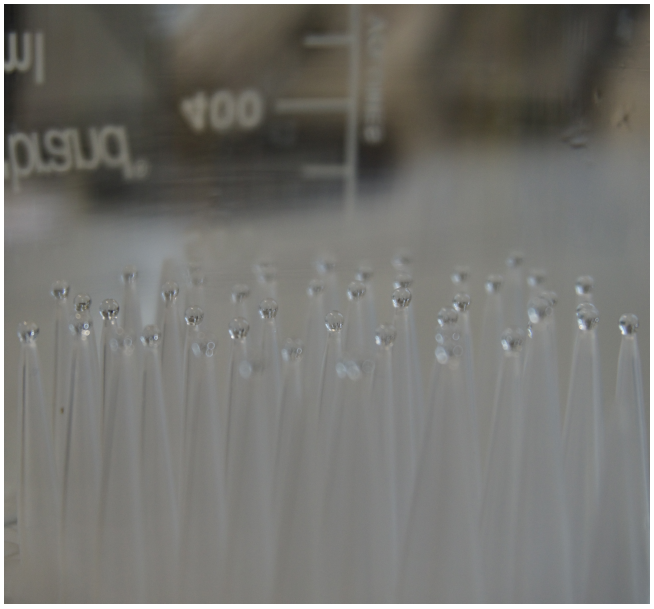

(a) Probes curing

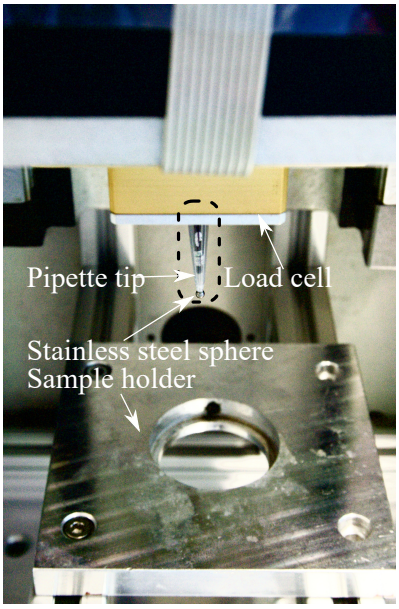

(b) Probe attached to load cell adapter

Figure 3.5: **(a)** Cyanoacrylate curing overnight during probe manufacturing. **(b)** Probe attached to UMT adapter.

addition to that, due to its symmetries, a spherical shape reduces misalignment issues. Stent struts usually have a rectangular profile, however, the edges are difficult to manufacture and reproduce in a defined manner. Defining the geometry is easier with a sphere that can be polished to reach the desired level of roundness. Medical devices can have different shapes or forms, however, to eliminate the influence of geometry and study the effects of different materials, a sphere is ideal. A spherical shape is also reproducible by other research groups and makes the results collected in this work more comparable to previous work. Furthermore, stresses can be calculated reliably.

For the sphere, a diameter of 2 mm was selected because acquisition of PTFE probes proved difficult and they were only available in imperial sizes. The pairing with the smallest relative difference was 2 mm metric-sized glass and stainless steel and $\frac{2}{32}$ inch = 2.38 mm imperial-sized PTFE bearings. As the diameters of the spheres are not the same, this must be considered when discussing results.

To avoid delays during cell testing, the probes were intended to be disposable. Therefore, the ball bearings were attached to pipette tips with cyanoacrylate glue. To attach the probes, a small amount of cyanoacrylate glue was applied to a pipette tip, then the pipette tip was pressed against the ball bearing. The assembled probe was turned by 180° and placed upside-down in a tube holder, shown in Figure 3.5a, in order to avoid glue flowing onto the surface that would be in contact with the cells. The glue was left to cure overnight.

The pipette tips could then be attached to an adapter that was mounted in the tribometers (the friction testing machine) load cell as shown in Figure 3.5b. This set-up allowed for quick changing of probes during testing so that several tests could be executed on one sample.

3.8 Roughness Measurements

Roughness describes the nature of the asperities of a surface and is an important surface parameter. Knowledge about the surface roughness can help to understand tribological processes and is especially important for hydrodynamic lubrication. Thefore, the surface roughness was measured and reported in this work to assess consistency between probes and see how it differed between materials, as it could influence the friction.

Roughness measurements were conducted using an Alicona 3D scanner. Probes were attached to a Petri dish lid in the same fashion described in Section 3.7. They were then washed with PBS, just as the probes used for cell testing were. Stainless steel probes could be scanned without any treatment. PTFE and glass probes had to be gold coated before testing in the Alicona. The Alicona produces a 3D geometry of the scanned item, which had to be projected on a sphere to generate a 2D height map. From there, roughness parameters Ra, Rq and Rz were measured. The Alicona features an accuracy of 200 nm with the objective used (5x).

3.9 Friction and Indentation Testing

Testing was performed on a Bruker UMT 2 shown in Figure 3.6a. In principle, the UMT 2 is a 3D computerised numerical control (CNC) device, capable of operating 3 stages simultaneously in x, y and z directions while measuring forces in z (normal) and x (friction). The coordinate system that the UMT 2 uses is also shown in Figure 3.6a. The machine features a modular structure to allow for a wide range of applications through compatibility with different load cells, rotary and linear stages, and attachments like oil baths.

3.9.1 Friction Testing

For this work, a custom sample holder was manufactured to be mounted in the UMT 2, which is also shown in Figure 3.6a. The stage is running on vertical (X) and horizontal (Z) rails and is moved in and by spindles which are attached to stepper motors. The position of the spindles (and therefore the stage) is measured with rotary encoders and fed back into the UMT 2. This allows for control of the stage's position in increments of 0.5 µm.

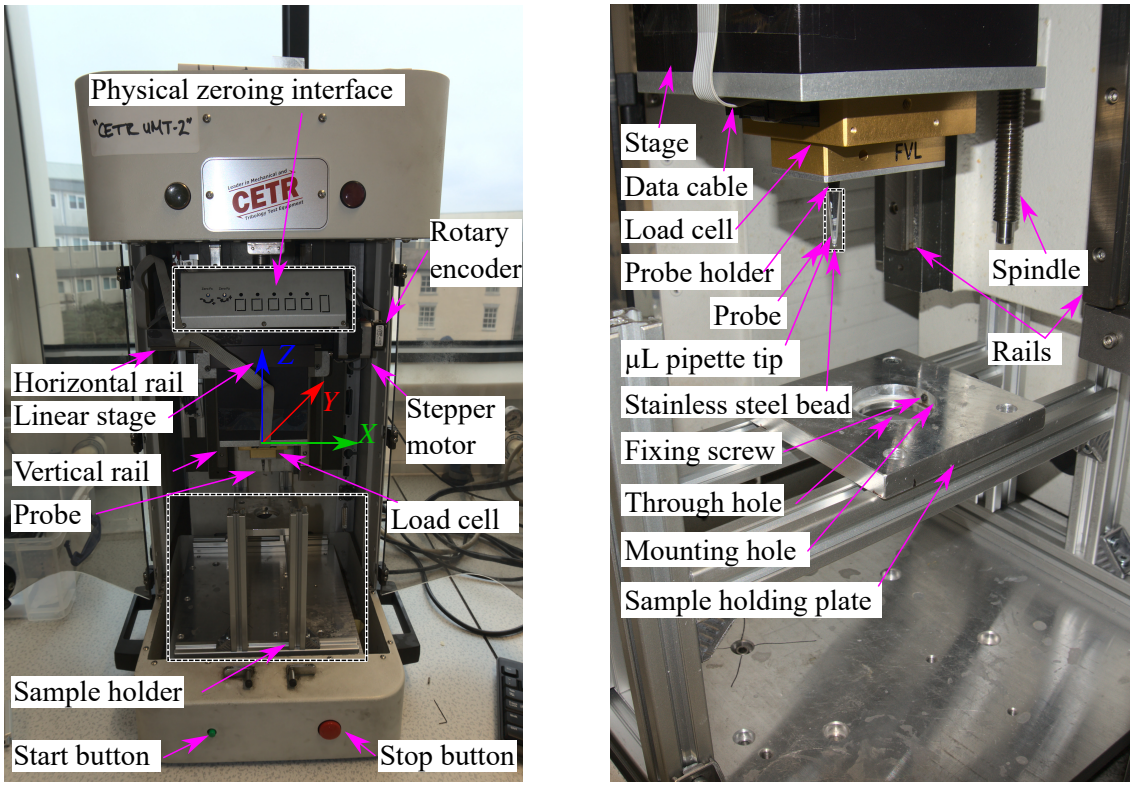

(a) UMT 2 **(b)** FVL

Figure 3.6: (a) UMT 2 with custom sample holder and main parts labelled. The coordinate system with X, Y and Z axes is also shown. **(b)** FVL load cell with attached probe and sample holder.

With the physical zeroing interface, the load cell's raw values can be zeroed physically, however, the UMT 2 also has a software zero. The load cell is mounted to the bottom of the stage. Tests were conducted with the probe fully submerged in the fluid bath. The probe was brought close to the surface and the forces were zeroed. Therefore, any apillary and buoyancy induced forces are accounted for.

For the measurement of forces in X and Z directions, the Bruker FVL load cell was used, which features a maximum load of 100 mN with a resolution of 1 µN. The load cell and the custom sample holder are shown in more detail in Figure 3.6b. The data cable transports the analog signal to the UMT 2s logic board where it is converted to digital. In this picture, the probe holder can be seen as it is mounted in the load cell. Attached to it is the probe, which consists of a µL pipette tip and a stainless steel bead. For testing, samples can be mounted in the sample holding plate via the mounting hole. For this, the sample is inserted into the hole and aligned. Then the fixing screw is engaged, securing the sample in place. The through hole on the bottom would allow for a microscope to collect *in situ* image data.

The UMT 2 applies a displacement along the Z coordinate in order to generate a normal

force $F_N(z)$ between two surfaces, until the specified force $F_N(z) = F_{N,spec}$ is reached at a displacement of $z = d_i$. This is shown for a stiffer and a more flexible substrate in the diagram in Figure 3.7. Similar to a soft spring, with a flexible substrate, the displacement d_i to obtain a given reaction force $F_{N,spec}$ is larger than for a stiffer one.

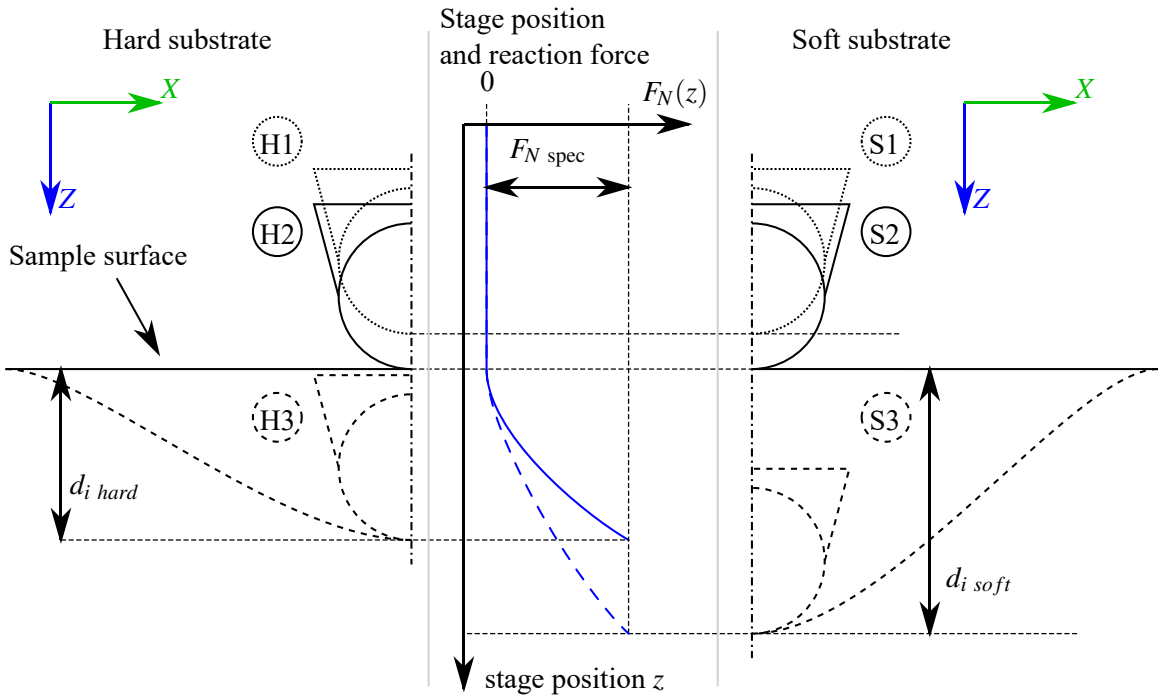

Figure 3.7: Stage position z and resulting reaction force $F_N(z)$ for a hard (left) and a soft (right) substrate. The stage is set to reach the specified normal force $F_{N\ spec}$. In Position H1/S1, there is some distance between sample surface and probe, resulting in a normal force of 0 N. In Position H2/S2, the probe touches the surface, starting to cause the sample to exert a reaction force on the probe. In Position H3/S3, the stage has reached the respective end position, displacing the substrate surface by $d_{i\ hard}/d_{i\ soft}$.

The UMT 2 is set to control F_N, however, the machine parameters have to be adjusted to the substrate. A stiffer substrate, like PS, requires slower displacement speed settings than a very flexible one, like PDMS. This is to avoid damage to the load cell, because even a small displacement causes a big change in reaction force and may exceed the limits of the load cell. On the other hand, a flexible substrate requires faster speeds in order to follow the slope of the surface, as PDMS samples also come with steeper slopes. If the speeds were set too low, the stage could not keep up with the slope and the real reaction force would slowly diverge from the set one. The parameters used for tests on PDMS and PS-based samples are reported in Table 3.1.

Figure 3.8 shows what happens during a friction experiment to normal force $F_N(t)$ and stage positions $x(t)$ and $z(t)$. The friction testing process can be separated into four phases. The first phase is the pre-touch, during which the stage's vertical position is lowered with

Parameter [Unit]	Polystyrene (PS)	Polydimethylsiloxane (PDMS)
$v_{Pretouch}$ [mm/s]	0.15	0.5
v_{Touch} [mm/s]	0.03	0.15
$v_{Tracking}$ [mm/s]	0.01	0.1
$F_{N,Touch}$ [mN]	-1	-0.3

Table 3.1: UMT engage and tracking settings used for experiments on PS and PDMS-based samples.

speed $v_{\text{pre-touch}}$ until a reaction force is detected, meaning that the probe is in contact with the substrate. At that point, the second (loading) phase is initiated which lasts a fixed amount of time $\Delta t_{\text{loading}}$. In this phase, z is adjusted with speed v_{touch} until the measured normal force $F_N(t)$ reaches the specified force $F_{N\text{ spec}}$ and is held there for the rest of phase two, when the third phase starts. In this phase, the actual friction experiment is conducted. $F_N(t)$ is kept at $F_{N\text{ spec}}$ and z is adjusted as necessary with speed v_{tracking}. At the same time, the probe is moved forward in the X direction with speed $v_{x\text{ spec}}$. After a set distance $\Delta x_{\text{sliding}}$, the stage stops and the phase is over. In the last phase, the stage moves up, unloading the sample.

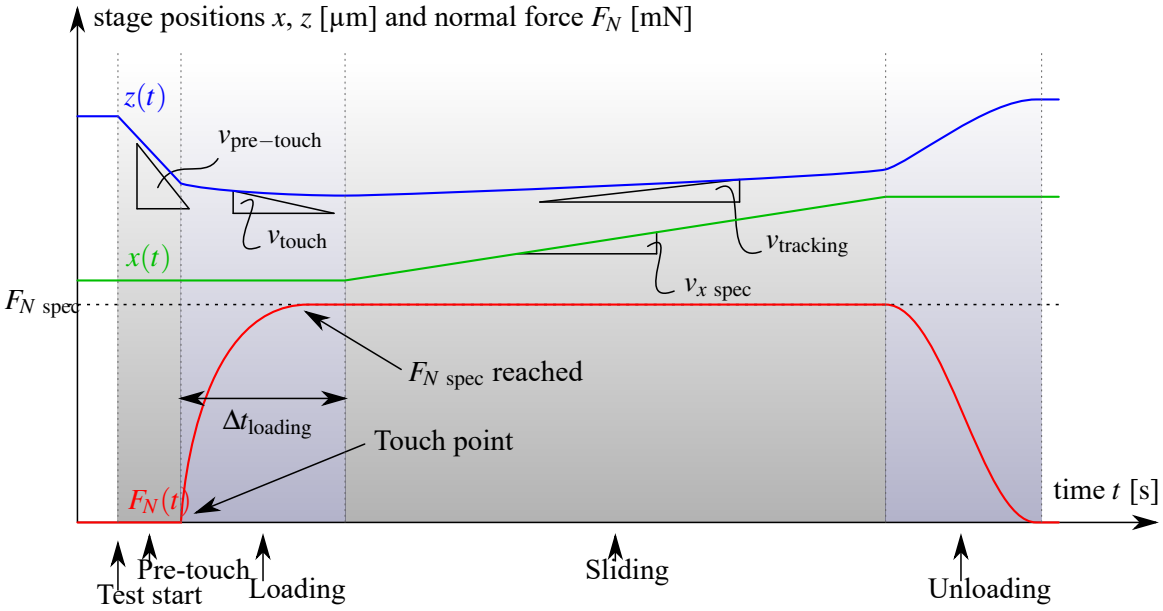

Figure 3.8: Normal force $F_N(t)$, vertical stage position $z(t)$ and horizontal stage position $x(t)$ during a friction test.

3.9.2 Indentation Testing

Indentation testing was conducted to investigate the cells and substrate reaction to a pure normal load. This procedure is different than for friction testing, as the relevant part is the loading. The program is also divided into phases, as seen in Figure 3.9, where x and y stage

positions and the normal force F_N are plotted. Similar to a friction experiment, there is a pre-touch phase during which the stage is continuously moved down with speed $v_{z\ \mathrm{pre-touch}}$ until a small force is detected. In the next phase, however, a small load of $F_{N,\mathrm{touch}} = 1$ mN is applied by moving the stage down with a maximum speed of v_{touch}. The z position at which the stage is at the end of this phase can be used as a reference position $x_{\mathrm{reference}}$. Then, the target load $F_{N\ \mathrm{spec}}$ is applied by moving the stage further, again with a maximum speed of $v_{z\ \mathrm{touch}}$. When $F_{N\ \mathrm{spec}}$ is reached, the load is held for a short time $\Delta t_{\mathrm{holding}}$ after which the stage is lifted up by $\Delta z_{\mathrm{unloading}}$ continuously with speed $v_{z\ \mathrm{unloading}}$, to remove the load. The Unloading stage concludes the indentation process, however, the stage can now be moved in the X direction in order to conduct another indentation test. The indentation test was carried out several times by moving the probe further and repeating the procedure above. There was enough space on one sample to carry out three experiments with five consecutive indentations each for a total of 15 indentations per sample.

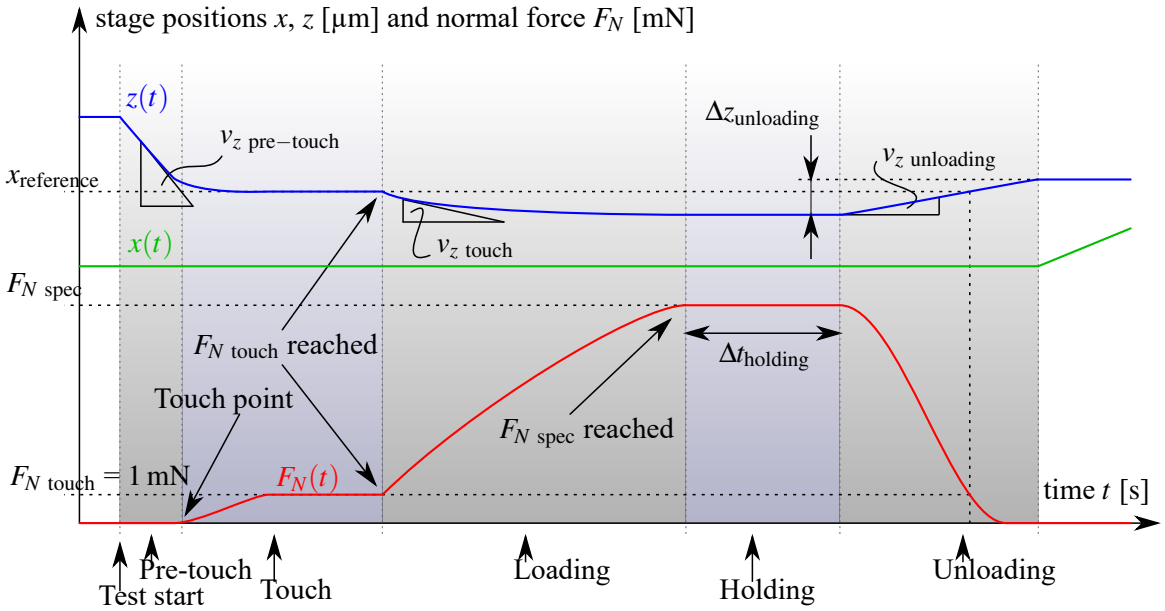

Figure 3.9: Normal force $F_N(t)$, vertical stage position $z(t)$ and horizontal stage position $x(t)$ during an indentation experiment.

3.10 Imaging

This section describes the methods used to make cells or certain parts of them visible and to collect this visual data. 4′,6-diamidino-2-phenylindole (DAPI)/phalloidin (Subsection 3.10.3) staining relies on fixation of the cells, described in Subsection 3.10.1, other stains cannot be used with prior fixing, however, fixing could be conducted after staining. Staining

in cell work always has the same fundamental motivation and is based on the same working principle. The motivation is that one or more parts of the cell must be made visible. The working principle is that a dye is able to bind (preferably exclusively) to the portion of the cell that is supposed to be made visible and that dye's presence can determined optically. Staining with Trypan Blue is essential in cell culture because it allows for differentiation between live and dead cells without relying on fluorescence, meaning it can be used with regular light microscopy. DAPI/phalloidin staining makes cell nuclei and the cytoskeleton show up in blue and red (different colours of phalloidin are available), respectively. PI/Hoechst staining was used for fluorescence live/dead assessment.

3.10.1 Cell Fixation

Cells were fixed before DAPI/phalloidin staining or after PI/Hoechst staining for preservation. First, the media was removed from the Petri dish followed by washing twice with PBS. Afterwards, samples were submerged in 800 µL 3.7 wt% formaldehyde (FA) in deionised water ($_{D}H_2O$) for 20 min. The FA solution was removed and the sample was washed twice with PBS. Afterwards, the samples were stained or filled with 800 µL PBS and stored in the fridge.

3.10.2 Trypan Blue Staining

Trypan Blue is a blue dye used in biosciences. As Trypan Blue cannot enter healthy cells with an intact cell membrane and binds to intracellular proteins (it is not a very specific dye), it is used to distinguish between live and dead cells. It is commonly used to stain dead cells blue, for example during cell counting with a hemocytometer. Trypan Blue has been used previously for tribological experiments on monolayers. As it is readily available, it was the first staining method tried.

Stain stock solution is made by diluting one part Trypan Blue with one part PBS. After tribological testing, 800 µL of staining solution was transferred into the Petri dish. The solution was left to incubate at 37°C for 5 min. Afterwards the Petri dish was imaged by standard light microscopy. In the resulting image, patches of live tissue are transparent while parts that are necrotic or apoptotic are stained in a dark blue colour.

3.10.3 DAPI / Phalloidin Staining

Simultaneous staining with DAPI and phalloidin (Sigma-Aldrich, catalog # P1951) is a common way to visualise the nucleus and the actin fibres in the cytoskeleton. The resulting images can be used to study alignment of cells and cytoskeleton, for example to external

influences like flow-induced shear stress. Both, DAPI and phalloidin are unable to permeate through the cell membrane of healthy cells. Therefore, for this stain, cells must be fixed and the cell membrane lysed in order to allow binding to actin and deoxyribonucleic acid (DNA) in the nucleus.

After fixating the cells as described in Subsection 3.10.1, the monolayer was submerged for 20 min at room temperature with 800 µL of immunocytochemistry buffer, containing 1 wt% bovine serum albumin and 0.1 vol% Triton X-100 in PBS. Immunocytochemistry buffer helps to improve the image quality by preventing binding of phalloidin / DAPI to proteins other than actin and DNA, respectively.

Phalloidin and DAPI were applied as a single staining solution. The staining solution consisted of 0.1 vol% of phalloidin stock solution and 0.25 vol% of DAPI stock solution in immunocytochemistry buffer. After aspirating the immunocytochemistry buffer from the sample, 800 µL of staining solution were added and samples were left to incubate for 20 min at room temperature wrapped in aluminium foil to protect them from light. Then, the staining solution was removed and, after the sample was washed once with PBS, it was submerged in PBS and was ready for imaging.

3.10.4 Propidium Iodide / Hoechst Staining

PI/Hoechst staining was used to visualise necrotic and apoptotic cells. It relies on a similar mechanic as the Trypan Blue staining methods described in Section 3.10.2, as PI is only able to permeate through dysfunctional cell membranes, however, it comes with some major advantages. In addition to PI staining damaged cells, Hoechst works as a counterstain, colouring the DNA of all other cells blue. Both, PI and Hoechst are fluorescent stains working on different excitation and emission wavelengths, meaning that the two signals can be distinguished easily with the appropriate filters by a fluorescent microscope. This means that live and dead parts of the monolayer can be distinguished and quantified.

The two dyes were applied as a single staining solution. 1.5 mL of PI stock solution and 5 µL of Hoechst stock solution were diluted in 8.5 mL PBS resulting in 10 mL staining solution with a concentration of 0.15 mg/mL PI and 1 µg/mL Hoechst.

Staining was conducted immediately after testing as fixing the cells first was found to have a detrimental effect on image quality. The sample was moved directly from the UMT 2 to the aspirator and the media was removed. After that, the sample was gently washed once with 1.6 mL PBS and, after the PBS was removed, the sample was filled with 800 µL staining solution and left to incubate at 37°C for 15 min. Afterwards, the staining solution was aspirated and the sample was washed with 1.6 mL PBS. The sample was submerged in 800 µL PBS and was ready for imaging. Before imaging, the glass on the bottom of the

dish was cleaned to avoid condensation affecting the image quality. Samples were then transferred to the microscope for imaging.

3.10.5 Fluorescence and Light Microscopy

The microscope used for imaging was a Nikon Eclipse Ti, shown in Figure 3.10 with its components annotated. A COOLLed pE-300 lite module generated light of the required wavelengths. Filters were used to filter out every wavelength but the ones around the respective emmission and excitation wavelengths for the blue (DAPI/Hoechst) and for the red (phalloidin/PI) channels. Those filters wavelengths can be found in Table 3.2. The irradiance spectrum generated by the pE-300 unit is shown in Figure 3.11 and covers all major excitation wavelengths used for fluorescent microscopy.

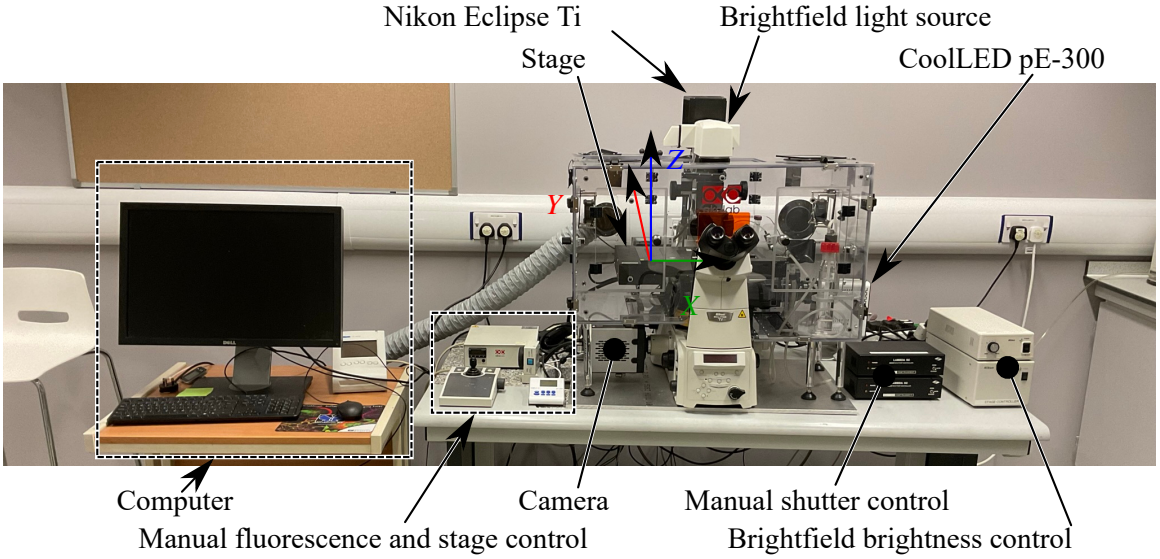

Figure 3.10: Picture of the Nikon Eclipse Ti microscope with annotations and stage coordinate system.

Parameter [unit]	Blue	Red	Brightfield
Acquisition time [ms]	50	50	0.2
Excitation wavelength λ_{ex} [nm]	359	493	-
Emission wavelength λ_{em} [nm]	457	636	-

Table 3.2: Acquisition settings used for capturing blue, red and brightfield channels. These are the settings used unless specified otherwise.

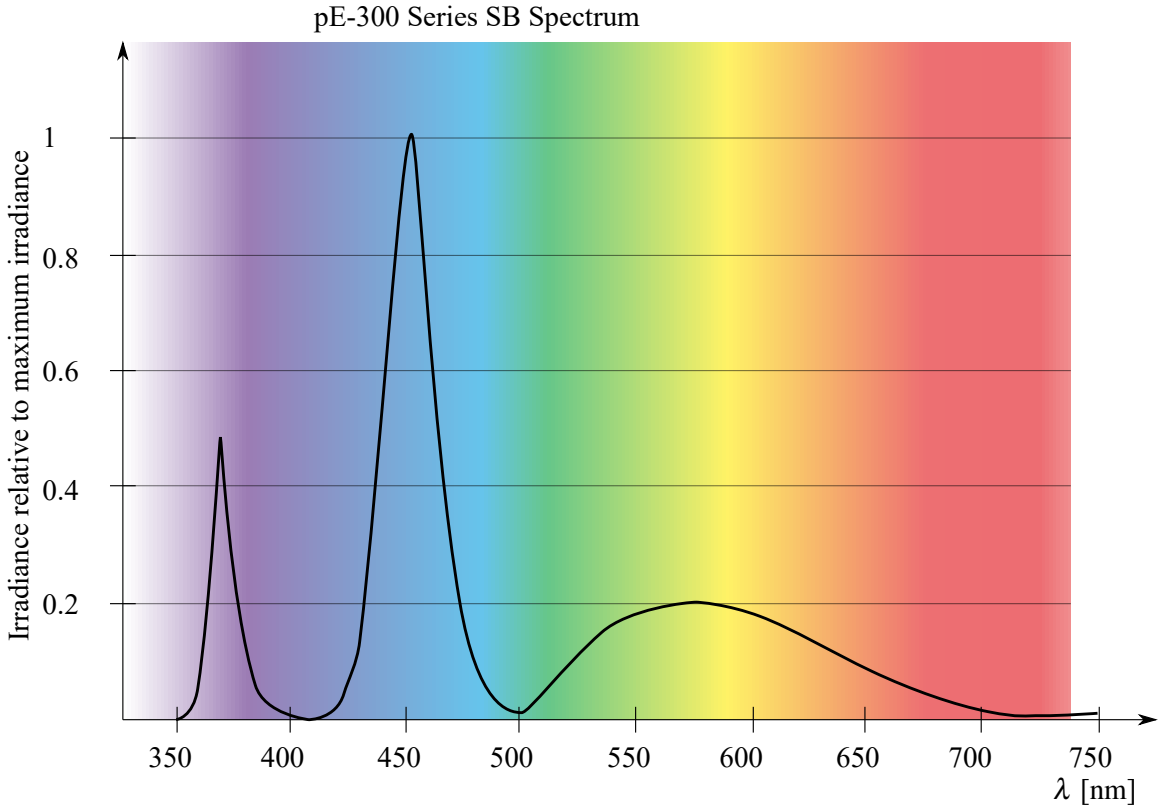

Figure 3.11: Fluorescent microscopy irradiance intensity graph of the light spectrum generated by the CoolLED pE-300 lite. Adapted from the manufacturer's website [106].

3.10.6 The Path of Light

The path of light for brightfield imaging is shown in Figure 3.12. The light is generated by a bright lamp and contains the full spectrum of visible light. This light is led to the top of the microscope where it shines down through the diaphragm and then through the sample. After that, it can either be directed through the eyepiece for observation of the sample by eye, or it can be directed to the left into the camera.

The path of light for fluorescent imaging is shown in Figure 3.13. The working method is shown on the example of a blue fluorescent molecule, like Hoechst, or DAPI. Irradiance spectrums are shown to depict the effect of excitation and emission filters. The wavelengths of these filters are shown in Table 3.2. The light is generated by the pE-300 fluorescent unit and led to one of the bottom ports of the microscope through the excitation wavelength filter which filters out wavelengths outside of the excitation range. The full range of wavelengths shown in spectrum a is filtered by the excitation filter, predominantly leaving light of wavelengths around the excitation wavelength λ_{ex} of the molecule investigated, as shown in spectrum b. From there, it is directed to shine up so that it hits the sample (marked by the red oval) from the bottom. When a fluorescent molecule like DAPI or Hoechst is hit by a

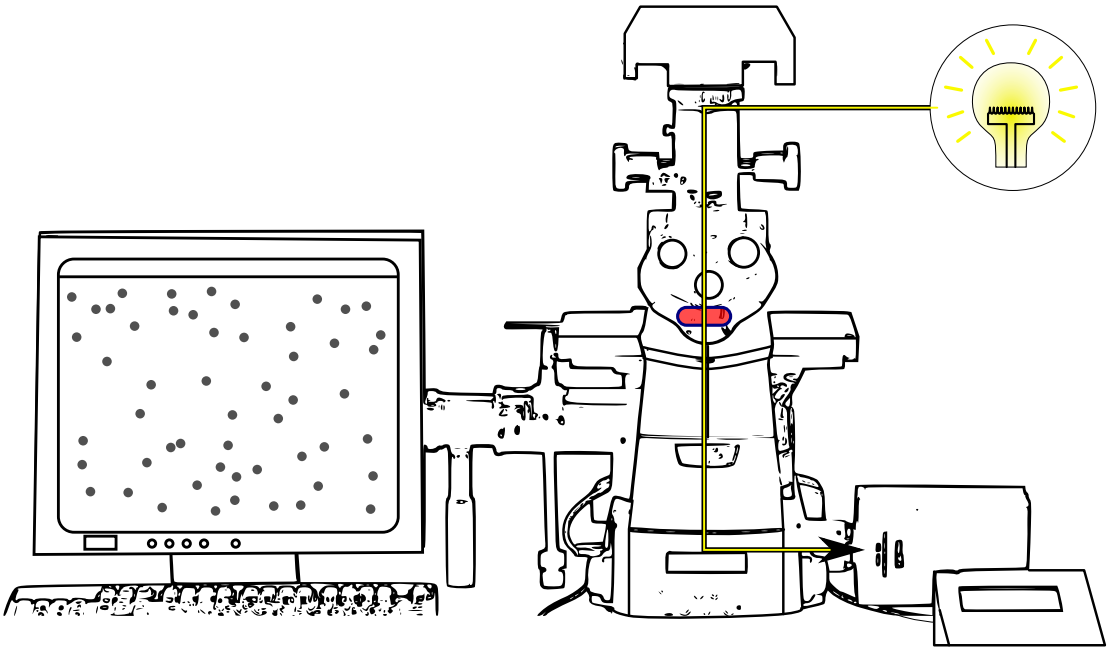

Figure 3.12: The path the light takes when travelling through the microscope during brightfield microscopy. The light is generated by a lamp and guided to shine through the sample (marked by the red oval) from the top. From there it is travelling down until it is directed through the camera port into the camera where it hits the sensor.

photon of the correct excitation wavelength (carrying the correct amount of energy), it can excite an electron to a higher energy level. As the electron jumps back to its initial level, it can emit a photon of the emission wavelength, a property called fluorescence. This photon may go back through the objective into the bottom of the microscope. Even though most of the light reaching the objective should be emitted from the desired fluorescent molecules, residual light coming into the objective from the room creates noise in the signal, as shown in spectrum c. Because of this, the incoming light is directed through the emission wavelength filter, which is responsible for filtering out any wavelength outside of the desired emission wavelength range (see spectrum d), enabling the camera to only capture the position of the respective fluorescent molecules. This light then reaches either the eyepiece, or the camera sensor, where it is converted to a digital signal that can be displayed by the computer or viewed by eye on the screen.

3.10.7 Stage Control

All three stages can be controlled by the user with a manual input device, or by the computer. The positions on the X and Y axes determine the position of the field of view on the sample. The position along the Z stage controls the focus because the plane of focus is at

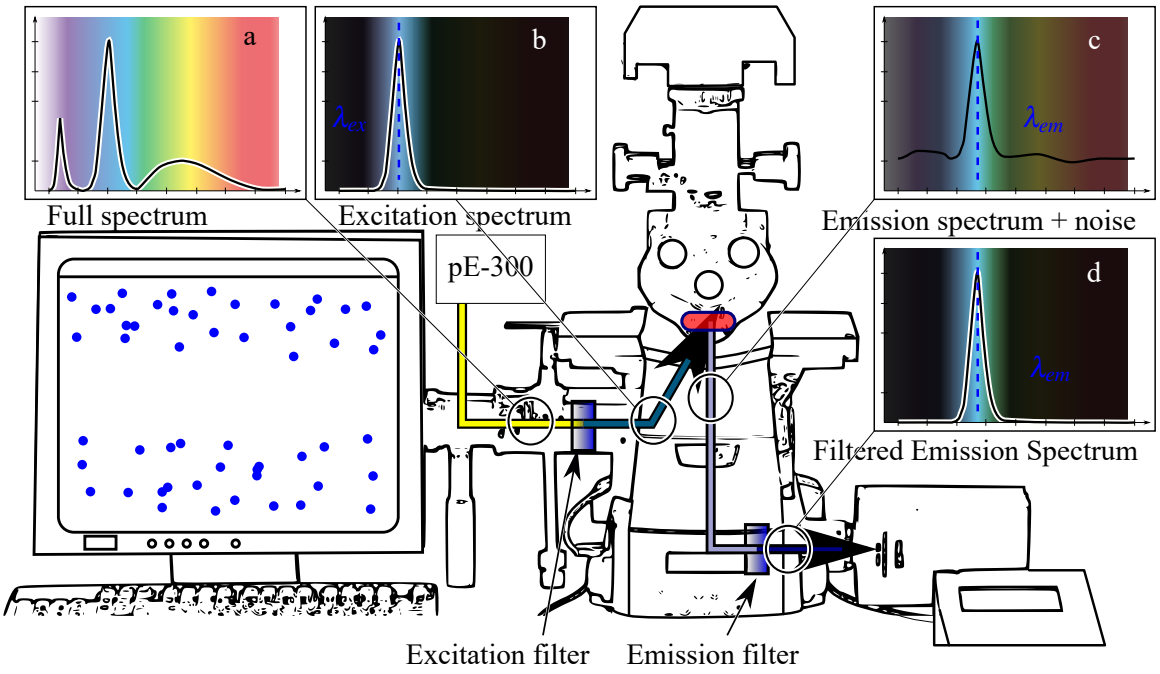

Figure 3.13: The path the light takes when travelling through the microscope during fluorescent microscopy. The working method is shown on the example of a blue fluorescent molecule, like Hoechst 33342. Irradiance spectrums are shown to depict the effect of excitation and emission filters. The full spectrum covering the whole range of visible light, shown in spectrum a) is filtered by the excitation filter, leaving spectrum b). The light is then guided on the specimen, where light of the emission wavelength is set free, when it hits a fluorescent molecule. The light is guided back into the microscope and filtered by the emission filter, as marked in spectrum d). This light is then directed into the camera or to the eyepiece.

a fixed distance from the objective as there is no focusing mechanic within the lens itself. Therefore, the sample must be brought into a position where the desired area is sufficiently close to the plane of focus. When acquiring a picture, the program reports the X, Y and Z positions in the metadata of the image file.

3.10.8 Capturing Images with Meta Morph

The software used to control the microscope and read sensor data is called Meta Morph. The software features a wide range of functions.

In the acquisition window, the main microscope parameters can be set. These are the filter settings - determining which wavelengths are captured - the exposure time - which determines how long the sensor is capturing data - stage positions, downsampling and measuring methods. Furthermore, autofocus can be activated through this window.

The live view image shows the current sensor readout, providing an indication of the image that may be captured if the shutter is activated. This function was used to adjust stage positions and to focus, as manual focus was used.

The multi-dimensional acquisition window was used to capture full slide images. This feature is used to acquire images in multiple "dimensions", meaning that several stage positions, wavelengths and timepoints can be set, which the microscope goes through automatically and captures images. In this work, three wavelengths and as many stage positions as necessary to capture a whole slide were specified. Then, the microscope was set to go automatically through all of these positions as this was found to be the quickest way to capture images covering the whole slide.

In the image metadata, the spatial calibration ξ is reported automatically based on the objective used. ξ is dependent on the magnification of the objective and was determined using a calibration ruler. The spatial calibration represents the relation between the size of a pixel and the respective length on the imaged sample surface in µm. Hence, it can be used to convert a distance $\Delta x'$ in pixels to a distance Δy in µm:

$$\Delta y = \xi \Delta x' \tag{3.1}$$

and following an area A' in pixels to an area A in μm^2 with

$$A = \xi^2 A' \tag{3.2}$$

The spatial calibration factors for the two objectives used in this work are shown in Table 3.3.

Objective	**spatial calibration** ξ [µm/pixel]
10x	0.64767
4x + tube	1.0799

Table 3.3: Spatial calibration factors ξ for 4x + tube and 10x objectives used to convert from pixel to real distances.

3.10.9 Imaging of a Whole Slide

After staining, the sample was transferred into the Petri dish holder of the microscope. The sample was examined in the live view window and all three slides were located. Afterwards, the stage was set in a way that the microscope would view the first slide and manually focussed. Then, the stage was moved by increasing the X position in the acquisition window by 10 mm to the right causing the stage to move over the whole slide. At that point, if the slide was not sufficiently centered within the field of view by the end of the slide, the sample was rotated slightly and the procedure was repeated. If the slide was centered by the end,

however, the sample was regarded as aligned enough with the X axis to continue with the next step.

In this next step, the stage was moved back to the start of the slide, ensuring that a sufficient compare area would be imaged, focussed and the position was marked in the multi-dimensional acquisition window. Then, the stage was moved by 2 mm and the above was repeated. This was repeated 4-5 times until the end of the slide was reached, again ensuring that a sufficiently large compare area at the end was imaged. This is shown in Figure 3.14. Once the stage positions were set for all three slides, the acquisition was started and the microscope acquired all images automatically.

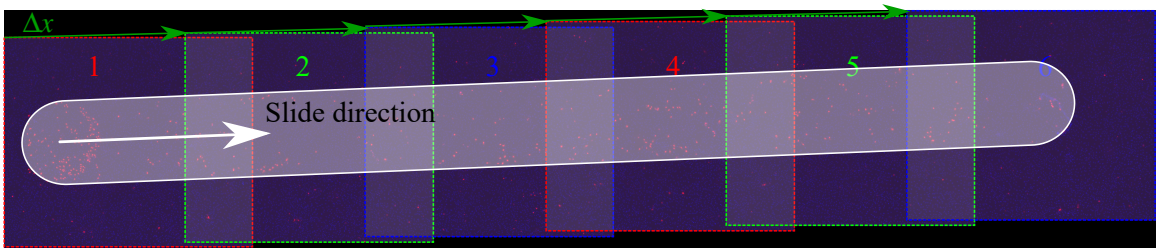

Figure 3.14: Covering of a full slide with multiple images 1 to 6. Each green arrow represents a displacement in the X direction Δx of 2000 µm. The slide that is imaged is highlighted in white and the white arrow indicates the sliding direction.

3.11 Friction Data Analysis

To measure friction with a machine like the UMT 2, the user needs to specify the desired test parameters and the machine gives out a friction coefficient. This works well with most applications relevant to mechanical engineering.

However, for cell work, things are a bit different. The main cause for this is the very low friction coefficients often found in biotribology. If the UMT 2 is used in the way described above, a lot of the detail is lost: the interaction between the two surfaces is still a mechanical system and should be considered as such. The surfaces may not be perfectly even, contact and friction forces could be misaligned to the axes they are expected to be aligned with. This can cause a part of the contact force to act along the axis which the friction force is measured in, affecting the measurement. Furthermore, friction coefficients calculated by the computer do not indicate the direction of the measured forces.

This was realised after conducting and analysing initial experiments on cells and looking at the raw data. Other researchers have reported this issue in conjunction with low-friction experiments [84][85][86]. In general, in these other studies the problem was solved by combining the measurements of two slides on the same track, one on the way forward and

one again on the way back. Unfortunately, the experiments carried out in the scope of this work only involved a slide in one direction. Even for multi-slide experiments, this approach comes with three major downsides which disqualified it for application in this work. Firstly, as with all tribological experiments, the interacting surfaces may change throughout the course of the experiment. For cell monolayers, this is even more factual than for traditional mechanical engineering materials because the cell layer may be damaged or destroyed in parts, or even be fully removed. Secondly, the approach makes it hard to measure the static friction coefficient as it (except during stick-slip) only occurs at the beginning of a slide. Hence, on the backwards slide, at the end (returning to where the forward slide began), only dynamic friction occurs making it impossible to average static friction. Thirdly, as the majority of this work was carried out using a soft substrate which may deform considerably due to shear, it cannot be ensured that positions are matched up exactly. Only the stage position can be measured, however, the respective position on the sample, and with it the slope, may be different on the way forward and on the way back for a single given stage position.

For these reasons, an alternative and novel approach to account for the issues of measuring low friction was developed in this work. For this, at first the problem was analysed on a mechanical level. During a friction experiment, the height of the probe was not consistent over the sample, indicating that the frictional interaction was taking place on a slope. As mentioned earlier, this originates from the soft sample creation. There are two reasons for this. Firstly, the probe height was observed to follow a meniscus shape. This is an issue of the methodology; the polymer is cured from a fluid base which causes a changing slope over the sliding distance. Secondly, the sample is always misaligned to the stage to some extent. All efforts have been made to counteract this effect by making sure the samples were level during curing on a flat glass plate and that they were also flat when inserted into the UMT 2. If using polystyrene dishes without a soft substrate, for example, the meniscus was not visible, but the misalignment between stage and sample still influenced the results. Misalignment and meniscus had to be considered; however, it turned out that the meniscus could be advantageous as it could allow for at least a small horizontal sliding section along the sliding distance.

The effect is shown in Figure 3.16 and overlayed with experimental data. It is posing a known problem with low-friction experiments, as mentioned above. The probe moves from left to right over the sample with speed v_t under set applied load F_Z while the force in X-direction F_X is measured. Under relative movement between the sample and the probe, contact force F_N causes friction force F_F in the interface which is acting against the movement, parallel to the sample surface. If the sample surface was perfectly aligned with the

force transducer and the direction of movement, the friction force would not have a vertical component and hence it would be $F_X = F_F$. However, in the real world, the sample surface will not be perfectly aligned and therefore the contact force between sample and probe will not only act in the vertical direction. This results in a horizontal component of the contact force, which will be detected by the load cell in the X-direction. As the sum of all forces in the horizontal direction is measured as F_X, the horizontal component of the contact force will have an impact on the measured friction force. For most traditional applications, this effect may be negligible as friction coefficients are usually much larger than they are in this work. In the case of cell biotribology, however, friction coefficients of around 0.03 to 0.06 can be expected [78]. For a sphere pressing on a surface with force F_Z under misalignment angle α, the relation between F_Z and the resulting force in X-direction F_X is $F_X/F_Z = tan(\alpha) \approx \alpha$. Hence, to obtain a reaction force in X-direction that would exceed the expected friction force, only a misalignment angle α of 0.03 rad = 1.72 °(which is equivalent to 30 µm height difference on 1 mm of sliding distance) up to 0.06 rad = 3.44 °(60 µm height difference on 1 mm of sliding distance) is necessary. Such a misalignment would cause the measured friction force to either completely cancel out, or double in value, depending on the direction of misalignment. As the misalignment necessary to significantly interfere with the measured friction force is clearly much smaller, this issue must be accounted for.

In Figure 3.15 the forces acting on the probe and the ones measured by the force transducer are shown. As the probe moves downhill on the sample, as seen in Figure 3.15 a, the respective measured force in X-direction $F_{X,downhill}$ is reduced by the X-component of the normal force between sample and probe $F_N sin\alpha$ and only the X-component of the friction force $F_F cos\alpha$ is measured:

$$F_{X,downhill} = F_F cos\alpha - F_N sin\alpha \tag{3.3}$$

If the probe moves uphill on the sample, as seen in Figure 3.15 b, $F_{x,uphill}$ is increased by $F_N sin\alpha$:

$$F_{X,uphill} = F_F cos\alpha + F_N sin\alpha \tag{3.4}$$

The measured force in Z-direction F_Z is influenced by this effect too, however, as both, the angle and the friction force are usually small, the effect on F_Z can assumed to be negligible.

In Figure 3.16, friction data from an experiment is shown with a schematic view of the corresponding probe position as it is sliding over the sample. The experimental data shows the probe height and measured friction force. The probe is shown in different states

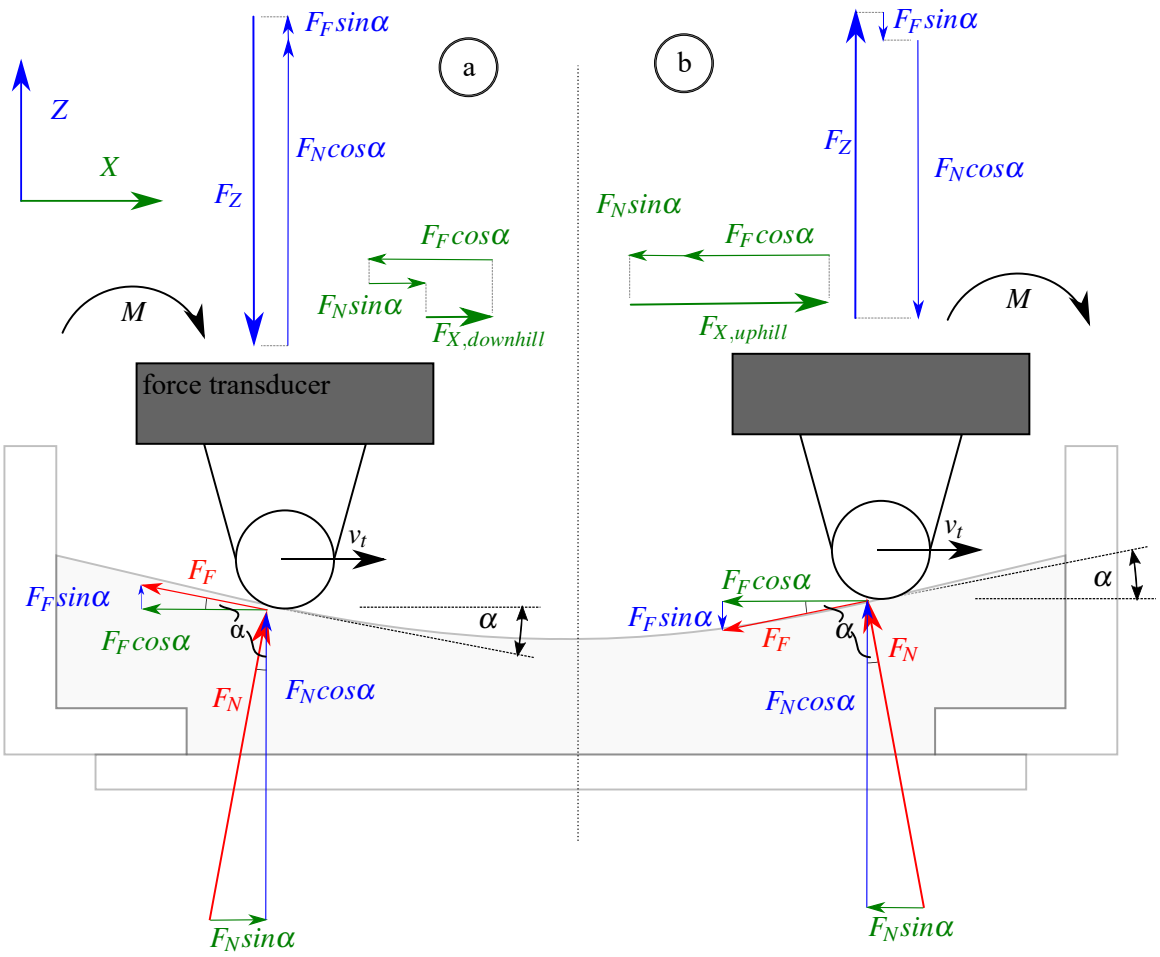

Figure 3.15: Free body diagram of forces acting on probe and registered by force transducer. a) Probe moving over a slide area that points downhill relative to the X-axis. b) Probe moving over a slide area that points uphill relative to the X-axis.

indicated by the numbers in circles. In Position a, the probe is in its start position, before relative movement is introduced and hence there is only static friction. In Position b, static friction has just been overcome and the probe has started moving. In Position c, the probe moves down the slope which causes the horizontal component of the contact force to act against the measured friction force. This causes the measured friction force to be smaller than the real friction force. In Position d, the probe is at the bottom of the meniscus. Therefore, the surface is flat, and the contact force is acting only vertically. For this reason, the friction force measured is not influenced by a component of the contact force. In Position 3, the probe is moving up the slope. Hence, the horizontal component of the contact force is acting towards the measured friction force. Therefore, the measured friction force is higher than the real friction force.

In the same figure, the friction and probe height data are plotted for a typical sliding

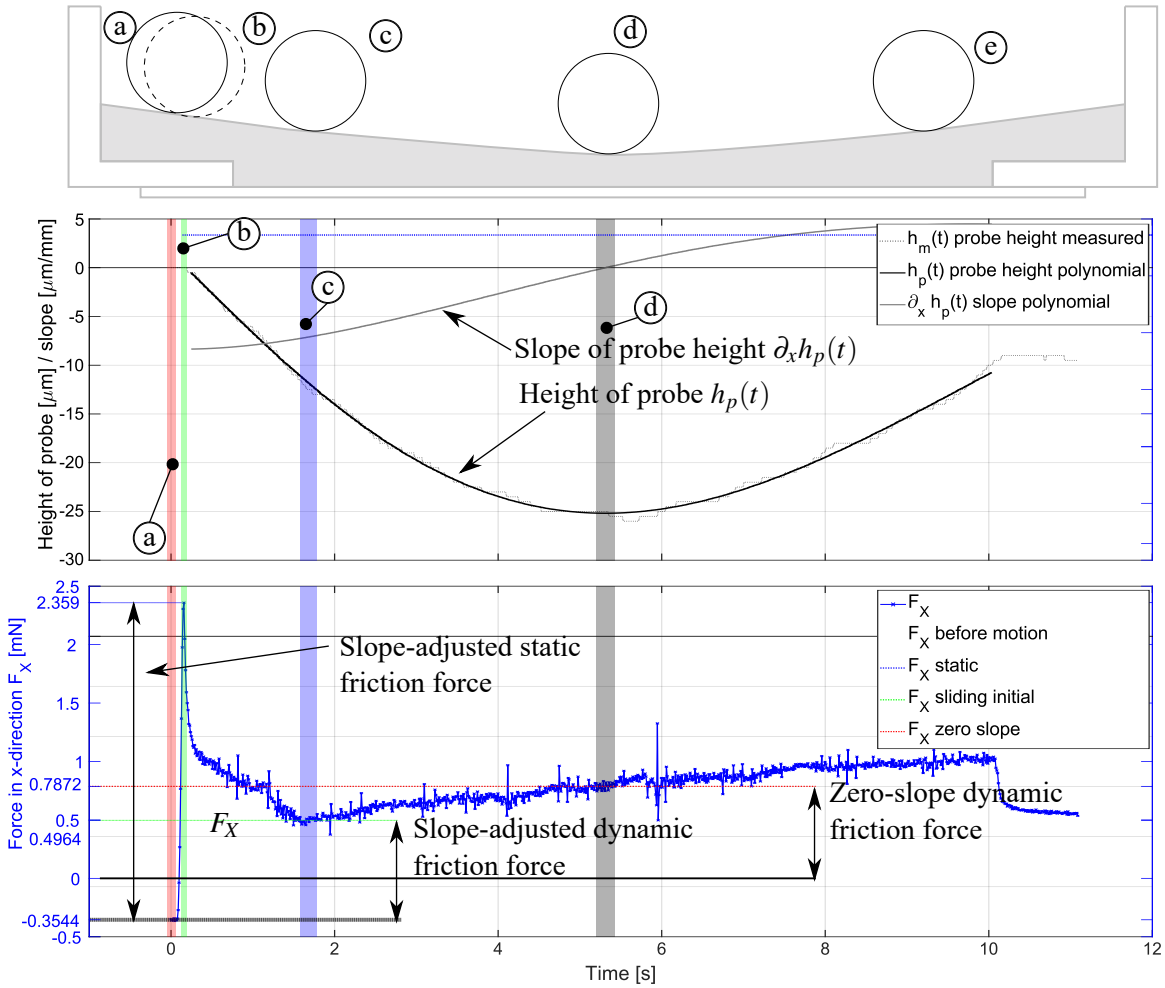

Figure 3.16: UMT friction force F_X (blue) height of probe h (black) and slope $\partial_x h$ (grey) plotted over time with probe position illustrations. Different stages are marked by coloured boxes: a (red) – pre-movement; b (green) – static friction; c (blue) – friction force stabilised; d (grey) - friction force at zero slope. e (only on probe position illustration) - sample is moving up the slope, hence the friction force gets bigger.

experiment carried out at $F_Z = 10\,\text{mN}$. In the figure, the measured friction force F_X starts at $-2.359\,\text{mN}$. This is static friction. The sliding friction (once stabilised) in the beginning is $-0.4964\,\text{mN}$. However, as the sliding continues, the change in slope affects F_X and at zero slope, $F_X \approx -0.7872\,\text{mN}$. This indicates that the friction force is influenced by the slope. For this reason, when conducting tribological experiments with such low friction coefficients, it is very important to make sure the sample is as level and flat as possible and, most importantly, to observe any irregularities in probe height. However, as perfect levelling of the sample is impossible, the meniscus effect may be beneficial as it can allow for a flat section during the sliding.

As mentioned above, the influence of sample alignment has been discussed earlier. Burris et al. approached this by sliding over the sample twice, forwards and reverse to calculate

an average friction coefficient for which the influence of the slope effectively cancels out [84]. While this is a valid approach, it may not be applied to the experiments carried out in this work: no reverse slide is carried out. Carrying out a reverse slide and averaging the friction coefficient may be problematic for any work involving materials that may change significantly by frictional interaction, such as cells.

Hence to reduce the effect of the slope, another approach was developed: when the desired load has been applied, but the stage has not moved yet and is stationary, the friction force is consequently 0. Accordingly, as per the mechanical model introduced earlier, the forces measured by the load cell consist entirely of the ones exerted on the probe by the substrate. When the stage is then moved, this information can be used to adjust for the slope. This is also shown in Figure 3.16. The value for the force measured during the loading phase a (red) is used as offset when calculating the static friction force measured during position b (green). The same approach can reduce the slope's effect on the dynamic friction force. In practice, there remains a residual influence. This is because the dynamic friction force takes a while to stabilise (c, blue box). A better way to measure the dynamic friction force is to measure it at the area where the slope is around zero. To find this area, the height of the probe $h_m(x)$ was approximated with a 5th order polynomial $h_p(x)$. The derivative of $h_p(x)$ in X-direction $h\prime_p(x) = \partial_x h_p(x)$ is the approximate slope of the sample. This can be used to find the location where the surface is horizontal, as shown in the figure (d, grey). However, the slope never reaches zero for some slides due to substantial misalignment. Hence, where possible, three values were calculated: the slope-adjusted static friction force $F_{Fs,adj}$, the slope-adjusted dynamic friction force $F_{Fd,adj}$ and the zero-slope dynamic friction force $F_{Fd,level}$.

3.12 Damage Analysis

To analyse the damage caused by a friction experiment, the sample was first stained with PI/Hoechst as described in Section 3.10.4 and images were taken of the full slide and its surrounding area as described in Section 3.10.5. First the images were stitched together as the field of view is not wide enough to cover the whole slide length of 10 mm. For this, the respective stage positions, which were written into the metadata of each picture, were used to position the images. Afterwards, the images were manually aligned and cropped and the slide area was defined. Control areas, where no interaction with the probe occurred, were generated automatically by the conditioning program. Then, the image was analysed using Cell Profiler determining and saving all nuclei positions. Finally, with this data, the nuclei densities could be calculated in the slide area and in the compare area and then compared.

This is a novel way of looking into friction-induced damage to an endothelial monolayer and therefore the approach is described in detail here.

3.12.1 Image Stitching

When taking a picture, the microscope software writes the current X, Y and Z coordinates into the image file. These coordinates can be used to generate a big image covering a large area from many images, each covering a small part of the total area. A MATLAB program was written for this process, but first it had to be determined how the images were aligned. Assume the two pictures in Figure 3.17 are to match up. There is a recognisable pattern of 3 cells in both images that can be matched up as marked by the arrows. The X and the Y stage coordinates had to be translated into X' and Y' pixel coordinates. As there is a slight misalignment between the camera sensor and the stages, a displacement of the stage in the X direction caused a displacement in the X' and the Y' direction in the image and the same applied for a displacement in the Y direction. This relation is shown in Figure 3.18.

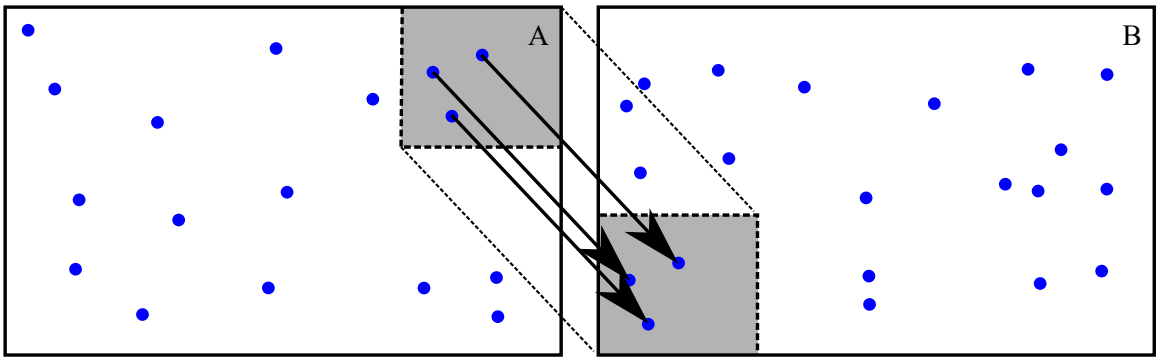

Figure 3.17: Matching up of images. The locations of the distinct formation of nuclei in the grey area must be matched up in order to stitch the images.

Therefore, 5 images of a calibration ruler were taken with given stage displacements in either X or Y direction Δx or Δy, respectively. Displacements were only applied in one direction at a time. The images were then aligned manually, and the resulting displacements in pixels in X' and Y' direction $\Delta x'$ and $\Delta y'$ were measured. From that, it was calculated, how big of a displacement in the pixel X' and Y' directions is caused by a respective displacement in the X or Y direction. These values were used to generate a transformation matrix M, which allowed to convert stage to pixel positions using the relation:

$$\begin{pmatrix} \Delta x \\ \Delta y \end{pmatrix} = \vec{p} = M\vec{p}' = \begin{pmatrix} m_{x'x} & m_{y'x} \\ m_{x'y} & m_{y'y} \end{pmatrix} \begin{pmatrix} \Delta x' \\ \Delta y' \end{pmatrix} \tag{3.5}$$

with stage coordinates $\vec{p}'$ and pixel coordinates $\vec{p}$. As seen from this relation, the unit of M is [pixel/µm], because the matrix converts from a length unit to pixels.

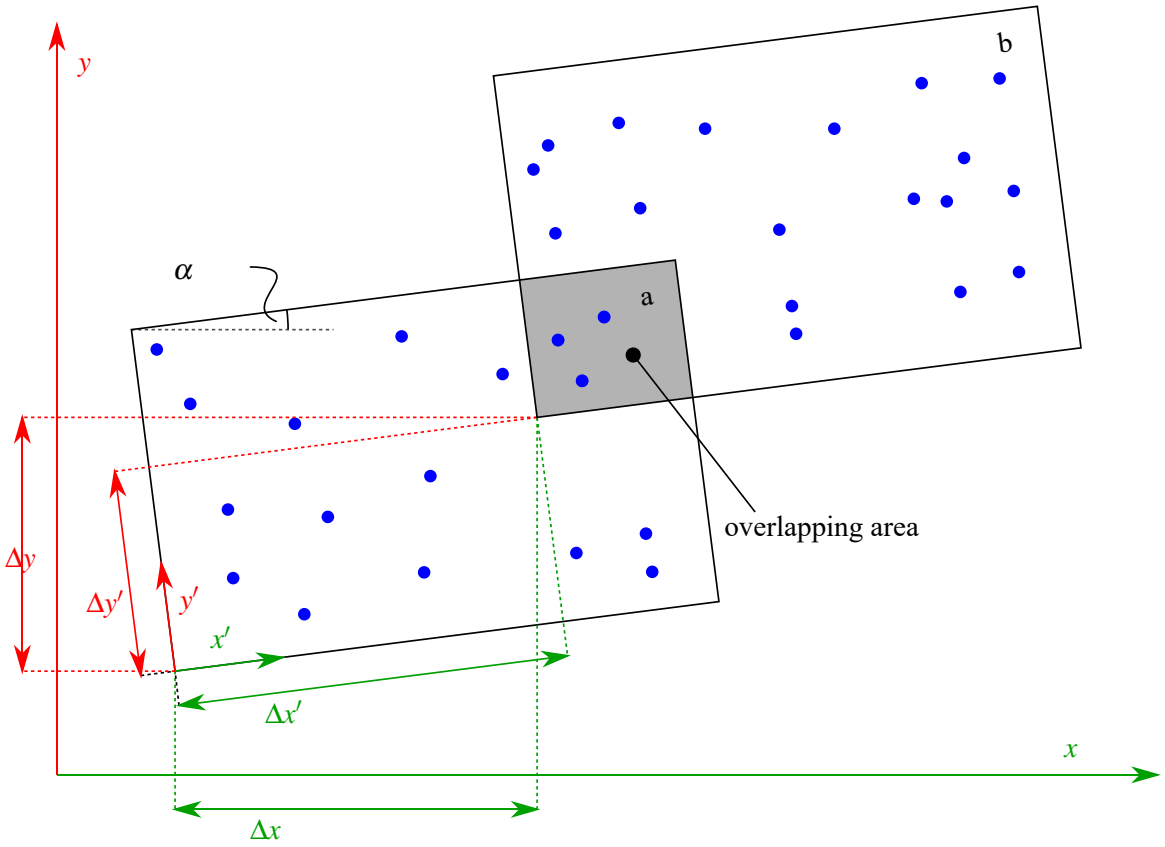

Figure 3.18: Coordinate transformation from X and Y to X' and Y' in order to stitch the two images together.

In this work, two sets of objective lenses were used: the 10x and the 4x objective + tube. M is essentially the same for different objective lenses as it only reflects the misalignment between the camera sensor and the stage. However, as the object magnification changes, a conversion factor is required if, for example, a 10x objective was used instead of a 4x objective + tube. Using the tube adds an additional 1.5x magnification. The respective transformation matrices are reported in Table 3.4.

The software was written using an object-oriented approach. The logical flow of the program is shown in Figure 3.19. When an instance S of the class ImageStitcher is initialised, it is created with all the necessary variables and functions. Upon initialisation, the UI window S.myInstanceControlFigure, shown in Figure 3.20, is created where the user interface is displayed and the data window S.myInstanceImageFigure, shown in Figure 3.21, is created, where the data is shown. S.myInstanceControlFigure shows the interface that is used to interact with the data. From here, data can be loaded, updated or saved. Brightness and contrast can be adjusted for the three channels and histograms of the images pixels intensities are displayed. Furthermore, any user interaction is documented in the event history. S.myInstanceImageFigure only shows the data. In the left column, the raw data for

Objective	**Transformation matrix** M [pixel/µm]
4x + tube	$\begin{bmatrix} -0.92725 & -0.028 \\ 0.028 & -0.92725 \end{bmatrix}$
10x	$\begin{bmatrix} -1.54 & -0.046667 \\ 0.046667 & -1.54 \end{bmatrix}$

Table 3.4: Transformation matrices M to convert from stage to pixel coordinates for 10x and 4x + tube objectives.

blue, red, blue/red combined and brightfield channels are displayed. In the column on the right, the adjusted counterparts are shown. After initialisation, the graphs in the data figure are empty because there is no data yet.

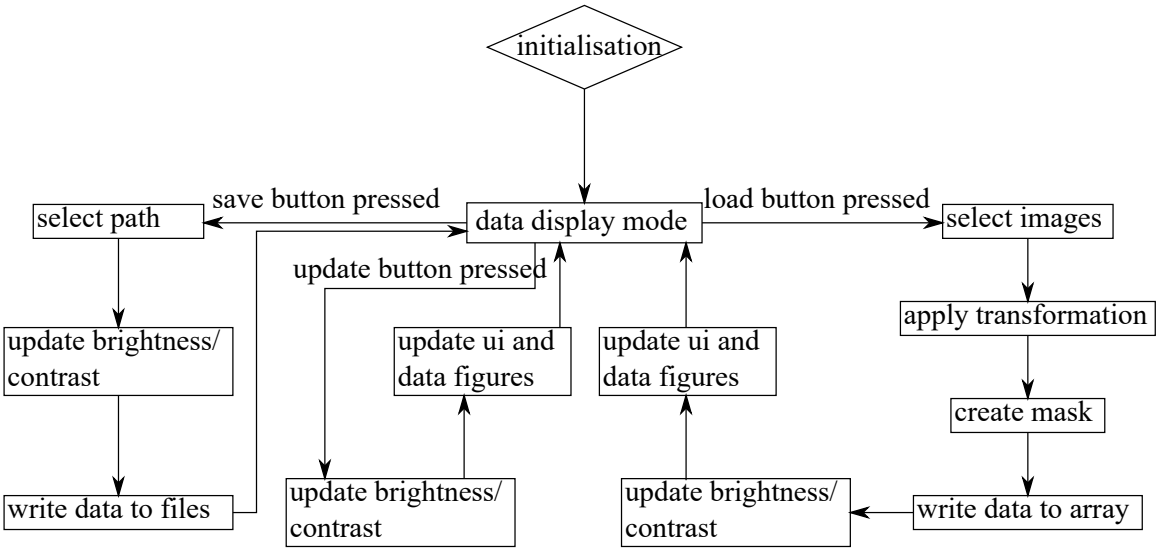

Figure 3.19: Image stitcher logic flow diagram.

Loading Image Data

A data structure array S.imgData[] is created to handle the image data. The image data of the *i*th brightfield image is loaded into S.imgData(i).img_bf. The respective image metadata is written into S.imgData(i).info_bf. That image data is then parsed to acquire X and Y stage positions, which are written into S.imgData(i).x_pos_bf and S.imgData(i).y_pos_bf, respectively. Red and blue channel images are processed in the same way, but with _red and _blue identifiers rather than _bf.

Afterwards, the stage positions are compared to make sure that they match for every set of images. If the stage positions are different between the brightfield, red or blue image, a warning is displayed. Afterwards, the image width and height in pixels are determined. The relative coordinates in micrometres of each image are calculated in relation to the image with the smallest x and y data, respectively. Afterwards, those relative coordinates are converted using the transformation matrix using the relation in Equation 3.5.

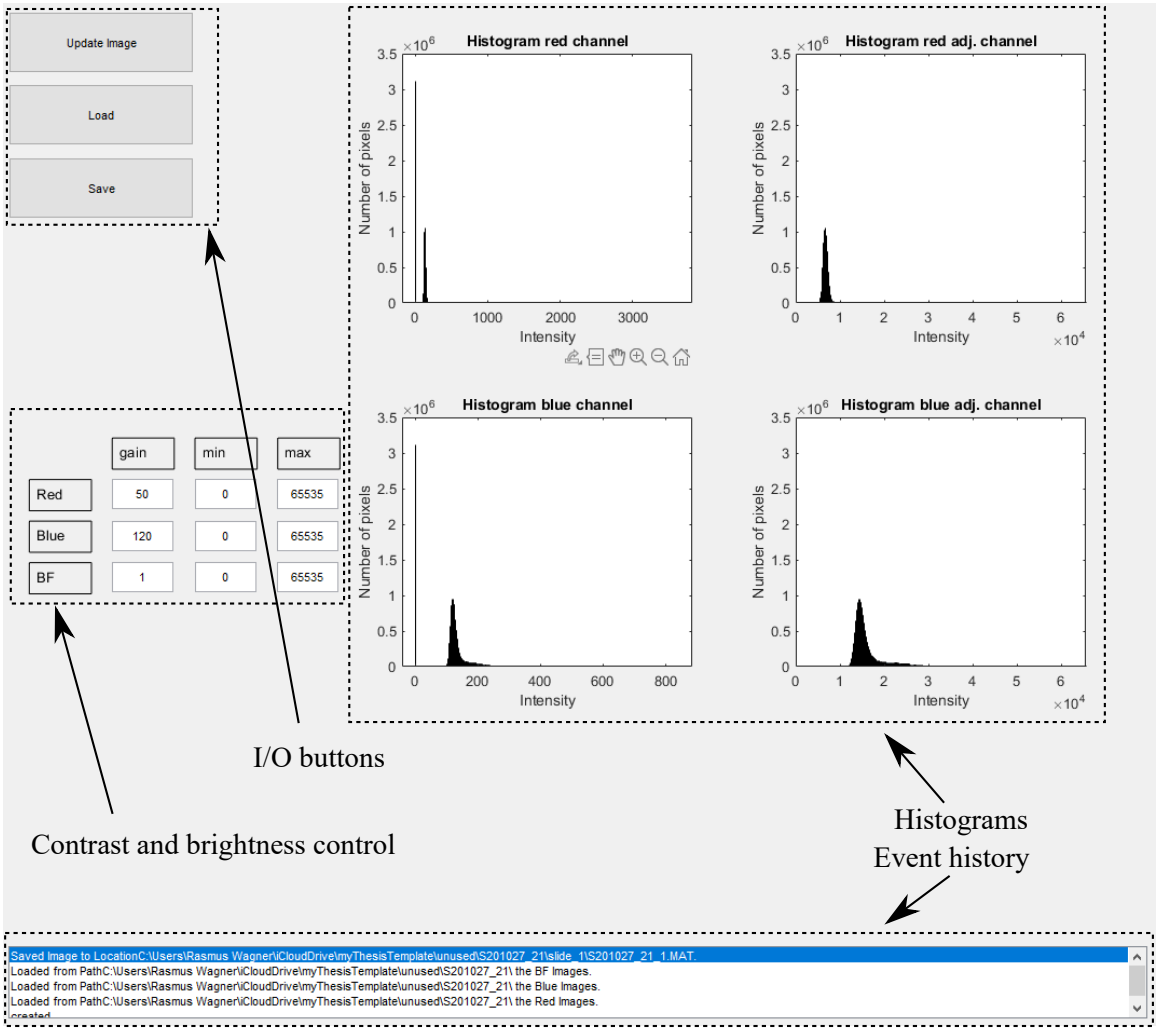

Figure 3.20: Image stitcher UI window with I/O, contrast and brightness controls outlined. Histograms of red and blue channels as well as their brightness/contrast adjusted counterparts are highlighted. At the bottom of the figure, the event log is displayed indicating any I/O processes initiated by the user.

Where two or more images overlap, the average of the images should be taken. For this, a mask img_mask is created. The mask is a 2D matrix of doubles with the same dimensions as the stitched image and is initialised with the value 0 in each field. For each image set, all pixels in img_mask that the image set would occupy are increased by 1. After this is repeated for all image sets, all zero values in the matrix are set to 1. Then, the reciprocal of

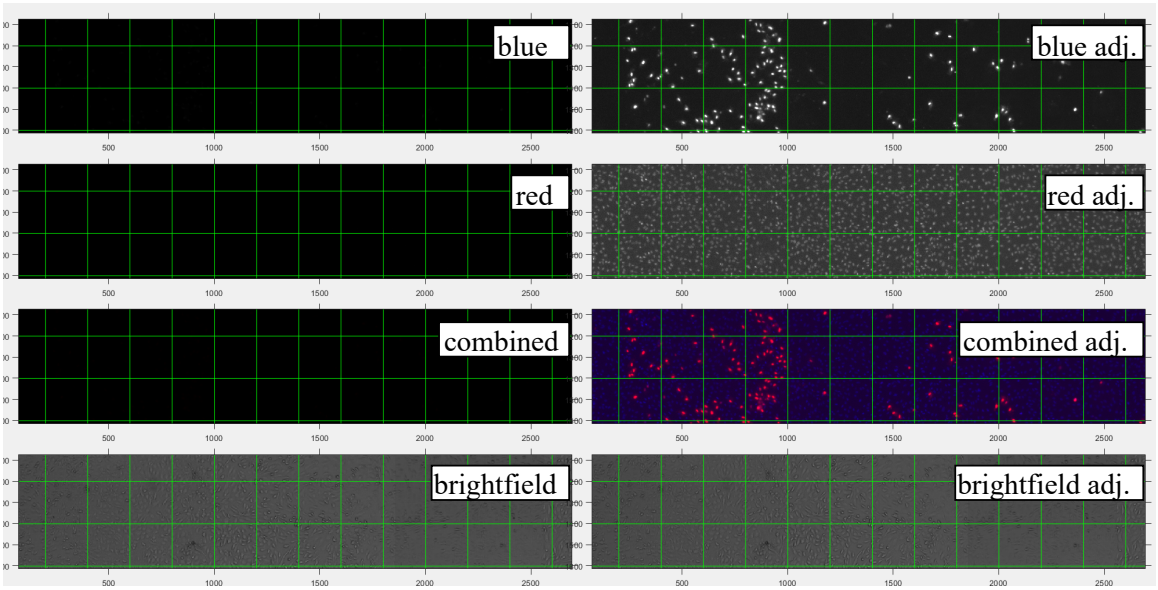

Figure 3.21: Image stitcher data window.

each individial value in the matrix is calculated. In positions no image data will be written to, or positions that are occupied by one image, the value of img_mask is 1, in positions where i images overlap, the value is $\frac{1}{i}$.

Afterwards, three 2D matrices (brightfield, blue and red) of 16 bit integers are created to hold the image data. The height of these matrices is determined by calculating the difference in pixels $\Delta Y'$ between the minimum and the maximum positions and adding the height of one image. The width of the matrices is determined similarly. Then, the data is multiplied with the mask and the data is written into the respective matrix. After this is carried out for each data set, the subroutine returns the image data for it to be stored and the program returns to the main window. The data that was generated is then updated and plotted in the data window and the program returns to the data display mode.

Adjusting Brightness/Contrast and Saving Image Data

When collecting the image data with the microscope, the raw data from the sensor is stored as a 16 bit deep bitmap which is saved as a .tif file. In MATLAB, this data is also handled as a 16 bit integer matrix, meaning that the range for the values is 0-65 535. Especially the blue and red channels absolute brightness may be fairly low due to low fluorescent light intensity, meaning that the measured values were on the lower end of the range. This can cause the images to show up as completely dark when plotted in MATLAB making it necessary to modify the brightness and contrast, as can be seen in Figure 3.21 in the left column. This causes problems as the user must be able to see the data and ensure the correct images were

loaded. Hence, brightness and contrast of the image can be conditioned within the stitching program by the user by setting minimum values, maximum values and gain parameters for each channel resulting in images the user can examine as seen in the right column in Figure 3.21.

After new data is loaded, and before data is saved to a file, these parameters are applied in the subroutine S.BCAdjustImages() and the updated data is displayed. Minimum values are applied by lowering all values that are below the minimum value to 0. Maximum values are applied by lowering all values exceeding the maximum value to the maximum value specified. Finally, the gain is applied by multiplying the whole image matrix with the respective gain value. To save the data as a file, the imwrite() function is used. The raw values were saved as a .tif file and the brightness/contrast adjusted values were stored as a .txt file.

3.12.2 Image Conditioning and Slide Area Identification

After Stitching, the images had to be manually aligned and where the probe interacted with the substrate had to be defined. For this purpose, a program called imageCropper was written that followed a similar, object-oriented approach as the imageStitcher class. The imageCropper program also uses 2 figures: a UI figure shown in Figure 3.22, that handles the user interface and a data figure, responsible for displaying the data. The program was created to achieve the following tasks: aligning the image so that the slide is vertical, cropping off all areas that contain no image data and defining the slide and compare areas.

All images of the same slide are then loaded automatically and written into the respective instance variables. The imageCropper program handles image data the same way the stitching program does. After that, cropping and rotation parameters are reset to standard values and the program returns to the data display mode, plotting the blue and red adjusted channel images in the data window, as seen in Figure 3.23.

Then, the image rotation and crop parameters section is used to first align the image horizontally and then crop off all black areas. This step is important because the slide overlay assumes the slide to be horizontal. The black areas must be cropped out because pixels of a brightness value of 0 cause problems during the nuclei detection, which will be described later. To help with that, an interface was implemented in the UI figure that shows how many black (brightness = 0) pixels are in each channel. When this number drops to 0, the indicator boxes and the save button turn green, indicating that no spots of zero brightness are left.

After aligning and cropping the image, the slide overlay must be aligned using the slide position and size parameter section in the UI window. The circle on the left marks the

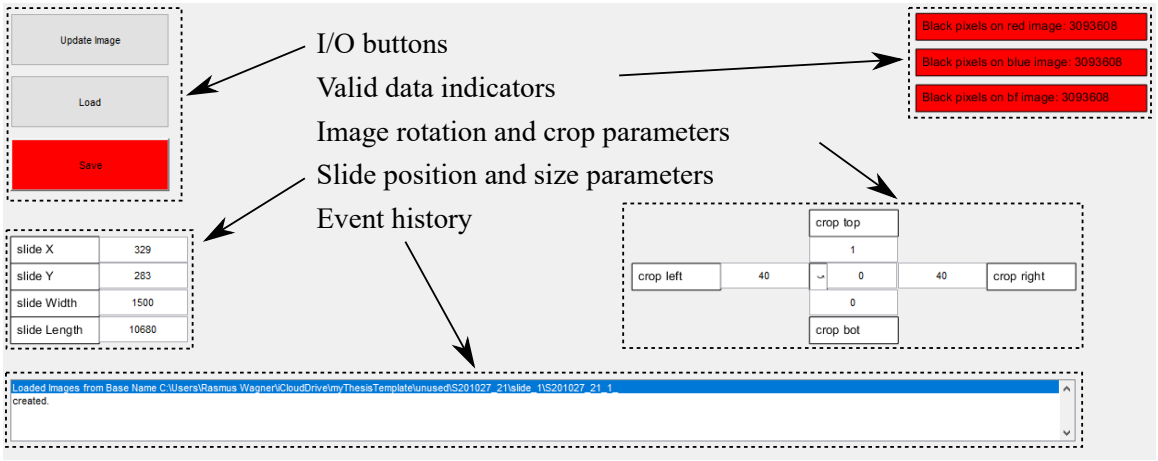

Figure 3.22: Image cropper UI window with I/O, slide position, cropping and rotation controls and valid data indicators highlighted. At the bottom of the figure, the event log is displayed indicating any I/O processes initiated by the user.

indentation area and should be lined up with the beginning of the slide where there can usually be found a circular pattern of dead cells. First, the top and the left edge of the slide are lined up. Then, the width and height are set. The data window as it looks when the slide is overlayed with the slide overlay is shown in Figure 3.24. The green compare boxes are generated automatically, covering the maximum possible area, while still allowing for a sufficient spacing to the edge of the image and the slide area.

The cropped and aligned images are saved as .tif files and the position and size of the slide overlay is written into a .txt file as it is required later.

3.12.3 Nucleus Identification

In order to quantify the number of nuclei that have been removed, they have to be identified first. As there are tens of thousands of nuclei in every full slide image, this process had to be automated. MATLAB's image processing library and a software called CellProfiler were assessed for this task. CellProfiler [107] is an open source software that is marketed specifically to biologists and aims to solve exactly the issue at hand: identifying cells and/or their nuclei. Results using MATLAB were inferior in terms of nuclei identification and after assessment of both approaches, using CellProfiler clearly was the superior approach. With more tweaking, similar results might have been achieved with a MATLAB code, but CellProfiler was quicker and offered a premade set of tools created by experts. Therefore, it was decided to use CellProfiler from hereon.

CellProfiler contains a wide range of advanced tools for a variety of applications. Therefore, the images generated in this work are comparitively easy to analyse for CellProfiler.

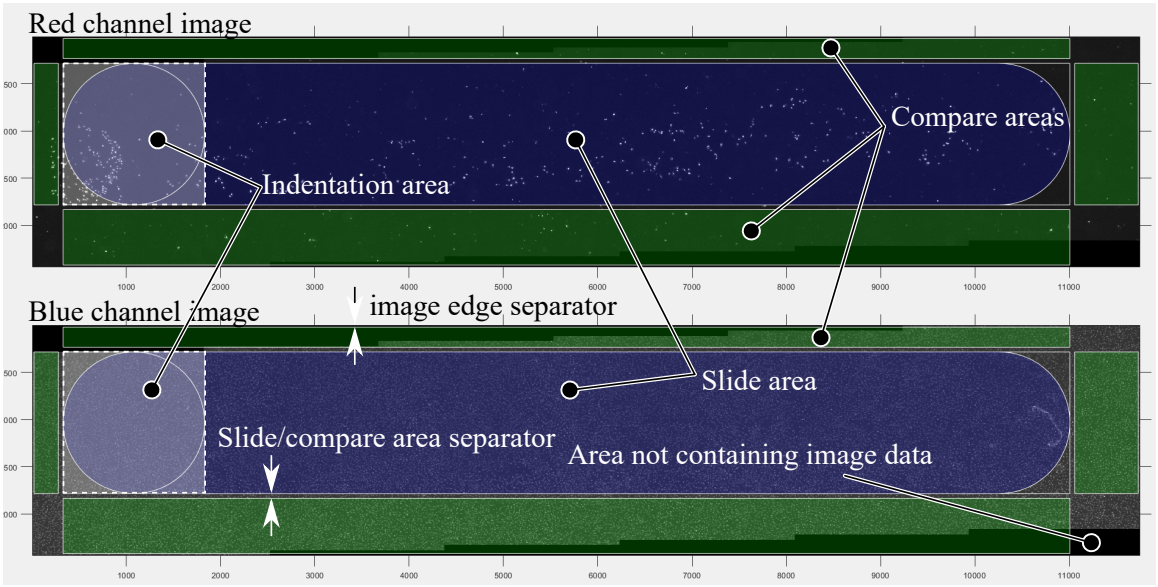

Figure 3.23: Image cropper data window displaying red and blue channel images with an unaligned slide overlay. The slide overlay indicates the position of indentation and slide areas, as well as the location of the compare areas, which are automatically generated. Separating distances between slide/compare areas and compare areas and the image edge are shown.

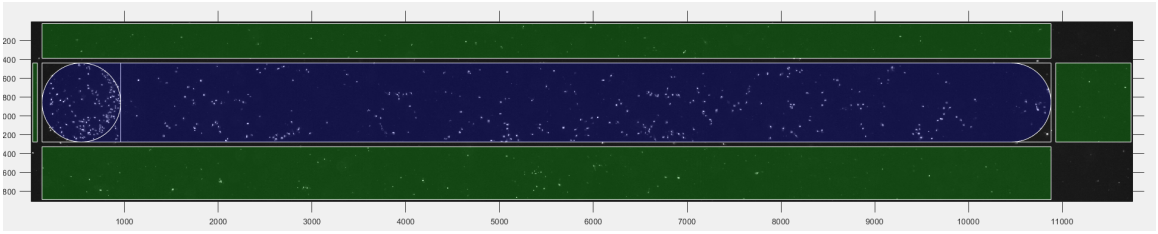

Figure 3.24: Image cropper data window with aligned slide overlay.

The more advanced features of this software have been examined and applied to the image sets, but did not noticably improve the reliability or accuracy of the results. The final cell profiler structure (or pipeline as it is called by the software) that was developed for this work first checks the filenames and, based on those and the folder names, matches corresponding red and blue images. This was manually rechecked.

Then, two “IdentifyPrimaryObjects” modules were utilised to identify the nuclei. The advanced settings were activated for those in order to use the Otsu thresholding method, which distinguishes between two classes of foreground and background pixels by minimising the respective variances [107]. Most parameters were left at their default. The “Size of adaptive window” setting was altered to 80 pixels and 150 pixels, for red and blue nuclei, respectively. Furthermore, the “Discard objects outside of diameter range” was deactivated and the “typical diameter of objects, in pixel units” was set to 10-30 for both “IdentifyPrimaryObjects” modules. Names were specified for the red and the blue objects to serve as

identifiers in the last step.

The final step of this process is to export the positions of all identified blue and red objects into the respective spreadsheets “hoechst_stained_nuclei.csv” and “pi_stained_nuclei.csv”. The spreadsheets are created in the same folder, that the images were originally loaded from and contain object numbers and X and Y positions of all identified objects.

3.12.4 Damage Quantification after Friction Experiments

The damage to the monolayer was assessed by nuclei counting using the previously generated lists of nuclei and the slide coordinates defined using the imageCropper program, which were saved to a .txt file previous previously. A MATLAB script called nucleiLoader.m was written to load and view this data. The script is run from the folder the data is in and requires the sample identifier and slide number to find the appropriate files. Both nuclei .csv files, as well as the slide overlay coordinate files are scanned using the fscanf() function. Red and blue nuclei coordinates are stored as matrices of doubles.

Based on the slide coordinates specified earlier, the indentation area, main slide area, end of slide area and four compare areas are defined. Using MATLAB’s logical indexing, nuclei are assigned, based on their coordinates, to groups belonging to slide or compare areas. To ensure the assignment has worked correctly, all nuclei are plotted with a white “×” and if they were found in a compare area, they are highlighted by a red circle. If they were found in the main slide area, they are highlighted with a cyan circle. These data are plotted as seen in Figure 3.25.

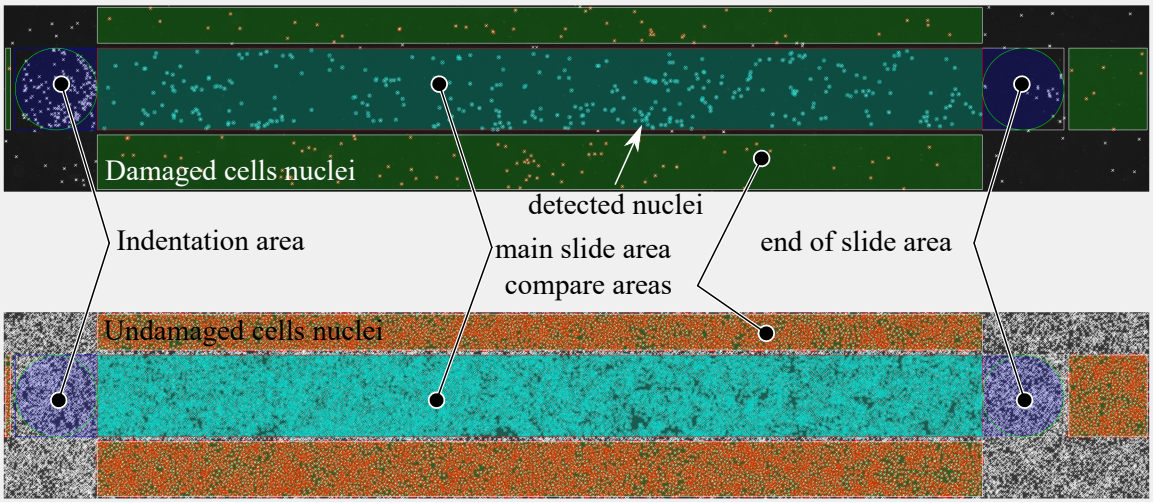

Figure 3.25: Nuclei loader data window of red and blue channels with aligned slide overlay and marked nuclei. Indentation, slide and compare areas are highlighted.

Then, the sizes of the four compare areas $A'_{comp\ i}$, and of the slide area A'_{slide} in pixels are calculated. All compare area's sizes are added to obtain the whole compare area size: $A'_{comp} = \sum_{i=1}^{4} A'_{comp\ i}$. Then, the numbers of nuclei in the respective areas $n_{comp\ i}$ and n_{slide} are determined. Similar to the area, the numbers of nuclei in all compare areas are added up to a total value n_{comp}. Generally, the absolute average nuclei density ε in nuclei/pixels of area A' containing n nuclei can be determined with

$$\varepsilon = \frac{n}{A'} \tag{3.6}$$

This relation is used to calculate red and blue nuclei densities for compare and slide areas $\varepsilon_{comp\ B}$, $\varepsilon_{comp\ R}$, $\varepsilon_{slide\ B}$ and $\varepsilon_{slide\ R}$ which are plotted as seen in Figure 3.26. However, when comparable absolute nuclei density values were to be given, the calibration of the microscope should be accounted for so that the nuclei densitity ρ_k is reported in nuclei/mm^2. The conversion is:

$$\rho_k = \frac{n}{\xi^2 A'} = \frac{1}{\xi^2}\frac{n}{A'} = \frac{1}{\xi^2}\varepsilon \tag{3.7}$$

with Equation 3.2 in Subsection 3.10.5 with previously determined spatial calibration factor ξ, which can be found in Table 3.3. Furthermore, the relative nuclei density P_{slide} is calculated and reflects the effect of frictional interaction on nuclei density relative to the compare areas:

$$P_{slide} = \frac{\rho_{slide}}{\rho_{comp}} \tag{3.8}$$

3.12.5 Damage Quantification after Indentation Experiments

The damage quantification for indentation tests is similar to the one carried out after friction experiments. It relies on the same staining techniques and nuclei identification solutions described above. Areas where they differ are how the testing site is determined and how damage is quantified.

After indentation was carried out as described in Section 3.9.2 and the samples were stained with PI/Hoechst, images of the five indentation sites were taken as laid out in Section 3.10.5 for each indentation run. Microscope settings were chosen to be the same as for imaging friction test sites. Microscope images of indentations did not have to be stitched as the field of view of an image taken with the 4x + tube objective lens is large enough to cover the whole testing site. As three indentation runs were executed per sample, this resulted in 15 images of red, blue and brightfield each. Therefore, the raw red and blue channel tiff images were organised and loaded into the same CellProfiler pipeline decribed in Section

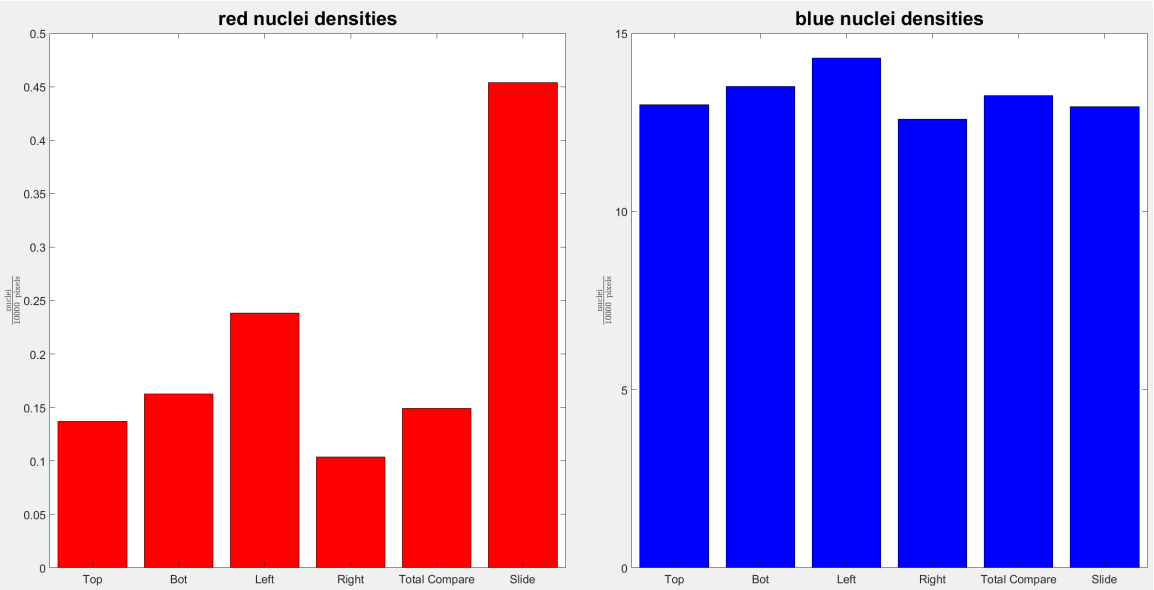

Figure 3.26: Nuclei densities plotted for top, bottom, left, right and total compare areas as well as main slide area.

3.12.3. After the script was run and for each red and blue image there was a corresponding file with nuclei positions, the data was analysed with MATLAB. One dataset was loaded and analysed at a time. Just like for the friction damage assessment, first, red and blue nuclei positions were read from the csv file. At this point, the approach differed because the testing site was defined by a centre point and a radius. Figure 3.27 shows two nuclei plots of the third indentation with a PTFE probe with a normal force of 10 mN. On the left, blue nuclei are plotted with white X markers. On the right side is a plot of the same site, but of the red nuclei marked with a white X. The centre point was not defined manually, but instead by calculating the mean of all red nuclei positions. This position is highlighted in both plots with the large, red X. After the position of the centre point was determined, the distance of each nuclei to the centre point was calculated. These distances were then discretised, i.e. they were binned into ranges spanning 25 µm each, up to a maximum range of 1000 µm. In the image there are concentric circles revolving around the centre point. These circles represent the bins in which the nuclei distance data is discretised and the two aforementioned distances are annotated.

Based on this discretisation, a histogram was created with red, blue and total cells. The total amount of cells in a bin was calculated as the sum of the amounts of red and blue nuclei. The histogram generated from the nuclei plot above is shown in Figure 3.28. Blue nuclei are plotted with blue bars, red nuclei with red ones. The combined amount is plotted with grey bars.

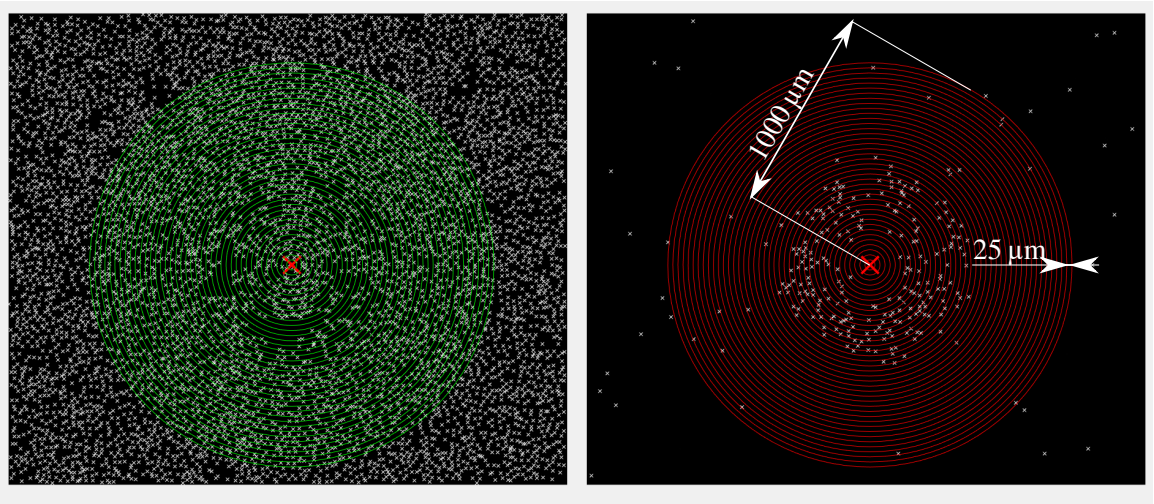

Figure 3.27: Blue (left) and red(right) nuclei plots after an indentation experiment with histogram bins indicated by concentric circles and calculated indentation centre marked with red X.

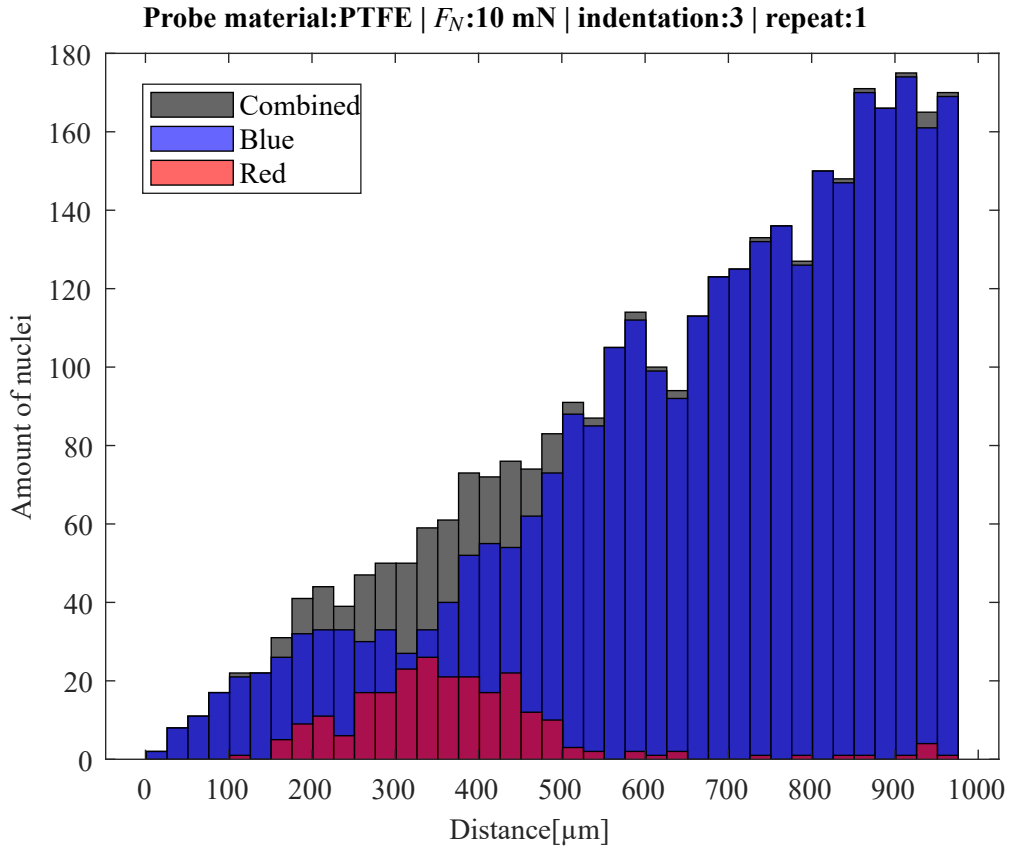

Figure 3.28: Histogram plot of nuclei based on distance to indentation centre.

3.13 Material Properties and Contact Theory

In this work, a number of materials were used and Hertzian contact mechanics [49] was used to calculate contact parameters. Probes were made from glass, stainless steel and PTFE. Unless stated otherwise, glass refers to soda lime glass, and stainless steel to 316L alloy. Another type of material mentioned later is borosilicate glass. Substrates were manufactured from soft PDMS and polystyrene.

Hertzian contact mechanics is maybe the most useful fundamental theory to describe the interaction of two bodies. It does not account for effects like adhesion and assumes linear material parameters, small deformations, no relative velocity and smooth surfaces. More advanced models (JKR, Winkler foundation or DMT) may cover some of the limitations the Hertzian model has, like adhesion. However, in order to apply those models, knowledge about surface parameters are necessary which are not easy to measure on a monoalyer which furthermore may change throughout the experiment. Many of the other limitations, especially the one of smal ldeformations, also apply to other standard models. The most accturate way of simulating the contact would be a finite element model that would take into account adhesive effects and large deformations. To apply such a model, however, also knowledge about the time variance of the monolayer would be required. According to Hertz, for a sphere and a contacting flat surface (halfspace), indentation depth d and reaction force F (also P_0) are linked through

$$F(d) = \frac{4}{3} E^* R^{1/2} d^{3/2} \tag{3.9}$$

with reduced Young's modulus E^* and sphere radius R.

R defines the geometry and E^* the material properties. In order to do calculations, knowledge of these material properties is required. The reduced Young's modulus E^* is calculated through:

$$\frac{1}{E^*} = \frac{1-\nu_{\text{sphere}}}{E_{\text{sphere}}} + \frac{1-\nu_{\text{halfspace}}}{E_{\text{halfspace}}} \tag{3.10}$$

with Young's moduli E and Poisson's ratios ν of the respective geometries. The radius of the contact area a can be calculated with the aforementioned variables with:

$$a^3 = \frac{3FR}{4E^*} \tag{3.11}$$

and the maximum pressure p_0, which occurs in the centre of the contact region with:

$$p_0 = \frac{3F}{2\pi a^2} \tag{3.12}$$

In Table 3.5, the relevant material properties of the aforementioned probe and substrate materials are listed. Whenever calculations were made, these parameters were used.

Material	Young's modulus E [Pa]	Poisson's ratio ν [-]
Soda-lime glass	6.3×10^{10} *	0.2 [108]
Borosilicate glass	6.3×10^{10} [109]	0.2 [109]
316L Stainless steel	1.93×10^{11} *	0.25 [110]
PTFE	3.40×10^{8} [111]	0.46 [112]
Soft PDMS	7.332×10^{4} [88]	0.5 [88][111]
Polystyrene	3.25×10^{9} [111]	0.3275 [111]

Table 3.5: Material parameters used for calculations. Parameters marked with * are adapted from respective manufacturers website.

3.14 Summary

In this chapter, a set of methods has been presented to conduct *in vitro* testing on a cell monolayer. Monolayers of cells have already been tested in previous studies, however, the methodology presented here comes with some advantages. While being a bit more complex and involving more steps than simple cell culture on polystyrene dishes, this methodology constitutes a way of conducting friction experiments under more realistic conditions and allows assessment of damage. In regards to damage assessment, a novel set of software was developed in this work to measure and compare the damage caused to the cell monolayer. Furthermore, the known issue of very low-friction tribological experiments, that the measured friction coefficient can be highly dependent on the alignment between the testing surfaces, has been identified and solved in a novel way.

This methodology could be adapted for different applications by changing the cell type. In this work, HUVEC have been used, which are veinal endothelial cells. By cultivating epithelial cells, for example, urinary tracts could be emulated and tested against urinary catheter materials.

To ensure that the cells are growing as expected and to identify the best way of making the PDMS inhabitable, a cell adhesion experiment was conducted, which is subject of Appendix B. Once it was clear that HUVEC grew well on the substrate and formed a full monolayer, this set of methods was applied to assess the influence of different materials and loads on damage and friction in Chapter 4.

Chapter 4

Friction Experiments with Subsequent Wear Assessment

This chapter investigates the influence of normal force (load) on the damage inflicted to the monolayer and the measured friction force. Furthermore, cells were tested against different materials and the damage was compared. In an effort to link this novel work to existing studies on (HUVEC) monolayers, baseline experiments were conducted on PS-based samples.

4.1 Background

Medical devices, such as stents and catheters interact with blood vessels inevitably as described in Section 2.3. The deployment and/or presence of such medical devices can cause serious complications for the patient, some of which can be linked to mechanical trauma and a damaged endothelium. The friction coefficients can be crucial in those applications, and the medical devices can be made less damaging with a small friction coefficient (for catheters), or a high friction coefficient to hold the medical device in place (for stents). In this experiment, friction and damage were investigated with an *in vitro* approach.

In vitro friction experiments have been conducted on (endothelial) cells before, however those studies were completed using cells cultured on either PS or glass, which are very good materials for cell culture. However, they are extremely hard, compared to *in vivo* conditions. Many of those studies have similarly used glass or stainless steel spheres for testing, which makes the experiments reproducible and compareable, as spheres of these materials can be procured anywhere in the world with relative ease. Nevertheless, these two things combined mean that the cells are stuck between a hard substrate and a hard sphere. Unless expensive microtribometers are available enabling extremely low loads, this results

in almost all of the cells in the contact area being squashed, which makes damage difficult to assess, produces conditions that are not realistic and leads to the total obliteration of the cells. Those conditions also raise the question of the quality of the lubricating layer: intact endothelial monolayer or disrupted cell membrane? The methodology to create soft substrate samples with a monolayer of HUVEC presented earlier was developed with this in mind and shall here be used to test cells in a more realistic way that also makes it possible to assess damage. In contrast, the exact same methodology (except for the soft substrate) was applied to PS-based samples, in order to see how the soft substrate influences the results.

4.2 Aims and Objectives

The aims of these experiments were to apply the methodology described in Chapter 3 to test an *in vitro* endothelial monolayer against spherical probes in a controlled environment, as realistically as possible, and to assess the damage that has been caused. By doing this, the influence of different materials and a range of normal forces was studied in terms of damage to the monolayer and occuring friction. To achieve these aims, the following objectives had to be met: *In vitro* surrogates for blood vessels with an endothelial monolayer to test were required; then, counter surfaces to test the monolayer against (probes) with relevant materials needed to be manufactured; the probes had then to be tested against the monolayer and the damage had to be measured in a way that allowed later analysis. On the analysis side, both friction and damage analysis required the development of custom techniques.

4.3 Methods

The methods used in this Chapter were largely applied as described in Chapter 3. Some of the results were collected using only a subset of the full methodology as is described in this section. Also, the rationale behind how the damage is assessed is explained here in detail.

4.3.1 Substrates

Soft PDMS substrates were cured and coated with fibronectin. HUVEC were seeded on these substrates and grown with regular media changes until a fully confluent monolayer was present. The protocols used are described in Sections 3.4, 3.5 and D.2, respectively. Cells were cultured on fibronectin coated PS (apart from soft substrate samples) in order to investigate the effect of the substrate. Fibronectin-coated and uncoated standard polystyrene dishes were also tested, to investigate the influence of a monolayer on friction.

4.3.2 Probes and Friction Apparatus

Probes were manufactured as explained in Section 3.7 by attaching 2 mm spheres to a pipette tip. For probe materials, stainless steel, glass and PTFE were used. Stainless steel was chosen to represent stents, glass was used for comparison with previous studies and PTFE was selected for its unique surface properties and because it is used as coating for some medical devices like catheters. Friction testing was conducted in the UMT 2 with the most sensitive load cell available, the FLV.

4.3.3 Test Layout and Repeats

The sample was tested at several locations to maximise efficiency and cost effectiveness as per the layouts shown in Figure 4.1. In this friction experiment, only a single slide in one direction over the monolayer was studied to limit complexity. A single slide script was created for the UMT 2, the sequence of which is described in detail in Section 3.9.1. One sample was large enough to conduct three friction experiments on, as shown in Figure 4.1.

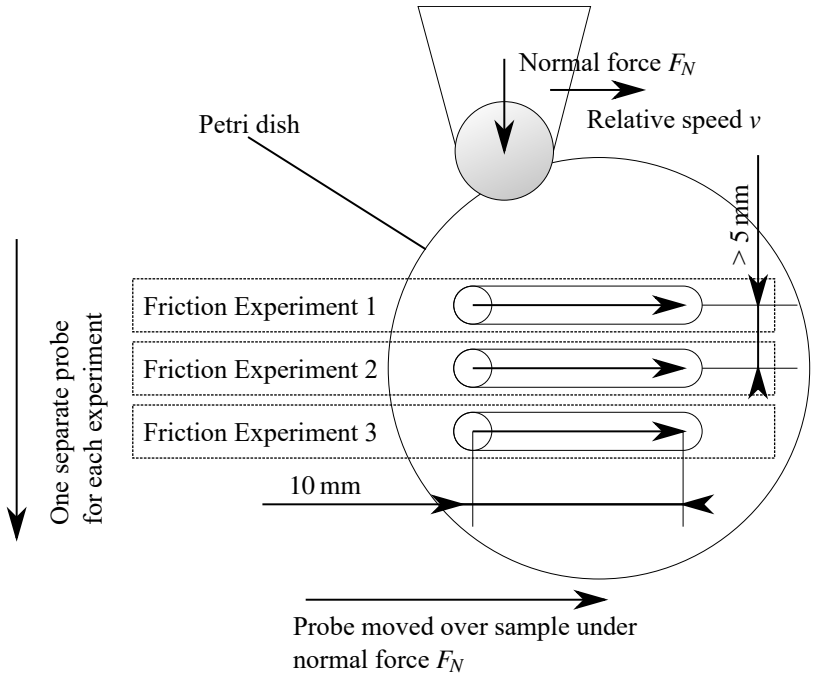

Figure 4.1: Test layout on sample for friction experiments.

All friction experiments were conducted for normal forces F_N of 10 mN, 20 mN, 40 mN and 80 mN. Thus almost the whole range of the load cell (up to 100 mN) was utilised. Friction experiments were all conducted at a speed of 1 mm/s.

An overview of the tests conducted in the context of this chapter with respective number of repeats n can be found in Table 4.1. Baseline experiments with glass probes were

conducted on PS and fibronectin-coated PS substrates to compare to experiments with cells later. As there were no cells present on these samples, only friction results were collected. Then, cells cultured on fibronectin coated PS based samples were tested against glass probes and the samples were imaged to collect damage data on the monolayer. These experiments (cells on a hard substrate against a glass probe) represent a similar set-up to most previous studies. Fibronectin is not necessarily required to attach cells to PS, but as it is required in the experiments on soft substrate samples, it was still used to coat the dishes. Finally, for friction experiments, soft substrate samples were tested against glass, stainless steel and PTFE probes to investigate the effect of different materials.

Substrate material	**Probe material**	**Relative speed**	**Repeats for each load condition** n
PS	Glass	1 mm/s	3
PS+FN	Glass	1 mm/s	3
PS+FN+HUVEC	Glass	1 mm/s	9
PDMS+FN+HUVEC	Glass	1 mm/s	9
PDMS+FN+HUVEC	Stainless Steel	1 mm/s	9
PDMS+FN+HUVEC	PTFE	1 mm/s	9

Table 4.1: Experiment overview

Immediately after testing, the medium was aspirated and cells were washed with PBS to clear the sample off any detached cells or cell parts in the medium. Then, the cells were stained with PI and Hoechst, which stained cells with an intact cell membrane (live cells) with Hoechst that showed up in the blue fluorescent channel of the microscope and cells with a damaged membrane (dead) cells with PI that showed up in the red channel. The sample was then washed and immediately imaged.

4.3.4 Damage Assessment

The rationale for the damage assessment was as follows. Damage was quantified by the proportion of damaged and removed cells per unit area.The relationship between amount of damaged endothelial area and complication severity or prevalence is difficult to measure and has not been attempted yet. However, in terms of quality, the less damage is inflicted, the better.

Cells could be in several states before and after testing. Before testing, most cells should be healthy, meaning they are attached to the surface and bear an intact cell membrane. Then, there are apoptotic cells that have reached their end of life, i.e. through a natural cause such as reaching a certain amount of cell divisions. These cells suffer apoptosis, a controlled cell

death, which cells initiate themselves. Apoptosis acts as a kind of self-destruct mechanism, part of which is the dissolving of the cell membrane. Furthermore, there are cells that have suffered irreversible damage and suffer an uncontrolled cell death, which is called necrosis. Necrotic cells should be the exception in a well-looked after cell culture vessel due to the lack of direct deadly external influences in general. However, after testing, many cells could be left with a ruptured cell membrane, which would cause them to be, or become, necrotic. Finally, cells could be completely removed from the surface.

State	Nucleus colour	Counts towards
Intact	Blue	Healthy
Apoptotic	Red	Dead
Necrotic	Red	Dead
Removed	—	Removed

Table 4.2: Cell States and respective PI/Hoechst stain.

By applying PI/Hoechst, cells could be assigned to the aforementioned states, which is shown in Table 4.2. A red nucleus showing up under the fluorescence microscope, indicates that a cell has ruptured or a dissolved cell wall, which could be caused either by necrosis or apoptosis. As both, apoptotic and necrotic cells nuclei show up red, it cannot be differentiated whether a cell died a controlled death prior to testing, or was destroyed due to friction. However, this issue is eliminated, because both of those states count towards damaged endothelial area and by using the compare areas, the normal amount of apoptotic cells that would occur is measured and hence can be accounted for. A blue nucleus meant that the respective cell was healthy, because PI could not enter the cell, indicating the presence of an intact cell membrane. The removal of a cell could not be determined as such because that would have required conducting pre-test imaging, which was not practical as a large area would have to be imaged before testing for each slide to ensure that the sliding area was in the image. This would have meant that the testing procedure would have taken much longer. An additional implication of this is that the cells would be in an uncontrolled environment for a much larger amount of time. An alternative solution was devised in which an area (the compare area), that was not in contact with the probe, was compared to the testing area. It can be assumed that the cells have experienced exactly the same life as the cells in the sliding area, except for the frictional interaction with a probe. Hence, by calculating the nuclei density in the compare areas, it was also known how many cells there should have been per unit area in the sliding area if there had been no frictional interaction. Therefore, the numbers measured in the sliding area could be set into relation to the compare areas to deduce the damage inflicted by the probe interaction.

4.4 Results

In this section, friction and damage results are presented for samples ranging from simple (PS dishes) to complex (soft PDMS substrate coated with fibronectin and seeded with HUVEC).

4.4.1 Samples without HUVEC

Here, friction results collected on uncultured PS dishes are presented. These experiments were conducted to draw a baseline in an effort to help later with studying the effects of cells on friction and to identify whether cells and their effects on friction could be detected. Three measurements were taken for each normal force and substrate.

Polystyrene Dishes

Polystyrene dishes were tested with and without fibronectin coating against glass probes. Static friction and dynamic friction once stabilised were extracted from the data per the methodology laid out in Section 3.11, i.e. the slope-adjusted static and dynamic friction forces are reported. Three measurements were taken for each test condition.

The friction force on these samples peaks (static friction) before it stabilises and oscillates around a more or less fixed value in a stick-slip pattern. This can be seen in Figure 4.2 which shows the raw data of a 10 mN slide with an overlay indicating the measured values of the forces and time ranges during which the forces were measured.

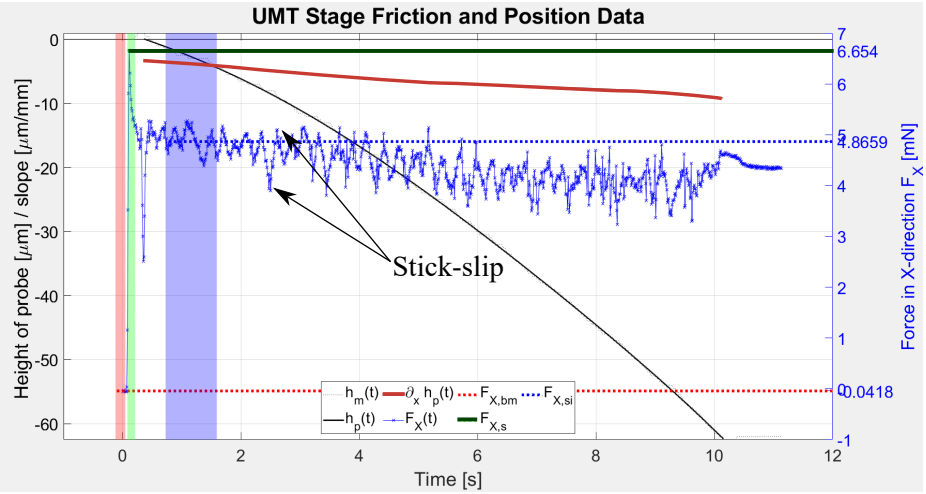

Figure 4.2: Raw friction force and stage position data for a 10 mN friction test on PS-based sample.

The relative effect of stick-slip on the friction force becomes smaller when F_N is increased. For F_N of 80 mN, the effect is still visible, but, compared to the overall friction

force, is much smaller, as seen in Figure 4.3.

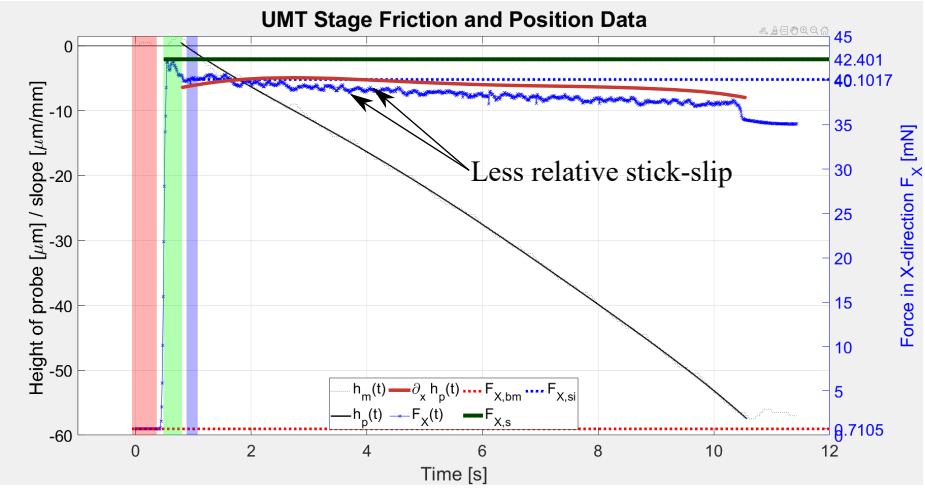

Figure 4.3: Raw friction force and stage position data for a 80 mN friction test on PS-based sample.

Coating with fibronectin did not change the interaction significantly, neither in terms of absolute measured values, nor in terms of stick-slip, as can be seen in the raw data presented in Figure 4.4 for a normal force of 10 mN and in Figure 4.5 for a normal force of 80 mN.

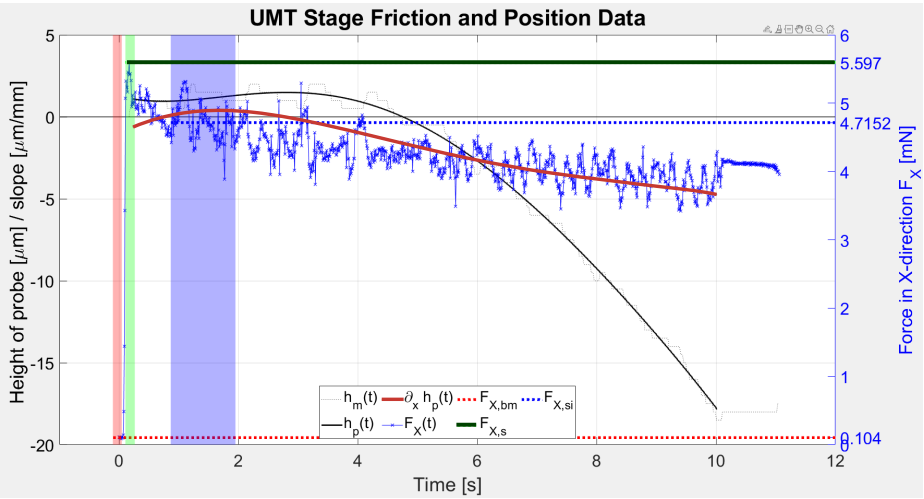

Figure 4.4: Raw friction force and stage position data for a 10 mN friction test on PS-based, fibronectin coated sample.

In Figure 4.6, static friction and dynamic friction forces once stabilised are reported over the range of tested normal forces. In Figure 4.6a, the static friction force $F_{F,s}$ is plotted over the applied normal force F_N and in Figure 4.6b, the dynamic one is plotted in the same fashion. The respective three individual measurements are plotted in grey and the average of those measurements with the respective standard deviation is plotted in black. The measurements were fitted with a model of Amonton's law $F_F = \mu F_N$ by varying μ

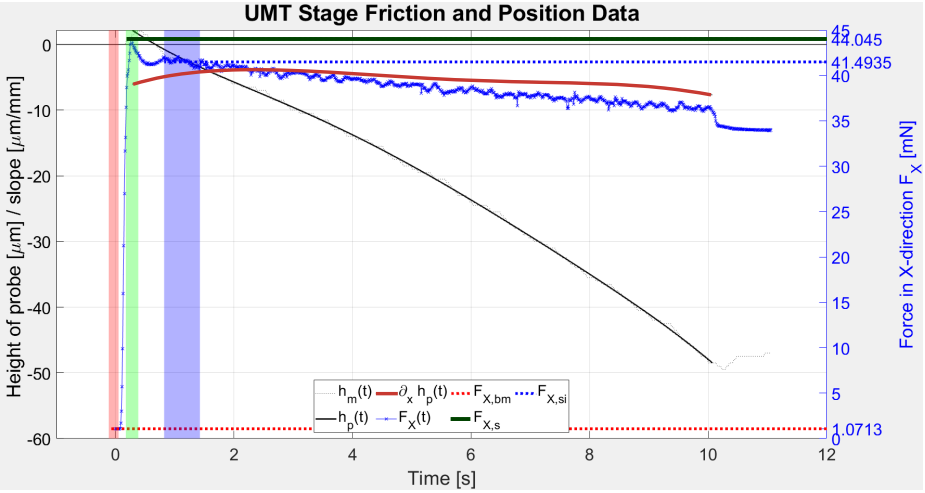

Figure 4.5: Raw friction force and stage position data for a 80 mN friction test on PS-based, fibronectin coated sample.

and show good correlation according to the coefficient of determination R^2 with number of repeats $N = 3$ for each measurement. Both, static and dynamic friction coefficients were slightly higher if the substrate was fibronectin coated and the dynamic friction was lower than the static one. The dynamic friction force at zero slope $F_{Fd,level}$ could not always be collected as the overwhelming majority of samples exhibited a lack of a level location where a measurement could be taken.

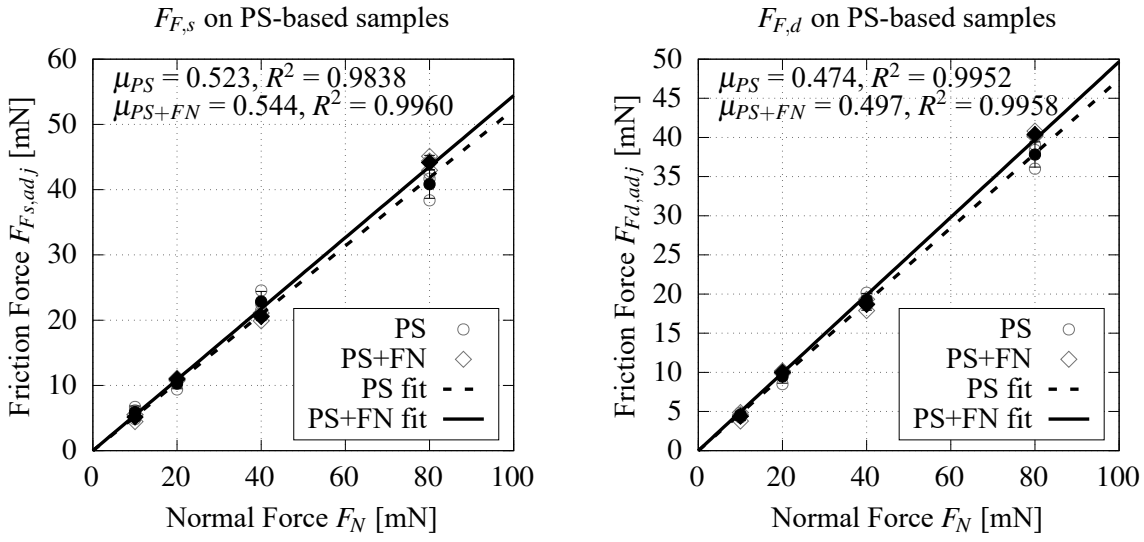

(a) Static friction force

(b) Dynamic friction force

Figure 4.6: Static **(a)** and dynamic **(b)** friction of glass on uncoated and fibronectin coated PS. Slope-adjusted static friction force $F_{Fs,adj}$ and slope-adjusted dynamic friction force $F_{Fd,adj}$ plotted over applied normal force F_N. Individual measurements and averages with standard deviation are plotted in addition to a linear fit as per Amonton's law $F_F = \mu F_N$ for both substrates.

4.4.2 Polystyrene Samples with HUVEC

The same standard polystyrene dishes, which were tested in Section 4.4.1, were coated with fibronectin and seeded with HUVEC according to the standard protocol (PS+FN+HUVEC). They were then tested in the UMT 2 against glass probes under the same conditions and with the same procedure used in Section 4.4.1.

Static and dynamic friction forces of glass probes on PS+FN+HUVEC were extracted from the friction data as described earlier and are plotted in Figure 4.7a and Figure 4.7b, respectively. In addition to the datapoints for static and dynamic friction forces on samples seeded with HUVEC, in these graphs, also the previously acquired data of fibronectin coated PS dishes is shown to make it easier to draw a comparison.

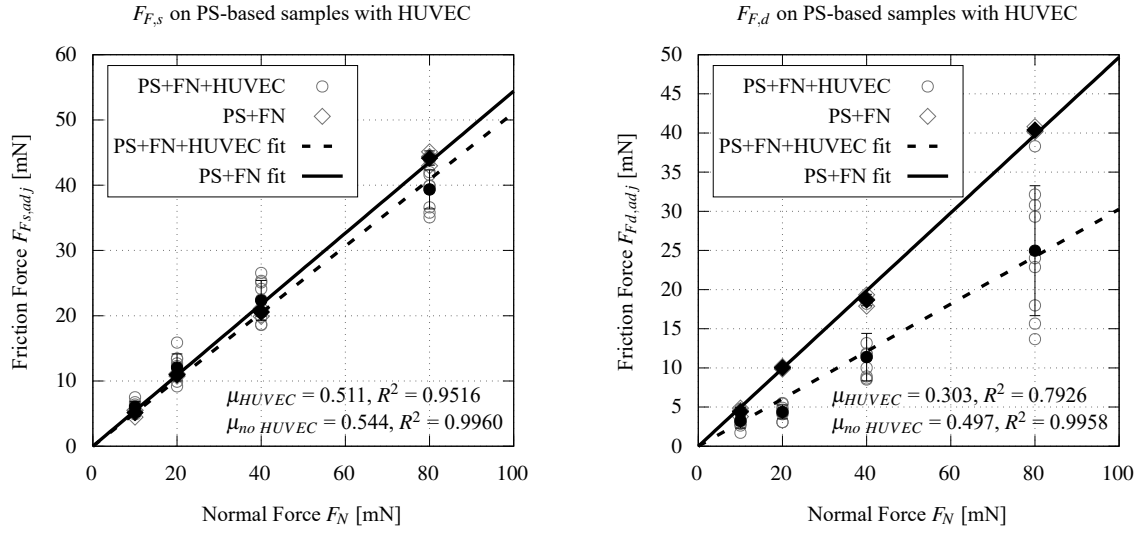

(a) Static friction force

(b) Dynamic friction force

Figure 4.7: Static **(a)** and dynamic **(b)** friction of glass against fibronectin coated PS with and without HUVEC. Slope-adjusted static friction force $F_{Fs,adj}$ and slope-adjusted dynamic friction force $F_{Fd,adj}$ plotted over applied normal force F_N. Individual measurements and averages with standard deviation are plotted in addition to a linear fit as per Amonton's law $F_F = \mu F_N$ for both materials.

For the static friction, the value for the friction coefficient $\mu_{s,HUVEC}$ = 0.511, as fitted with the linear model Amonton's law suggests, is smaller than the one of just fibronectin coated PS ($\mu_{s,PS+FN}$ = 0.544). μ_{HUVEC} is also slightly smaller than $\mu_{s,PS}$ of uncoated PS dishes.

For the dynamic condition, the friction coefficient $\mu_{d,HUVEC}$ = 0.303 was significantly smaller than the one on the same substrate without cells ($\mu_{d,PS+FN}$ = 0.497) and the one on just polystyrene ($\mu_{d,PS}$ = 0.474). It should be noted that especially for dynamic friction, the spread of the measured values is higher than it is when no cells are present. However,

the highest measurement for the dynamic friction force is just below the ones of fibronectin coated PS.

As in these experiments cells were present on the sample, data was collected on the state of the monolayer after testing. An example of a 10 mN normal force slide is shown in Figure 4.8. As can be seen in this image, even for small forces, the monolayer was completely destroyed within the wear track. When the normal force was increased up to 80 mN, the width of the wear track did not increase significantly, as can be seen in Figure 4.9. The width of the wear track was estimated manually, as indicated by the circles. For a normal force F_N of 10 mN, the average width r was approximately 77.8 µm and for F_N of 80 mN around 81 µm. However, it should be noted that the width could vary along the track.

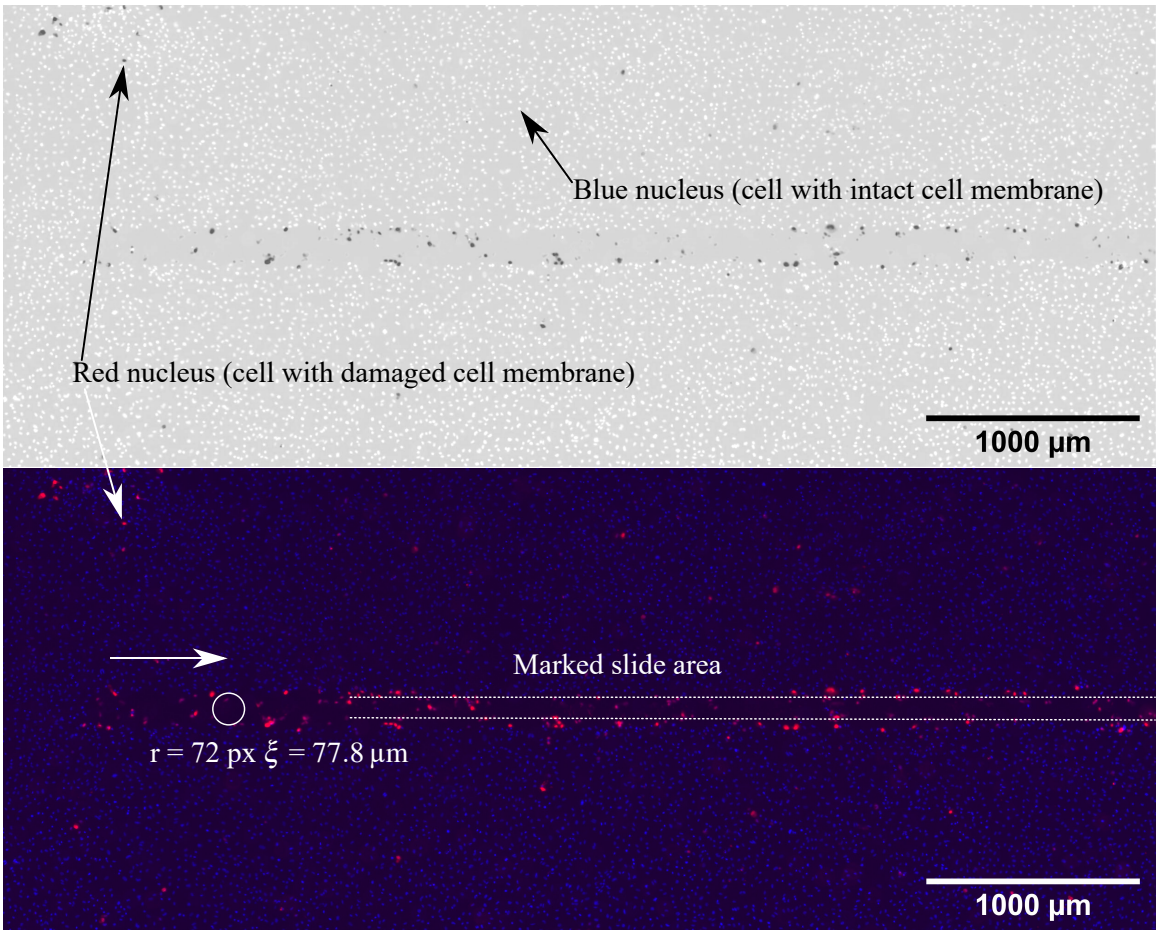

Figure 4.8: Red/blue combined image of a 10 mN normal force slide. Live cells nuclei show up as blue, while damaged cells nuclei are red in the image. The slide direction is marked by a white arrow. The width of the wear track r is approximately to 72 pixels and indicated by the circle. The radius of the circle was measured and converted to 77.8 µm using the spatial calibration factor ξ. Bottom: colour image with original red/blue channels. Top: inverted black and white image with contrast boost. Blue nuclei show up as white and red ones as dark.

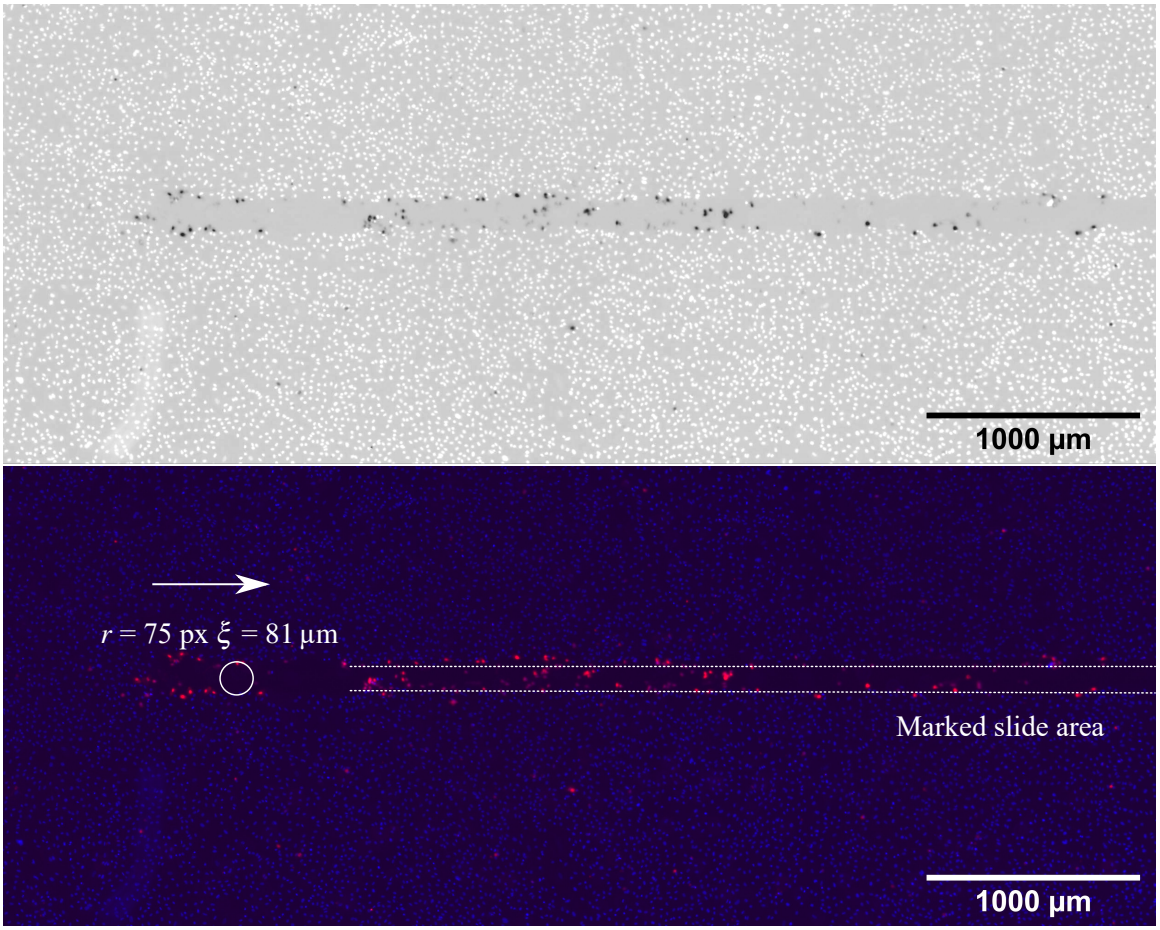

Figure 4.9: Red/blue combined image of a 80 mN normal force slide. The slide direction is marked by a white arrow. Again, an approximate for the wear track width was made. For this slide, the estimated width r was 75 pixels, or 81 µm. Bottom: colour image with original red/blue channels. Top: inverted black and white image with contrast boost. Blue nuclei show up as white and red ones as dark.

Apart from estimating the width of the wear track, the slide images that were collected were used to study the damage caused to the monolayer. As mentioned, the width of the wear track varied throughout the length of the slide, hence, for consistency, the slide area was defined where a clear distinction could be made between it and the surrounding monolayer for the whole length of the slide (i.e. the track width was chosen small enough that the entire area would occupy an area that was within the slide). This is illustrated in Figure 4.8 and Figure 4.9, where the specified width of the slide area is marked. The figure shows the red/blue image on the bottom and a greyscale version on the top. The contrast was boosted and the brightness adjusted so that blue areas show up bright and red ones show up dark. Therefore, when talking about blue and red nuclei from hereon forth, this is equivalent to bright and dark nuclei in stained microscope images. For each inverted image, the original red/blue channel can be found in the appendix and is referred to in the figures caption.

The damage data is plotted over the range of normal forces in Figure 4.10. Three values are shown in this graph. The red and blue circles represent the relative red and blue nuclei densities in the slide area $P_{\text{slide,red}}$ and $P_{\text{slide,blue}}$, which are calculated by putting the absolute nuclei densities $\rho_{\text{slide,red}}$ and $\rho_{\text{slide,blue}}$ in respect to the ones in the compare areas $\rho_{\text{compare,red}}$ and $\rho_{\text{compare,blue}}$. The black circles indicate the calculated percentage of cells that were removed from the wear track as calculated per the equation

$$P_{\text{removed}} = 1 - \frac{P_{\text{slide,blue}} + P_{\text{slide,red}}}{P_{\text{compare,blue}} + P_{\text{compare,red}}} \tag{4.1}$$

Hollow symbols represent a single slide, while filled symbols stand for the respective average of a group of slides conducted under the same experiment parameters. For the averages, the standard deviation is plotted.

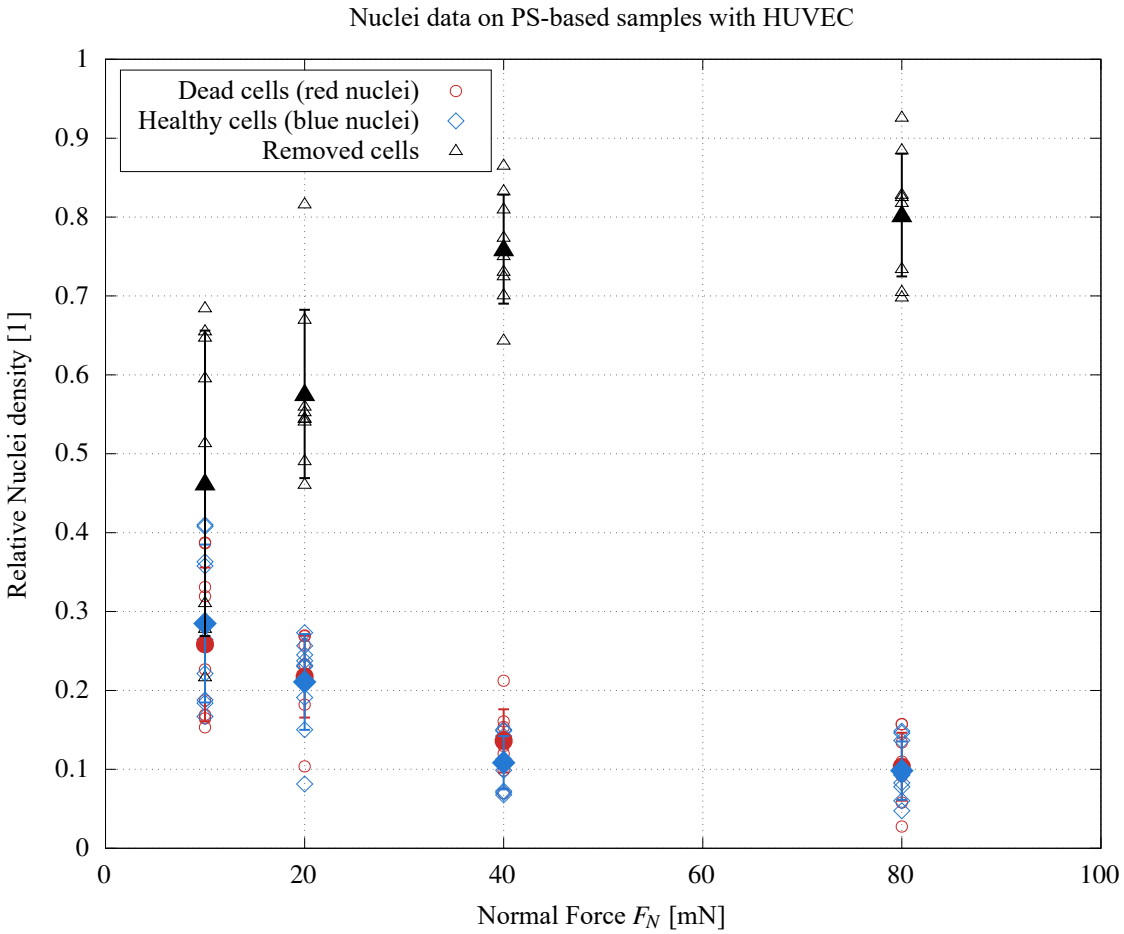

Figure 4.10: Damage caused to HUVEC monolayer on PS by glass probe. Nuclei densities in the slide area relative to the blue nuclei density in the respective compare areas P are plotted over F_N. Measurements of one slide are plotted as hollow circles, while averages are represented by filled circles. Blue circles stand for blue density measurements, red circles for red ones and black circles for the calculated percentage of removed cells.

On average, for normal forces of 10 mN, 28 % of cells remained healthily in the slide area, while 26 % were dead. Overall, 46 % of all cells were removed in the slide area. When the normal load was increased to 20 mN, 21 % of healthy cells remained, with 22 % dead and 58 % removed. Increasing the normal force further to 40 mN, resulted in 11 % of healthy cells remaining and 14 % dead ones with 76 % of cells removed. Finally, an increase of F_N to 80 mN prompted the most fatal damage to the monolayer that was recorded with 10 % healthy cells and also 10 % dead cells in the slide area. In total, 80 % of the cells within the slide area were removed in the friction process on average.

4.4.3 Soft Substrate Samples with HUVEC

In these experiments, the soft sample methodology including PDMS-based samples was utilised to study the interaction between HUVEC and a range of different probe materials, under more realistic conditions than was possible with PS-based samples. HUVEC seeded on PDMS were tested against glass, stainless steel and PTFE probes. The friction forces were measured with the same procedure that was used in the previous sections and nuclei data was collected in line with the procedures used in Section 4.4.2.

The static, slope-adjusted friction forces $F_{Fs,adj}$ are plotted over F_N in Figure 4.11, with individual measurements and averages presented in the established way. Glass and stainless steel show a very similar friction behaviour against HUVEC on PDMS, while the measured friction force against PTFE probes was significantly higher. For all probe materials, the friction coefficient was fitted with Amonton's law again, with friction coefficients μ_{glass}, μ_{SS} and μ_{PTFE} of 0.053, 0.057 and 0.109, respectively. However, these fits do not correlate very well according to the coefficient of determination R^2, which is 0.5350, 0.8282 and 0.5823, respectively.

The data for the static friction force was also fitted with another function under the assumption that the static friction regime is heavily adhesion-dominated and could therefore be dependant on the (apparent) contact area. Furthermore, the assumption was made that the adhesive force is load-independent. According to the Hertzian contact theory for a sphere and a flat surface, the contact area radius a is related to the normal load P_0, which here is F_N by $a \propto F_N^{\frac{1}{3}}$.

$$a = \sqrt[3]{\frac{3R}{4E^*}F_N} = \sqrt[3]{\frac{3R}{4E^*}}\sqrt[3]{F_N} \tag{4.2}$$

with reduced elastic modulus E^* and sphere radius R. This Hertzian approach does not account for adhesive effects, however, also, in the JKR model (a more advanced contact

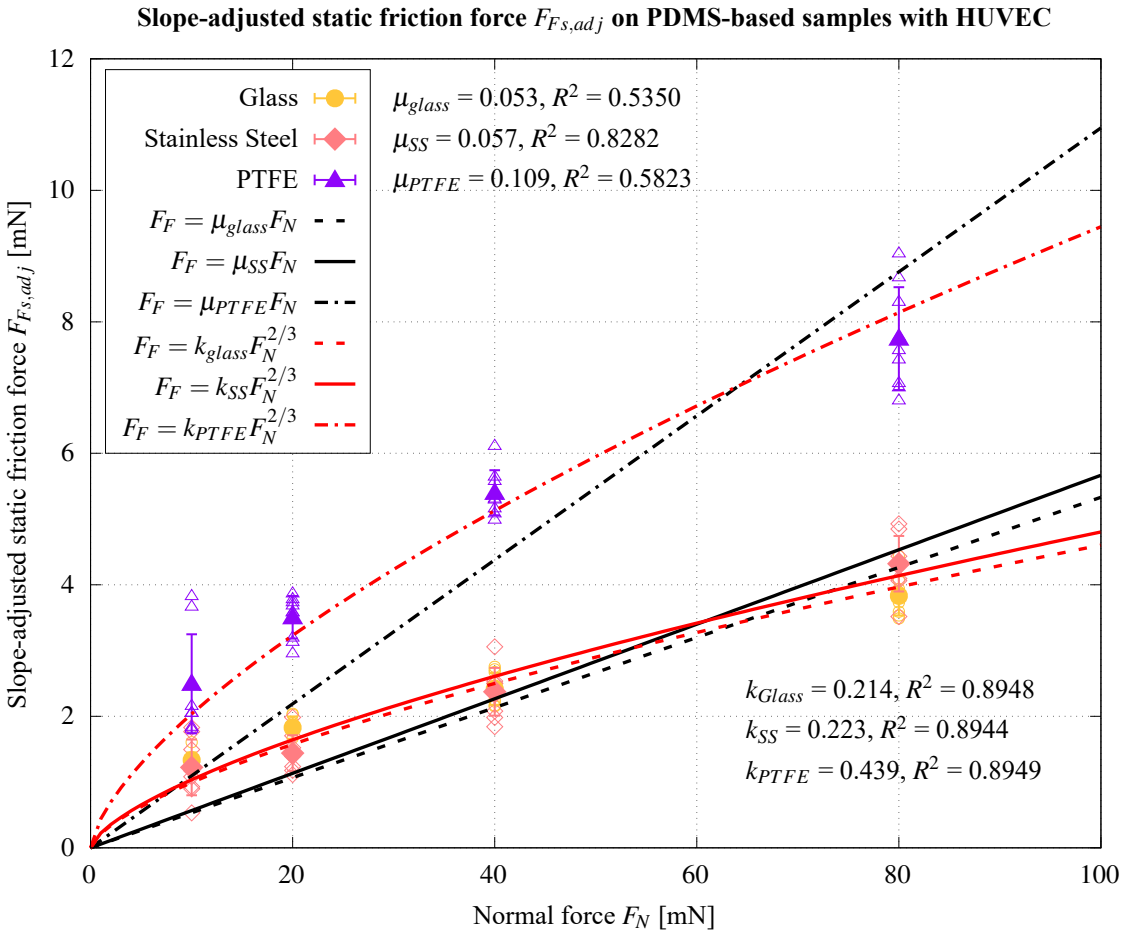

Figure 4.11: Slope adjusted static friction force $F_{Fs,adj}$ on PDMS-based samples with HUVEC against glass, stainless steel and PTFE probes plotted over applied normal force F_N. Individual measurements are plotted as hollow symbols, while averages are indicated by filled ones with standard deviations. Amonton's law-fits $F_F = \mu F_N$ (in black) and a Hertzian contact area based fit $F_F = kF_N^{2/3}$ (red) are plotted for each probe material and the respective R^2 is stated.

theory model), a is largely proportionally related to $F_n^{\frac{1}{3}}$. Therefore, the contact area $A_H = \pi a^2$ is assumed proportionally related to $F_N^{\frac{2}{3}}$ by:

$$A_H = \pi a^2 = \pi \sqrt[3]{\frac{3R}{4E^*}}^2 \sqrt[3]{F_N}^2 \tag{4.3}$$

If the friction force is mainly caused by adhesion which is assumed load-independent, this results in the relation $F_F = kF_N^{\frac{2}{3}}$, with factor k incorporating parameters like reduced elastic modulus, sphere radius and the strength of adhesion. The plots for this model are shown in Figure 4.11 in red. The model fits the static friction data much better than Amonton's law with respective R^2s of 0.8948, 0.8944 and 0.8949 for glass, stainless steel and PTFE.

In Figure 4.12, the occuring slope-adjusted dynamic friction forces $F_{Fd,adj}$ are plotted

over F_N in the same way. Overall, the friction forces are much smaller and it should be noted that a fit with Amonton's law correlates well with this data as per the coefficient of determination for glass and PTFE with R^2 of 0.9618 and 0.9389, respectively and slightly worse for the data on stainless steel probes with R^2 of 0.8982. Amonton's law predicts dynamic friction far more accurately than it does for static friction. Dynamic friction coefficients $\mu_{d,glass}$, $\mu_{d,SS}$ and $\mu_{d,PTFE}$ were generally low, but in this context, friction against PTFE was significantly higher with a friction coefficient of 0.044 compared to 0.018 for both, glass and stainless steel.

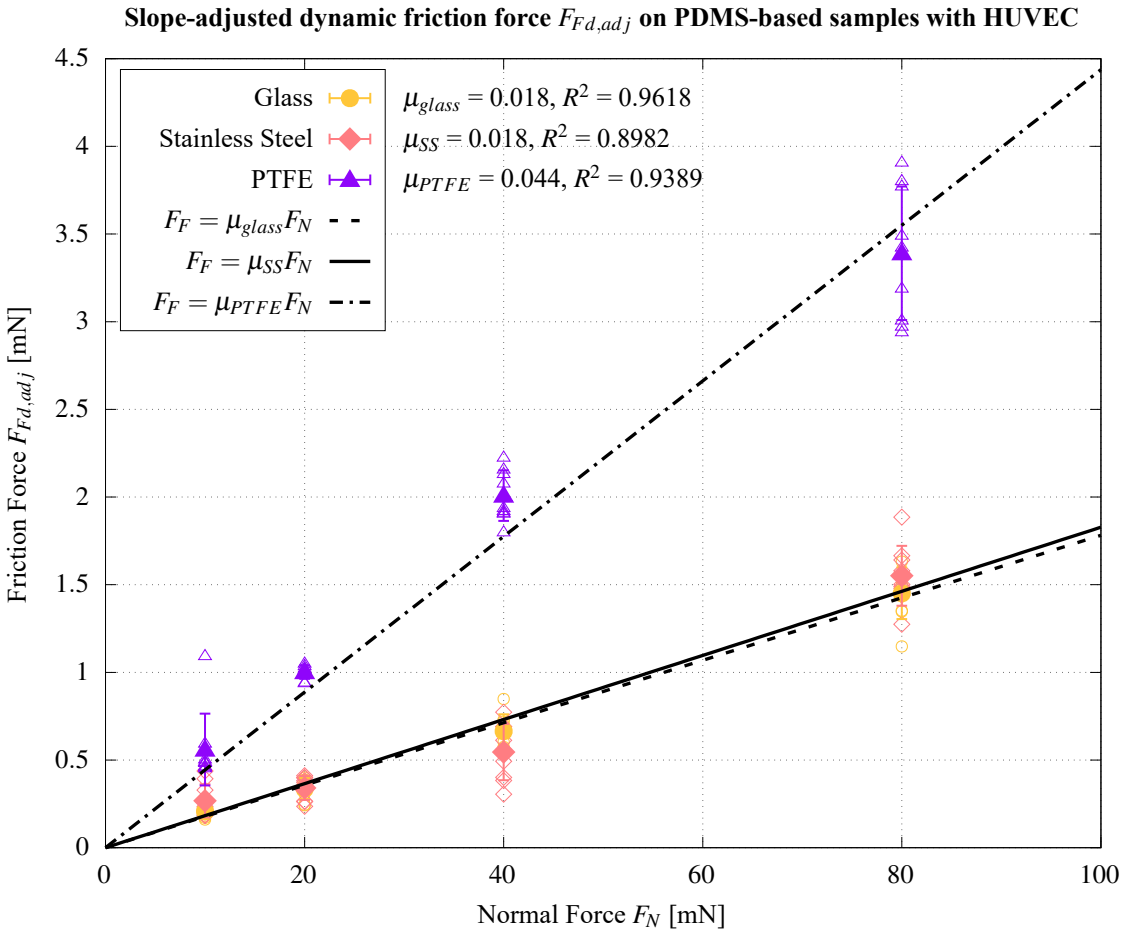

Figure 4.12: Slope adjusted static friction force $F_{Fs,adj}$ on PDMS-based samples with HUVEC against glass, stainless steel and PTFE probes plotted over applied normal force F_N. Individual measurements are plotted in grey, hollow symbols, while averages are indicated by filled, black symbols with standard deviations. Amonton's law-fits $F_F = \mu F_N$ are plotted and the R^2 is stated.

On the soft PDMS-based samples with HUVEC that were sufficiently aligned with the stage, the zero-slope (or level) dynamic friction force was measured. As not all samples were level enough (42.6 % allowed measurement of the zero-slope friction force), this value

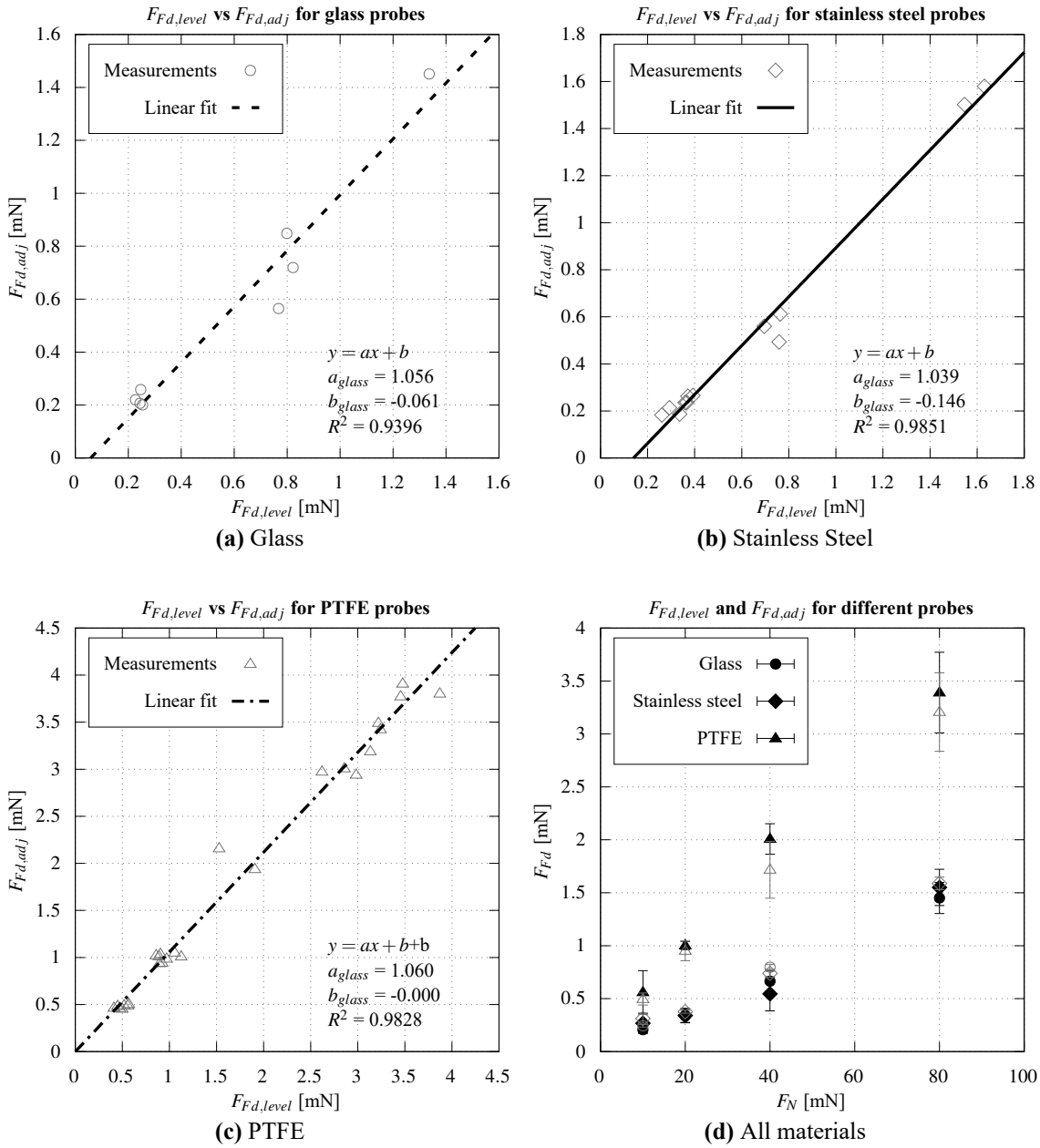

Figure 4.13: Zero-slope and slope-adjusted dynamic friction forces for different materials. Figures **a**, **b** and **c** show the slope-adjusted dynamic friction force $F_{Fd,adj}$ plotted over the zero-slope one $F_{Fd,level}$ for glass, stainless steel and PTFE to give an indication of how these correlate. Figure **d** shows the two aforementioned forces plotted as a function of the normal load F_N for all materials tested. $F_{Fd,adj}$ is plotted in filled, black symbols and $F_{Fd,level}$ in hollow, grey symbols.

cannot be reported for all slides, however, as a different way of acquiring dynamic friction data it was used to validate the approach of slope-adjusting the static and dynamic friction forces, which is so far only justified by the mechanical model. The data is presented in two ways:

Firstly, in Figure 4.13d, the slope-adjusted and zero-slope dynamic friction forces $F_{Fd,adj}$

and $F_{Fd,level}$ are plotted over F_N for all three probe materials tested. The full, black symbols represent $F_{Fd,adj}$ as in Figure 4.12, while the hollow, grey ones stand for $F_{Fd,level}$. Glass, stainless steel and PTFE data is plotted, again, as circles, squares and triangles, respectively. In this figure, only the averages are plotted with the respective standard deviations as available. Only one 80 mN normal force slide with a glass probe was level enough to take a measurement of $F_{Fd,level}$, so there is no standard deviation for these specific parameters. Furthermore, there is no measurement of $F_{Fd,level}$ available for glass slides of 20 mN normal force. Overall, the respective $F_{Fd,adj}$ and $F_{Fd,level}$ values for each probe material are close together, with some deviation between the averages of the two forces for 40 mN and 80 mN slides with PTFE probes and 40 mN slides with stainless steel probes. However, the distances between the two types of measurements are not much larger than the normal standard deviation for measurements of the same type.

Secondly, in order to study the correlation of $F_{Fd,adj}$ and $F_{Fd,level}$, the two forces are plotted against each other in Figure 4.13a, 4.13b and 4.13c for glass, stainless steel and PTFE, respectively. By plotting individual slides' measurements with the zero-slope dynamic friction force $F_{Fd,level}$ on the X-axis, and the slope-adjusted counterpart $F_{Fd,adj}$ on the Y-axis, along with a linear fit of the form $y = ax + b$, the correlation between the two can be assessed. Ideally, the two should match up perfectly, resulting in a line with a slope of 1 that intersects the Y-axis in the origin. The fitting parameters are stated in the respective graphs. For glass probes, the slope a was 1.056 and the line intersected the Y-axis at b = -0.061. With R^2 of 0.9396, this is a reasonably good fit. For stainless steel, the fit resulted in a of 1.039 and b of -0.146 with R^2 of 0.9851. The PTFE fit returned a = 1.060, b = 0.000 and R^2 = 0.9828. All are good fits and indicate that there is a correlation between the two values, as is expected. For glass, the coefficient of determination is lower than for stainless steel and PTFE, so for the latter two materials it is an accurate fit, while for the former, it is less accurate. Furthermore, for glass and stainless steel, there is an offset of the line, while for PTFE the line nearly perfectly intersects the origin. All fits exhibit a slope slightly greater than 1. It should be noted that as more measurements are available, the fit became better as can be seen when comparing the results using glass probes with a total of 8 measurements of $F_{Fd,level}$ with the ones of PTFE probes out of which 26 slides allowed measuring $F_{Fd,level}$.

Overall, considering the standard deviation of these measurements and the fact that more available datapoints meant a far better fit, this data confirms the expectation that a given slope-adjusted friction force measurement matches the respective zero-slope measurement. Assuming that $F_{Fd,level}$ is the acurate dynamic friction force, a being consistently larger than 1 indicates that $F_{Fd,adj}$ is consistently overestimating the dynamic friction. The reason for

for this, as was postulated in the methodology, is likely that the dynamic friction force can only be measured once it has stabilised. Therefore, as long as the sample is not perfectly flat, there will be a difference in the slope between the location where the initial slope influence was measured and the location on the slide where the dynamic friction force has stabilised and is measured. Accounting for the overestimation when using $F_{Fd,adj}$ is difficult and would require a more advanced model. However, from the fitting data, it can be deduced that the implications of this effect are not significantly large when compared to the standard deviation, as a is between 1.039 and 1.060; the effect can be estimated to be in the order of 3.9 %-6.0 %.

On all soft substrate samples, the damage was measured in terms of healthy remaining, dead and removed nuclei. As these samples consist of multiple layers (PDMS, fibronectin, HUVEC) and hence are fairly complex, when analysing cell behaviour, outliers are to be expected. The data was analysed regarding outliers manually through plots and the extreme studentized deviate test, by iteratively performing a Grubb's test for outliers [113] with a significance level of $\alpha = 0.05$. Because Grubb's tests assume normally distributed values [114], Shapiro-Wilk tests [115] for normality were conducted to ensure the datasets without the suspected outliers fulfilled that condition.

The resulting damage caused to the monolayer by the interaction with glass probes is shown in Figure 4.14 for different loads. The data is presented similarly as for PS-based samples, by showing the relative densities of nuclei in respect to the compare areas. Singular slide measurements are plotted as hollow symbols and averages as larger, filled ones with the respective standard deviation. Blue nuclei densities are represented by blue symbols, red by red symbols and the calculated removed densities by black symbols.

For 10 mN normal force, barely any cells are removed from the sample. Such few cells are removed that for some slide areas, measurements of removed cell densities are below 0, which means that there are more cells in the slide area per unit area than in the compare areas, implying that cells were added in the process of sliding. This is likely due to natural variances in the cell density of the monolayer. On average, -0.04 % of cells are removed. As this value is negative, that implies that more cells were found in the wear track than there were before. This is not intuitive and possible reasons for this result will be discussed later. 9.52 % of cells are dead in the slide area, in respect to the density of healthy cells in the compare areas, and 91.57 % are healthy. This means that essentially no cells were removed and the damage is limited to individual cells being killed. The values for red and blue relative nuclei densities do not add up to 100 % despite barely any cells being removed, which is again likely due to variances in the initial nuclei density and the fact that relative nuclei

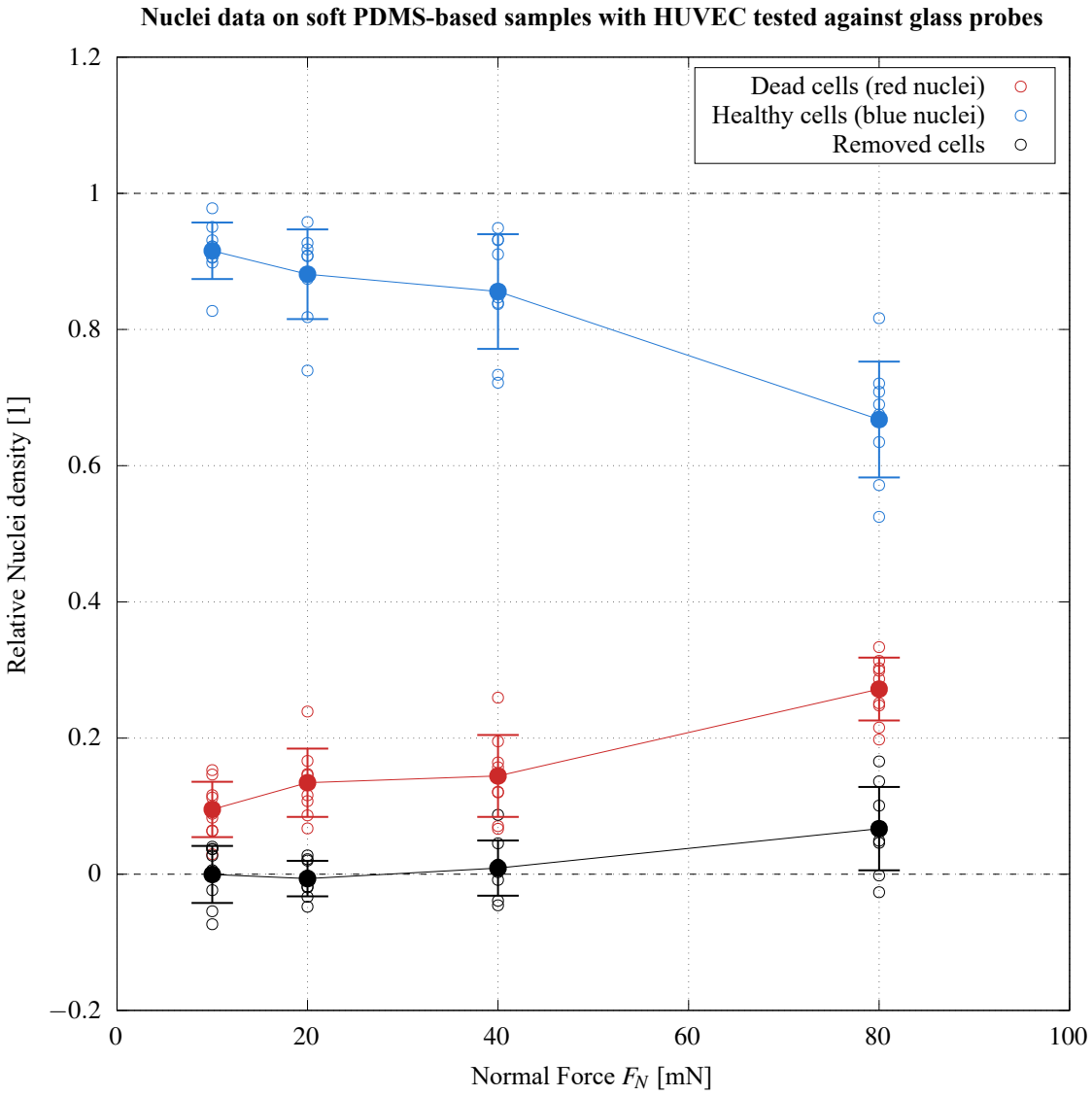

Figure 4.14: Monolayer damage data for PDMS-based samples with HUVEC tested against glass probes presented as relative nuclei densities in respect to the compare areas. Dead cell densities are plotted red, densities of healthy nuclei in blue and calculated removed densities in black. Individual measurements are plotted as hollow symbols, while averages are represented by full symbols with standard deviation.

densities are based on the blue nuclei density in the respective compare areas. For a normal force of 20 mN, still no significant amount of cells (−0.64 %) was removed. However, more cells (13.44 %) were dead for this increased normal load, which was naturally accompanied by a reduction in the rate of healthy cells in the slide area (88.12 %). An increase of F_N to 40 mN caused 0.90 % of cells to be removed. The rate of dead cells increased slightly further to 14.43 %, while the amount of healthy nuclei decreased to 85.58 %. Overall, the damage inflicted on the monolayer increased only slightly from 20 mN to 40 mN normal force. Finally, for a normal force of 80 mN, the amount of removed cells became signifi-

cant as it increased to 6.70 %. Also, the amount of dead nuclei increased further to 27.19 % while only 66.78 % of cells remained in the slide area.

In Figure 4.15, representative images of the wear track are shown for the full range of forces. The circular initial indentation area and its right hemisphere are marked. The right hemisphere is the one facing towards the sliding direction. The sliding direction is

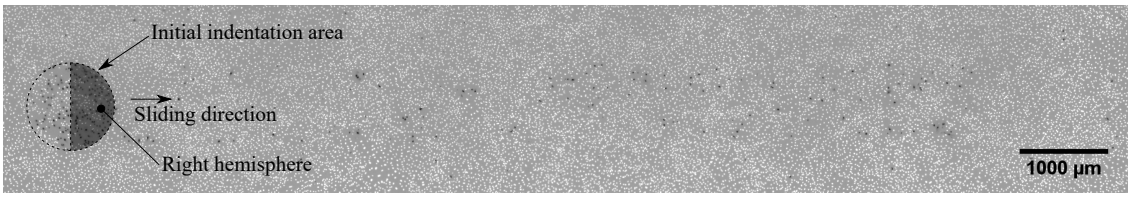

(a) 10 mN

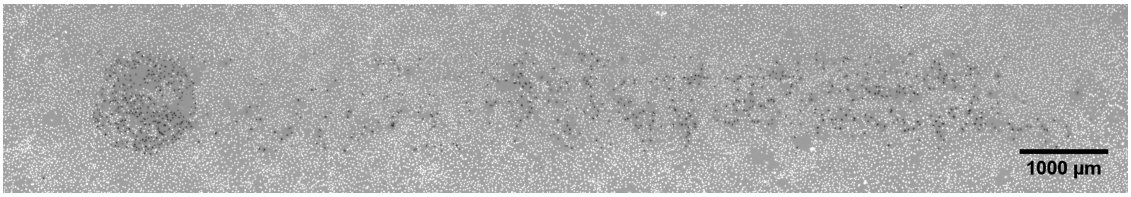

(b) 20 mN

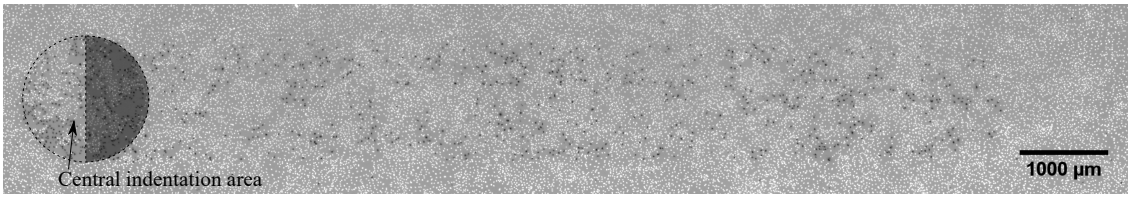

(c) 40 mN

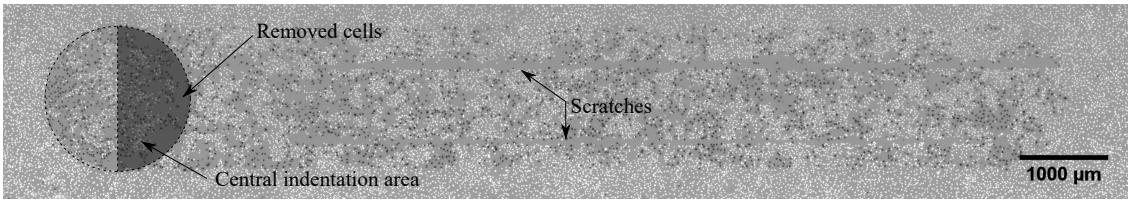

(d) 80 mN

Figure 4.15: Wear track images of soft substrate samples tested against glass probes for F_N of 10 mN, 20 mN, 40 mN and 80 mN. Colour blue/red channel images can be found in Appendix C.1

indicated in the first slide image and is the same in all other images. As a general trend, in the right hemisphere, the damage to the monolayer was noticably higher. For normal forces of 10 mN and 20 mN, this resulted in more cells found dead in that region and for higher normal forces of 40 mN and 80 mN, rather than more dead cells being present, more cells were removed there. For a normal force of 80 mN, scratches in the monolayer become apparent which are highlighted in the respective image.

The data for stainless steel probes are presented in Figure 4.16. For F_N = 10 mN, 0.53 %

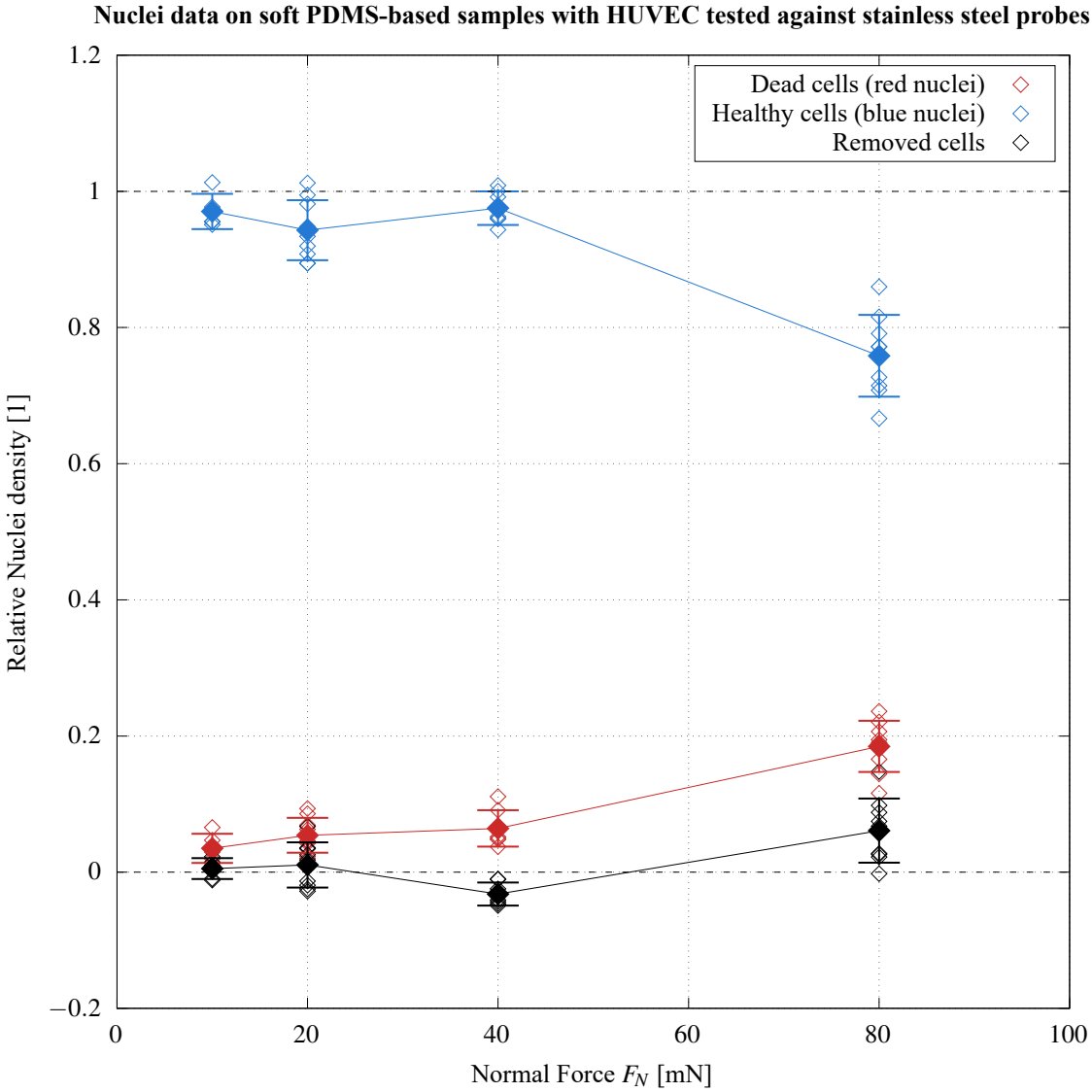

Figure 4.16: Monolayer damage data for PDMS-based samples with HUVEC tested against stainless steel probes presented as relative nuclei densities in respect to the compare areas. The notation is equivalent to the one in previous figures.

of cells were removed from the substrate with 3.50 % of cells dead and 97.04 % of cells remaining healthy within the slide area. When the normal force was increased to 20 mN, the damage inflicted to the monolayer increased: 1.07 % of the cells are removed, 5.42 % of cells were dead and 94.30 % of cells are still healthy in the testing site. A further increase of F_N to 40 mN, causes −3.21 % of cells to be removed, with 6.43 % dead, leaving 97.53 % healthy. For 80 mN of normal force, damage increased further, with 6.10 % of cells being removed from the slide area, 18.48 % dead and 75.85 % remaining healthily within the slide

site. Overall, the damage inflicted to the monolayer by a stainless steel probe is very similar to that inflicted by a glass probe.

Representative images of the wear track are are shown in Figure 4.17. A similar behaviour can be observed as in the images taken of the monolayer after interactions with glass probes. Again, in general, there is more damage on the right hemisphere of the in-

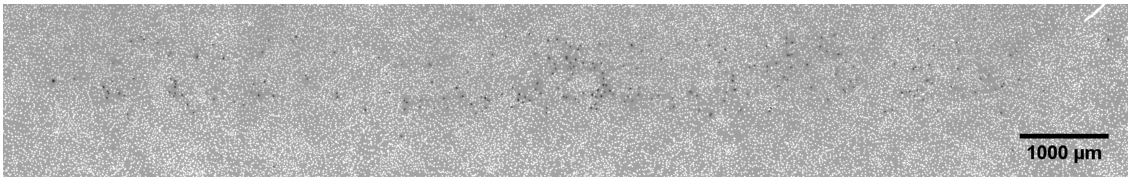

(a) 10 mN

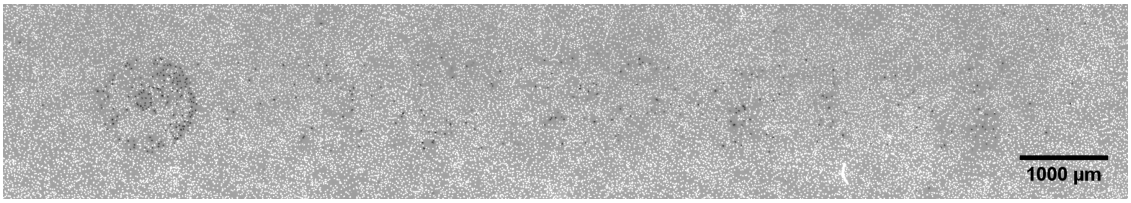

(b) 20 mN

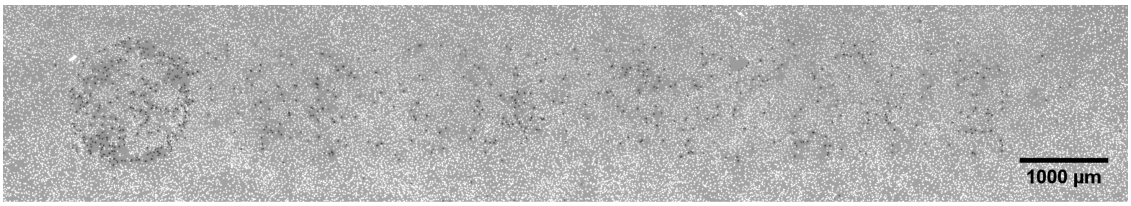

(c) 40 mN

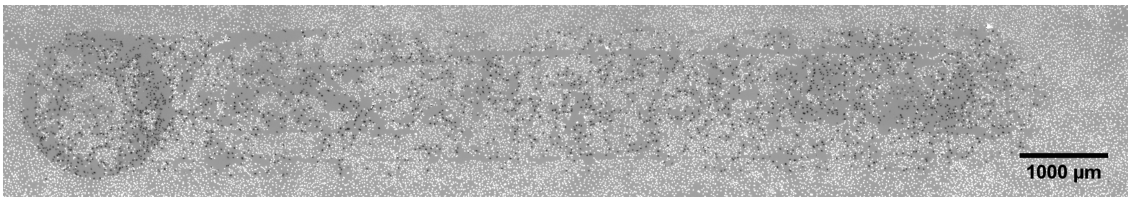

(d) 80 mN

Figure 4.17: Wear track images of soft substrate samples tested against stainless steel probes for F_N of 10 mN, 20 mN, 40 mN and 80 mN. Colour blue/red channel images can be found in Appendix C.2

dentation than in the left one and noticably more damage on the outer sections of the initial indentation area than in its centre. Furthermore, scratches in the monolayer develop at normal loads of 80 mN. It is evident, however, that generally more cells survive the interaction unharmed for all loads, both in the indentation area and in the wear track area. This can be seen especially well for 10 mN, where almost no cells are harmed.

The last material tested was PTFE. The results are shown in Figure 4.18. With only a 10 mN normal force, with a PTFE probe, already 20.03 % of cells are removed, while

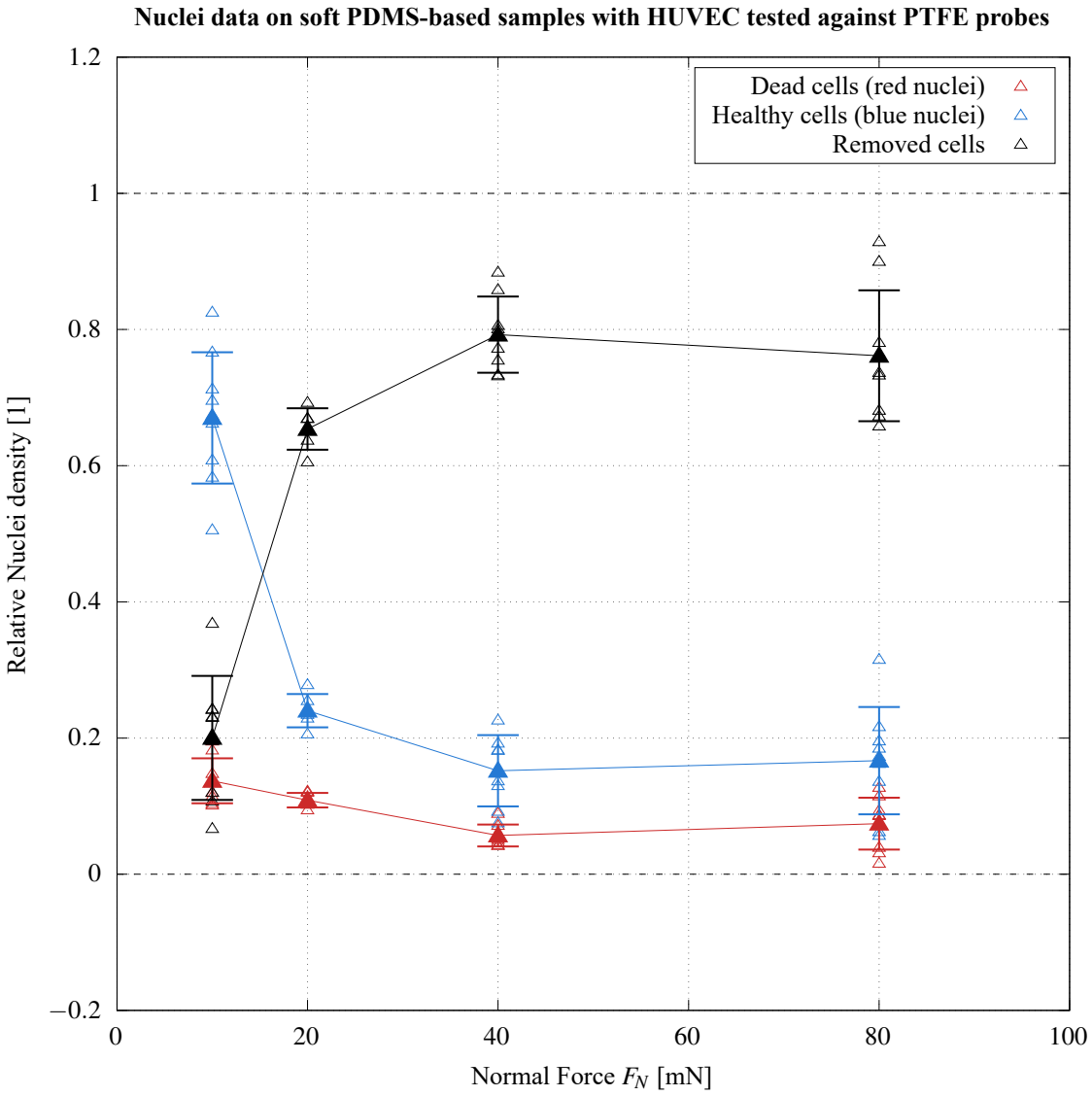

Figure 4.18: Monolayer damage data for PDMS-based samples with HUVEC tested against PTFE probes presented as relative nuclei densities in respect to the compare areas with the same notation used in previous figures.

67.01 % survived the friction test and 13.72 % died. When increasing the normal force to 20 mN, the survival chances of the cells in the wear track drop steeply. More than half (65.39 %) are removed, with only 24.02 % remaining healthy and 10.87 % dead. Here, it should be noted that the amount of dead cells that remained in the slide area did not increase, but in fact dropped a little, when increasing the normal load. It can be assumed that this is due to higher percentages of cells being removed, thus leaving limited deaths to be recorded. Further increase of the normal force to 40 mN had even more severe implications for the cells seeded on the substrate. Here, 79.25 % of cells were removed. 15.19 % remained

healthily in the testing site and 5.70 % were still attached, but dead. Again, it should be pointed out that the amount of dead cells within the slide area decreased with an increase in F_N attributing to the higher removal rate as outlined above. Finally, for the highest normal force tested, which was 80 mN, slightly less cells (76.15 %) were removed. The amount of cells that survived the slide healthy was 16.68 %. For these tests, the amount of dead cells in the slide area was 7.43 %. If the data for 80 mN slides is compared to the results for 40 mN, the damage seems to have converged and is even slightly lower for the higher load.

In the beginning, the damage caused to the monolayer increased very steeply with an increase of the normal load, however, past 40 mN, not much changed in terms of damage. While the overall damage increased when the normal force is increased, the amount of dead cells that remained within the wear area actually decreased. Overall, the monolayer experienced a much sharper rise in damage when F_N was increased than with glass or stainless steel probes. To compare the effect of the probe material, healthy (blue), dead (red) and removed nuclei data are plotted for different materials in Figure 4.20, Figure 4.22 and Figure 4.21.

For PTFE, the high damage inflicted to the monolayer in the wear track presented in the graphs is reflected by the track images shown in Figure 4.19. Even for low loads, large parts of the monolayer were removed. Many of the cells that remained were dead with a limited number of healthy cells remaining. In these images, the state of the monolayer clearly changes with the sliding distance. It is noticable that at the start of a slide, the width of the wear track changes significantly and then stabilises for 10 mN. For the higher loads, this is also the case, however it is the most noticable for 10 mN. Furthermore, with increasing sliding distance, the damage inflicted to the monolayer reduces. In the 10 mN track image, in the indentation area, all cells are removed. In the first third of the slide, most cells are removed and the ones that are still there are almost all dead. As the slide goes on into the second third, more and more healthy cells appear until, after around two thirds into the slide, large patches of healthy cells remain. Also, at this force, scratches in the monolayer were observed. For 20 mN, a similar behaviour is the case. After around a third into the slide, more cells survive, however, only in smaller patches. For 40 mN and 80 mN, in the beginning of the slides, almost all cells are removed. The damage also decreases with sliding distance, albeit mainly in the form of more cells remaining dead on the surface and not being removed.

For a better overview, the averages of the healthy, dead and removed relative nuclei densities measured on soft substrate samples are shown again in tabular form in Table 4.3 for the three probe materials tested and for the whole range of normal forces. To compare the different probe materials, the respective data are also plotted together. Figure 4.20

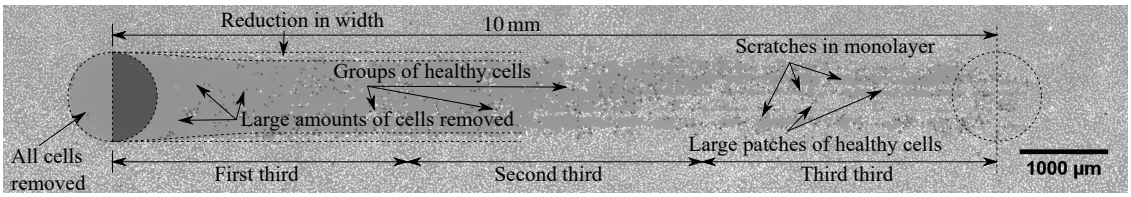

(a) 10 mN

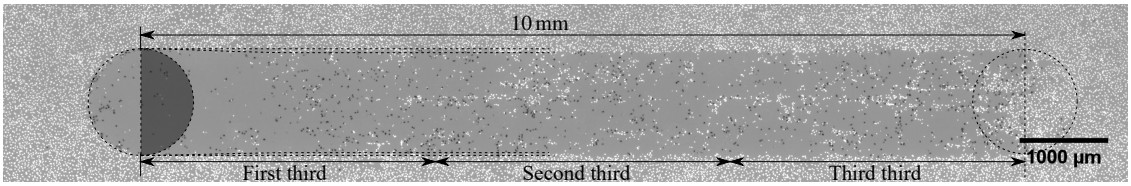

(b) 20 mN

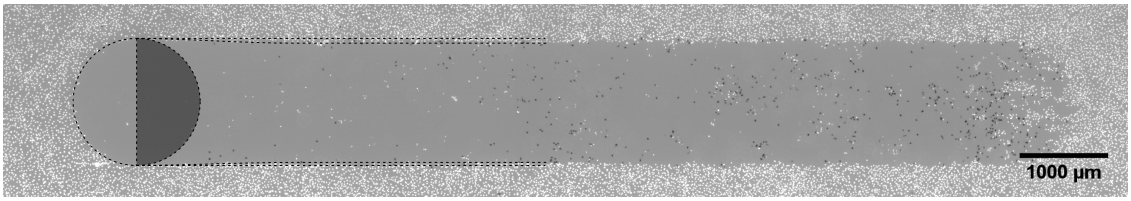

(c) 40 mN

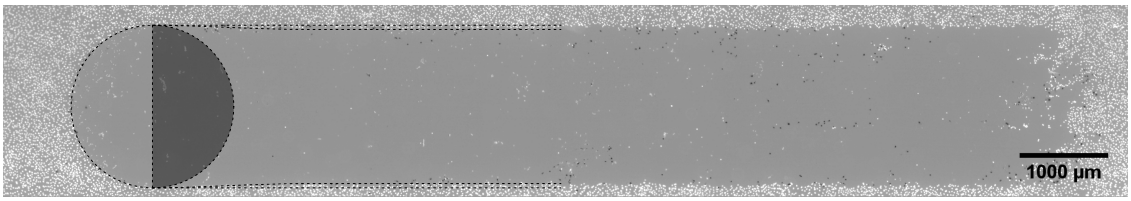

(d) 80 mN

Figure 4.19: Wear track images of soft substrate samples tested against PTFE probes for F_N of 10 mN, 20 mN, 40 mN and 80 mN. Colour blue/red channel images can be found in Appendix C.3

Material	State	10 mN	20 mN	40 mN	80 mN
Soda-lime glass	Healthy	91.57 %	88.12 %	85.58 %	66.78 %
	Dead	9.52 %	13.44 %	14.43 %	27.19 %
	Removed	−0.04 %	−0.64 %	0.90 %	6.70 %
Stainless Steel	Healthy	97.04 %	94.30 %	97.53 %	75.85 %
	Dead	3.50 %	5.42 %	6.43 %	18.48 %
	Removed	0.53 %	1.07 %	−3.21 %	6.10 %
PTFE	Healthy	67.01 %	24.02 %	15.19 %	16.68 %
	Dead	13.72 %	10.87 %	5.70 %	7.43 %
	Removed	20.03 %	65.39 %	79.25 %	76.15 %

Table 4.3: Overview over damage inflicted to the monolayer by different probe materials under different normal loads.

shows the healthy nuclei densities within the slide area. For both glass and stainless steel, the amount of healthy cells decreases consistently - almost linearly - with increasing normal load. Stainless steel probes consistently leave more cells intact than glass ones, on average, albeit mostly within the range of standard deviation. Even the most destructive load condition for either of those materials (80 mN glass), however, is just on par with the damage inflicted to the monolayer by 10 mN slides with PTFE probes. From there, the amount of cells that survive drops rapidly for higher loads as it seems to converge to around 15 % as described earlier.

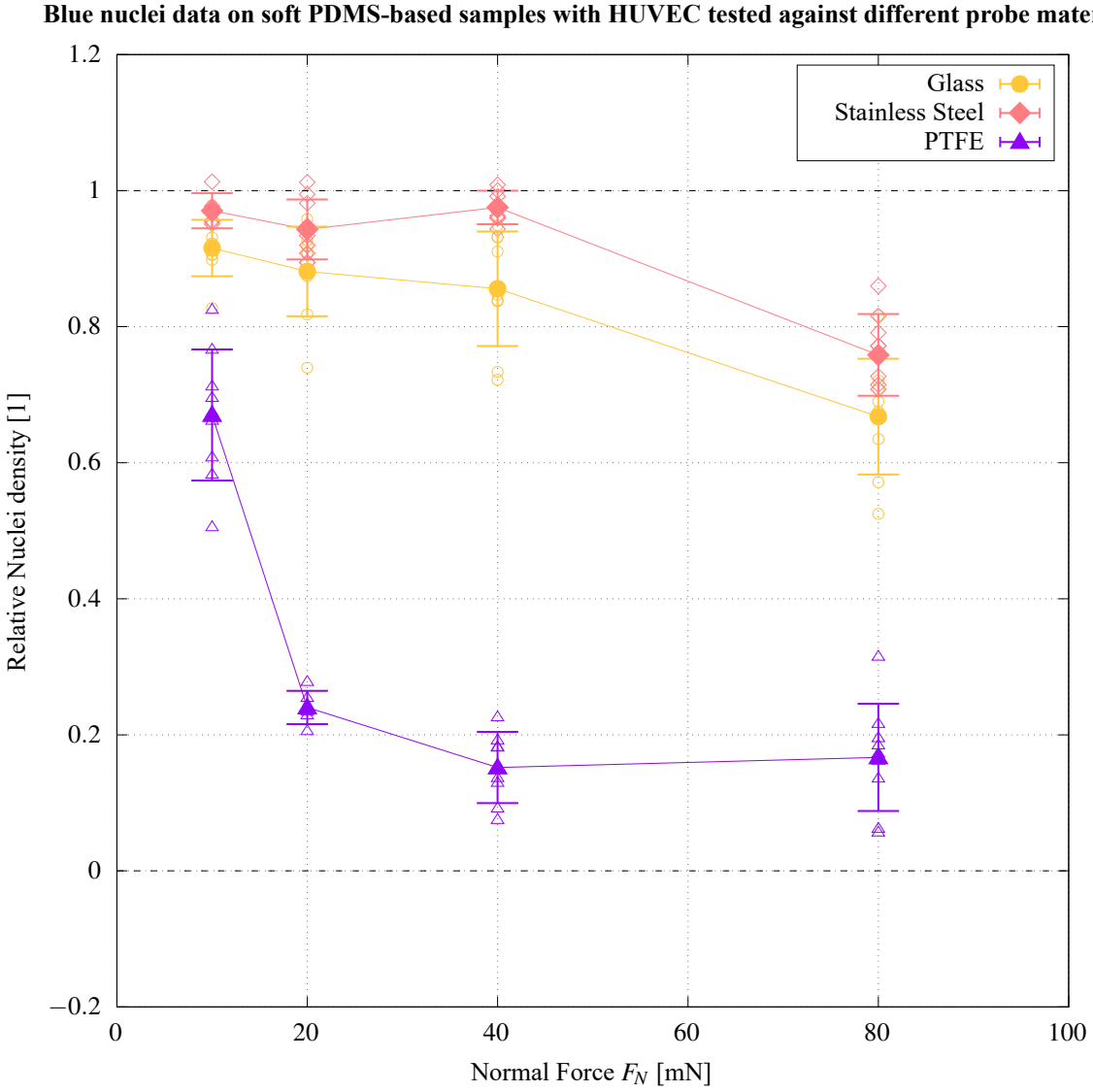

Figure 4.20: Blue (live) nuclei density in slide area for PDMS-based samples with HUVEC for different probe materials. Individual measurements and averages are plotted according to the established notation. Circles, squares and triangles represent glass, stainless steel and PTFE probes, respectively.

The situation is similar for the densities of removed cells which are plotted in Figure 4.21. However, the difference between glass and stainless steel materials in regards to cells removed are well within the range of standard deviation. In terms of the amount of cells that were removed, glass and stainless steel probes for the highest load of F_N = 80 mN do not even come close to the amount of cells that were removed by PTFE probes for 10 mN. For both, glass and stainless steel, a small increase of removed cells with higher normal forces can be observed, however, all the way to 40 mN, the amount of cells removed remains very small. This stands in contrast to PTFE, for which the amount of removed cells as a function of normal load follows the equivalent for healthy cells inversely, as it rises steeply and then converges at around 40 mN.

The data for dead cells that were still attached to the sample surface after testing, which is shown in Figure 4.22, tells a slightly different story. For both glass and stainless steel, the amount of dead cells increases consistently with higher loads. Also, the amount of dead cells is consistently higher for glass probes than for stainless steel. Apart from glass probes consistently leaving more cells dead, the two materials behave in a very similar way. Both of these material's behaviours stand in stark contrast to that of PTFE probes. Instead of increasing consistently, for PTFE the amount of dead cells drops significantly and then increases again slightly. This may be surprising at first because the data for healthy and removed cells suggested that PTFE was far more destructive than glass and stainless steel as a probe material. Looking at this graph alone tells a different story, since for the latter two materials at 40 mN and 80 mN of normal force, the amount of dead cells in the wear track is significantly higher. The likely cause for this is that PTFE does not leave many dead cells within the wear track because the majority is not just killed but completely removed.

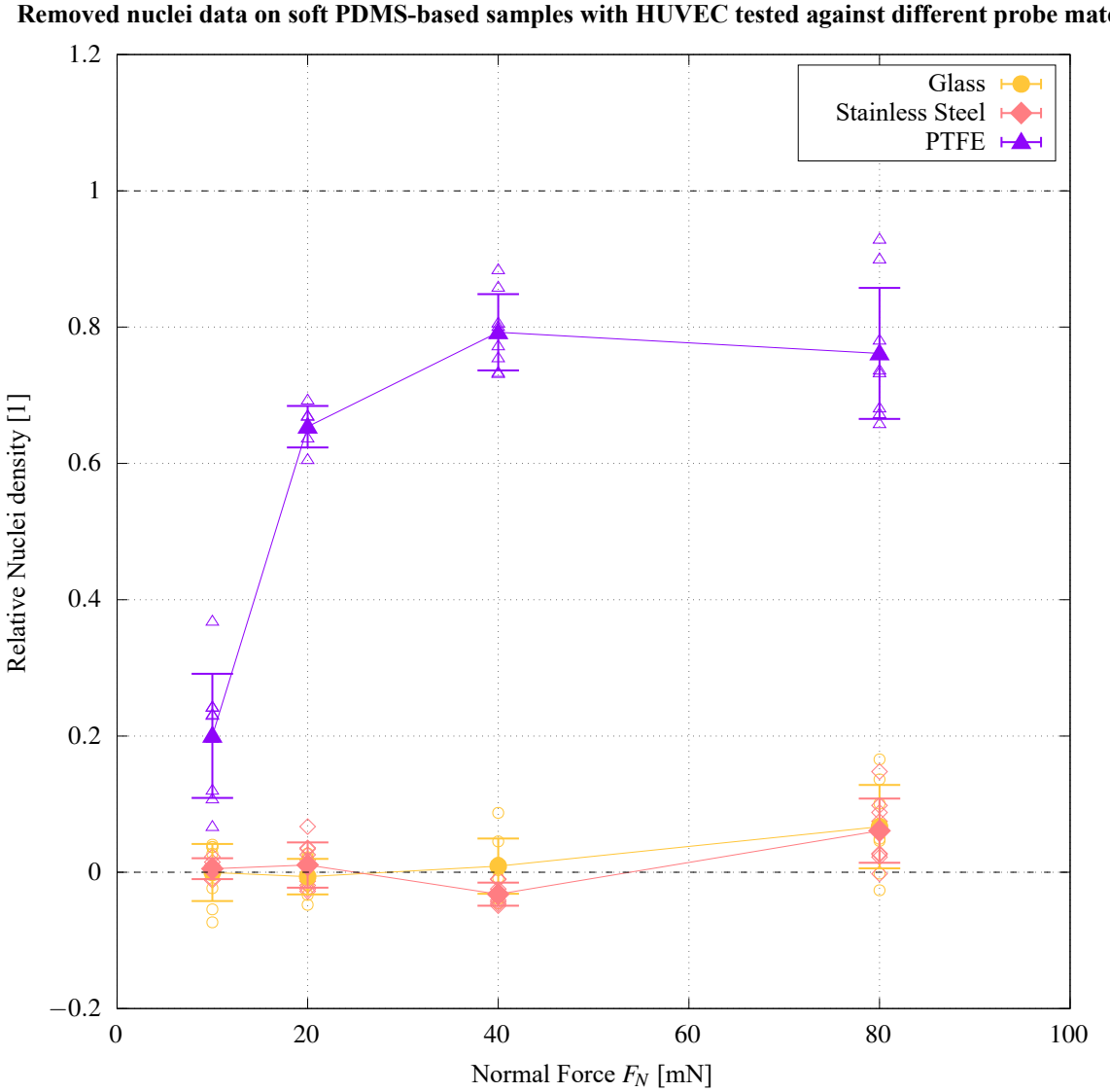

Figure 4.21: Removed nuclei density in slide area for PDMS-based samples with HUVEC for different probe materials. The notation is equivalent to the one in Figure 4.20.

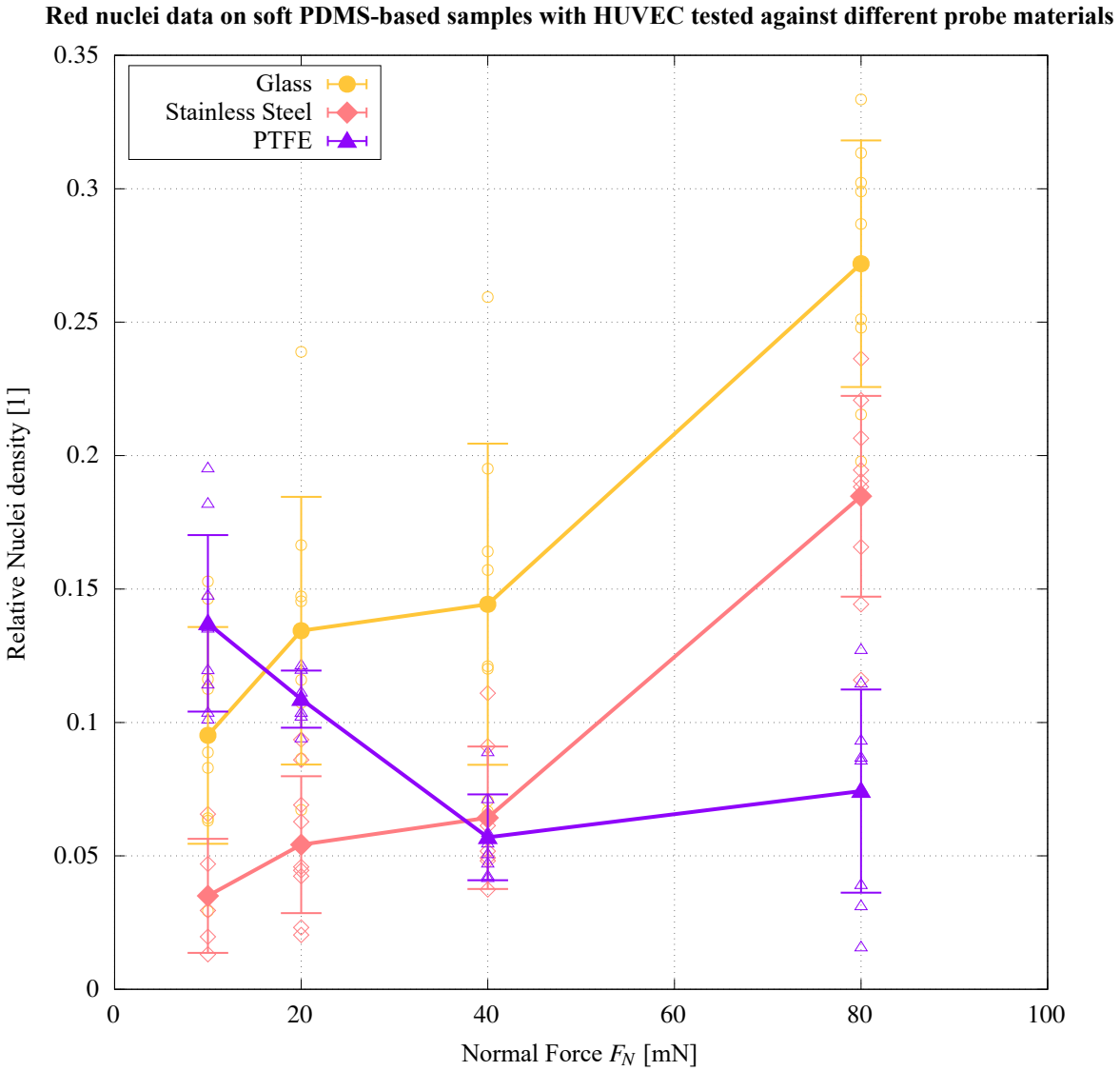

Figure 4.22: Red (dead) nuclei density in slide area for PDMS-based samples with HUVEC for different probe materials. The notation is equivalent to the one in Figure 4.20.

4.5 Discussion and Conclusions

4.5.1 The Issue of PS Sample Contact Area Width

For standard PS dishes with HUVEC, it was observed that the wear track was significantly wider than the Hertzian contact theory implies for a PS - glass contact. Furthermore, the width of the wear track did not increase to the extent suggested by Hertz with increasing normal force. What could have caused such significant deviations from the fundamental contact theory? There certainly are effects which Hertz does not account for, such as: adhesion, surfaces that are not perfectly flat and nonlinear material parameters. Plastic deformation is unlikely to occur at the pressures applied within the PS (it is however, occuring within the cells). Overall, these effects are unlikely to cause such significant deviations. Two things have to be considered when looking at the width of the wear track in this way and interpreting it with Hertzian contact mechanics. Firstly, the width was measured based on the damaged, removed and healthy cells. Secondly, the calculation of the Hertzian contact area width was conducted, neglecting the cells which sit on top of the PS. From a purely mechanical standpoint, this assumption seems fair. Cells do have a significantly lower Young's modulus than polystyrene. They are also destroyed in the testing process, and there are no models to simulate that. However, the fact that cells are mechanically fragile compared to the other materials involved in the interaction may help to explain what is actually going on, focusing on the issues of deviations to the contact theory model and, consecutively, with the one of a minimal change in contact width with increasing normal force. Still assuming a largely Hertzian-dominated contact interaction, and cells being so soft and fragile that they play no role in the interaction from a mechanical point of view, giving way to the probe material when there is any contact, the following would be the case:

The interaction is drawn to scale in Figure 4.23. A cross-section of a Hertzian indentation is shown between a glass sphere of radius r_{sphere} = 1 mm and the polystyrene dish as was tested in those experiments. In between those materials, HUVEC were trapped in the interaction. However, due to their low Young's modulus (reported values range from 400 Pa [116] to 1 MPa [117], depending on the measurement location) compared to PS (3.25 GPa), their influence on the contact geometry can be neglected and is hence only determined by the glass sphere and the PS dish. ECs are generally between 0.1 µm-10 µm thick [118][119]. A full height of an EC monolayer (10 µm) is shown in the figure with a full height cell. On the left, an indentation is shown with a load of 10 mN and on the right side there is one with 80 mN. Several distances from the centre line are annotated. The Hertzian contact radius a is shown for both cases. Additionally, the estimated contact width radii from Figure 4.8 and Figure 4.9 are annotated for 10 mN and 80 mN, respectively. Furthermore, the

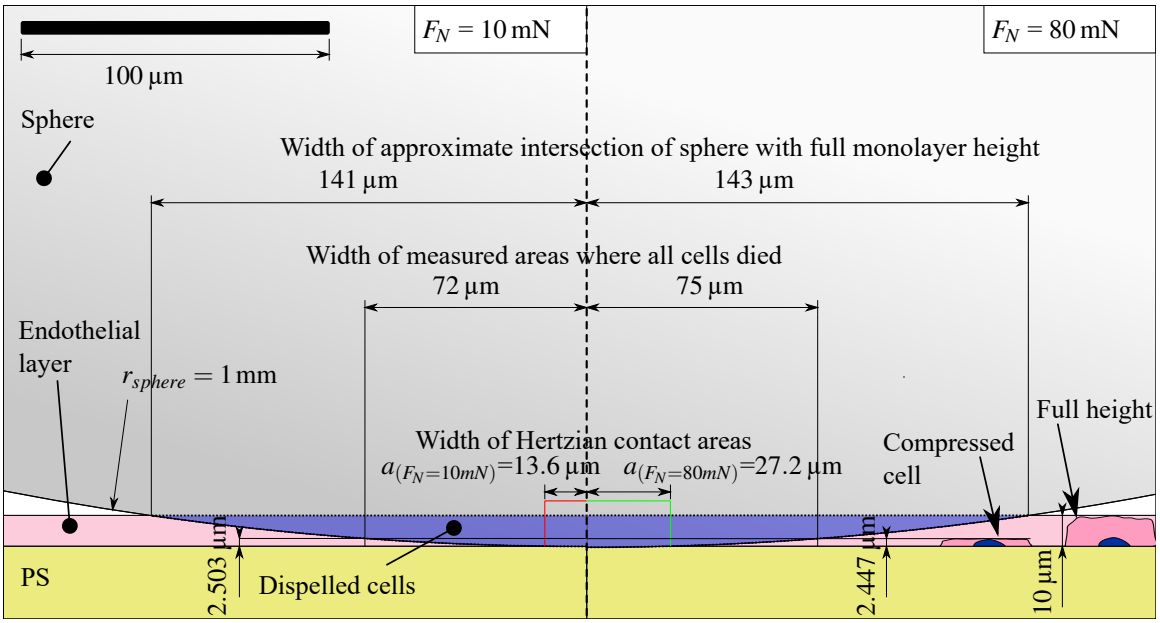

Figure 4.23: Contact geometry approximation between cells seeded on PS and a 1 mm radius glass sphere for a 10 mN (left)) and an 80 mN (right) interaction, drawn to scale. The scale is shown in the top left corner. A schematic cell layer height of 10 µm is annotated in addition to some important distances to the centre line. These include the calculated radius of the Hertzian contact area, the experimentally determined distance in which all cells died and the distances to the centre line where the gap size (distance between sphere and PS surface) is equal to the half and the full cell monolayer height. For the distance below which all cells died, the respective gap size is annotated.

maximum distances are shown at which sphere and polystyrene surfaces are 10 µm away from each other. These locations constitute limitations as to the distance to the centreline where the sphere could still be in physical contact with cells. From this model it is obvious that even though sphere and dish are not in immediate contact with each other beyond the Hertzian contact radius, the distance between them (also referred to as gap/gap size from here) may be too small to allow a cell to survive in the gap between them as it would simply get squashed. Such a cell would be damaged or partially or completely removed from the surface as the sphere moves along it (once relative movement is introduced). By annotating the measured width of the contact, which was extracted from the microscope images, the respective gap size was determined. For 10 mN, this is 2.503 µm and for 80 mN of normal force, it is 2.447 µm. Next to the cell on the right, a cell that was squashed to that height is shown. As the measured values are very close together, this supports the thesis that the size of the gap between the two surfaces is crucial for the survival chances of a cell that is trapped in it.

This model has some limitations. As already mentioned, it still only considers the most basic of contact mechanics, which is not an accurate representation of the contact (especially once the sphere and the dish move relative to each other) due to adhesive effects, relative

movement of the interacting bodies, etc. A Hertzian calculation of the contact, however, should still give a good estimate of the contact width. Furthermore, the model disregards deformations of the cells. While this may not have any significant mechanical implications, it leads to the monolayer geometry not being represented accurately. As the cells must be squashed outwards, they may bulge along the sphere, possibly deforming the monolayer around them which could lead to more cells being in contact with the sphere. Also, a cell monolayer is not flat, but it has junctions and varies in height [120]. However, the 10 µm line represents a gauge for the maximum height of the monolayer. Furthermore, a pure interaction (with a low pressure) between probe and cell is not necessarily deadly for the latter, neither is it likely to remove the cell as was shown with the experiments on PDMS-based substrates.

Overall, despite its limitations, the model can explain some findings. Firstly, the observation that the experimentally determined wear track width is greater than the predicted Hertzian contact width can be attributed to the fact that even outside of the contact area the distance between sphere and PS dish is too small for a cell to fit in. This can lead to cells being squashed and removed, or standing a good chance of remaining unharmed, depending on their height and distance to the centreline. This also explains why there are variances in the wear track width along the slide where some cells may be dead, but are often not removed. Those cells were likely too big to fit between sphere and dish and hence got destroyed, but did not quite have enough contact with the sphere to remove the cell remains from the PS. Finally, this model also explains why, despite increasing the Hertzian contact area with an increase in normal force, the experimentally determined wear track width does not increase to the same extent. This is because it seems the survival of a cell is strongly determined by the size of the gap between the sphere and dish surfaces on which the Hertzian contact radius only has a limited influence. The experiments on PDMS have shown that a simple interaction between sphere and cell is likely not deadly for glass probes. Therefore, the survival chances of a cell that is trapped in the gap between sphere and dish depend largely on the cell size and its distance to the centreline. Hence, it is unlikely to find cells that were killed by the interaction past a certain distance because apart from the ones that are too big, they can deform and survive. On the other hand, there is a zone within a certain distance to the centreline, in which almost all cells are removed and only very few survive healthily, due to the small gap size. The latter distance can be gauged to around 72 µm-75 µm with the gap distance around 2.5 µm. This is slightly dependant on the load condition and highly dependant on the sphere diameter. It is not immediately clear why the critical gap distance was 2.5 µm.

Peeters et al. studied the failure properties of single mouse myoblasts. They compressed attached cells with a flat indenter and studied reaction forces and strains. The authors report cell bursting to occur at a load of 8.7 µN ± 2.5 µN at a strain of 72 % ± 4 % [33]. Assuming similar mechanical and failure properties for HUVEC, a cells maximum height at failure point can be estimated with 10 µm × (100 % - 72 %) = 2.8 µm. Thus, the observation of 2.5 µm being the size of the critical gap size agrees well with the findings of Peeters et al. [33].

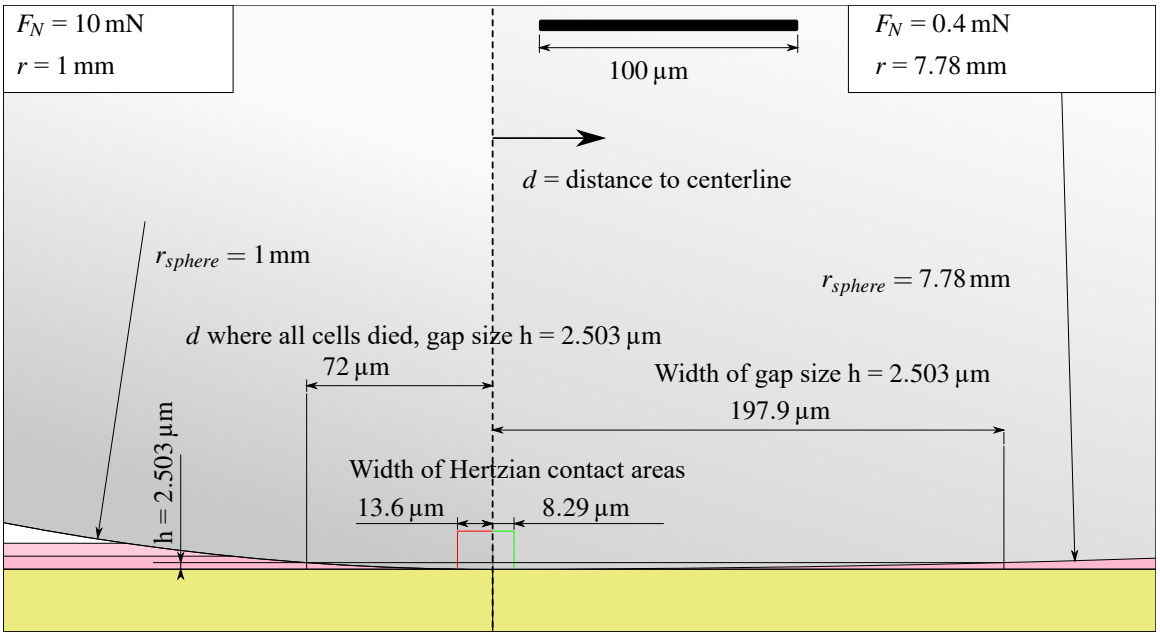

Figure 4.24: Hertzian contact geometry approximation of a 10 mN interaction with a 1 mm radius sphere compared to an experiment carried out by Dunn et al. [78] with a 7.78 mm glass sphere under a normal load of 0.4 mN. The figure follows the same notation style as in Figure 4.23 and is also drawn to scale for both sides. The seemingly crucial gap distance of 2.5 µm was transferred to the approximation of Dunns experiment and the respective distance to the centre line of 197.9 µm is annotated.

The implications of this model should have also affected previous studies. Dunn et al. [78] have conducted experiments with a different type of cells (bovine aortic endothelial cells) which were cultured on cell culture grade PS, which is the same type of material used in the experiments here. The monolayers were tested against a borosilicate glass probe of radius 7.78 mm under normal loads of 0.4 mN-1.2 mN [78]. For reference, the probes used here were made from soda lime glass and of 1 mm radius. Also the normal load in the experiments here was much higher with 10 mN-80 mN. A schematic of the contact geometry for the experiment of Dunn et al. is shown in Figure 4.24 on the right side for a normal force of 0.4 mN against an experiment conducted in the context of this work for 10 mN on the left. Both sides are drawn to scale. From the experiment here, the width of the wear track was estimated to a radius of 72 µm with a respective gap size h of 2.503 µm. Transferring this

gap size to the experiment of Dunn et al. results in a distance to the centreline of 197.9 µm. Here, it should be noted that cells also adhere to each other through adherens junctions. If the cells adhere stronger to their neighbours than they do to the substrate, the adhesive forces may cause larger portions of the monolayer to be ripped off than were initially in contact with the probe. Therefore the width of the wear track may not only be defined by the probe geometry but also by the strength of the adhesive forces between cells and between cells and substrate.

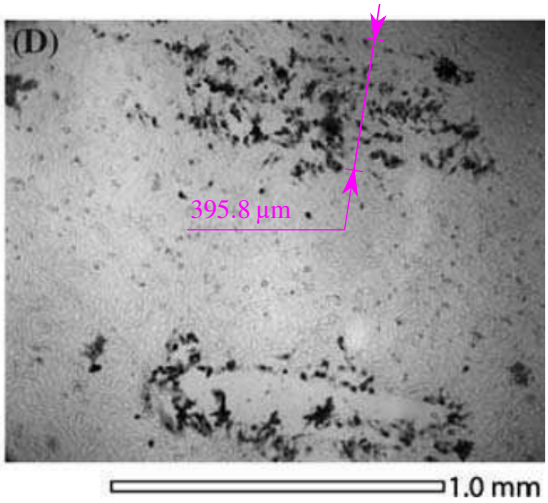

Figure 4.25: Trypan Blue stained monolayer of bovine aortic endothelial cells after friction testing. Adapted from Dunn et al. [78]. The annotation, marking a distance of 395.8 µm in pink, was added.

Dunn et al. included images of the post-friction testing, Trypan Blue-stained monolayer in their publication. One of their images is adapted in Figure 4.25. In addition to their microscope picture, in the figure, a distance of $2 \times 197.9\,\mu m = 395.8\,\mu m$ is marked. In the case of their experiments, this distance seems to give a good estimate of the width in which cell death was found, however, in this particular experiment, not many cells were removed. It should be noted that the authors achieve very low pressures with their testing methodology by both applying forces which are orders of magnitude lower than the ones used in this work, and also by using a sphere of a radius that is much larger than the one used here as a countersurface. These low pressures likely lead to a reduced damage to the monolayer and the lack of cell death that is observed in this specific experiment. Dunn et al. computed the occuring pressures to be in the range of 3 kPa-5 kPa with significant damage to the cell monolayer occuring from 5 kPa [78].

The dimensions of an endothelial cell are 50 µm-70 µm in length and 10 µm-30 µm in width [119]. Knowing these dimensions, one cell covers an area of around 500 μm^2-2100 μm^2. The critical pressure at which cells burst and are thus destroyed can be estimated

now with that area and the finding of Peeters et al. that a load of $8.7\,\mu N \pm 2.5\,\mu N$ results in a cell bursting. The estimated bursting pressure is in the range of 4.143 kPa-17.4 kPa. Even though this is only an estimate, the resulting pressure is of the same order of magnitude as the calculation of Dunn et al. Estimating the contact pressure from the measured contact width (like Dunn et al. did) for the experiments conducted here, yields a pressure of 614 kPa to 4527 kPa, for normal forces of 10 mN to 80 mN with contact radii of 72 µm and 75 µm, respectively. This calculation was made assuming a circular-shaped contact area. The pressures occuring in the experiments here are much larger than the ones Dunn et al. [78] report to cause significant damage. They are also much larger than the estimated burst pressure calculated with the results of Peeters et al. Therefore, it is not surprising that in the experiments here almost all cells in the wear area were completely destroyed.

As a conclusion, the observations that the contact area width is larger than Hertz predicts, and that it only changes slightly when increasing the normal force, make sense in the context of the model. While the model has its limitations, it agrees with the findings of previous studies and qualitatively explains the observations made when testing a monolayer cultured on PS against a glass probe. The model validity was confirmed when applying it to the results of Dunn et al.

4.5.2 Friction on Polystyrene Based Samples

This section looks at the friction results collected from PS samples coated with fibronectin (PS+FN) and PS samples that were coated with fibronectin and cultured with HUVEC (PS+FN+HUVEC). Furthermore, the results collected on soft substrate samples are taken into account. Earlier, the question about the nature of the contact was being raised: are cells being tested, or are they merely a lubricant between PS dish and glass sphere?

In Figure 4.7a, the static friction data for PS+FN and for PS+FN+HUVEC samples are plotted. The fitted friction coefficients from this figure are shown in Table 4.4. Comparing the data in the figure indicates that cells do not have a major influence on the static friction force. This is also reflected by the static friction coefficients 0.544 and 0.511 for PS+FN and PS+FN+HUVEC, respectively. The friction force is slightly reduced. However, it is still much higher than the static friction force measured using soft substrate samples, where the pressures were much lower and hence significantly more cells survived and remained in the wear track. As shown earlier, the static friction does not behave according to Amonton's law for soft substrate samples, but for reference, the fitted static friction coefficient was 0.053. Also, on soft substrate samples, the qualitative friction force behaviour as a function of normal load is very different. Both PS-based sample's results were in reasonably good

Substrate (reference)	μ_{static}	$\mu_{dynamic}$
FN coated PS without HUVEC (PS+FN)	0.544	0.497
FN coated PS with HUVEC (PS+FN+HUVEC)	0.511	0.303
FN coated soft PDMS with HUVEC (soft substrate sample)	0.053	0.018

Table 4.4: Friction coefficients of PS+FN and PS+FN+HUVEC and soft substrate samples against glass probes.

accordance with Amonton's law of friction, while the results using the soft substrate samples were not.

For the dynamic load condition, the difference between the PS+FN and the PS+FN+HUVEC samples was more significant, as is evident from the fitted dynamic friction coefficients 0.497 and 0.303, respectively. Despite being smaller, the values for PS+FN+HUVEC stand in stark contrast with the dynamic friction coefficient fitted from measurements on soft substrate samples, 0.018. The latter stands in much better accordance with literature values (Dunn et al. report a friction coefficient of μ = 0.03-0.06 [78]).

In Figure 4.26, the indentation process is shown at different stages. The sphere is shown as it just contacts the monolayer in position a). In position b), the cells in the centre of the contact are compressed to h_{crit} and are thus about to burst. The probe is lowered further in position c), destroying the cells and squeezing out their contents. Detail d) shows the bursting. As the pressure gradient is directed outwards from the contact area, the cell bursts at the side. Cells mainly contain cytoplasm which is largely made up from water, so a good analogy is a balloon filled with water that is squeezed. It will burst somewhere at the side of the cell facing away from the centre of the contact area (i.e. it will burst in the direction of the pressure gradient). When that happens to the cells, most of the contents, like cell organelles, will be flushed out with the cytoplasm. As the sphere moves further down until it is in contact with the PS (i.e. the probe is fully loaded with the PS taking the main load), all liquid parts of the cell will be squeezed out and only viscous and elastic parts can remain. Those are mainly parts of the cell that were in some way attached to the substrate, such as the nucleus, parts of the cytoskeleton and the cell membrane which are bound to the substrate through adherens junctions. At this point, an area will have formed where the glass and the PS are very close. This area will be approximately circular due to the symmetrical geometry with the radius $a_{contact}$. Detail f) shows this area on a microscopic level. The asperities of the glass and the PS may contact each other, as those materials are very hard compared to

the cell organelles, and the pressures between the asperities can be expected to be very high. This would mean that in the static friction case, which has been preceded by 10 s of loading, the friction behaviour is largely equivalent to PS against glass, with some cell parts trapped in the asperities. This could be the reason why barely any difference was measured between PS+FN and PS+FN+HUVEC.

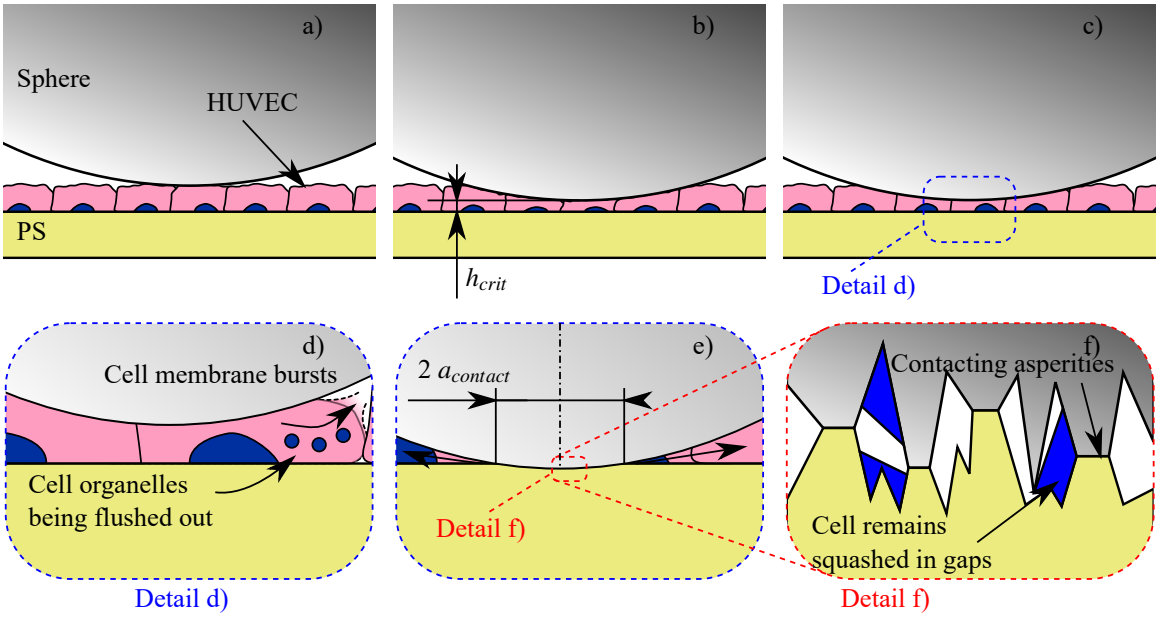

Figure 4.26: Schematic of the interaction between a glass sphere and a PS sample with HUVEC.

When the probe starts moving, more and more cell material comes into the contact area. As it is continuously moving, there may not be enough time for the probe to squeeze the more viscous cell parts out of the contact. Also, it is possible that at some point the asperities of the sphere are saturated with cell matter. Both could lead to a separation of the asperities on a microscopic level as cell matter is squashed between them. This would mean changing the dynamic of the contact mechanics and thus could be the reason for the observed reduction in friction coefficient. In this case, the cells would act as a lubricant rather than as a surface in the interaction. This is supported by the observation that only 28.5 % of the cells in the monolayer remain healthy, even for the lowest load tested, on polystyrene samples.

4.5.3 Damage to Monolayers Cultured on Polstyrene-based Samples

The damage inflicted to the monolayer for different normal forces can still be differentiated for PS-based samples, so the point of absolute destruction has not been crossed. This means that the effect of the load regime on the monolayer damage can be studied. Factors

that influence the severity of the load regime are certainly load, the underlying substrate parameters and relative velocity. As the velocity is the same in all experiments, the theoretical maximum Hertzian pressure between probe and substrate without HUVEC p_0 may be a good indicator for the severity of the load condition, as it captures both, load and material parameters. Also, pressure is an intuitive gauge of how damaging a load condition may be. In Figure 4.27, this is visualised. Two datasets are plotted: the removed nuclei data for PDMS-based samples on the left and the equivalent for PS-based samples on the right. Both sets of data are plotted over the Hertzian contact pressure on the X-axis. The calculations were made for the respective substrate and an $r = 1$ mm glass probe. Note that the X-axis is in log scale and there is a gap of two orders of magnitude between the two subplots. PDMS-based and PS-based experiments stand for mild and harsh load regimes, respectively, as indicated per the Hertzian pressure p_0. When putting those two load regimes side by side, the bigger picture seems to become more apparent. For a mild load regime, the cells are capable of remaining on the substrate to a large extent even if some die, as evident from the plots, including the dead nuclei data in Figure 4.14. However, the damage inflicted to the monolayer stays around zero and then rises relatively steeply towards the end of the mild load regime. On the other hand, for the harsher load conditions, the damage rises steeply, but then seems to converge towards 1 (full destruction of the monolayer). Put together, the graphs look like they form the ends of a saturation curve, albeit the transition area between those ends is not depicted and there is a fairly large gap in between. Qualitatively, this makes sense, as for mild loads, few cells are being removed, while for harsh loads, nearly all are. Quantitatively, the large gap indicates that Hertzian pressure may not be the best measure for load regime severity. While the damage may be compared, the friction data may not because, as laid out earlier, it seems likely that the probe is considerably interacting with the underlying substrate as the monolayer is breached to a large extent for all cases tested on polystyrene.

Therefore, as a conclusion, the experimental set-up, as used in this work, is considered unable to test friction on cells cultured on polystyrene-based samples. Instead, the load conditions are so harsh that the monolayer is destroyed to a large extent and, consequently a polystyrene substrate was tested against glass with cell matter as a lubricant. This is evident from several observations. Firstly, the majority of the monolayer was destroyed. As a large portion (46.3 %-80.3 %) of cells does not remain in the track area, the probe has clearly penetrated the monolayer and must hence be interacting with the polystyrene to a large extent. As most cells are destroyed and the friction force in the dynamic case is significantly reduced, that implies that the cell's remains are acting as some sort of lubricant. However, the friction forces are not reduced to a point where they would be comparable to literature

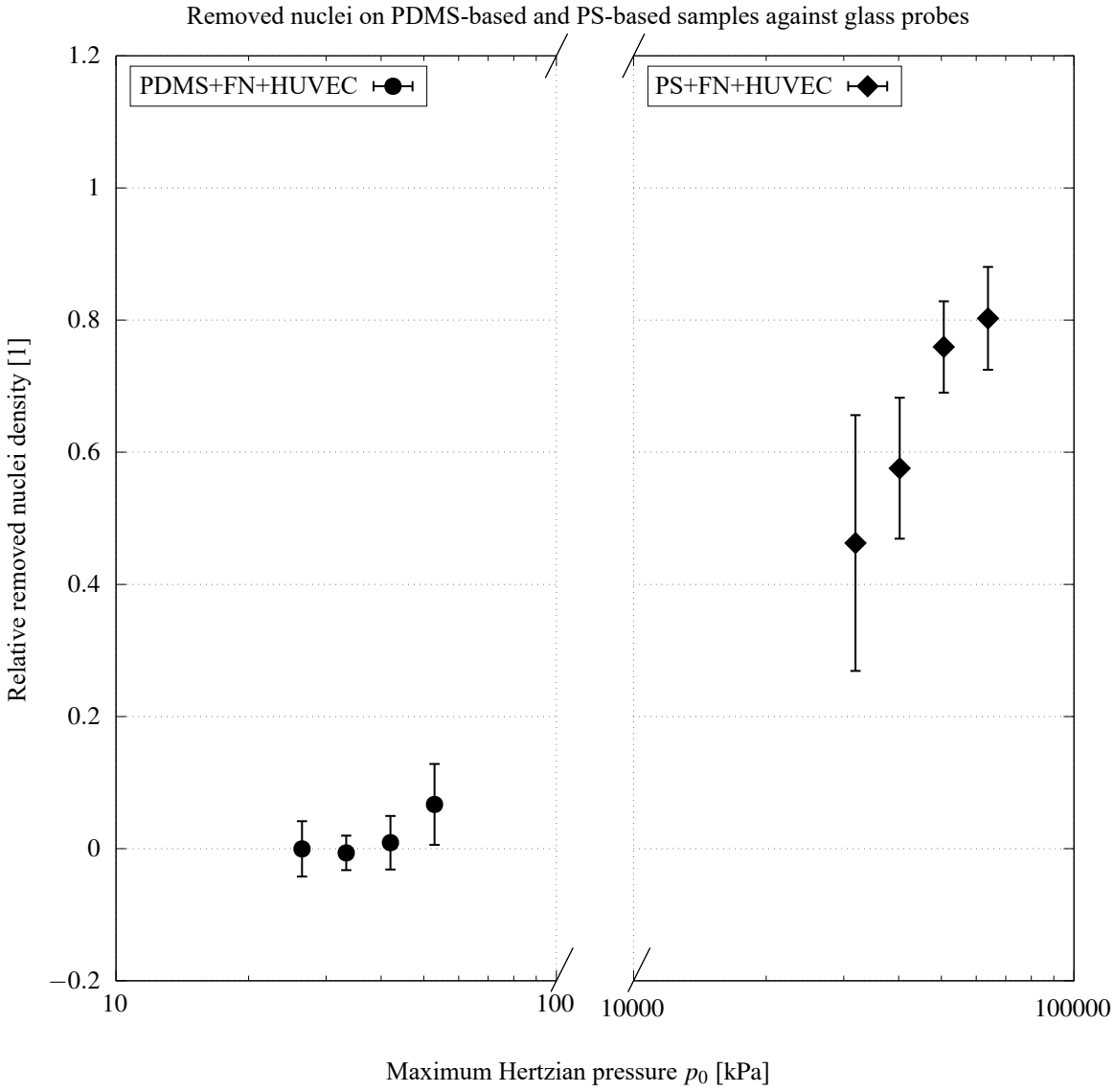

Figure 4.27: Removed nuclei data on PDMS-based and PS-based samples against glass probes over Hertzian contact pressure.

values, or those collected on soft substrate samples. Overall, the load condition is simply too harsh for enough cells to survive in the wear track, which prevents testing the desired material pairing (cells against probe material). Experiments could still be conducted with different probe materials on PS samples, however, any differences in friction resulting from cell/probe interaction could not be easily differentiated from the ones resulting from cell-matter-lubricated PS/probe interaction. To ensure testing of the desired material pairing, a different, much more expensive, set-up would be required. Therefore, friction experiments with different probe materials were conducted on soft substrate samples. After all, differences in terms of damage caused to the monolayer were still measureable on PS samples

and made sense when compared to the data collected on soft substrate samples, considering the harsher load regime. It should be noted however, that the indicator used to quantify the severity of the load condition here (p_0) does not give credit to all factors that may influence the harshness for the cells and is thus almost guaranteed to not cover all cases of load conditions. This is evident from the large gap that extends over two orders of magnitude in Figure 4.27. Furthermore, the friction data is not directly comparable between PS-based and PDMS-based samples as testing does not take place in the same load regime despite the same normal forces being used. The load cell that was used in this experiment was almost pushed to its upper limit by testing a normal force of 80 mN (the limit is 100 mN). To obtain a more continuous version of the plot and hence gain a broader view of the load regimes, soft substrate samples and the same type of probe could be used in conjunction with load cells capable of exerting higher loads. This would allow collecting data to cover the transition area and also compare friction data over the whole range of load regimes, although still, at high loads, the substrate may be tested rather than the cells.

4.5.4 Damage to Monolayers Cultured on Soft Substrate Samples

This section first looks at peculiarities observed in the slide images and will investigate general trends in terms of damage later on. In Figure 4.19a, a 10 mN slide image with a PTFE probe is shown and it was noted that the width of the wear track significantly reduced and then stabilised at the beginning of the indentation. Assuming that the material is sufficiently flat, the substrate will reach steady-state geometry at some point. What this means is that at some point from a probe view, the deformation of the substrate will be time invariant. For this, imagine a pin on disk test where a fixed probe is pressing on a rotating disk. At some point, the disk surface geometry will have adopted its final form, which will not change apart from wear. This is the case if there is no stick-slip occuring. If there is stick-slip, the geometry will change within certain boundaries in a reciprocating fashion. In the case of this particular instance, any stick-slip that may be occuring on a small scale, does not seem to propagate into the image data to a noticable extent as the wear track width stays the same once it has stabilised. As the substrate is very soft, after the indentation phase, when motion is introduced initially, the underlying material has not reached steady-state geometry yet from a probe-centered inertial system, as evident by the change in width. An explanation for this could lie in bulging of the material. This is shown in Figure 4.28. On the top row, the process is shown schematically from the side (S). In the middle row, sections of the wear track image with the probe position on the substrate are shown, which is equivalent to a top or bottom view (T). In the bottom, the process is shown schematically from the front (F). The coordinate system X and Z is shown for all positions and views. It

is set so that the origin is in the centre of the probe when it is fully loaded. In position a, the probe is indenting the material without movement in X direction, hence, due to symmetrical loads and initial geometry, the contact is symmetrical around the Z axis as indicated in the side and top view. The contact radius is highlighted in the track image labelled "aT" by the circle with the white dotted line. As the contact is symmetrical in position a, and the probe moves to the right from there, the initial contact radius can be determined by measuring R on the left side. As a circle with radius R describes the contact geometry on the left hand-side reasonably well, and the wear track width is equivalent to $2R$, it can be deduced that the contact width is the widest during the initial indentation and decreases from there as the probe moves. The projected contact geometry is marked by the green line. In position b, initial motion has begun. The contact geometry is not symmetrical around the Z axis as the substrate bulges on the side the probe is moving towards. Symmetry will, however, theoretically be retained at the Z/X plane as loads and initial geometry are symmetrical to that plane. The contact geometry can be estimated from the wear track width. In position c, the underlying substrate has reached its steady-state deformation. The wear track width was measured from the image. Bulging on the sides and in front of the probe decreases once the initial bulge has been overcome.

Another observation that was made when investigating the track images was that the monolayer could be intact to a large extent, but a very high, local damage in the form of scratches occurs, as seen for example in Figure 4.19a. These scratches did not necessarily occur in the centre, where the highest pressure would be expected. The localised nature and orientation of the damaged patches suggests that it was not pure pressure that removed the cells, but rather the movement of the probe. It seems that once the monolayer is breached in one location, the chances of subsequent cells remaining are low. The reason for this might be that once one cell is removed, the next cell takes the brunt of the load alone and hence its chances of staying attached are greatly reduced. As this cell detaches, the next cell takes the brunt and so on. The subsequent cells would peel off. This is supported by the observation that scratches, once initiated, often continue all the way through to the end of the slide. It is also possible that material deformations in certain areas are especially unfavourable for the cells. This could be investigated in the future with a finite element analysis.

Overall, the damage throughout a single slide could be highly time dependent, especially for more damaging load conditions and experiments with PTFE probes. This may be caused by changes to the interface by cell parts sticking to the probe. Investigating this was one of the motivations to conduct the consecutive indentation experiments which are presented in Chapter 5.

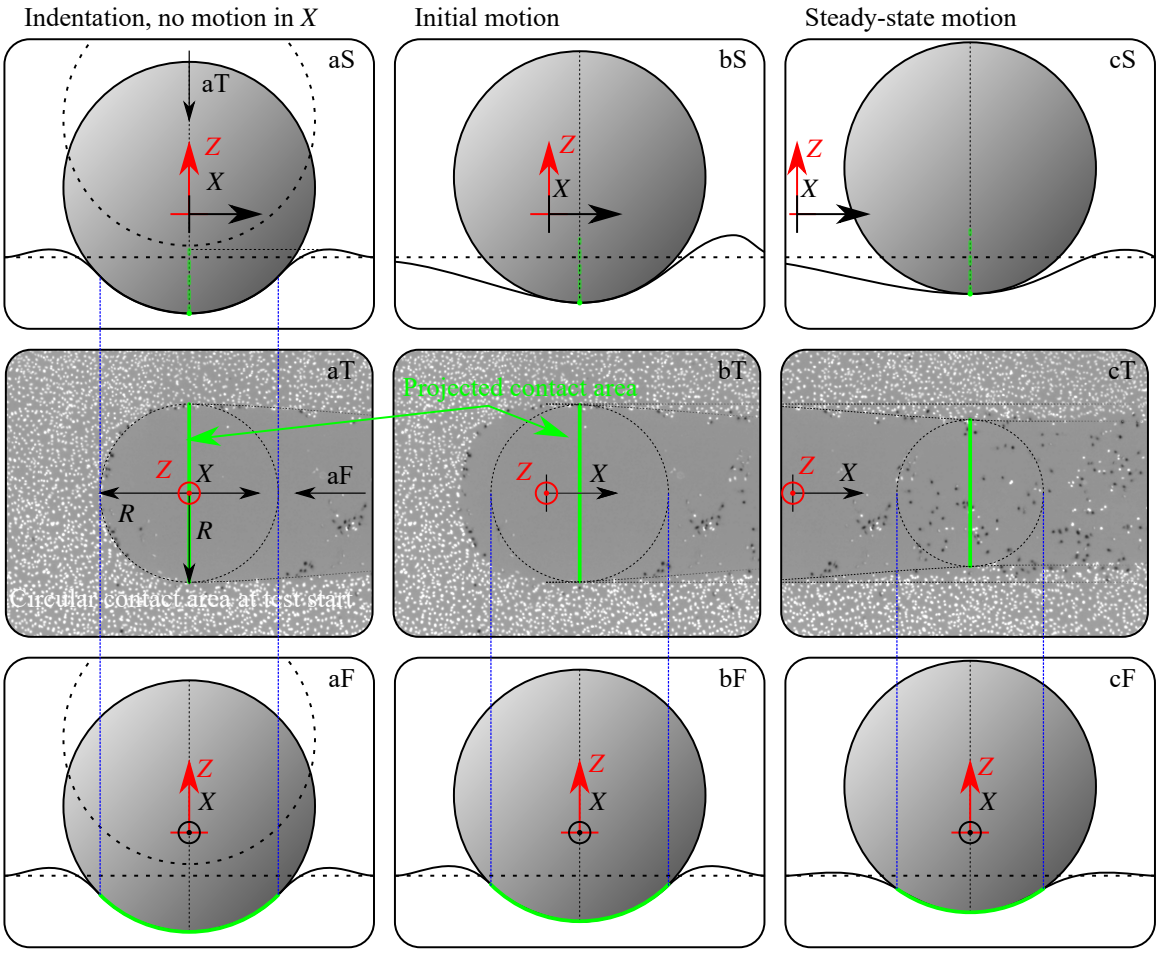

Figure 4.28: Effect of bulging during indentation and friction experiments. Probe and bulging material underneath are shown in different positions a through c and in side (S), top (T) and front (F) views. Version with blue/red channel images in colour can be found in Appendix C.4

Conclusively, the damage to the monolayer was successfully measured for glass, stainless steel and PTFE probe materials. Stainless steel was the most harmless material of them. For the whole range of loads, it exhibited more healthy and less dead cells than glass, and around the same number of removed cells. The amount of dead cells follows the same trend for both materials with a small offset, indicating that the two materials behave similarly, but stainless steel is less harmful overall. This result is reflected by the wear track images, where for both materials, large parts of the monolayer were still intact. However, for stainless steel, a lower amount of dead cells was noticable throughout the range of normal forces. PTFE probes, on the other hand, inflicted large amounts of damage for all normal forces. Even for 10 mN, the portion of removed cells was large and the portion of healthy cells is far lower than for the other two materials. From there, increasing the normal force causes even more cells to be removed which is accompanied by even less healthy cells in the wear track. In Figure 4.22, the dead nuclei densities were plotted for different materials. As mentioned

earlier, this data on its own could imply that PTFE is in fact the least invasive material of the three tested. It looks like PTFE is a more harmful material than the other two for the lowest force and then acts less harmful as the normal force increases. This result however, must be seen in the context of the proportions of healthy and removed cells. The reason for the low portion of dead nuclei in the wear track that was observed for higher forces is clearly that the majority of cells are not only killed, but completely removed from the surface as evident from the data for removed cells. This also becomes clear when looking at the wear track images for PTFE and comparing them to the other two materials. The former inflicts much more damage to the monolayer than the latter two materials by removing a large portion of cells. Overall, stainless steel and glass both caused relatively small amounts of damage to the monolayer in terms of removed cells, however, stainless steel was consistently superior in leaving more cells intact. PTFE was found to be the most harmful of the materials. In real applications, this is relevant since PTFE is used as a coating. Catheters [121][122][123], stents [124][125][126] and guidewires [127][128] have used and still use PTFE coatings claiming to lower friction and ease passage. The results of this work, however, suggest that the opposite is the case: PTFE causes higher friction than the other materials and at the same time causes higher damage.

The pressures are around the same for experiments of the same normal force with probes of the same diameter, as deformation is mainly dependant on the properties of the softer material. It should be noted here that PTFE probes had a larger diameter than stainless steel and glass ones. This was due to the lack of availability of 2 mm PTFE spheres. For this reason, the normal pressures can be expected to be slightly smaller for tests with these probes. In light of this, the extreme damage inflicted by PTFE probes is all the more remarkable.

4.5.5 The Issue of Negative Cell Removal

As mentioned earlier, in some cases, the amount of removed nuclei was negative, implying that more cells were found in the wear track than there were before. There are two possible causes for these initially counterintuitive measurements. Firstly, the cell density varies throughout the dish. As they grow naturally, cells are difficult to control. This includes seeding and consecutively proliferation, which determines nuclei density. The slide area only makes up a fairly small part of the whole dish, however, it stretches out over a very large area in terms of cell dimensions. This means that the cell density at the beginning of the slide may be slightly different to that in the middle of the slide which, again, may be different from that at the end of the slide. Therefore, the initial cell density in the slide area could be slightly higher or lower than it is in the compare areas. One of the reasons why the

experiments were repeated multiple times was to diminish the effect of such natural variances of the sample, however, there is still a remaining variance. Secondly, the implication mentioned earlier that cells were added to the slide area may not be completely wrong. After testing, the cells that were removed from the surface have nowhere to go except for the surrounding media. Therefore, some will inevitably be over the slide area. However, the effect of this should be rather small for several reasons. Firstly, the sample is being washed twice in total before imaging, once before and once after staining. The washing should aready remove the majority of detached cells. Secondly, the surface area of the Petri dish is very large compared to the slide area. This means that only a small amount of the cells that were removed from the surface and swim in the medium will actually be above the sliding area and hence counted there. Thirdly, the removed cells that happen to swim exactly above the sliding area then have to be close enough to the surface to be within the microscopes depth of field. Cells that are too far away will be out of focus and not recognised by CellProfiler. Finally, as they are in the same dish, compare areas and slide area are affected by this equally. Therefore, any differences in the density caused by nuclei swimming around should be accounted for.

Overall, the main reason for the observation that negative amounts of cells were removed will likely lie in the fact that those had to be calculated and could not be measured. Because the amount of removed nuclei is calculated based on the densities in the compare area and the wear track area, natural variances in nuclei densities throughout the sample will impact that value. As a conclusion, the errors are noticable, but are expected to be rather small compared to the standard deviations. To approach the issue, before and after images could be taken. However, this is difficult because the friction experiment must be conducted exactly at a site that was imaged before. *In situ* visualisation of the contact is another approach to counter this issue. However, for the experiments conducted here, a very large area of more than 10 mm length would have to be imaged. Microscopes usually do not have such a wide field of view. A higher number of tests could also help to reduce the influence of natural variances in nuclei density.

4.5.6 Friction on Soft Substrate Based samples

Friction was measured successfully with a good degree of accuracy for three different probe materials against HUVEC. Static and dynamic friction forces were reported for a range of normal forces. In previous works, the known problem of potential misalignment in the tribometer [84][85][86] was accounted for by executing the experiment more than once on the same track and averaging the results. As described in Section 3.11, this comes with several disadvantages. The methodology presented here uses a novel approach to tackle

this issue by adjusting for the slope. It was shown that there was good agreement between slope-adjusted measurements and ones conducted on a flat portion of the sample, indicating that the concept was accurate and successful in accounting for the misalignments.

The values measured in this work are reported in Table 4.5. The amount of literature values for these material pairings is limited and most studies only report values for the dynamic friction coefficient. Dunn et al. [78] have reported friction coefficients of μ = 0.03-0.06 for borosilicate glass against bovine aortic endothelial cells seeded on PS. In their work, the measured friction coefficients were higher than the ones measured here, however, it should be noted that the monolayers in their work partially suffered heavy cell removal, whereas the ones tested here were intact to a large degree. Chen et al. [17] reported static and dynamic friction coefficients under a normal stress of 3.3 kPa for HUVEC against a glass plate as 0.050 76 and 0.0229, which agrees well with the data measured in this work. The monolayers in their work were largely intact after testing. In terms of values for steel probes, Takashima et al. [54] measured friction coefficients of a steel ball against pig aorta. The values they measured for the dynamic friction coefficient ranged from < 0.017 to around 0.09, with an average of 0.046 , depending on the the angle under which they applied the normal force. The average static friction coefficient they measured was at around 0.08 The lower end of their measured values agrees well with the ones measured here, but their reported static friction coefficient is significantly higher which could be down to the angle under which they measured friction. For PTFE, no values for static friction or dynamic friction on any type of cells have been reported yet.

Substrate	Static friction coefficient	Dynamic friction coefficient
Glass	0.053	0.018
316L	0.057	0.018
PTFE	0.109	0.044

Table 4.5: Friction coefficients on soft substrate samples against different probe materials.

Overall, the friction coefficients measured in this work agree well with the ones found for equivalent material pairings in the literature. However, the amount of studies is fairly limited and some studies do not report the state of the monolayer after testing and therefore it is not always clear what load regime is tested, whether perhaps the monolayer is destroyed and, as such, whether the substrate was tested.

In this work, after testing with glass and stainless steel probes, the monolayer was largely intact, which suggests cells were tested and not the underlying substrate. For PTFE, however, the question may be raised: which interface exactly was tested? On this note, experiments were also conducted with glass, stainless steel and PTFE probes against fibronectin

coated and uncoated PDMS. For glass and stainless steel, the friction coefficients were above 1 and for PTFE above 2 with very little difference between static and dynamic friction coefficients. While this does not guarantee that there is no interaction whatsoever between the PDMS and the probe, it does imply that there is almost none as with cells the friction dropped significantly ($> 94.55\,\%$ for static and $> 97.8\,\%$ for dynamic) compared to the pure substrate.

However, why the friction on PTFE was so much higher than for the other materials should be discussed. The monolayer was almost completely removed by PTFE probes. As the normal pressure was lower for PTFE probes than it was for glass and stainless steel probes, the cells were not simply squashed. Therefore, it can be assumed that the removal may rather stem from material-based interaction between PTFE and cells. The friction occuring in the experiments conducted here is assumed to mainly happen in the boundary lubrication regime (as opposed to mixed or (elasto)hydrodynamic lubrication regimes) due to the low speeds. These lubrication regimes originate from conventional mechanical engineering tribology and are used to describe the extent of which the respective surfaces are touching, or are separated. They describe different parts on the Stribeck curve which correlates the friction coefficient to the parameters relative speed v, lubricant viscosity η and load P, which are relevant to the hydrodynamics of the system. For boundary lubrication, there is only a limited amount of lubricant (medium) and almost no hydrodynamic pressure which is not sufficient to significantly separate the surfaces. In the context of cells, this results in parts of the cells (the cell membrane as well as any receptors, adhesive junctions and the glycocalyx) potentially touching the probe material and, therefore, possibly binding to it chemically. For the static friction, this is the case per definition. In the dynamic case, it is evident from the damage caused to the monolayer. If there was a significant hydrodynamic lubrication film in all cases, the damage caused by the probes would be almost the same for stainless steel and PTFE, since their surface roughnesses are very similar. Therefore, in all cases, the contact is likely dominated by boundary lubrication to a large extent. The glycocalyx layer, which is on top of ECs has been confirmed to play a large role in friction [17].

A possibly similar structure that has been studied in tribology are so called polymer brushes. Polymer brushes consist of long chains of polymers which can have functional groups attached [129]. As such, they could be similar to the proteoglycans of the glycocalyx which is a network of sugars (i.e. carbohydrates) connected together to form glycans [130]. Polymer brushes achieve extremely low friction coefficients if attached to opposing surfaces when they are swollen because, upon compression, it is energetically favourable for them to become less swollen [131] i.e. release water. The frictional properties of the endothelial

glycocalyx which Chen et al. [17] observed may be due to a similar mechanism as Klein et al. [131] described with hydrated polymer chains. If there is a higher amount of glycocalyx, they can trap more water and hence it is easier for them to reduce friction. The effect may not be as pronounced because only one side (HUVEC) possesses a polymer-brush-like surface, whereas the other (probe material) does not, however, the effect the glycocalyx had on the friction was clearly measureable by Chen et al., who also used a steel probe [17]. PTFE is a very hydrophobic material. It may be possible that the hydrophobic PTFE drove out any water (which is the main ingredient of the media) from the contact which is crucial for lubrication through hydrated polymer chains. Glass and stainless steel, which are both more hydrophillic, may not do this and hence more water can be in the contact for those probe materials. Extremely hydrophobic materials paired with hydrophilic materials have been shown to be capable of very low friction coefficients of $\approx$ 0.003-0.009 [132]. However, this is only the case when the water film can be trapped in the interface which may not be possible due to the glycocalyx and asperities through which the water could escape. Furthermore, hydrophilic materials have been recently shown to reduce wear to the glycocalyx [74].

As the monolayer is largely removed by PTFE, it seems likely that the probe binds to the cell surface. What could be happening is shown in Figure 4.29. As mentioned, initially, there is a layer of water (media) on top of the cells in position a. Then, as the probe is lowered in position b, the water is squeezed out of the contact. As most water has left from the glycocalyx and there is direct contact now between cell and probe material, the glycocalyx and parts of the cell membrane may attach to the probe in position c. The normal load F_N will be balanced through interfacial normal stress σ by the underlying cells in which a pressure P will build that is equal to σ. A tangential load is then introduced as the probe starts moving in position d. The cells carry that load until they break in position e. As, on average each cell may be able to carry a certain tangential load $F_{T,\text{break}}$ and will have a certain surface area A_{cell}, that would explain why the static friction force behaves more proportionally to the calculated Hertzian contact area than it does to F_N, as Amonton's law suggests. This causes the cell membrane to burst and shed its contents into the environment. Due to the pressure P within the cells, the liquid cytoplasm will be squeezed out of the cells which is naturally accompanied by a drop of pressure in the cells in position f. In position g, this drop in pressure causes the probe to move down as the load is force controlled. At this point, the contact may be lubricated by cell remains (parts of the membrane, the cytoskeleton, nuclei and cell organelles). These may not do a sufficient job in keeping the PTFE and the PDMS apart, so there could be some interaction, however, at least for lower loads, this seems to be (if at all) only the case during the start of the slide because as

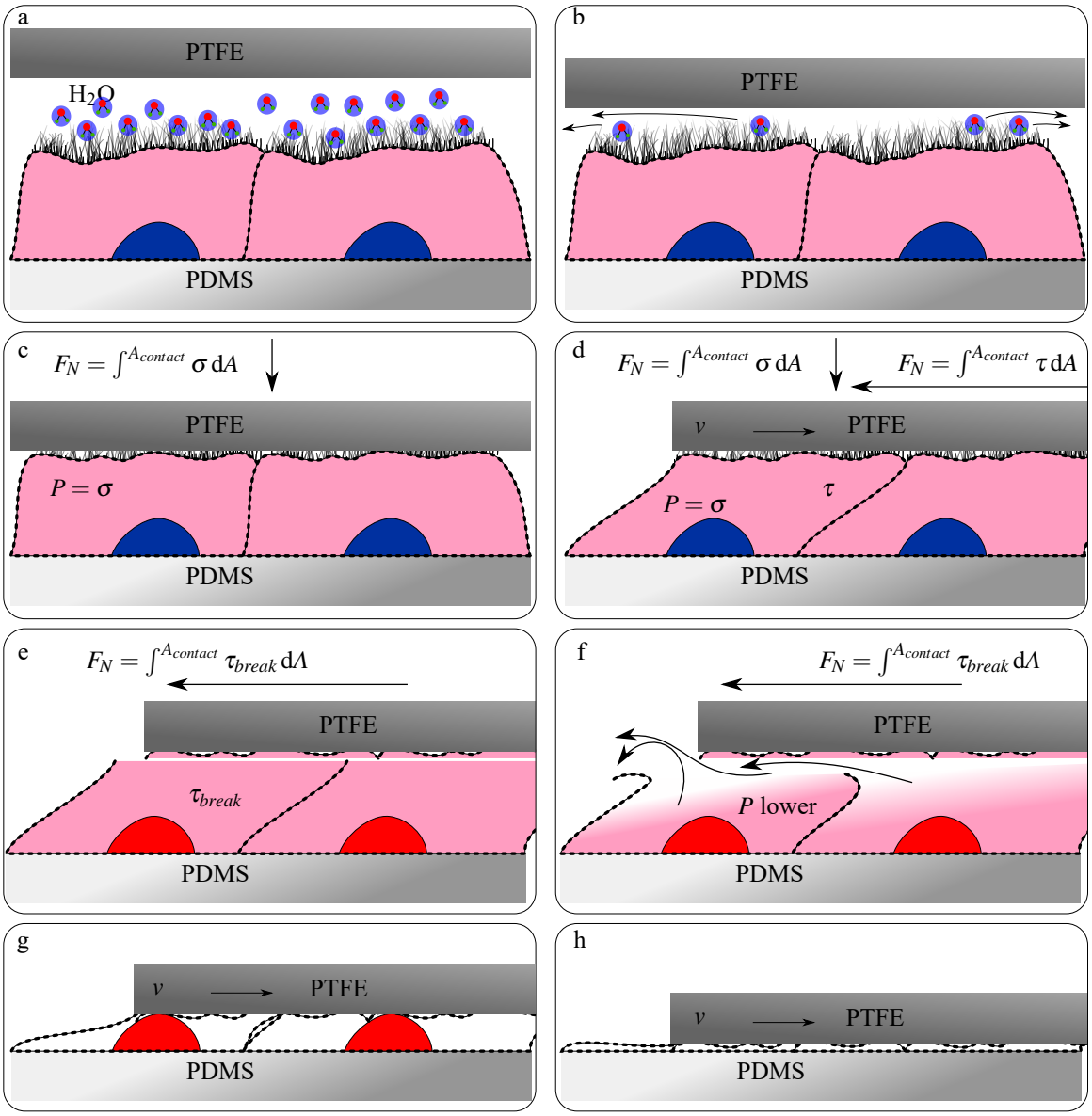

Figure 4.29: Schematic interaction of PTFE probe against HUVEC monolayer.

it progresses, more cells remain in the contact, suggesting that also the separation between PTFE and PDMS increases. Whether this is due to changes of the surface or because of a change in the lubrication regime, will be explored in the next chapter by conducting consecutive indentations. This allows to eliminate the possibility for a change in load regime and to only study effects caused by changes to the probe induced by an increasing number of interactions with cells.

Chapter 5

Indentation Experiments with Subsequent Damage Assessment

Friction experiments were used to study the monolayer behaviour on a soft sample substrate under different loads with relative movement for glass, stainless steel and PTFE probe materials in the last chapter. In this chapter, indentation experiments are presented which were conducted using the same loads and probe materials to study the damage inflicted to the monolayer without relative movement. The protocol for these experiments has been described in Section 3.9.2 and the subsequent damage quantification in Section 3.12.5.

5.1 Background

In Chapter 4, the damage to the monolayer was found to change throughout the track. Furthermore, PTFE was found to be very harmful in general. This chapter focuses on the indentation, thus simplifying the load conditions.

5.2 Aims and Objectives

The aims of the experiments presented in this chapter were to extend the results from Chapter 4 and to investigate whether the probe changes with consecutive indentations after continued interaction with the monolayer. Furthermore, the material parameters and the validity of the Hertzian approximation which was used throughout this work had to be confirmed. In order to do this, the experiment set up from Chapter 4 had to be adapted to perform experiments with subsequent indentations. The staining procedure did not have to be changed, but the damage analysis had to be adapted.

5.3 Methods

The experiments in this chapter were executed using the same methods used in Chapter 4, which are described in detail in Chapter 3. In this chapter, however, no relative movement between probe and sample by moving the stage was introduced.

5.3.1 Substrates

Soft PDMS substrates were cured, coated with fibronectin and seeded with HUVEC as per the protocols described in Sections 3.4, 3.5 and D.2.

5.3.2 Probes and Friction Apparatus

The probes were manufactured in the same way as they were for Chapter 4 in Section 4.3. Friction testing was conducted in the UMT 2 again with the FLV load cell.

5.3.3 Test Layout and Repeats

Indentation experiments were conducted using the sequence described in Section 3.9.2. One indentation run (or repeat) consisted of five consecutive indentations in a distance of 3 mm in between with the same probe. Similar to friction experiments, a sample was large enough to execute three indentation repeats on it for a total of 15 individual indentations in order to maximise efficiency and cost effectiveness. The test layout for indentation experiments is shown in Figure 5.1.

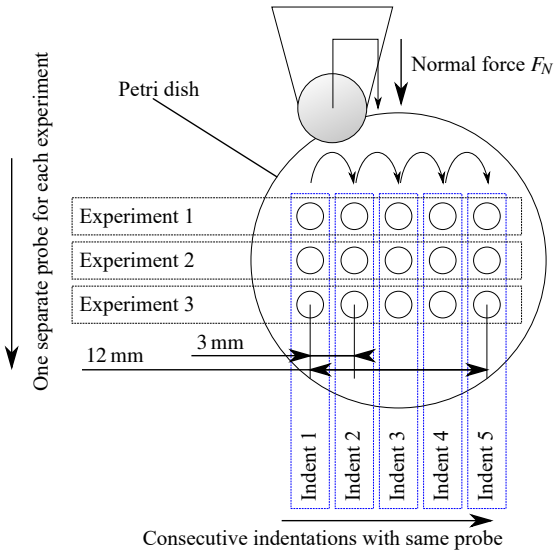

Figure 5.1: Test layout on sample for indentation experiments.

Similar to friction experiments, indentation experiments were conducted for normal forces F_N of 10 mN, 20 mN, 40 mN and 80 mN in order to utilise almost the whole range of the load cell. An overview over the tests conducted in the context of this chapter with respective number of repeats n can be found in Table 5.1. Again, as with the friction experiments, glass, stainless steel and PTFE probe materials were tested with the indentation script on soft substrate samples. Damage data on the monolayer was recorded afterwards. Data from the UMT 2 was also collected, not to investigate friction, but rather to measure the indentation depth and reaction force in order to study how the substrate behaves. In the context of the indentations, also the probe roughness is reported, which was tested on 11 beads for each material.

Substrate material	**Probe material**	**Relative speed**	**Repeats for each load condition n**
PDMS+FN+HUVEC	Glass	0 mm/s	3
PDMS+FN+HUVEC	Stainless Steel	0 mm/s	3
PDMS+FN+HUVEC	PTFE	0 mm/s	3

Table 5.1: Experiment overview

5.3.4 Damage Assessment

After indentation testing, the staining and imaging protocols were applied unchanged to how they were after friction experiments. However, the damage was assessed in a different way than it was with friction experiments. The centre of the indentation was calculated automatically based on the red nuclei in the image. Then the distance of all dead and healthy cells was calculated and presented as a histogram. This makes it easy to see where cell death and removal occured. The protocol is described in detail in Section 3.12.5.

5.4 Results

5.4.1 Probe Surface Roughness Measurements

The probe roughness was tested for 11 new spheres of each tested material with the Alicona. Each probe was 3D scanned and projected to a flat surface (spherical form removed) and a measurement line was defined across the probe as seen in Figure 5.2. The surface geometry parameters Ra, Rq and Rz which were measured in this fashion are plotted for all three probe materials in Figure 5.3. All of them reflect the roughness of the surface, but they differ in their definition. Despite the absolute values of Ra, Rq and Rz differing by a large amount,

all of them show the same trend. PTFE is the smoothest of all the materials, followed closely by stainless steel. Glass spheres had by far the roughest surface and also showed the largest standard deviation. The absolute values for all materials and surface roughness types with standard deviations are shown in Table 5.2. For context, the roughness of stainless steel and PTFE probes is fairly low, i.e. the surface finish is smooth and comparable to what would be present after grinding and a bit rougher than honing [133]. The glass probe's surface finishes were more in the region of milling [133]. Ra, Rq and Rz are reported. Ra gives the arithmetic average of the profile height from the mean line. Rq gives the quadratic average of said profile height and hence highlights larger deviations from the average line. Rz gives the maximum peak to valley height. Ra is a general measurement of surface roughness, while the other two focus on the peaks and valleys of the asperities on a surface and may hence give an idea of how spikey a surface is.

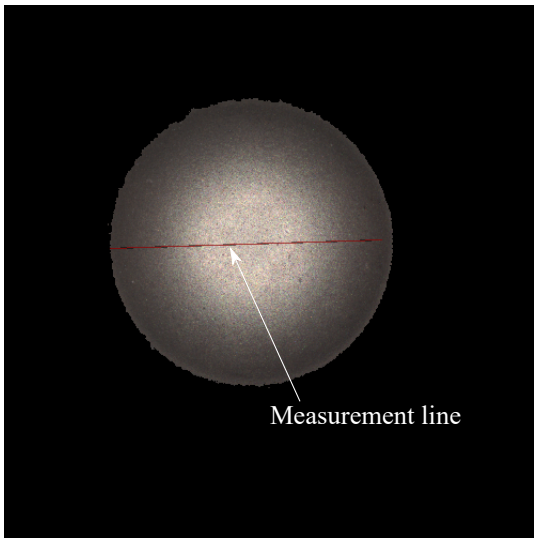

Figure 5.2: Surface roughness measurement of a stainless steel probe along the red measurement line marked in the picture.

Material	Ra [µm]	Rq [µm]	Rz [µm]
Glass	1.571 ± 0.525	2.291 ± 0.938	9.156 ± 3.488
Stainless steel	0.683 ± 0.05	0.867 ± 0.065	4.022 ± 0.33
PTFE	0.577 ± 0.159	0.762 ± 0.27	2.871 ± 0.796

Table 5.2: Surface roughness values.

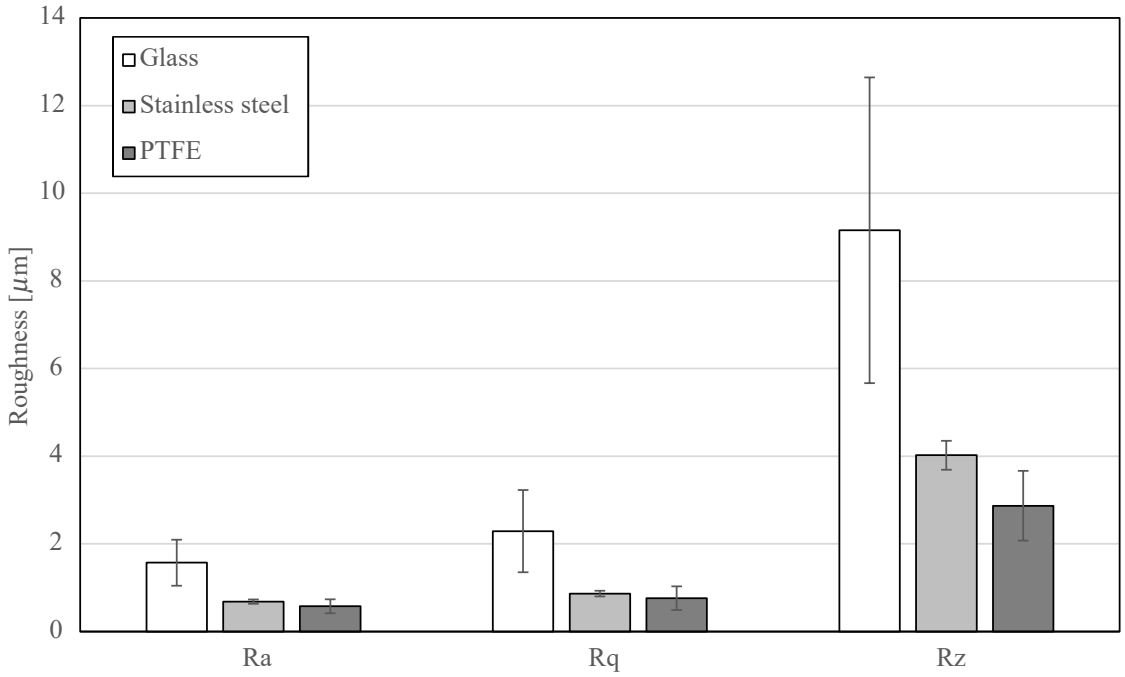

Figure 5.3: Probe surface roughness parameters Ra, Rq and Rz for glass, stainless steel and PTFE spheres.

5.4.2 Damage to the Monolayer

From the red and blue channel images, a dataset was generated for each individual indentation. This dataset contained two lists of the distances of each individual nucleus to the respective indentation centre, one for the red ones and one for the blue ones.

The lists of distances were discretised and plotted as a histogram. Such a histogram for one repeat and the respective blue and red channel images are shown in Figure 5.4. The data is from the fifth indentation with a glass probe and a normal force of 10 mN which was one of the least invasive conditions tested. As such it comes the closest to what would be expected if no indentation was executed.

For each bin, nuclei within a specific area are counted. This area is the one of a ring and can hence be calculated with:

$$A = \pi r_o^2 - \pi r_i^2 = \pi(r_o^2 - r_i^2) \tag{5.1}$$

with its inner radius r_i and its outer radius r_o. These radii correspond to the lower and higher edges of the bin, respectively. As the width of each bin is fixed to t = 25 µm, this can be written as:

$$\begin{aligned} A &= \pi(r_o^2 - r_i^2) = \pi((r_i + t)^2 - r_i^2) = \pi(r_i^2 + 2tr_i + t^2 - r_i^2) \\ &= \pi(2tr_i + t^2) \end{aligned} \tag{5.2}$$

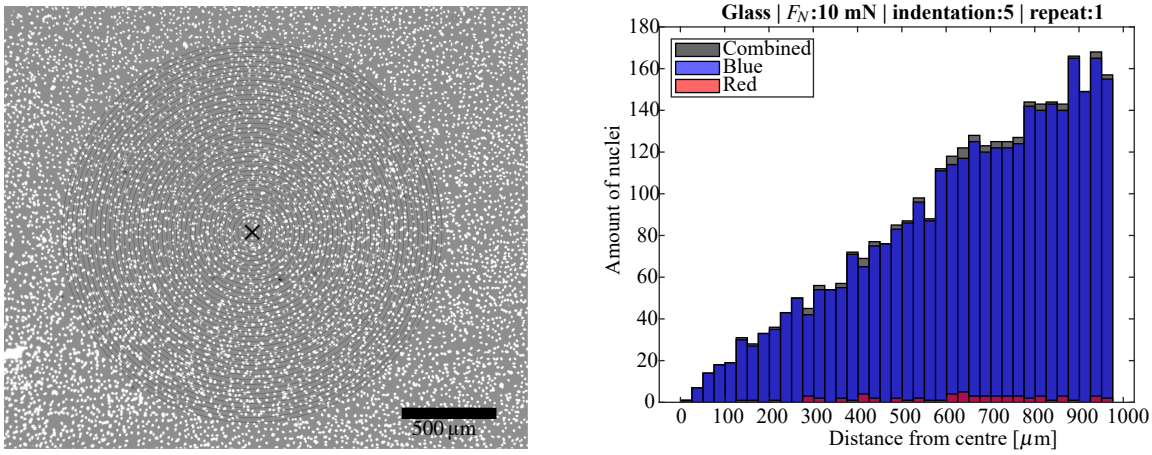

(a) Red and blue channel images **(b)** Histogram

Figure 5.4: Red and blue channel images **(a)** and histogram **(b)** for a fifth 10 mN indentation with a glass probe. Version with blue/red channel images in colour can be found in Appendix C.5

with $r_o = r_i + t$. Then, because bin number i and lower bin edge r_i are related through bin width t with $r_i = ti$:

$$\begin{aligned} A &= \pi(2t(ti) + t^2) \\ &= \pi(2t^2 i + t^2) \\ &= \pi t^2(2i + 1) \end{aligned} \tag{5.3}$$

which shows that the area covered by the bins increases linearly with bin number. This means that if there was no indentation, i.e. no cells are removed, the amount of cells should increase linearly with bin number i, given an even distribution of cells. This expected behaviour is confirmed within natural variances of nuclei densities as seen in Figure 5.4b in particular, and was generally observed for all testing conditions that were only slightly invasive. Apart from differences in nuclei densities, reasons for variances from this predicted pattern are: slight mispositioning of the centre point, and the narrow discretisation size (bin width t).

For harsher testing conditions, i.e. higher normal forces, lower indentation numbers, and PTFE probes, the linear trend was still observed, but a portion of the cells were dead. Such a test is shown in Figure 5.5 for the first indentation with a stainless steel probe and a normal force of 10 mN, constituting a lower indentation number. The healthy (blue) nuclei count experiences a dip, whereas the dead (red) count peaks at around 275 µm-375 µm. The linear increase in nuclei count that was observed before is still valid; however, this is now the case for the combined count only. This indicates that almost all cells remained on the surface, but some of them suffered death.

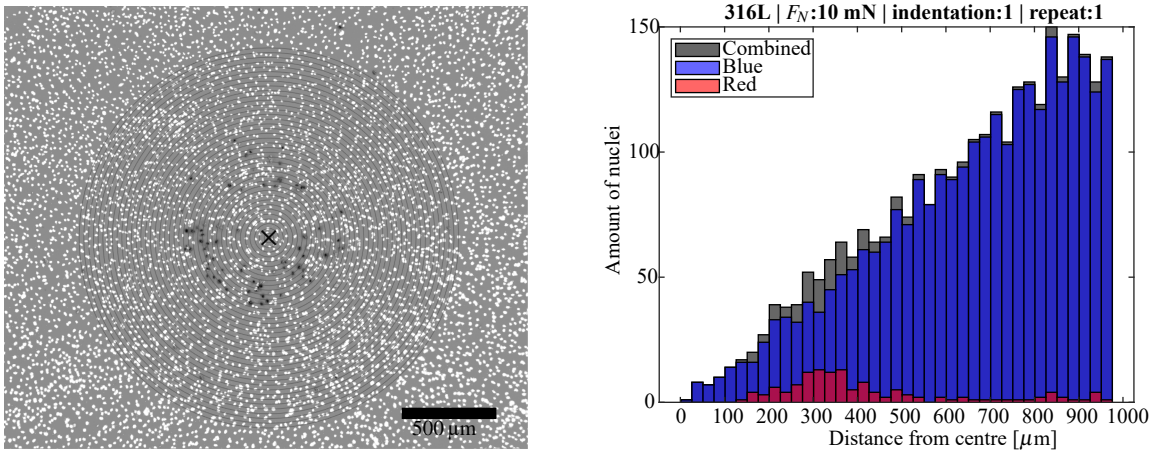

(a) Red and blue channel images **(b)** Histogram

Figure 5.5: Red and blue channel images **(a)** and histogram **(b)** for a first 10 mN indentation with a stainless steel probe. Version with blue/red channel images in colour can be found in Appendix C.6

As testing conditions become even harsher, a larger and larger portion of dead cells show up, with some areas of complete cell removal. For example, for the first indentations with 10 mN for PTFE probes, or 40 mN with stainless steel probes. The indentation test with 10 mN for a PTFE probe is shown in Figure 5.6. There is a large area and some smaller ones of removed cells. A large portion of cells has also been killed. It is noticable that the cell death and cell removal occurs mainly in the marked distance range of 125 µm-450 µm from the centre point. This is reflected in the histogram, where this range is also marked. The area in the centre of the indentation is largely unharmed. The indentation test with a stainless steel probe and a load of 40 mN is shown in Figure 5.7. After this indentation, areas of removed cells are apparent. The damaged area is larger, which is due to the higher normal load and hence larger contact area. A dip in cell count is very noticable in the histogram and has been marked in the indentation image.

For the harshest of load conditions, which were the first indentations of 80 mN tests with PTFE probes, the severity of the interaction is even more obvious. The respective data is shown in Figure 5.8. In the image, large portions of the monolayer were removed and, of the cells that remained, many were killed. This can also be seen in the histogram, where the amount of remaining cells stays constantly low up to around 600 µm. After that, more and more cells remain and survive closer to the edge of the indentation. In this histogram, the trend does not resemble a linear relation between amount of nuclei and distance to the centre anymore, indicating severe damage.

A trend that emerged for subsequent indentations was that the damage to the monolayer decreased with increasing indentation number. As examples, the data of two subsequent indentations executed after the one shown in Figure 5.8 is presented. Figure 5.9 shows the

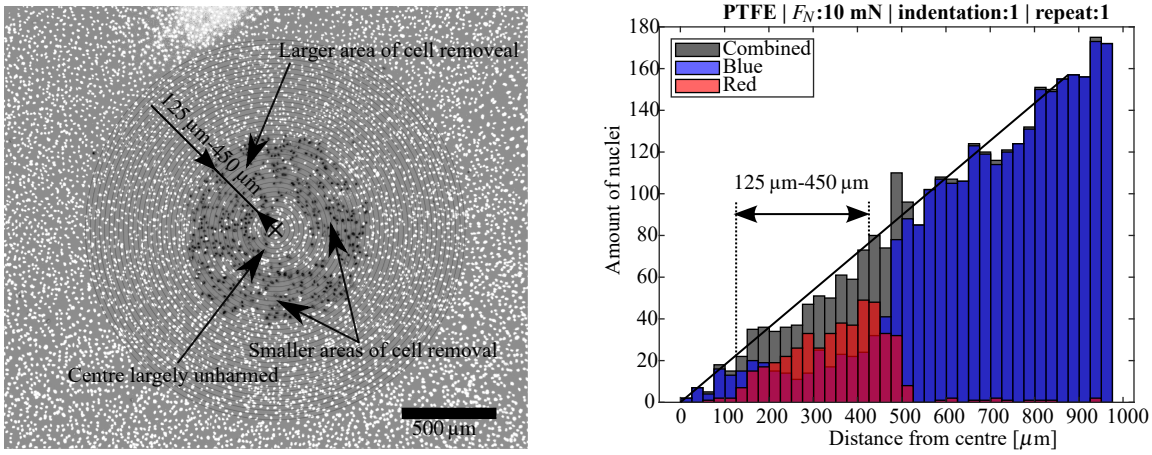

(a) Red and blue channel images **(b)** Histogram

Figure 5.6: Red and blue channel images **(a)** and histogram **(b)** for a first 10 mN indentation with a PTFE probe. Version with blue/red channel images in colour can be found in Appendix C.7

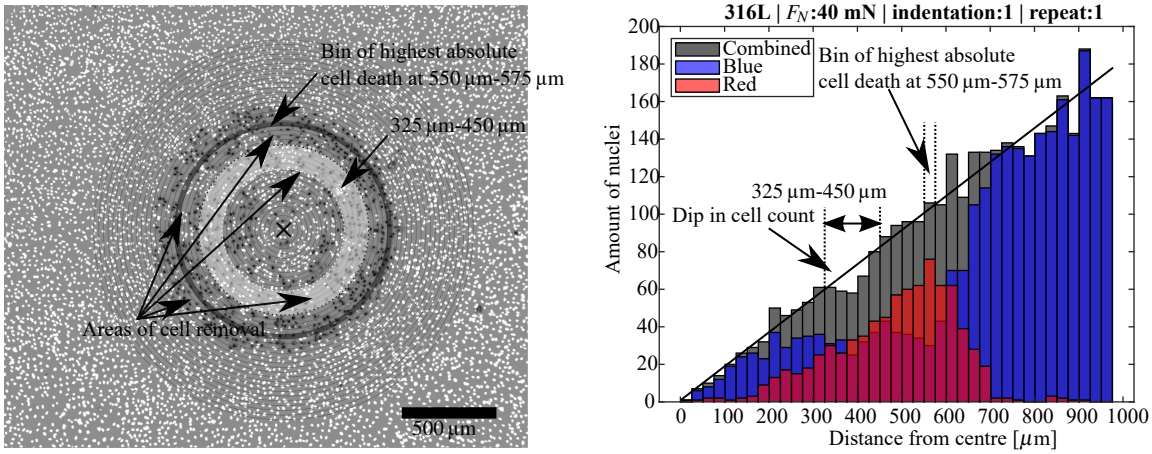

(a) Red and blue channel images **(b)** Histogram

Figure 5.7: Red and blue channel images **(a)** and histogram **(b)** for a first 40 mN indentation with a stainless steel probe. Version with blue/red channel images in colour can be found in Appendix C.8

indentation site at the second indentation. This is the indentation executed directly after the one shown in Figure 5.8. The damage inflicted to the monolayer is still very high, however, it is noticable that far less cells were removed during this indentation. Also, more healthy cells were detected and the trend of total amount of cells as a function of distance to the centre is closer to a linear relation. The data of the fifth indentation of this repeat is shown in Figure 5.10. The amount of healthy cells has not increased significantly, but the area of cell removal has decreased again, causing the trend in the histogram to converge to a linear relation even further, mainly in the range up to 250 µm.

As mentioned in Section 5.3, for each load condition the experiment was repeated three times and images were taken. A dataset was generated for each individual indentation. The

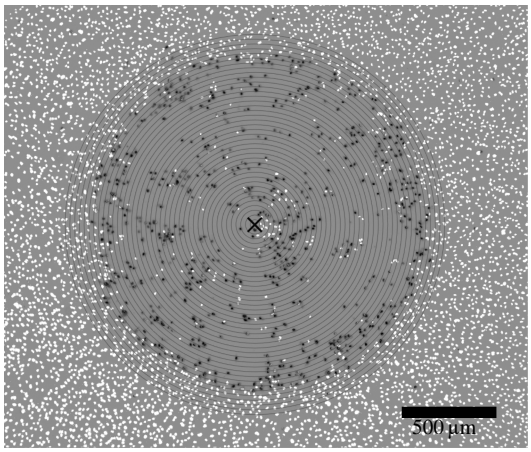

(a) Red and blue channel images

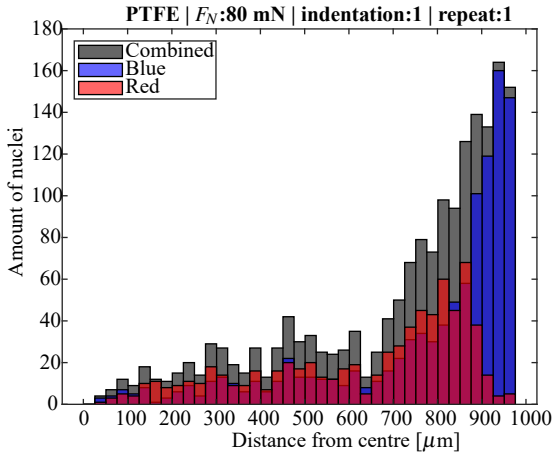

(b) Histogram

Figure 5.8: Red and blue channel images **(a)** and histogram **(b)** for a first 80 mN indentation with a PTFE probe. Version with blue/red channel images in colour can be found in Appendix C.9

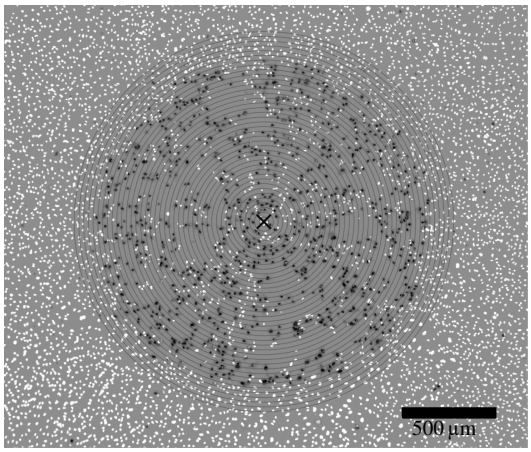

(a) Red and blue channel images

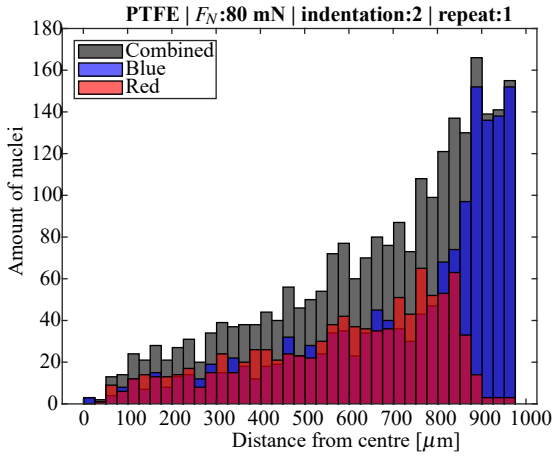

(b) Histogram

Figure 5.9: Red and blue channel images **(a)** and histogram **(b)** for a second 80 mN indentation with a PTFE probe. Version with blue/red channel images in colour can be found in Appendix C.10

results of these repeats were collated for each respective test condition and indentation number by joining the distance vectors of red and blue nuclei of each image allowing plotting of one histogram plot for each condition.

In Figure 5.11, all histograms that were generated for indentations with glass spheres are plotted and a schematic of a sample used for indentation is shown. The figure is a miniature and is there to show how the data can be read. The full-scale version of this figure can be found in Figure 5.12. Each histogram contains the data of three repeats; therefore, the counts are around triple of what they are for single indentation histograms. Each row in the histogram plot stands for one normal force and columns 1 to 5 stand for the first to fifth indentation within an indentation run/repeat as indicated in the figure. The data is plotted

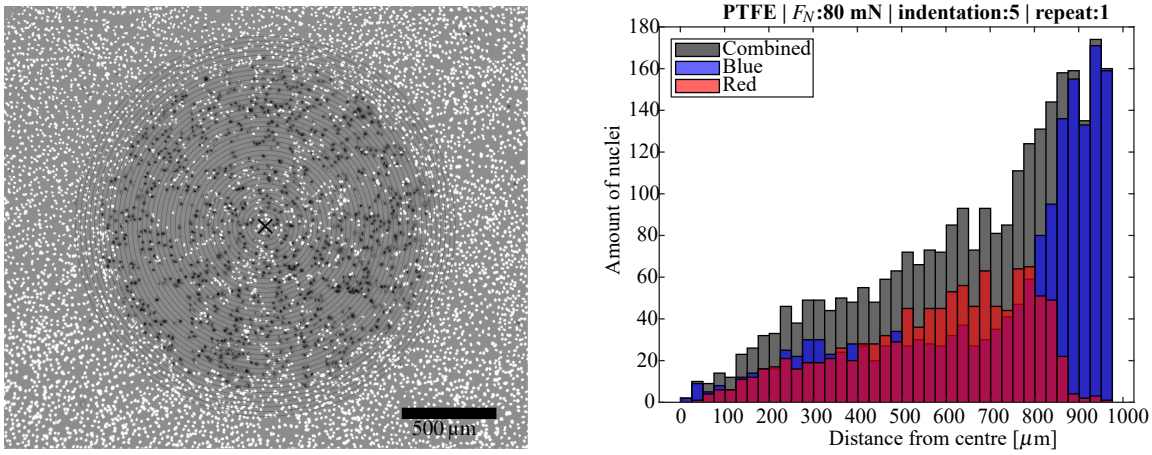

(a) Red and blue channel images **(b)** Histogram

Figure 5.10: Red and blue channel images **(a)** and histogram **(b)** for a fifth 80 mN indentation with a PTFE probe. Version with blue/red channel images in colour can be found in Appendix C.11

using this notation in full-size in Figure 5.12, Figure 5.13 and Figure 5.14 for glass, stainless steel and PTFE, respectively.

These collated figures make it easier to look at trends in the data. For all materials, an increase in normal force causes an increase in damage to the monolayer and also a larger damaged area. Furthermore, consecutive indentations are never more invasive than the previous one: the damage seems to converge after enough indentations with the same probe were executed for some testing conditions, but generally it does not increase. Examples for the damage stabilising are 10 mN and 20 mN tests with glass probes and 10 mN tests with stainless steel probes. 20 mN tests with stainless steel probes may be converging from the fourth indentation onwards, but more consecutive indentations would be required to confirm this.

While the decrease in damage for consecutive indentations is shared among all materials tested, they differ in terms of quantitative damage to the monolayer. For first indentations, glass and stainless steel are almost the same in terms of damage, with stainless steel having the edge, especially for 10 mN and 20 mN. When looking at the subsequent indentations, however, this changes and glass starts to cause noticably less damage than stainless steel does. This can be seen for the whole range of normal forces, but is especially obvious for 10 mN and 20 mN of normal force, for which glass probes inflicted virtually no damage to the monolayer from the second and fourth indents onwards, while stainless steel probes still left behind a substantial amount of dead cells. Both of these materials, however, caused very little damage after the first indentation compared to PTFE. It is obvious that PTFE is by far the probe material that causes the most damage to the monolayer for any given load condition and indentation number. Although less damage is caused with consecutive in-

dentations with PTFE probes, the material also retains its damaging properties much longer than the other two materials. For 40 mN, the first indentation is very harmful, removing a large part of the monolayer in around 450 µm distance; for 80 mN tests with PTFE probes, the first indentation removed even more cells. For consecutive indentations, the damage decreased and shifted mainly towards destroying cells rather than fully removing them.

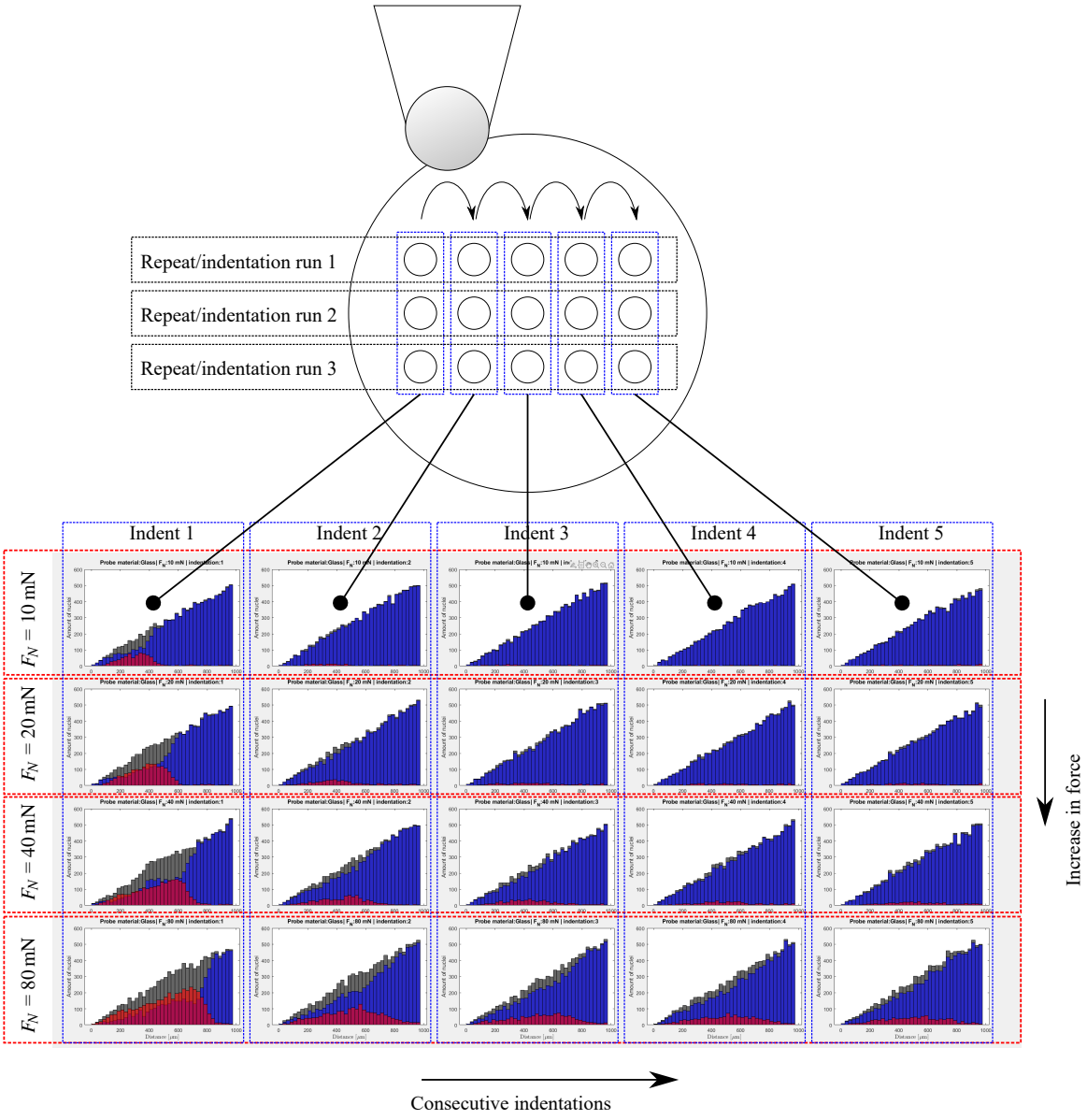

Figure 5.11: Schematic of how the histogram data of several indentations is presented. Full-scale version of the plot can be found in Figure 5.12

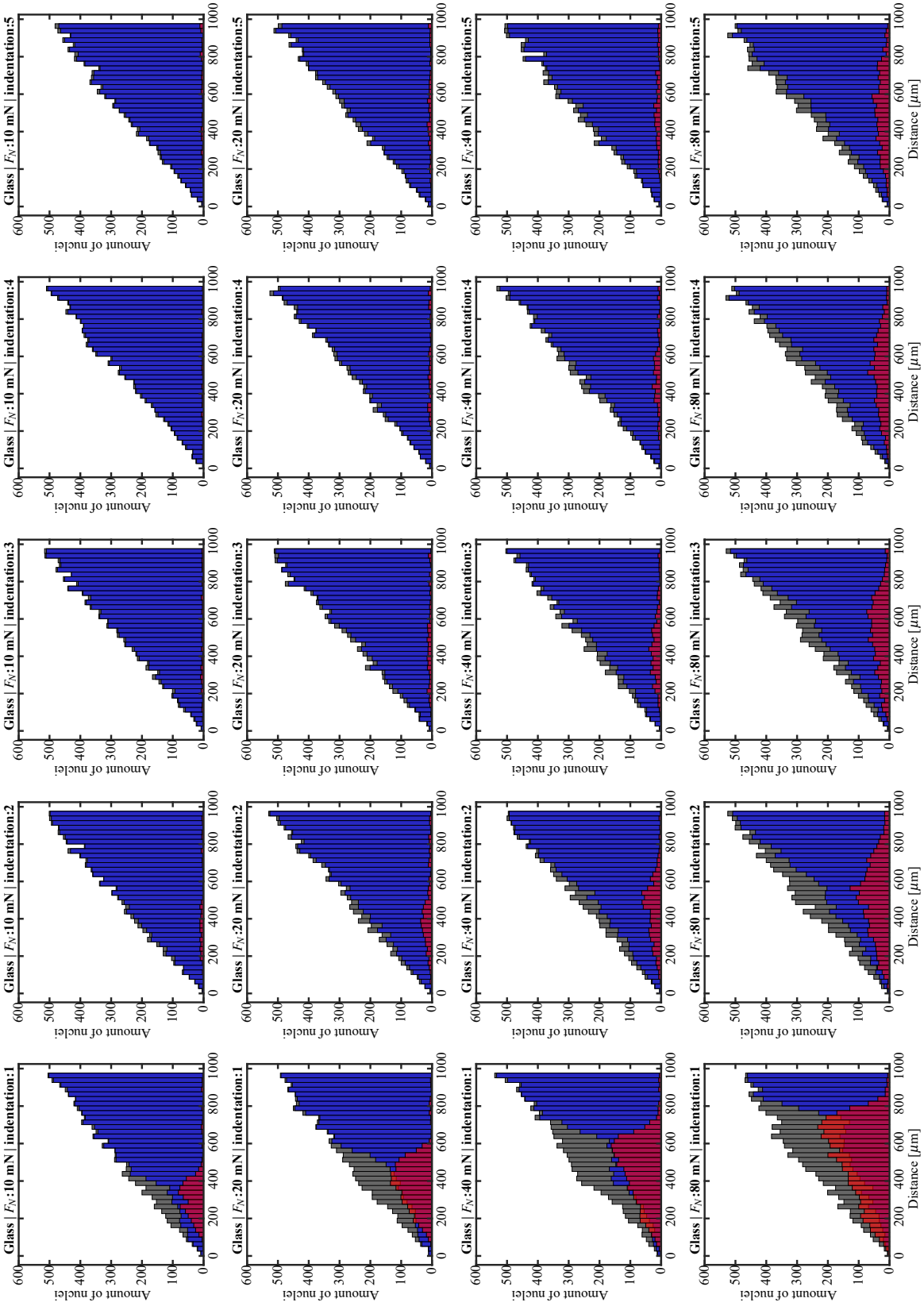

Figure 5.12: Damage after indentations with glass probes.

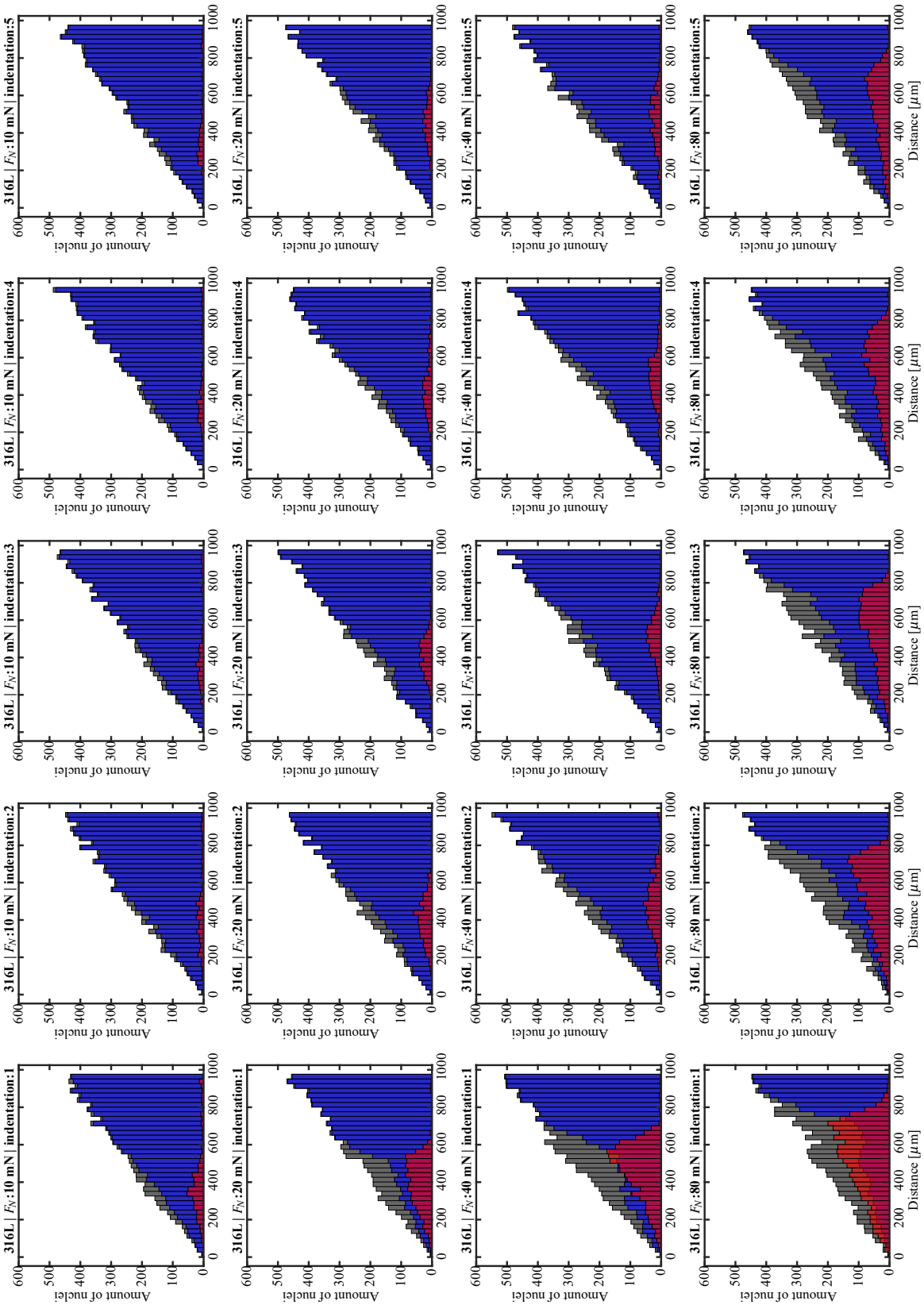

Figure 5.13: Damage after indentations with stainless steel probes.

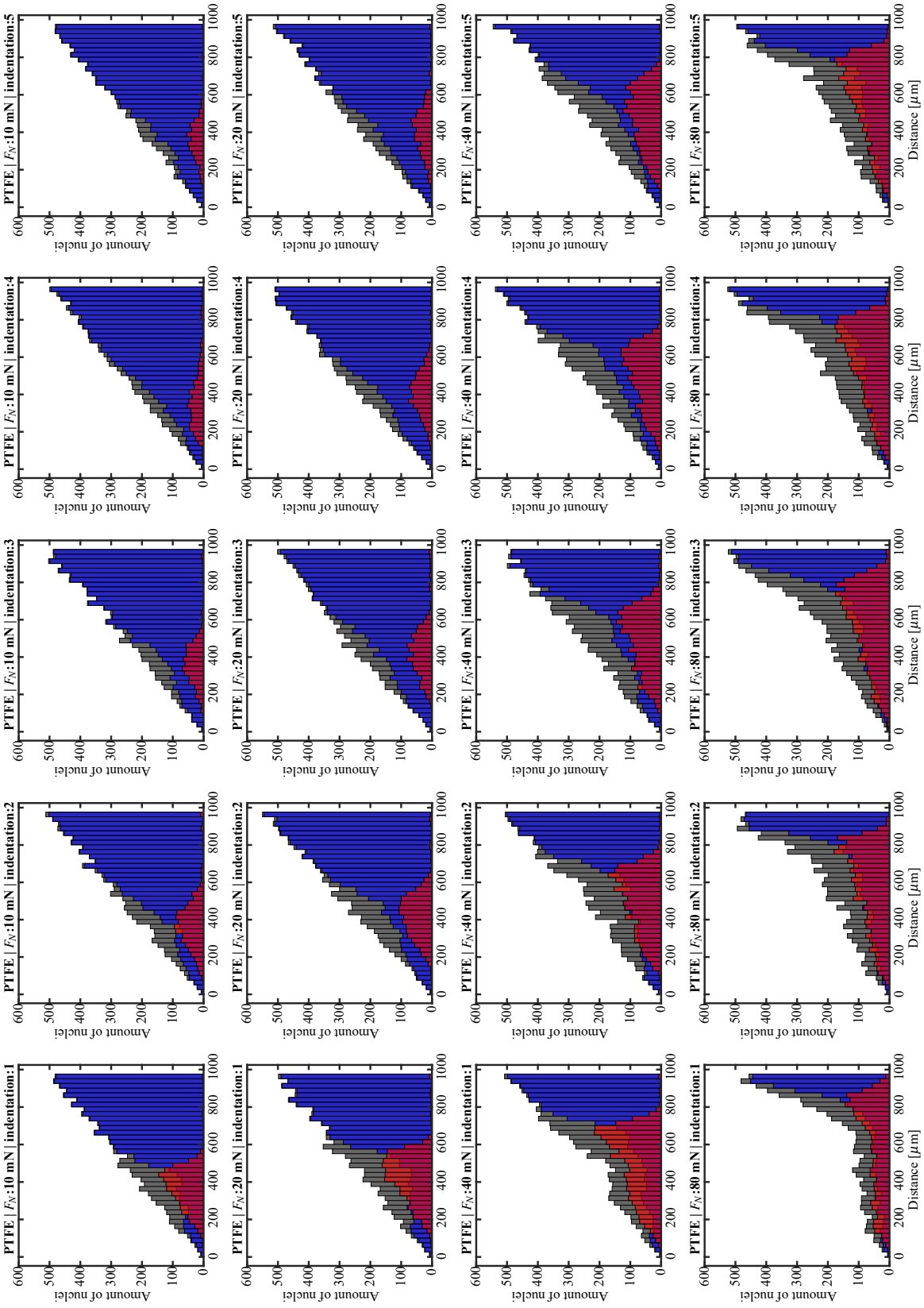

Figure 5.14: Damage after indentations with PTFE probes.

5.4.3 Indentation Depth and Reaction Force

The stage position and force data was recorded during the indentation tests and thus the indentation depth d and reaction force F_Z. Figure 5.15 shows d and F_Z in the time domain for a typical indentation experiment. This experiment was conducted with a PTFE probe for a normal force of 80 mN. The loading, holding and unloading phases can be clearly distinguished. As the stage moves down in the loading phase, the load increases, is then held constant at the specified force of 80 mN in the holding phase, and decreases in the unloading phase as the stage is moved up with a constant speed.

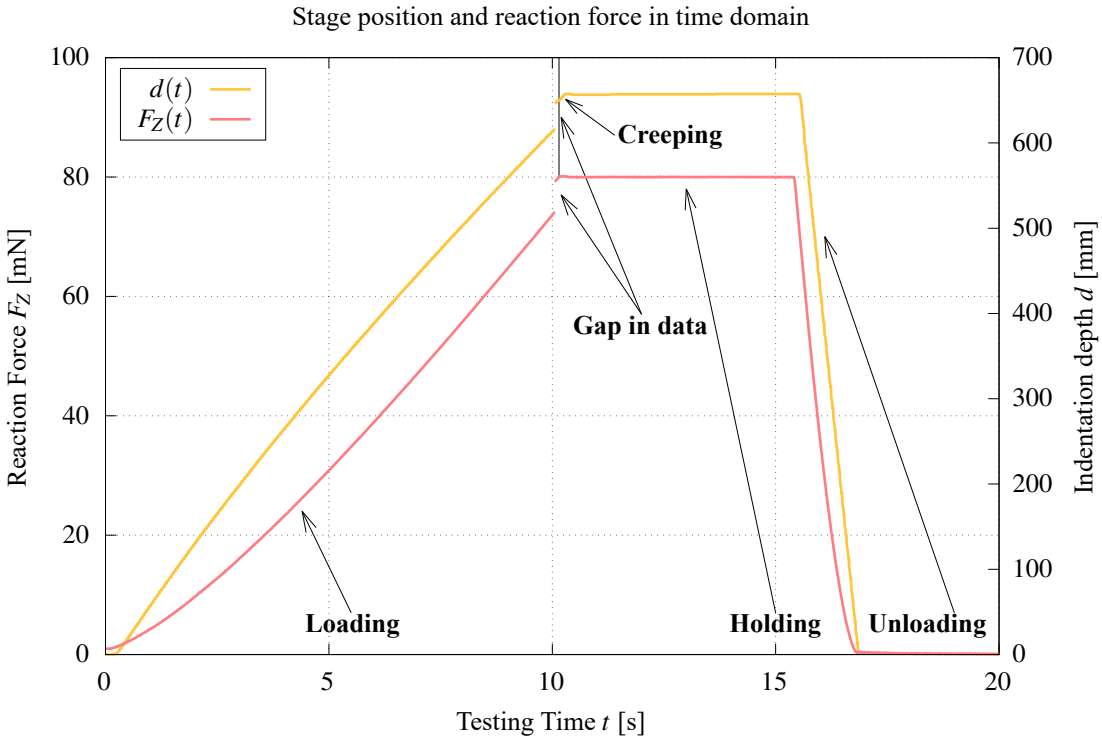

Figure 5.15: Indentation depth d and reaction force F_Z for an indentation with a PTFE probe in the time domain.

In order to study material parameters or the behaviour of the system as such, the reaction force can be plotted over the indentation depth. This allows comparison to time invariant models like Hertz. The data from Figure 5.15 is shown in this way in Figure 5.16; Figure 5.17 and Figure 5.18 show equivalent data for glass and stainless steel probes, respectively. In those figures, in addition to the measured data, the Hertzian model for the reaction force

$$F(d) = \frac{4}{3} E^* R^{1/2} d^{3/2} \tag{5.4}$$

with probe radius R, and reduced Young's modulus E^* is shown as a function of indentation depth d. The Hertzian model was plotted with an offset in indentation depth Δd because the

actual origin of this dimension is difficult to determine. This is because the UMT 2 only starts recording data when a contact force is detected, which was set to 1 mN. Therefore, the offset Δd in the model was chosen so model and measured force matched in the origin, at a reaction force of 1 mN, as per the experimental value at the start of the loading phase. The measured data from the three different phases is plotted in different colours.

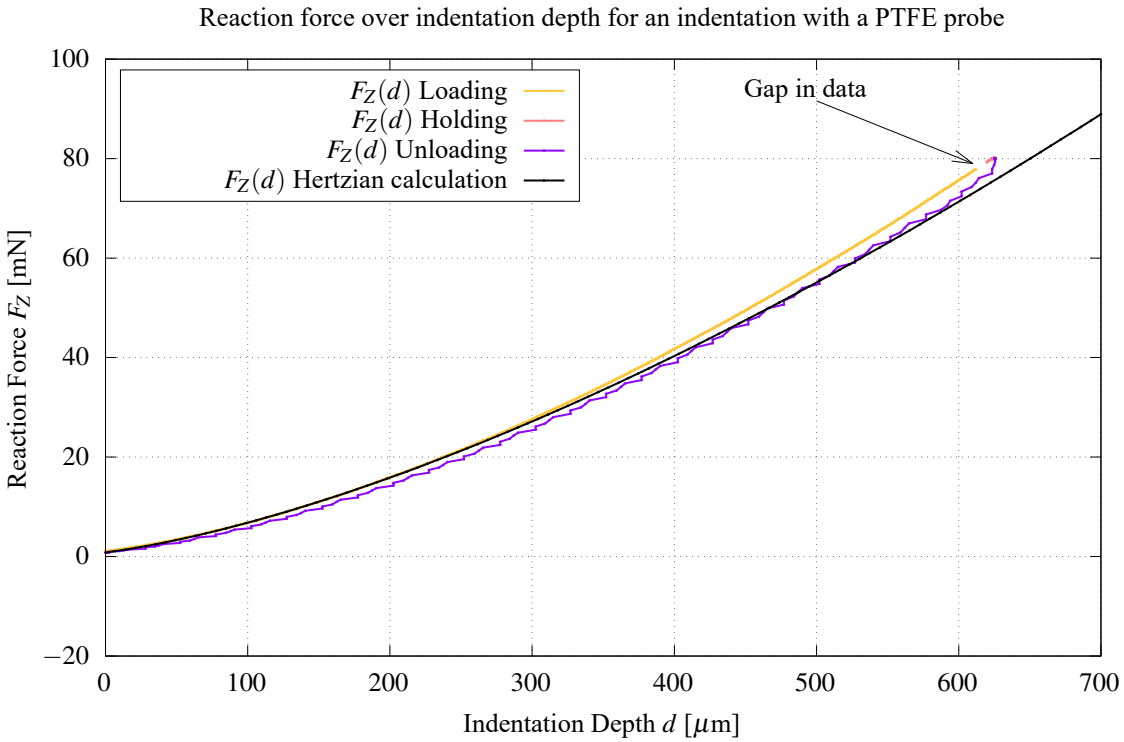

Figure 5.16: Reaction force F_Z over indentation depth d for an indentation with a PTFE probe.

Overall, for all probe materials, the measured reaction force during the loading phase is in good agreement with the Hertzian model up to an indentation depth of 300 µm or a reaction force of 35 mN, at which point the two start to diverge noticably. Another detail that shows up in all of these graphs, which can also be seen in the time domain, is that there is a gap between the loading and the unloading phase. This gap stems from the UMT 2, which has a user-specified phase time which was set to 10 s for the loading phase. The UMT 2 aims to linearly increase the force in this time and thus has to estimate how quickly it loads the sample. As the machine consistently needed slightly longer than it initially estimated, this meant that no data was recorded for a short period of time. However, the specified force was still reached as can be seen in the graph. Samples tested against PTFE probes were indented around 625 µm from the origin, while samples tested against glass and stainless steel probes were indented a bit deeper to around 660 µm.

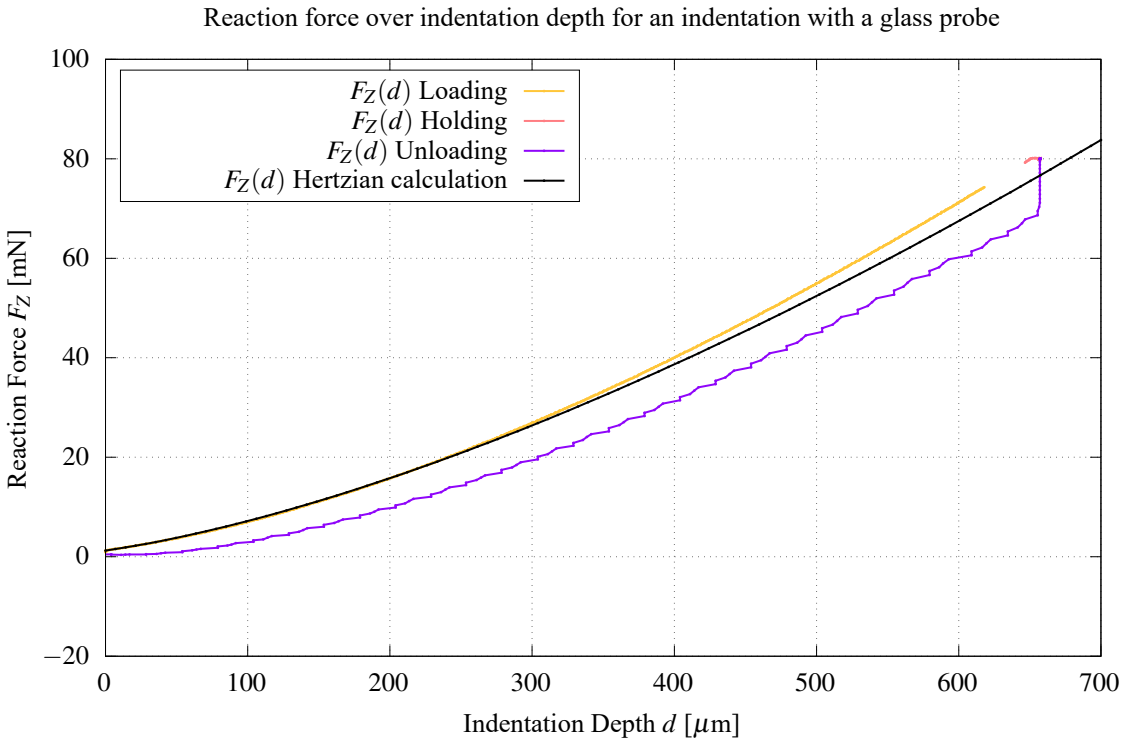

Figure 5.17: Reaction force F_Z over indentation depth d for an indentation with a glass probe.

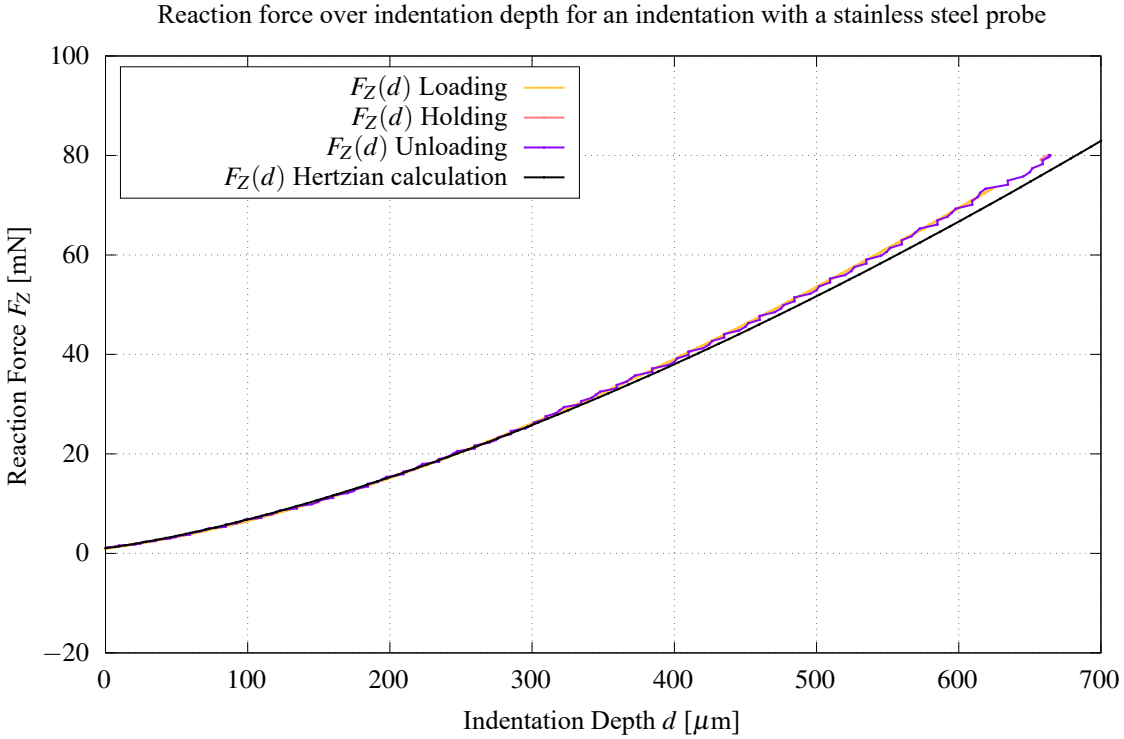

Figure 5.18: Reaction force F_Z over indentation depth d for an indentation with a stainless steel probe.

Another mutual characteristic of the graphs for glass and PTFE probes is that the reaction force during the unloading phase was consistently lower than it was during loading for any given indentation depth d. Where they varied is the extent of this feature. It is stronger for glass probes. The difference in reaction force ΔF_Z during loading and unloading was measured to be up to 10 mN. For PTFE probes, the effect is still very visible, but smaller with a ΔF_Z of up to 3 mN. For stainless steel probes, this property is barely noticable and can only be seen at all when zooming in. The reaction forces are the same during loading and unloading, with some very small dips during unloading. These trends were reproducible between repeats and did not vary noticably with indentation number.

5.5 Discussion and Conclusions

5.5.1 Damage to the Monolayer by Consecutive Indentations

In this chapter, an approach was presented to evaluate the damage due to different probe materials qualitatively. This complements the quantitative analysis from Chapter 4. One of the aims of this study was to test the same probe materials under a simplified load condition by essentially removing the sliding movement. Apart from different materials, changes in the interaction and damage could be examined. The results of this chapter confirmed that PTFE is a very harmful material when interacting with a HUVEC monolayer. Even without a quantitative analysis, it is clear that extensive portions of the monolayer were killed or destroyed. For this material, for lower forces, mainly cell death was detected, however, from 40 mN of normal force, interactions also presented significant rell removal. Glass and stainless steel were far less invasive than PTFE, causing mainly cell death even for higher forces.

Apart from confirming the “harmfulness ranking” of the materials from Chapter 4, the simplified load conditions of this experiment allowed additional observations. Firstly, probes of the same geometries and dimensions inflicted different amounts of damage (PTFE probes had a larger diameter, so exterted lower pressures, but caused more damage), implying that the damage is probe material-related. Secondly, consecutive indentations with the same probe made the interaction less and less damaging, again, implying that the damage is related to the probe material. This also suggests that previous interactions of a probe with cells influences how much damage that same probe causes in future indentations, which indicates lower adhesion of cells to the probe. Thirdly, the monolayer in the centre of the indentations was, in general, less damaged than the parts further away from it. This was the case for all materials, even PTFE. However, glass and stainless steel probes killed cells in the centre of the indentation for 80 mN.

The last observation may seem surprising at first because the pressure in the centre of the indentation should be the highest because that is where the substrate is deformed the most. However, pressure is not the only parameter that should be taken into consideration. Earlier, it was stated that one of the aims of this experiment was to test the interaction without relative movement. This was achieved by keeping the stage position fixed. However, as the substrate is very soft, the deformations and displacements when loading the material are large. Apart from deformations normal to the probe surface, which will occur to exert the reaction force, displacements will occur tangential to the probe surface. Due to the symmetry of the set up, tangential deformations and displacements cannot occur in the very centre of the indentation. Further out, however, the substrate will be stretched and thus also displaced relative to its initial contact position with the probe, which will cause displacement, i.e. relative movement between probe surface and substrate on a small scale. Due to this, it can be concluded that pressure alone, up to a certain extent, is not necessarily destructive. At some point, cells will be destroyed by pure pressure. This may be the reason why stainless steel and glass probes killed cells in the centre of the indentation, whereas PTFE probes, which exerted lower pressures due to their larger radius, left those cells unharmed, despite the indisputably higher inherent cell-damaging properties of the material. However, below this critical load, cells that experienced no, or a low amount of, relative movement stood unharmed.

As a conclusion, as input parameters, neither the probe material, nor pressure nor relative movement alone were sufficient to cause serious harm to the monolayer, as long as the pressure did not surpass a critical value. The following examplar load conditions A-H are listed in Table 5.3 and are marked up in respective histograms in Figure 5.19. If none of

Example	Pressure	Relative movement	Destructive probe material	Condition
A				10 mN - centre - glass, i=5
B			X	10 mN - centre - PTFE, i=1
C		X		10 mN - perimeter - glass, i=5
D	X			80 mN - centre - glass, i=5
E		X	X	10 mN - perimeter - PTFE, i=1
F	X	X		80 mN - perimeter - glass, i=5
G	X		X	80 mN - centre - PTFE, i=1
H	X	X	X	80 mN - perimeter - PTFE, i = 1

Table 5.3: Load condition examples with input parameters pressure, relative movement and probe material. An “X” indicates that the input parameter is in a potentially damaging range for the monolayer.

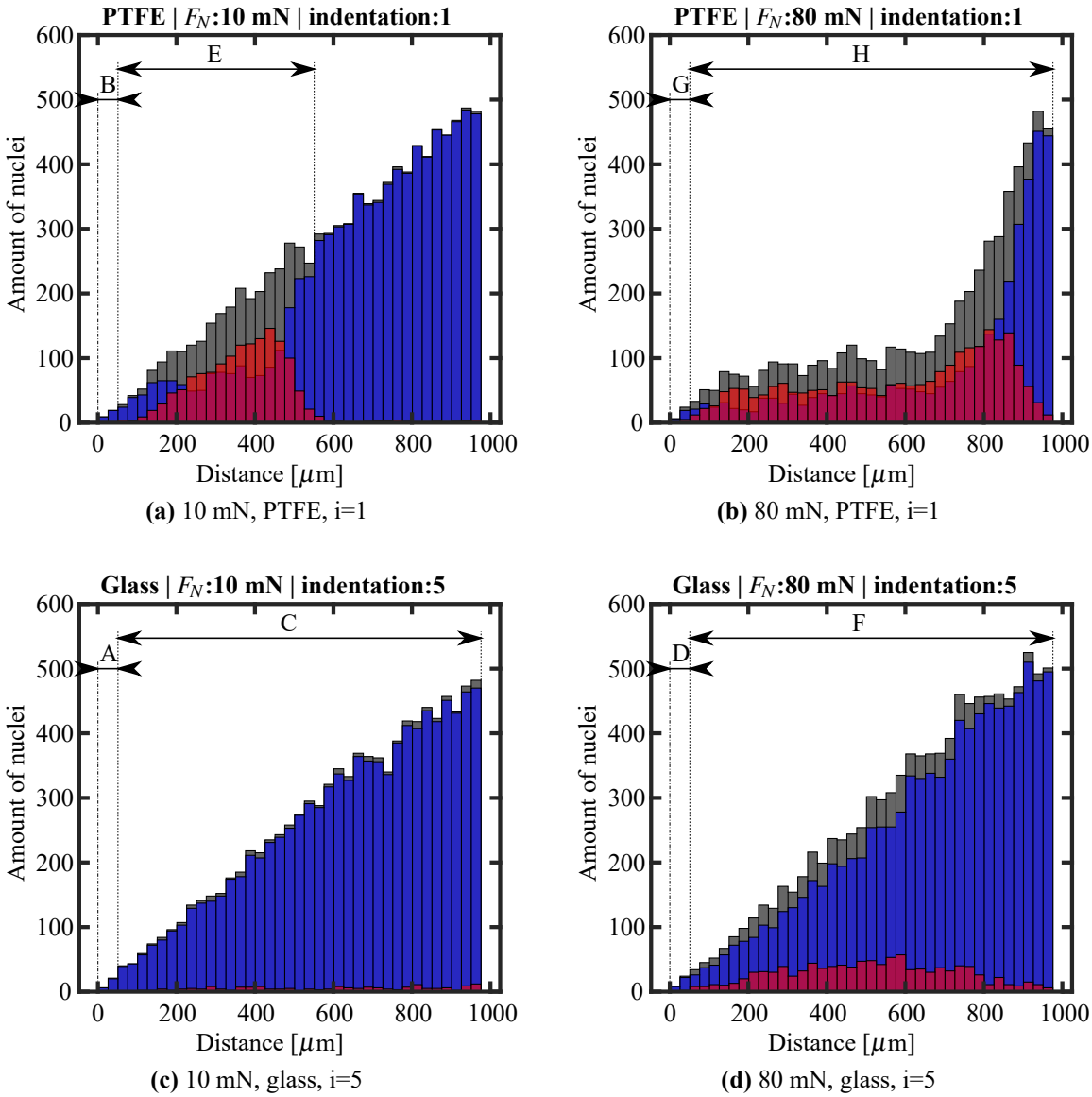

(a) 10 mN, PTFE, i=1 **(b)** 80 mN, PTFE, i=1

(c) 10 mN, glass, i=5 **(d)** 80 mN, glass, i=5

Figure 5.19: Examples for different load conditions A-H highlighted in histograms for 10 mN and 80 mN indentations with PTFE probes (**(a)** and **(b)**, respectively) and glass probes (**(c)** and **(d)**, respectively).

the parameters are critical, such as for cells in the centre of fifth indentations with a glass probe for a 10 mN load, the monolayer stayed completely unharmed (Example A). If one of these input parameters was critical, still no major damage was observed. PTFE, as the most harmful material in general, did not cause any damage in the centre of 10 mN indentations (Example B). Glass at its fifth indentation (the most harmless material) caused no significant damage for 10 mN loads for any distance outside of the centre (where relative displacement will occur) (Example C). In the centres of fifth 80 mN indentations with glass probes, there was also no major damage (Example D). If two of these three input parameters are critical, serious damage to the monolayer occurs. PTFE, as a destructive probe

material, caused much harm, killing many cells further out from the centre even for low loads at 10 mN (Example E). High pressures and relative movement (at locations further out from the indentation centre) caused damage even for glass on the fifth indentation, the material that was generally the least harmful (Example F). Finally, PTFE probes were not able to kill cells at a high pressure if no relative movement was introduced (at the centre of an indentation) (Example G). If, however, all three input parameters are destructive, the monolayer suffers heavy damage. The most prominent example for this are monolayers indented with PTFE probes loaded with 80 mN of normal force outside of the centre of the indentation (Example H).

5.5.2 Reaction Force and Hertzian Model

Throughout this work, the Hertzian contact theory was used to approximate the contact. This was done deliberately despite almost all of the assumptions of this model being violated. The main ones are as follows: firstly, only small strains should occur and the deformations should be within the elastic limit; secondly, the contact area must be small compared to the characteristic dimensions of the bodies (the radius of the sphere); thirdly, the interaction should be frictionless, and, finally, Hertzian contact theory does not account for adhesion. The former of these assumptions are violated simply because the deformations are too large which is due to the soft substrate. The third assumption is violated in the case of any real contact to some extent, but the violation in this case could arguably be relatively small because the friction is very low, even for PTFE. Finally, there will be adhesive effects.

However, the main contributor to the differences for higher normal forces may lie in deep indentation of the material. As mentioned, from 1 mN to 80 mN, the stage was lowered by 625 µm and 660 µm, respectively. Up to around 250 µm, the Hertzian model is in good agreement, despite large deformations already occuring. As the indentation depths are so large, at some point there may be an influence of the underlying material. As the glass is significantly stiffer than the PDMS, if indenting deeper and deeper, the underlying glass may play more and more of a role in the response of the mechanical system.

There are ways to counter these issues. More advanced models have been developed to account for adhesion, like the JKR or the DMT model. Multi-layered systems have been modelled before, for example by Mcguiggan et al. [134] with Hertzian and JKR approaches. However, this requires knowledge about additional parameters, namely the surface free energy of the the materials. Measuring the surface free energy is fairly straightforward given the required equipment and specimen are present. The parameter can either be measured or

simply extracted from a textbook for all probe materials. Measuring it on live cells, however, may be difficult. Prokopovich et al. have measured the surface free energy parameters of lamb aorta and vena cava after drying the specimens, so in principle, acquiring information on the required properties is possible [64]. It is something that could be tried in the future for the *in vitro* samples. It should be noted however, that in their work, the samples had to be dried in order to obtain a stable contact angle [64], which could change the surface, for example by cells detaching. Even if a way was found to measure the required parameters on an intact monolayer, it was demonstrated in the experiments in this chapter and in Chapter 4 that the monolayer changes when interacting with the probe as it becomes damaged, which could change the surface free energy. Finally, apart from the adhesion, the other assumptions, especially small deformations, which are violated, still apply for the more advanced theories and the standard models.

As a conclusion, modelling of the contact geometry could help in order to gain a more accurate insight into the load conditions. For modelling the mechanical system, a multilayered JKR approach as used by Mcguiggan et al. [134], and surface free energy parameters measured according to the protocol of Prokopovich et al. [64] could be used. Another option is finite element analysis which could describe the experiment with great accuracy. Such a model could also overcome the issue of the large deformations and elasticity constraints which the JKR model bears. However, for either of these models to give an accurate representation, the change in surface due to cell death and removal would have to be modelled first, in some form. For the experiments in this work, the Hertzian approach was very accurate up to 35 mN of normal force. For loads higher than that, the indentation depth was overestimated. For a given, sufficiently large indentation depth, the experimental reaction force was noticably higher than expected by the Hertzian model, which likely resulted in an underestimated contact pressure.

5.5.3 Hysteresis and Friction

In Figure 5.16, Figure 5.17 and Figure 5.18, representative force versus indentation depth curves were presented for PTFE, glass and stainless steel, respectively. In the 80 mN graphs for PTFE and glass probes, it was observed that the measured reaction force was different during loading and unloading for a given indentation depth. This effect was most noticable with glass probes, which is why data of these is presented and discussed here as examples. However, the PTFE graphs exhibited the same features, just less pronounced. Figure 5.20 shows the indentation data as force versus indentation depth curve with additional annotations and the stage in four distinct positions. As such, the reaction force F_Z is plotted as a

function of indentation depth d. Now per definition of work as:

$$\mathrm{d}W = F \times \mathrm{d}d \tag{5.5}$$

$$W = \int F \,\mathrm{d}d \tag{5.6}$$

the area under each curve in one of these diagrams corresponds to an energy.

Hence, during loading, the mechanical tester does work on the substrate by deforming it. Position A (not to be confused with Detail A) marks the position where the UMT 2 has detected a touch force, i.e. the probe is in contact with the substrate. This position was chosen as the origin for d. The force origin was defined before by zeroing the load cell. Some of this work goes into elastic deformation, which can be partially retrieved from the system; some dissipates due to viscoelastic effects. The latter cannot be retrieved as it is converted into heat (another form of energy). As a full cycle is performed, it is possible to calculate how much energy dissipated. This energy is sometimes referred to as hysteresis area and is defined by the difference between the (full) loading and unloading curves. In the case here, the full loading curve is defined as loading+holding in order to obtain a closed cycle. The cycle is closed by connecting the end of the loading and beginning of holding phase with a straight line as shown in the Detail A in the force indentation graph in Figure 5.20. Doing this allows graphical (with Inkscape) or numerical (with MATLAB) determination of the area between the curves which corresponds to the dissipated energy W_d. In this case, W_d was determined graphically as 4867 nJ which was very reproducible throughout the repeats and also did not change much with indentation number, which was tested numerically with MATLAB.

In Detail A, in Figure 5.20, the area where the specified load is reached is shown in detail. During the loading phase (which was recorded as part of the holding phase due to recording timeouts), after the specified load is reached in Position B, the force is constant (as this is a force-controlled step). However, to keep that constant reaction force of $F_{Z,spec}$ = 80 mN, the UMT 2 is lowering the stage by Δd_c, meaning the material is creeping.

This happens until equilibrium is reached in Position C. In the respective schematic, $d(F_Z = F_{Z,spec})$ and Δd_c are marked up. The creeping effect did not take long, which was checked in the time domain, meaning that the reaction force at the end of the holding cycle has reached equilibrium, i.e. is time invariant. Until it reaches equilibrium, however, the response of the mechanical system is time-variant, which is an effect often observed with materials which possess viscoelastic properties. The viscoelasticity of the substrate is symbolised here with a spring and dashpot in parallel (also called a Kelvin-Voight element) which seems a more accurate representation of the system than a spring and dashpot in series (a Maxwell element) because there is a constant long-term response, however, other

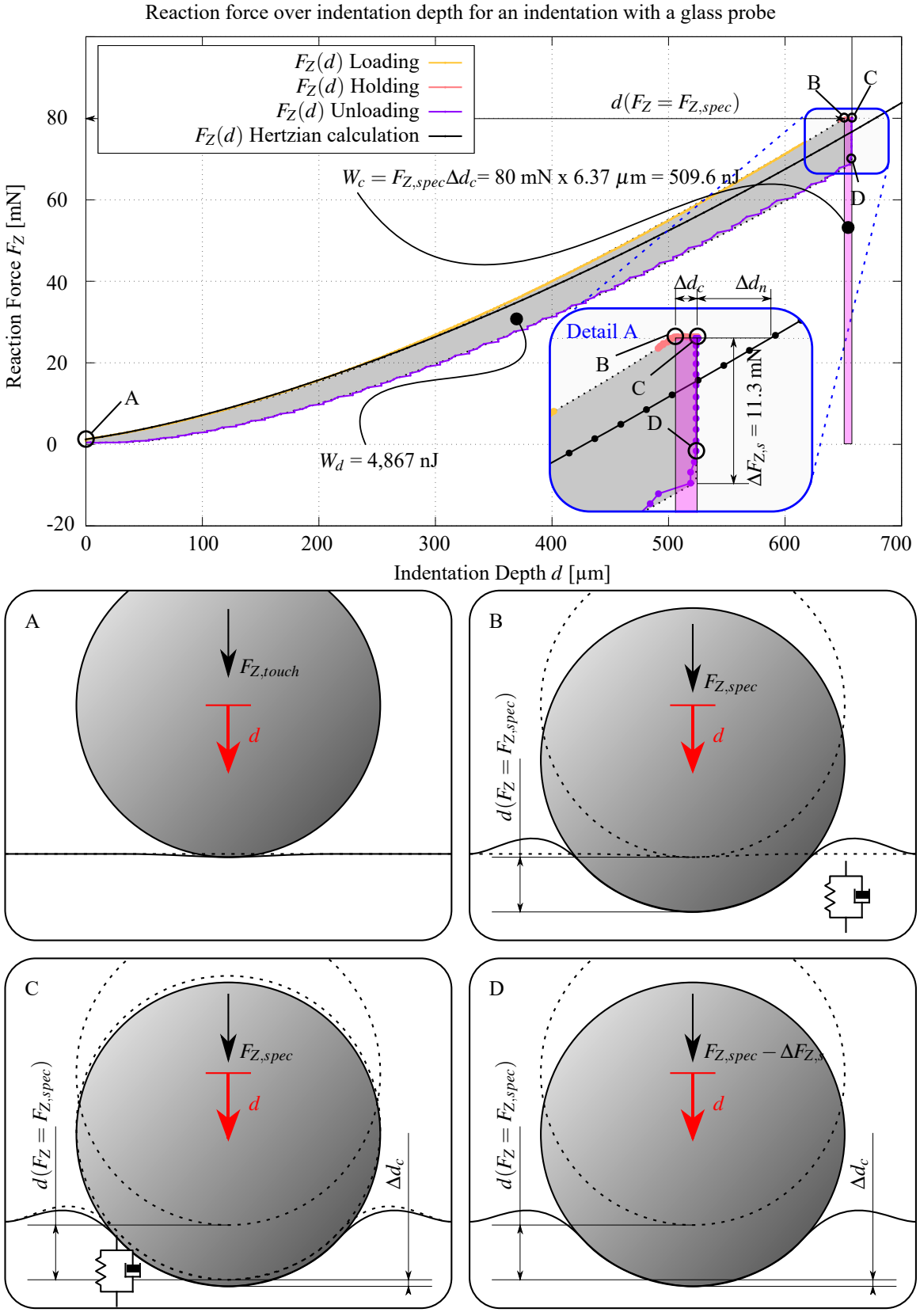

Figure 5.20: Reaction force F_Z over indentation depth d for an indentation with a PTFE probe with annotations.

viscoelastic models may describe the system more accurately. At any rate, the energy that is going into the creeping W_c can be calculated. In this case, due to the constant force, the integral is equivalent to the surface area of a square with $W_c = F_{Z,spec}\Delta d_c$, which equates to 509.6 nJ and is marked up in the figure. Another distance is marked up in Detail A, which is the residual, time-invariant difference between the Hertzian solution and the measured result Δd_n. As such, the differences to the model due to viscoelastic effects (time-variant) and nonlinear elastic and inelastic effects (large deformations and hard substrate) can be distinguished.

After the probe has reached equilibrium in reaction force and indentation depth (Position C), the unloading step begins. Soon after this phase starts, the reaction force breaks down as it reduces by $\Delta F_{Z,s}$, which in this case is 11.3 mN, and the probe is in Position D. In the transition phase $\bar{CD}$, almost no work is done on the probe because the probe moved almost no distance. After that, d decreases slightly as the force drops further and then the unloading cycle commences which is dominated sudden changes in the measured normal force which may be due to sticking and slipping on the interface.

These aforementioned features are less pronounced for PTFE probes and were not observed to any significant extent for stainless steel probes. An explanation for this not immediately obvious. Two reasonable explanations are palpable. The first one is that the work is dissipated while deforming the substrate. This would be classic hysteresis. It could be argued that the polymer chains in the PDMS are moving relative to each other and are hence rearranged as the material is deformed. This relative motion and friction on a molecular level could lead to energy losses (loss as in work converted into heat) on a macroscopic level. The work is certainly converted into deformation of the substrate, that is clear from the diagram. However, it is not clear what portion of it is recoverable due to deformation within the elastic range. Indeed, Efremov et al. [135] recently simulated a range of viscoelastic material models under a variety of load conditions and their results for a spherical indenter on a Kelvin-Voight element-based substrate match the observations made here very closely. It should be noted that their simulation was based on a triangular indentation shape without a holding phase. Therefore, the phase where the force is constant but the probe moves deeper and deeper into the material until it finds an elastic reaction force does not exist in their graphs. While energy could be dissipated within the material, it must be considered that for stainless steel probes, almost no energy was lost. This stands in contrast to glass probes which share the same geometrical parameters, but exhibited the highest amount of energy loss. Therefore, friction within the substrate on its own cannot explain this effect and the cause must be related to a property of the probe material. Friction within the probe materials can be ruled out because the deformation within the probes is negligible

and the Young's moduli order is $E_{\text{stainless steel}} > E_{\text{glass}} > E_{\text{PTFE}}$, so the largest deformation, and hence hysteresis, would be expected in PTFE.

A second, directly palpable possible explanation is that the energy difference could go into breaking frictional bonds. This is generally possible, however, glass and stainless steel are on opposite ends of the spectrum when it comes to amount of dissipated energy, although they showed a very similar friction behaviour in the experiments in Chapter 4. PTFE, on the other hand, showed a much higher friction than the two other materials but the amount of energy dissipated for PTFE sits between the dissipation results for the other two. Hence, frictional interaction on its own also does not explain this effect.

In an attempt to find out what could cause the different amounts of energy dissipated, a set of material properties was identified and the values are shown in Table 5.4. In each column, one parameter is shown. The materials are organised in descending order for each column depending on their respective surface properties. In the first column, the measured, dissipated energy W_d is shown. In the other columns, Young's modulus E, static and dynamic friction forces $F_{F,s}$ and $F_{F,d}$ at $F_N = 80$ mN (from Chapter 4), Ra (from Section 5.4.1) and the surface free energy γ is reported, however, none of the parameters seems to stand in a direct correlation to W_d.

W_d [nJ]	E [MPa]	$F_{F,s}$ [mN]	$F_{F,d}$ [mN]	**Ra [µm]**	γ [mJ/m^2]
Glass (4800)	316L (193)	PTFE (7.745)	PTFE (3.39)	Glass (1.571)	Glass (83.4 [136])
PTFE (1000)	Glass (63)	316L (4.321)	316L (1.551)	316L (0.683)	316 (61.68 [137])
316L (0)	PTFE (0.34)	Glass (3.833)	Glass (1.451)	PTFE (0.577)	PTFE (19.1 [138]

Table 5.4: Probe material properties which could be related to hysteresis effects during indentation.

The working theory for what happens is as follows. In Figure 5.21, the interaction is shown schematically with the same steps A-D that were discussed earlier. For each step, there is a respective detail to try and understand what happens on a material level. In Position A, the probe is just touching the material. Therefore, the surrounding material is not yet experiencing any (major) shear stress τ or stress σ. As the probe is loaded with $F_{Z,spec}$ in Position B, the substrate naturally deforms to exert an equivalent reaction force. This deformation results in strain and hence stress within the material, therefore $\sigma \neq 0$. The probe and substrate interface is symbolised by a linear bearing with friction coefficient μ and any deflection of the substrate surface will deform the underlying substrate visualised by a viscoelastic (Kelvin-Voight) element, assuming equilibrium (neglecting inertia). The strain and stress of the elastic part of the viscoelastic element represent an energy that is partially rertrievable as the element deforms back. Note here that the Kelvin-Voight element is only there for illustrative purposes to express the viscoelastic property of PDMS

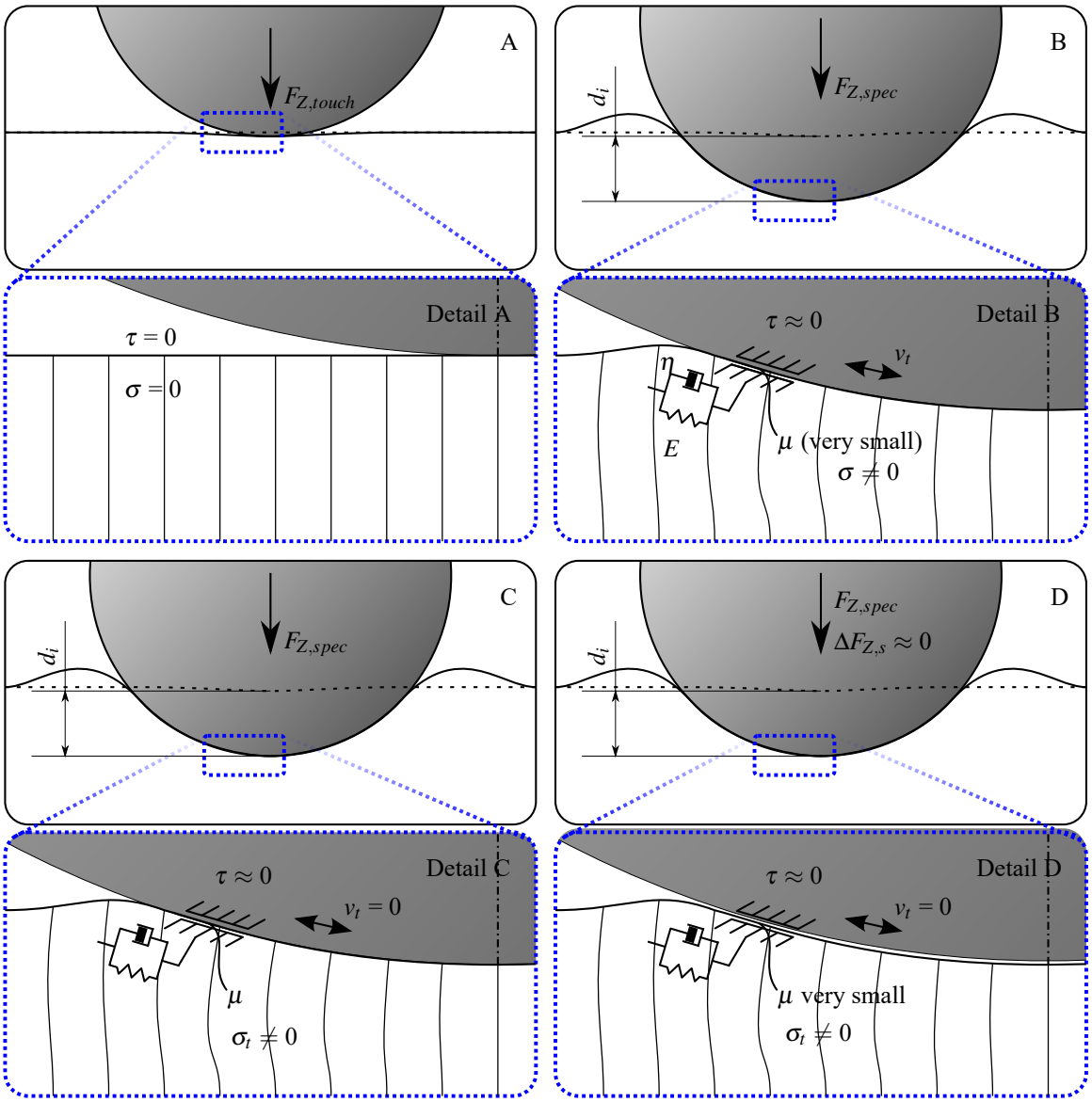

Figure 5.21: Surface interactions during indentation with a stainless steel probe. Shown for distinctive steps A through D which correspond to Positions A through D in Figure 5.20.

and other models may be more accurate. Assuming (based on the low friction coefficients measured in Chapter 4) that the friction is low, the exerted shear stress on the substrate surface by the probe surface τ is almost zero ($\tau \approx 0$). Therefore, relative, tangential movement (v_t) between the two surfaces is possible without large amounts of resistance. The indented geometry is defined by indentation depth d_i. At the end of the holding phase (Position C), not much has changed. The probe is still loaded with $F_{Z,spec}$ and the respective indentation depth has not changed which is evident from the experimetnal data. Therefore, we must assume that no (measurable) creeping is happening. This is likely due to the low amount of friction. Although a relative, tangential movement is possible, none occured since Position

C, because the system was already in equilibrium. This suggests that creeping stems from surface interactions and not from viscoelastic effects within the substrate. Those viscoelastic effects will have ended very shortly after the probe is fully loaded. In position D, the probe is raised, which causes the amount of friction to reduce, however, as the substrate is already in equilibrium, no sudden change in the geometry occurs, which is evident from the fact that force versus indentation depth curves for stainless steel exhibited no measurable reaction force break down. During unloading, the material goes back into its original state and (according to the experimental data), near 100 % of the work is recovered. This means that almost no work is dissipated deforming the dashpot part of the Kelvin-Voight element.

Next, PTFE will be discussed. An equivalent schematic for this material is shown in Figure 5.22. The starting position A is exactly the same, however, in Position B, relative, tangential movement between probe and substrate surfaces is restricted ($v_t = 0$) because of relatively high friction. This friction causes tangential stress τ in the interface and the resulting restriction in movement causes the substrate materials deformation to differ from where it would be without such a high friction, indicated by the lines in the substrate. In Position C, μ is still large, however, the stress in the interface is working against the friction. Therefore, small tangential movement v_t can occur and the substrate moves closer to where it would be without friction. This can happen until the friction generated by the normal pressure within the interface is equivalent to the tangential stress and means that the material relaxes (σ gets smaller). Then, as the probe is raised, the friction coefficient breaks down, similar to how it did with stainless steel probes (Position D). In the case of PTFE, however, this means a significant change in the mechanical system because the material was not in equilibrium and the shear stress τ has no equivalent reaction force anymore. This causes the substrate to relax. At some point, friction may occur again and therefore, the material may not reach its ”desired” geometry. However, it can relax by a significant amount. Earlier, it was stated that the work in the transition $\bar{CD}$ was zero. Technically, this is true for the probe. As said before however, in the material, energy is saved like in a spring through strain ε and stress σ. As the material relaxes and springs, naturally, this energy is set free just like in a spring that relaxes and it is evidently (from the force versus indentation depth curves) not converted into work on the probe. The energy will likely go into acceleration of the surrounding substrate and the media, i.e. a shockwave. From there, it may dissipate into heat. The residual energy that is stored within the material through σ and ε may be partially retrieved. The strain is symbolised by the lines within the material and their distances ε_p and ε_s. ε_s represents the strain the material has relaxed by due to slipping, and ε_p represents the strain that stands for a stored potential energy and can hence still be retrieved.

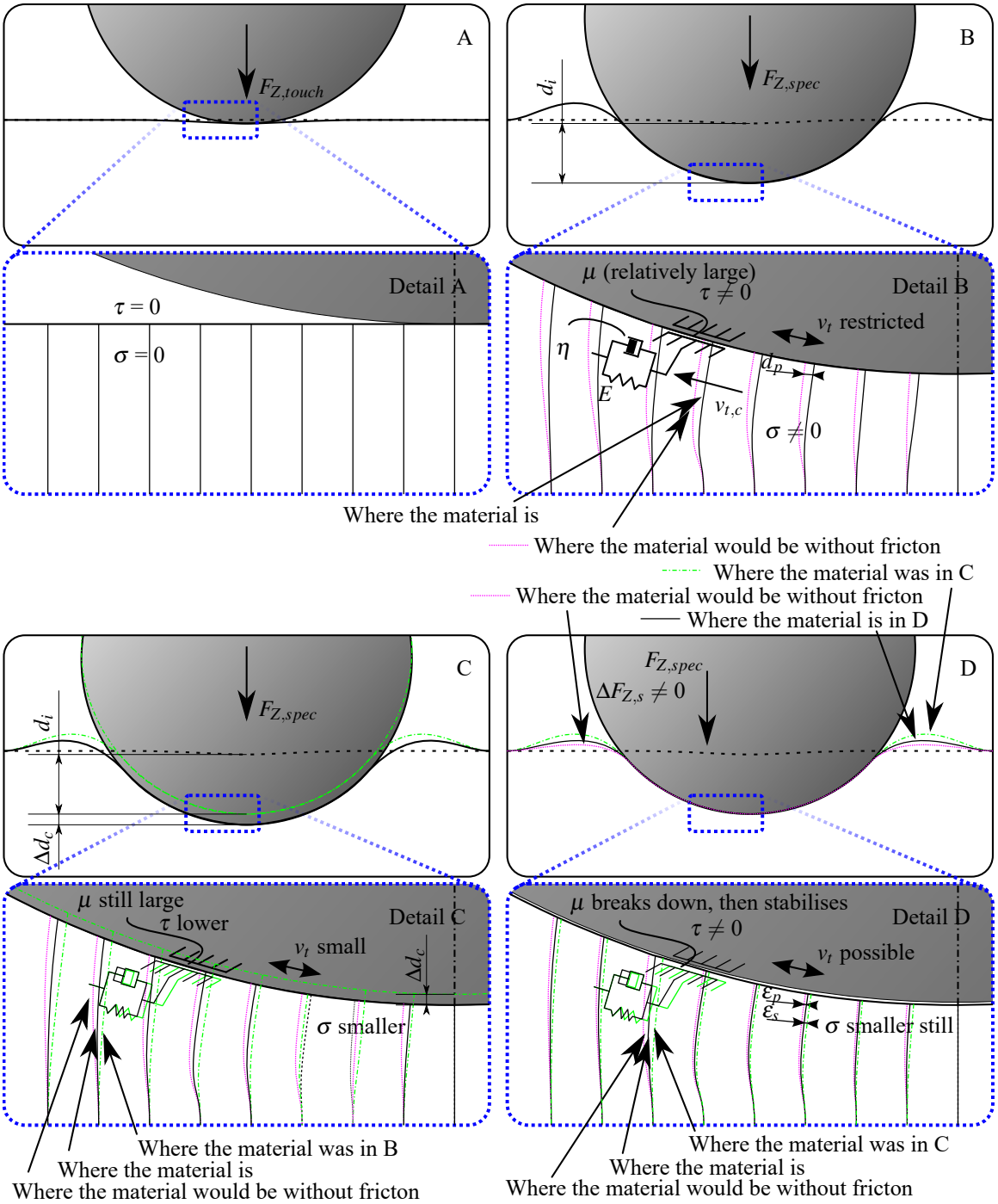

Figure 5.22: Surface interactions during indentation with a PTFE probe. Shown for distinctive steps A through D which correspond to Positions A through D in Figure 5.20.

Finally, glass showed the highest amount of energy lost in the cycle. The reason for this may not be clear because PTFE showed much higher friction coefficients. From Table 5.4, the only metric where glass beats PTFE, that could clearly cause an effect on a surface level, is the roughness. For this reason, in the equivalent schematic for glass in Figure 5.23, Position A is omitted as it is the same as in Figure 5.21 and Figure 5.22 and instead a theory for what happens on the asperity level for the other three positions is shown. In position B, relative sliding is possible to a certain extent under friction coefficient μ as the asperities slide over each other. As the probe is fully loaded, the substrate slides by a substantial amount, releasing strain and hence stresses σ within it until, in Position C, the asperities interlock. This effect cannot be confirmed with the information that is available from this experiment set-up, however, it could explain why PTFE, which has a higher friction coefficient on this substrate, slides less. Then, as the probe begins to raise during the unloading phase, the asperities move away from each other and the friction breaks down. Because the material is moving now and the friction coefficient of glass probes on this substrate is much lower than it is for PTFE probes, almost all potential energy which was stored within the material (due to shear stresses within the interface) through strain ε is released ($\varepsilon_p \approx 0$). There is still potential energy in the material because it is still deformed, however, a substantial amount is lost.

Determining the exact amount of energy that was lost during that relaxation may not be possible here, however, there is a strong indicator that almost all of the total energy that was lost in the cycle is lost in the transition period $\bar{CD}$. To point this out, the force versus indentation depth curve is plotted once again in Figure 5.24. The total dissipated work W_d and the creep work W_c are shown in addition to the energy W_s. The latter energy attempts to approximate the energy which was lost due to relaxation of the material in the transition $\bar{CD}$. W_s was determined as follows. After relaxation of the material, a residual reaction force F_D is measured. An equivalent state B$'$ during the loading curve was found by using the reaction force F_D as defining parameter. An indicator that B$'$ is indeed an equivalent state is that if overlaying the unloading curve (purple) with the loading curve (green) that was set off in d by Δd_o so that it would go through point D, the two curves match very well. From there, the integral was determined (graphically) to the point where the probe was fully loaded. The resulting amount of energy is very close to the one that was dissipated in total. This energy may not be absolutely correct because during loading (and hence in state B$'$), the friction forces the material into a slightly varied geommetry whereas in the assumption here, the material is relaxed. Therefore, this calculation should be seen as an approximation. It shows however, that likely almost all energy is lost during the relaxation, or slip in $\bar{CD}$.

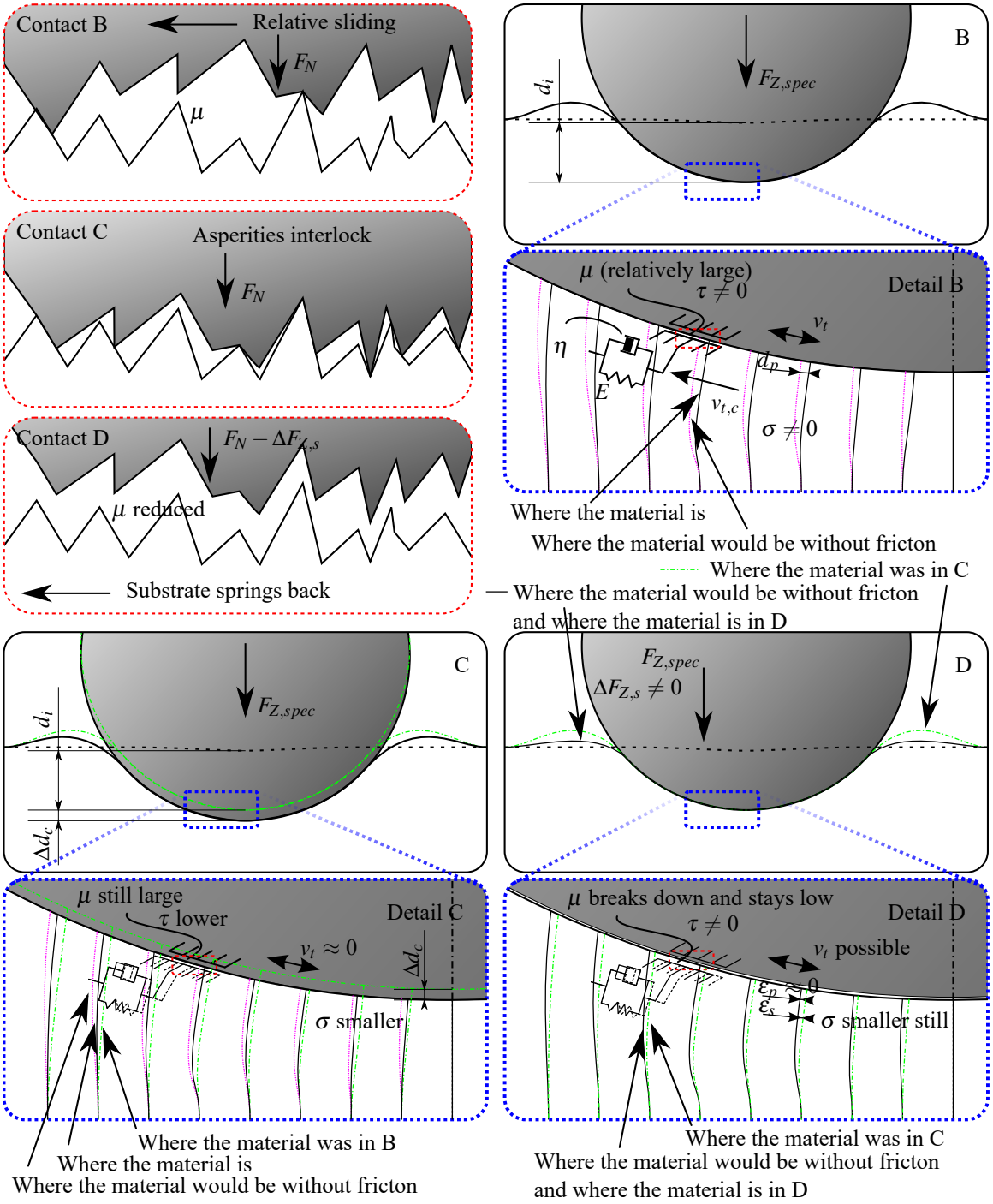

Figure 5.23: Surface interactions during indentation with a glass probe. Shown for distinctive steps B through D which correspond to Positions B through D in Figure 5.20.

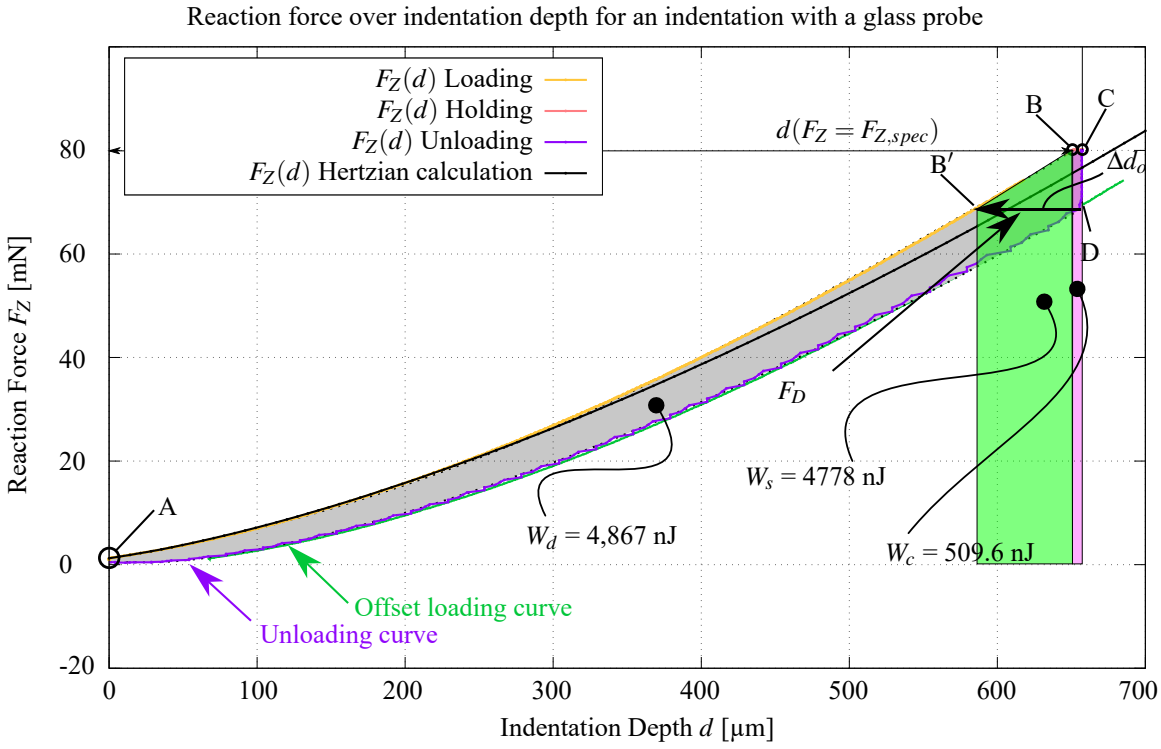

Figure 5.24: Reaction force F_Z over indentation depth d for an indentation with a PTFE probe with annotations.

Chapter 6

General Discussion

Medical devices touch the wall of blood vessels during their application. During this process, friction is generated and damage may be caused to the endothelium. A damaged endothelium is a risk for the patient since the endothelium‘s job is to inhibit thrombosis. Transcatheter cardiovascular intervention is often accompanied by complications that can be linked to mechanical interaction between vessel wall and catheter [68]. Apart from the direct medical implications of damaging the endothelium, it can also increase friction [76]. Weiss et al. simulated catheter-vein contact to investigate thrombophlebitis (sterile inflammation with formation of a blood clot) [71], a common complication with intravenous therapy [72]. For stents, a dysfunctional or damaged endothelium has possibly even more severe implications because it promotes in-stent thrombosis and restenosis [44]. The damaged endothelium tries to repair itself and, in the process, can cover the stent struts [45] and can lead to stent thrombi [46]. The inflamed monolayer may also cause atherosclerosis [47]. Catheter and stent applications are very different in terms of desirable friction. As laid out in Section 2.3.3, for cathethers, a low friction coefficient is important because it is likely to reduce damage [66] and makes the intervention more convenient for the patient [54]. The situation for stents was analysed in Section 2.3.1 and it was concluded that for stents, a higher friction coefficient is beneficial because it can help to prohibit stent migration [82][63] and to simulate migration, reliable friction coefficients are required [63][83]. Therefore, the aim of this study was to mimic the frictional interaction between blood vessels and medical device materials under laboratory conditions. For this, a soft substrate sample with a HUVEC monolayer seeded on top was developed. Then, the damage caused in the slide area was measured with a live/dead assay and compared to control areas. Finally, this methodology was applied to assess damage and friction of glass, stainless steel and PTFE probes.

6.1 Medical Relevance of the Results

Potential for optimisation of previous *in vitro* studies to produce more realistic testing conditions and hence more meaningful results was assessed and several possible issues were identified. The substrate in most of these studies was very hard (around $E = 3.25\,\text{GPa}$ for PS or $E = 63\,\text{GPa}$ for glass) which, unless paired with extremely low normal forces, introduces unrealistic loads to individual cells and hence could make meaningful damage assessment very difficult and friction results questionable because it is not clear what role the cells play in the interaction. This was tackled by developing a soft substrate based sample with a Young's modulus E of 73.3 kPa [88] that represented the mechanical parameters of the underlying tissue in the *in vivo* situation ($E = 125\,\text{kPa}$ [87]) better than most previous studies. The indentation experiments showed that the substrate behaved as predicted by the Hertzian model up to an indentation depth of 300 µm, or 35 mN. For deeper indentations than that, the experimental results diverged from the model, which can be expected as the underlying glass begins to play a more significant role in the mechanical response. An issue that is not commonly discussed is the problem of aligning sample and load directions. Existing methodologies to account for any residual misalignments were assessed and a novel one was developed and validated. According to the results in this work, this novel methodology was able to account for misalignments in the set up within a margin of 6 %. Furthermore, a workflow was created to quantify damage inflicted to the monolayer. The methodology was then applied to test and compare the interaction of a HUVEC monolayer against three probe materials. Glass was tested because it makes the friction results here more comparable to other studies. 316L stainless steel was tested because it is a common stent material. PTFE was tested because it possesses unique surface parameters such as high hydrophobicity. Significant differences in friction and damage behaviour for the different materials were observed.

Catheters [121][122][123], Stents [124][125][126] and guidewires [127][128] have used and still use PTFE coatings in an attempt to lower friction and ease passage. This work was conducted with HUVEC which, while they are a type of ECs, may exhibit slightly different properties than ECs located in some of the locations where these devices operate [103]. In terms of friction, PTFE probes showed the highest values, so the potential of PTFE coatings to reduce friction in catheter or guidewire applications stands in conflict with the results of this work. Since in Section 4.5.6 the extremely hydrophobic surface of PTFE was suspected to be linked to the large amounts of damage and friction that were observed, the trend towards more hydrophilic coatings for catheters [73][53][69][66][56] seems reasonable which is supported by recent findings that hydrophillic materials reduce wear to the

glycocalyx [74].

For stents, the high friction values could be beneficial as they may reduce the risk of stent migration. This must be seen however, in context with the damage results. PTFE was also the material that caused the most damage to the endothelium. Next to stent migration, a common problem in stents is restenosis which can be caused by a damaged or dysfunctional endothelium [44][45][46]. Great parts of cells were wiped by PTFE probes, which indicates that it is not a suitable material for stent applications. Even with no major relative movement between endothelium and probe, major damage to the monolayer was observed. This was explained by the hydrophobic probe material repelling the water out of the contact and hence allowing cell parts to adhere to the probe. According to the results presented in this work, stainless steel seems to be by far the safer choice for stent materials in terms of risk of damage to the endothelium and hence in-stent restenosis and thrombosis. It should be noted here that the role of the lubricant (in this case the medium) is not clear. Despite the medium used for these experiments has a fairly low serum content (2 %V/V), the proteins it contains could influence the interaction of the probe with the glycocalyx. They could either provide additional lubrication, or act as a glue causing the top of the cells to adhere more to the probe. In order to find the exact nature of the role of the medium as a lubricant, additional tests would be required with a control group, that may use PBS rather than media.

However, PTFE probes represent an interesting case because they showed the highest friction and almost complete removal of cells. The indentation tests with glass probes show that pressure alone does not kill major amounts of cells and is not able to penetrate through the monolayer. This means that at the moment of initial motion, when static friction is measured (before major relative movement occurs), the cells were either ripped off the substrate, or sheared apart due to adhesion to the probe. This has implications for stent applications. Since HUVEC were shown to fail under that load, that means that friction can only be pushed so far to avoid stent migration without causing extreme damage to the endothelium. It means also that the experiment should be repeated with other types of ECs because they could vary in the load they are able to withstand or attach firmer to the substrate which could affect the maximum friction coefficient that can be applied without removing the endothelium.

For the development of future stents, it may be important to note that the static friction force did not obey Amonton's law, but it much rather correlated with apparent contact surface area. The results show that while stent oversizing is a valid approach to increase friction and hence reduce the risk of migration, the reason it works may not be just an increased normal pressure but that rather the increased surface area plays a major role. Knowing this, the contact area could be varied as a design parameter in future stents which may allow

to keep the shear stresses on the endothelium low, whilst maximising the friction force. The results also show that up to a normal force of 40 mN (Hertzian pressure of 27.99 kPa), the damage was consistently low, but shows a sharp rise when the load was increased to 80 mN (35.26) Another valuable insight for stent applications is that normal pressure alone inflicted considerably less damage to the endothelium than a combination of normal load and relative movement or tangential load. With this knowledge, it can be suspected that since stents are only intended to move relative to the vessel surface for around 30 s [38][39] when they are inflated, this time period carries an increased risk of thrombosis and restenosis complications. This hypothesis is supported by the fact that stent thrombosis with bare metal stents (like stainless steel) usually happens in the acute (within 24 h) or the subacute (30 days) timeframe after implantation [139][140]. For restenosis, the timeframes are usually much larger, around 6 months [141][142][143], which can be explained by the longer time it takes cells to grow than blood to coagulate. The relative movement at the beginning of the stents deployment may pose an opportunity for improvement. If the damage could be lowered during the deployment phase, for example by a biodegradable low-friction lining or a biodegradable lubricant that quickly disperses, that could help to protect the endothelium in that crucial timeframe. After that, when no relative movement occurs but static friction is desired to be high, the lining/lubricant would be gone and friction could return to normal levels. In practice, this has been tried successfully [144][145] and Singh et al. report that stent migration happened in none of the 20 patients [145]. This work gives an explanation for why their tests were successful and potential lubricants effectiveness could be tested with the technique developed in this study. A future study could look into whether a biaxial load condition can be responsible for those increased amounts of damage alone, or if a relative movement is required. This could be done by adding a further step to the indentation sequence after the holding phase to load the substrate with a controlled force in the tangential axis in addition to the normal load. This tangential load must be small enough to not move the probe.

6.2 Adhesion as Dominant Underlying Friction Mechanism

While the friction experiments on their own may not give an explanation for the friction mechanisms governing the interaction, they do suggest that the interaction is heavily determined by the probe material. This could either be due to microscopic geometry properties i.e. surface roughness, or the chemical composition. The first would point towards mechanical mechanisms, i.e. abrasion whilst the latter would be an indicator for adhesion. A definite answer for which mechanism dominates, or whether it is a mix of the two may

not be answered within this study. It is worth noting, however, that the measured surface roughness Ra was very similar for stainless steel and PTFE probes with PTFE being slightly smoother. Glass probes were significantly rougher. Still, stainless steel and glass probes were very close in terms of damage and friction with glass being slightly more damaging, while PTFE and stainless steel were at two ends of the spectrum. The glass probes' higher surface roughness could be the reason why they caused higher amounts of damage compared to stainless steel. It does not explain, however, why interactions with PTFE probes were so devastating for the monolayer compared to those with stainless steel probes. As the surface roughnesses of these probes were fairly close to each other, and glass probes caused less damage than PTFE and more than stainless steel while being much rougher than both, it seems likely that adhesion was the driving factor. This is supported by the indentation results in two ways. Firstly, again, the damage caused to the endothelium was much higher for PTFE probes than for stainless steel probes. This was the case despite the fact that one would expect surface roughness to have less of an influence if no relative movement was applied. Also, glass probes with their much rougher surface caused far less damage than PTFE probes again. Secondly, the damage caused to the monolayer decreased significantly with consecutive indentations for all materials. This can be explained by parts of the cells sticking to the probe material and providing a separating, low-adhesion layer for following interactions. Adhesion has been proposed as a driving factor during interactions with endothelial monolayers before [56][64] which was confirmed through the experiments conducted in this work. Future work could look into the influence of surface roughness of the probe as well as which molecules adhere to certain types of medical device materials. This could then help to develop medical device materials the cells cannot adhere to, which may prevent them from getting destroyed during the interaction.

6.3 Comparison with Previous Studies and Limitations of this Work

Compared to most previous studies, this work has some advantages. Excellent work has been done previously to understand the tribological behaviour of monolayers. Generally, since the applied normal forces have to be fairly low, high-end, and often customised, friction testers are used. The need for such expensive equipment results from the stiffness of substrate and probe. This work tackles this issue by introducing a soft substrate which, whilst not matching *in vivo* mechanical parameters perfectly, come close to these and hence are capable of achieving low pressures without the need for such expensive equipment.

Such apparatuses are expensive and are hence not very accessible for many research institutions. Furthermore, groups with an expensive microtribometer have reported heavy damage on bovine endothelial cells with a glass probe under pressures of 5 kPa [78], however, this result may be due to the hard probe and substrate since this work proves that human endothelial cells can sustain pressures of 35 kPa and such a drastic difference would not necessarily be expected between bovine and human cells. This shows using a soft substrate may be a cost-effective alternative for future experiments. The tribometer that was used in is work, or an equivalent one, is available to most tribology-focused research groups. The load cell is more niche and not all institutions may have the exact one, however, it is still affordable (£ 5000) and also the higher range load cell could be used, especially in conjunction with larger probe diameters. This can help to promote friction research on monolayers at other institutions which maybe did not have the necessary funds to invest into an expensive biotribometer.

Furthermore, in this work, the problem of misalignment for low friction experiments was observed and tackled using a novel approach. It was shown that results from this approach matched the values collected on aligned stretches on the respective samples. Up to now, this issue was negated by carrying out multiple tests on the same location and averaging the results. However, apart from other minor implications applying this approach would have had for this work, it inherently cannot be used for single-slide experiments and does not allow to test static friction. The technique presented here allows both.

Finally, the cells were counted and a way of quantifying the damage caused to the monolayer in terms of percentages of live, dead and removed cells was presented. The methodology was then applied to study friction and indentation tests of HUVEC against different probe materials in an attempt to mimic vessel against medical device interactions. Significant differences between the probe materials were found.

This work does however have some limitations. Since the substrates' surfaces were cultured with HUVEC, they, first and foremost, represent the surface parameters of a human umbilical vein. As mentioned before, endothelial cells can exhibit different properties, i.e. size of individual cells, shape, thickness [103] and therefore, the experiments should be repeated on other types of ECs. However, since all types of vascular endothelial cells share similarities and functions (glycocalyx on top, forming the barrier between blood and vessel, controlling flow of chemicals, keeping the underlying tissue healthy), the results of this work are still relevant. Another limitation is the absence of blood in the contact. In the *in vitro* situation, blood is the available natural lubricant. Instead of blood, in this work medium was used. The implications of this are not clear; however, a future study could look at the lubricating properties of blood. Since the interaction took place in the boundary

lubrication regime, the influence of the lubricant is expected to be limited. Introducing blood to this set up requires techniques to stop it from coagulating, ensuring that the cells are still healthy underneath and ethical approval.

The purpose of this work was to investigate the influence of material on cell friction and damage, and so, to limit the influence of geometrical design parameters, spherical probes were used. PTFE probes were larger than glass and stainless steel ones, which was due to availability and the experiment should be repeated with probes of the same diameter, should they become available. As PTFE probes were larger, however, this meant that the pressures were lower, and still PTFE inflicted the most damage to the monolayer by far. Therefore, the conclusions of this work seem still valid and are expected to be amplified if the experiment was repeated with 2 mm PTFE probes. In the future, real medical device geometries could be tested and compared to the results of this work to study the implications of geometrical design parameters on friction and damage.

A limitation in terms of damage quantification is that the methodology only distinguishes between dead and healthy cells. While dead cells that show up through propidium iodide are certainly an important metric, not all healthy cells may survive because the nucleus could react to external forces which could promote an apoptotic pathway. Cells which are on such a pathway may not be recognised by propidium iodide as long as they have a functional cell membrane. Hence it would be desirable to have more resolution in terms of which cells with a healthy cell membrane are going to survive and which ones are on an apoptotic pathway. Apoptosis is a complex process and mainly dictated by caspases [146]. Friction has been shown to cause expression of apoptotic markers in the medium [25], and has recently been visualised locally after friction experiments on epithelial cells [147]. To determine which cells exactly are on an apoptotic pathway, immunohistochemistry assays staining for caspase can be utilised which could be based on fluorescent or light microscopy [146][148][147].

The relative velocity in the experiments presented here is comparable to other studies [147][76][25] on cell monolayers and on the lower end of medically relevant insertion velocities for catheters (0.6 mm/s-4.746 mm/s[149][150]). For stents, relative velocities are expected to be very low (they expand over $\approx$ 30 s, [38][39]) so the speeds applied in this work are certainly higher than in the real application. However, since mainly static friction is to occur, the respective results from this work are still relevant. In terms of normal load conditions, forces between 5 g-20 g (49.05 mN-196.2 mN) have been reported for catheter tip/tissue contacts, with the higher forces creating larger lesions [151], while Xiao et al. mention ranges of 0 N to more than 1.5 N [48]. This means that the normal loads tested here are relevant in a medical context and were at the lower end of what would be expected

between a catheter tip and a real vessel. The load cell's range was almost fully utilised here, so if a future study were to look at the higher range of the expected normal forces, a bigger load cell could achieve that.

For stents, the experiments conducted here are difficult to put into context because measuring the normal pressures between them and blood vessels *in vivo* is challenging. The pressure the ballon catheter is inflated with is between 8 and 20 atm (811 kPa-2027 kPa) [37]. Using this, the pressures in the contact of this experiment are not as high as the ones occuring in the real situation. However, the exact pressure depends on the deformation of the arterial wall as per $\sigma = E\varepsilon$. Since during stented balloon angioplasty the balloon can only expand this far, the artery will deform equivalently. That means that the remaining load is carried by the balloon and the resulting pressure depends on the final geometry. In order to obtain realistic pressures for future experiments, a finite element simulation could help to obtain the pressures resulting from the mechanical response of the system caused by a specific deformation. For now, however, this is certainly a limitation of this work in terms of relevancy for stent applications.

Cells can behave differently *in vitro* than they do *in vivo*. In the case of endothelial cells, this can affect the maturity of glycocalyx, which has been linked to the static fluid shear stress conditions during conventional laboratory cell culture [152][153] and leads to thinner glycocalyx [154][155][152]. Since the experiments in this work were carried out without any applied shear stress during culture, they share this limitation which is common to most *in vitro* studies. It could be overcome in the future by applying a fluid shear stress to the samples while they are being cultured in order to develop a more representative monolayer.

Finally, it must be considered that the samples used in this study are PDMS-based. PDMS has become a popular material to generate microfluidic scaffolds in an attempt to obtain physiologically realistic environment parameters [92][156]. However, whilst it is a widely used material for cell culture, there are concerns whether PDMS is appropriate for the job [92][157][158][159]. Namely, the disadvantages of PDMS are: its tendency to absorb small hydrophobic molecules which may cause an imbalance of nutrients [92][93][94][95], its leaching of oligomers into water [92][93][96] and its ability to release silicon into the media at higher than physiological levels which could trigger a response from some cell types [92]. In summary, this means that the HUVEC behaviour here may have been influenced by the PDMS and could hence have been different from ECs in physiology. In terms of mechanical parameters, however, PDMS comes much closer to the physiologically relevant values which is also important as has been shown in this study. In the future, polyacrylamide hydrogels could present an alternative way of fabricating soft substrate samples. Repeating the experiment with polyacrylamide hydrogels as substrates

could help determining the influence of the issues PDMS may have for this application for cell culture.

Chapter 7

Conclusions and Future Work

The methodology and results presented in this work allow some interesting and relevant conclusions:

- Misalignments within the friction testing set up and unevenness of samples can cause significant deviations in the measured friction. The smaller the friction coefficient, the higher the influence of misalignments. Whilst this effect has been accounted for in reciprocating experiments for dynamic friction, this work presents a new approach that also works for static and dynamic friction of single-slide experiments.
- Damage and friction on an *in vitro* endothelium are highly dependent on the probe material. PTFE is a highly destructive material while exerting large amounts of friction. This makes its application in cardiovascular catheters for lowering friction and easing passage questionable. By extension, this could also apply for urinary catheters.
- The indentation experiments suggest that the governing friction mechanism is adhesion which is in line with previous assumptions from the literature.
- The soft substrate samples have proven an extremely affordable alternative to expensive microtribometers when used in conjunction with the approach to account for misalignments and unevenness.

In the future, this work could be built upon by testing other cell types (e.g. epithelial cells) to investigate whether friction and damage behave in a similar fashion. This could have implications for other medical devices, for example urinary catheters. Also, more probe materials should be tested; this methodology could be used to investigate, for example, hydrophillic catheter coatings. With some modifications to the set up, more aspects of the cells behaviour could be studied. A microscope with a sufficient (phase detect) autofocus could be mounted underneath the sample to allow *in situ* visualisation of the contact.

Medium containing PI (or other dyes) could then allow to determine where exactly during the interaction cells die. With modifications to the sample holder, real device geometries and their influence on damage and friction could be tested. Finally, if sterility could be guaranteed, the samples would not have to be imaged and then fixed immediately after friction testing. This would allow to study how an endothelium grows back after an interaction with a medical device. Finally, compatibility of HUVEC with the substrate must be confirmed to ensure that cells behave as they would *in vivo*. This can be done by using a different soft substrate (i.e. polyacrylamide hydrogels) and *ex vivo* samples.

References

[1] F. Martini, *Fundamentals of anatomy & physiology*, 5th ed. Upper Saddle River, N.J.: Prentice Hall, 2001.

[2] I. Xanthis, C. Souilhol, J. Serbanovic-Canic, H. Roddie, A. C. Kalli, M. Fragiadaki, R. Wong, D. R. Shah, J. A. Askari, L. Canham, N. Akhtar, S. Feng, V. Ridger, J. Waltho, E. Pinteaux, M. J. Humphries, M. T. Bryan, and P. C. Evans, "β1 integrin is a sensor of blood flow direction," *Journal of Cell Science*, vol. 132, no. 11, 2019. [Online]. Available: https://pubmed.ncbi.nlm.nih.gov/31076511/

[3] C. Givens and E. Tzima, "Endothelial Mechanosignaling: Does One Sensor Fit All?" *Antioxidants and Redox Signaling*, vol. 25, no. 7, p. 373–388, sep 2016. [Online]. Available: /pmc/articles/PMC5011625//pmc/articles/PMC5011625/?report=abstracthttps://www.ncbi.nlm.nih.gov/pmc/articles/PMC5011625/

[4] C. Souilhol, J. Serbanovic-Canic, M. Fragiadaki, T. J. Chico, V. Ridger, H. Roddie, and P. C. Evans, "Endothelial responses to shear stress in atherosclerosis: a novel role for developmental genes," *Nature Reviews Cardiology*, vol. 17, no. 1, p. 52–63, jul 2020. [Online]. Available: https://www.nature.com/articles/s41569-019-0239-5

[5] S. Godo and H. Shimokawa, "Endothelial Functions," *Arteriosclerosis, Thrombosis, and Vascular Biology*, vol. 37, no. 9, p. e108–e114, sep 2017. [Online]. Available: https://www.ahajournals.org/doi/abs/10.1161/ATVBAHA.117.309813

[6] C. Michiels, "Endothelial cell functions," *Journal of Cellular Physiology*, vol. 196, no. 3, p. 430–443, sep 2003. [Online]. Available: https://pubmed.ncbi.nlm.nih.gov/12891700/

[7] J. D. Pearson, "Endothelial cell function and thrombosis," *Bailliere's Clinical Haematology*, vol. 7, no. 3, p. 441–452, 1994. [Online]. Available: https://pubmed.ncbi.nlm.nih.gov/7841594/

[8] J. Torrado, L. Buckley, A. Durán, P. Trujillo, S. Toldo, J. Valle Raleigh, A. Abbate, G. Biondi-Zoccai, and L. A. Guzmán, "Restenosis, Stent Thrombosis, and Bleeding Complications: Navigating Between Scylla and Charybdis," *Journal of the American College of Cardiology*, vol. 71, no. 15, p. 1676–1695, 2018. [Online]. Available: https://doi.org/10.1016/j.jacc.2018.02.023

[9] L. Shapiro and W. I. Weis, "Structure and biochemistry of cadherins and catenins." *Cold Spring Harbor perspectives in biology*, vol. 1, no. 3, 2009. [Online]. Available: /pmc/articles/PMC2773639//pmc/articles/PMC2773639/?report=abstracthttps://www.ncbi.nlm.nih.gov/pmc/articles/PMC2773639/

[10] S. Yonemura, "Cadherin–actin interactions at adherens junctions," *Current Opinion in Cell Biology*, vol. 23, no. 5, p. 515–522, oct 2011.

[11] L. R. Anderson, T. W. Owens, and M. J. Naylor, "Structural and mechanical functions of integrins," *Biophysical Reviews*, vol. 6, no. 2, p. 203, 2014. [Online]. Available: /pmc/articles/PMC5418412//pmc/articles/PMC5418412/?report=abstracthttps://www.ncbi.nlm.nih.gov/pmc/articles/PMC5418412/

[12] F. G. Giancotti and E. Ruoslahti, "Integrin Signaling," *Science*, vol. 285, no. 5430, p. 1028–1033, aug 1999. [Online]. Available: https://science.sciencemag.org/content/285/5430/1028https://science.sciencemag.org/content/285/5430/1028.abstract

[13] S. Alimperti and S. T. Andreadis, "CDH2 and CDH11 act as regulators of stem cell fate decisions," *Stem Cell Research*, vol. 14, no. 3, p. 270–282, may 2015. [Online]. Available: https://pubmed.ncbi.nlm.nih.gov/25771201/

[14] A. M. Malek, S. L. Alper, and S. Izumo, "Hemodynamic shear stress and its role in atherosclerosis," *Journal of the American Medical Association*, vol. 282, no. 21, p. 2035–2042, 1999. [Online]. Available: www.jama.com

[15] S. Reitsma, D. W. Slaaf, H. Vink, M. A. M. J. van Zandvoort, and M. G. A. oude Egbrink, "The endothelial glycocalyx: composition, functions, and visualization," *Pflügers Archiv - European Journal of Physiology 2007 454:3*, vol. 454, no. 3, p. 345–359, jan 2007. [Online]. Available: https://link.springer.com/article/10.1007/s00424-007-0212-8

[16] H. Vink, A. A. Constantinescu, and J. A. Spaan, "Oxidized lipoproteins degrade the endothelial surface layer: Implications for platelet-endothelial cell adhesion,"

Circulation, vol. 101, no. 13, p. 1500–1502, apr 2000. [Online]. Available: https://pubmed.ncbi.nlm.nih.gov/10747340/

[17] Y. M. Chen, T. Kurokawa, T. Tominaga, K. Yasuda, Y. Osada, J. P. Gong, K. Yamamoto, and J. Ando, "Study on the sliding friction of endothelial cells cultured on hydrogel and the role of glycocalyx on friction reduction," *Advanced Engineering Materials*, vol. 12, no. 11, p. B628–B636, nov 2010. [Online]. Available: https://onlinelibrary.wiley.com/doi/full/10.1002/adem.201080021https://onlinelibrary.wiley.com/doi/abs/10.1002/adem.201080021https://onlinelibrary.wiley.com/doi/10.1002/adem.201080021

[18] C. Lin, H. J. Kaper, W. Li, R. Splinter, and P. K. Sharma, "Role of endothelial glycocalyx in sliding friction at the catheter-blood vessel interface," *Scientific Reports*, vol. 10, no. 1, p. 1–10, jul 2020. [Online]. Available: https://www.nature.com/articles/s41598-020-68870-x

[19] K. Burridge, E. Monaghan-Benson, and D. M. Graham, "Mechanotransduction: from the cell surface to the nucleus via RhoA," *Philosophical Transactions of the Royal Society B*, vol. 374, no. 1779, aug 2019. [Online]. Available: https://royalsocietypublishing.org/doi/abs/10.1098/rstb.2018.0229

[20] N. Belaadi, J. Aureille, and C. Guilluy, "Under Pressure: Mechanical Stress Management in the Nucleus," *Cells*, vol. 5, no. 2, p. 27, jun 2016.

[21] E. Roux, P. Bougaran, P. Dufourcq, and T. Couffinhal, "Fluid Shear Stress Sensing by the Endothelial Layer," p. 861, jul 2020.

[22] K. Van Der Heiden, F. J. Gijsen, A. Narracott, S. Hsiao, I. Halliday, J. Gunn, J. J. Wentzel, and P. C. Evans, "The effects of stenting on shear stress: Relevance to endothelial injury and repair," p. 269–275, 2013. [Online]. Available: https://academic.oup.com/cardiovascres/article/99/2/269/345569

[23] S. Lehoux and A. Tedgui, "Bases cellulaires de la mécanotransduction dans la cellule endothéliale," *médecine/sciences*, vol. 20, no. 5, p. 551–556, may 2004. [Online]. Available: http://www.medecinesciences.org/10.1051/medsci/2004205551

[24] S. Lehoux, Y. Castier, and A. Tedgui, "Molecular mechanisms of the vascular responses to haemodynamic forces," in *Journal of Internal Medicine*, vol. 259, 2006, p. 381–392.

[25] A. A. Pitenis, J. M. Urueña, S. M. Hart, C. S. O'Bryan, S. L. Marshall, P. P. Levings, T. E. Angelini, and W. G. Sawyer, "Friction-Induced Inflammation," *Tribology Letters*, vol. 66, no. 3, p. 81, 2018. [Online]. Available: https://doi.org/10.1007/s11249-018-1029-7

[26] E. A. Dawson, S. Rathore, N. T. Cable, D. J. Wright, J. L. Morris, and D. J. Green, "Impact of introducer sheath coating on endothelial function in humans after transradial coronary procedures," *Circulation: Cardiovascular Interventions*, vol. 3, no. 2, p. 148–156, apr 2010.

[27] S. Pellegrin and H. Mellor, "Actin stress fibers," *Journal of Cell Science*, vol. 120, no. 20, p. 3491–3499, 2007.

[28] N. Prasain and T. Stevens, "The actin cytoskeleton in endothelial cell phenotypes," *Microvascular Research*, vol. 77, no. 1, p. 53–63, 2009.

[29] I. M. Herman, A. M. Brant, V. S. Warty, J. Bonaccorso, E. C. Klein, R. L. Kormos, and H. S. Borovetz, "Hemodynamics and the vascular endothelial cytoskeleton." University of Pittsburgh School of Medicine, Tech. Rep. 1, 1987.

[30] A. M. Malek and S. Izumo, "Mechanism of endothelial cell shape change and cytoskeletal remodeling in response to fluid shear stress," *Journal of Cell Science*, vol. 109, no. 4, p. 713–726, 1996.

[31] K. Haase and A. E. Pelling, "Investigating cell mechanics with atomic force microscopy," *Journal of the Royal Society Interface*, vol. 12, no. 104, 2015.

[32] S. Barreto, C. H. Clausen, C. M. Perrault, D. A. Fletcher, and D. Lacroix, "A multi-structural single cell model of force-induced interactions of cytoskeletal components," *Biomaterials*, vol. 34, no. 26, p. 6119–6126, aug 2013.

[33] E. A. Peeters, C. W. Oomens, C. V. Bouten, D. L. Bader, and F. P. Baaijens, "Mechanical and failure properties of single attached cells under compression," *Journal of Biomechanics*, vol. 38, no. 8, p. 1685–1693, aug 2005.

[34] P. A. Janmey and R. T. Miller, "Mechanisms of mechanical signaling in development and disease," p. 9–18, jan 2011.

[35] N. Wang, J. D. Tytell, and D. E. Ingber, "Mechanotransduction at a distance: Mechanically coupling the extracellular matrix with the nucleus," p. 75–82, 2009. [Online]. Available: www.nature.com/reviews/molcellbio

[36] A. Degani, H. Choset, A. Wolf, and M. A. Zenati, "Highly articulated robotic probe for minimally invasive surgery," in *Proceedings - IEEE International Conference on Robotics and Automation*. NIH Public Access, 2006, p. 4167–4172. [Online]. Available: /pmc/articles/PMC2923469//pmc/articles/PMC2923469/?report=abstracthttps://www.ncbi.nlm.nih.gov/pmc/articles/PMC2923469/

[37] J. Dirschinger, A. Kastrati, F. J. Neumann, P. Boekstegers, S. Elezi, J. Mehilli, H. Schühlen, J. Pache, E. Alt, R. Blasini, G. Steinbeck, and A. Schömig, "Influence of balloon pressure during stent placement in native coronary arteries on early and late angiographic and clinical outcome: A randomized evaluation of high-pressure inflation," *Circulation*, vol. 100, no. 9, p. 918–923, aug 1999. [Online]. Available: https://www.ahajournals.org/doi/10.1161/01.CIR.100.9.918

[38] Y. Iwamoto, M. Okamoto, M. Hashimoto, Y. Fukuda, A. Iwamoto, T. Iwasaki, H. Kinoshita, and Y. Kihara, "Better stent expansion by two-time inflation of stent balloon and its responsible mechanism," *Journal of Cardiology*, vol. 59, no. 2, p. 160–166, mar 2012.

[39] J. Skowroński, R. Wolny, J. Jastrzebski, P. Tyczyński, K. Szlazak, J. Pregowski, G. S. Mintz, K. Liżewska, W. Świeszkowski, Z. Chmielak, and A. Witkowski, "Impact of the Balloon Inflation Time and Pattern on the Coronary Stent Expansion," *Journal of Interventional Cardiology*, vol. 2019, 2019.

[40] D. Laroche, S. Delorme, T. Anderson, and R. DiRaddo, "Computer prediction of friction in balloon angioplasty and stent implantation," in *Lecture Notes in Computer Science (including subseries Lecture Notes in Artificial Intelligence and Lecture Notes in Bioinformatics)*, vol. 4072 LNCS. Springer, Berlin, Heidelberg, 2006, p. 1–8. [Online]. Available: https://link.springer.com/chapter/10.1007/11790273{_}1

[41] T. M. Bedair, M. A. ElNaggar, Y. K. Joung, and D. K. Han, "Recent advances to accelerate re-endothelialization for vascular stents," *Journal of Tissue Engineering*, vol. 8, jan 2017.

[42] C. Chaabane, F. Otsuka, R. Virmani, and M. L. Bochaton-Piallat, "Biological responses in stented arteries," *Cardiovascular Research*, vol. 99, no. 2, p. 353–363, 2013. [Online]. Available: https://academic.oup.com/cardiovascres/article-abstract/99/2/353/347941

[43] S. O. Marx, H. Totary-Jain, and A. R. Marks, "Vascular smooth muscle cell proliferation in restenosis," *Circulation: Cardiovascular Interventions*, vol. 4, no. 1, p. 104–111, feb 2011. [Online]. Available: /pmc/articles/PMC3816546/https://www.ncbi.nlm.nih.gov/pmc/articles/PMC3816546/

[44] A. Cornelissen and F. J. Vogt, "The effects of stenting on coronary endothelium from a molecular biological view: Time for improvement?" p. 39–46, jan 2019. [Online]. Available: /pmc/articles/PMC6307786//pmc/articles/PMC6307786/?report=abstracthttps://www.ncbi.nlm.nih.gov/pmc/articles/PMC6307786/

[45] S. T. Hsiao, T. Spencer, L. Boldock, S. D. Prosseda, I. Xanthis, F. J. Tovar-Lopez, H. Van Buesekamp, R. Y. Khamis, N. Foin, N. Bowden, A. Hussain, A. Rothman, V. Ridger, I. Halliday, C. Perrault, J. Gunn, and P. C. Evans, "Endothelial repair in stented arteries is accelerated by inhibition of Rho-associated protein kinase," *Cardiovascular Research*, vol. 112, no. 3, p. 1–13, dec 2016. [Online]. Available: https://pubmed.ncbi.nlm.nih.gov/27671802/

[46] Y. Uchida, Y. Uchida, T. Sakurai, M. Kana, S. Shirai, T. Oshima, A. Koga, and A. Matsuyama, "Possible role of damaged neoendothelial cells in the genesis of coronary stent thrombus in chronic phase: A dye-staining angioscopic study," *International Heart Journal*, vol. 52, no. 1, p. 12–16, 2011. [Online]. Available: https://pubmed.ncbi.nlm.nih.gov/21321462/

[47] R. Ross, "Atherosclerosis - an inflammatory disease," *The New England journal of medicine*, vol. 340, no. 2, p. 115–126, 1999. [Online]. Available: https://pubmed.ncbi.nlm.nih.gov/9887164/

[48] N. Xiao, J. Guo, S. Guo, and T. Tamiya, "A robotic catheter system with real-time force feedback and monitor," *Australasian Physical and Engineering Sciences in Medicine*, vol. 35, no. 3, p. 283–289, 2012.

[49] H. Hertz, "Ueber die Beruehrung fester elastischer Koerper," *Journal für die reine und angewandte Mathematik*, 1882.

[50] K. L. Johnson, K. Kendall, and a. Roberts, "Surface energy and the contact of elastic solids," *Proceedings of the royal society of London. A. mathematical and physical sciences*, vol. 324, no. 1558, p. 301–313, 1971.

[51] E. Winkler, *Die Lehre von der Elasticitaet und Festigkeit: mit besonderer Rücksicht auf ihre Anwendung in der Technik, für polytechnische Schulen, Bauakademien, Ingenieure, Maschinenbauer, Architecten, etc*. H. Dominicus, 1867.

[52] K. D. Schulze, "The Contact Mechanics of Soft Surfaces: Cells, Gels, and Elastomers," Ph.D. dissertation, University of Florida, 2017.

[53] Y. Uyama, H. Tadokoro, and Y. Ikada, "Low-frictional catheter materials by photo-induced graft polymerization," *Biomaterials*, vol. 12, no. 1, p. 71–75, 1991.

[54] K. Takashima, R. Shimomura, T. Kitou, H. Terada, K. Yoshinaka, and K. Ikeuchi, "Contact and friction between catheter and blood vessel," *Tribology International*, vol. 40, no. 2 SPEC. ISS., p. 319–328, feb 2007.

[55] T. Takahashi, R. Murayama, M. Abe-Doi, M. Miyahara-Kaneko, C. Kanno, M. Nakamura, M. Mizuno, C. Komiyama, and H. Sanada, "Preventing peripheral intravenous catheter failure by reducing mechanical irritation," *Scientific Reports*, vol. 10, no. 1, p. 1–13, jan 2020. [Online]. Available: https://www.nature.com/articles/s41598-019-56873-2

[56] S. P. Ho, N. Nakabayashi, Y. Iwasaki, T. Boland, and M. LaBerge, "Frictional properties of poly(MPC-co-BMA) phospholipid polymer for catheter applications," *Biomaterials*, vol. 24, no. 28, p. 5121–5129, 2003.

[57] W. W. Nichols, M. F. O'Rourke, C. Vlachopoulos, and D. A. McDonald, *McDonald's blood flow in arteries : theoretical, experimental and clinical principles.* London: Hodder Arnold., 2011.

[58] Z. M. Jin and D. Dowson, "Elastohydrodynamic lubrication in biological systems," *Proceedings of the Institution of Mechanical Engineers, Part J: Journal of Engineering Tribology*, vol. 219, no. 5, p. 367–380, oct 2005. [Online]. Available: https://journals.sagepub.com/doi/abs/10.1243/135065005x33982

[59] S. L. Marshall, K. D. Schulze, S. M. Hart, J. M. Urueña, E. O. McGhee, A. I. Bennett, A. A. Pitenis, C. S. O'Bryan, T. E. Angelini, and W. G. Sawyer, "Spherically capped membrane probes for low contact pressure tribology," *Biotribology*, vol. 11, p. 69–72, sep 2017. [Online]. Available: https://www.sciencedirect.com/science/article/pii/S2352573816300774

[60] A. C. Dunn, W. Gregory Sawyer, M. Sarntinoranont, and R. Tran-Son-Tay, "Mechanical Response of Living Cells to Contacting Shear Forces," in *Studies in Mechanobiology, Tissue Engineering and Biomaterials*. Springer, 2011, vol. 4, p. 125–141. [Online]. Available: https://link.springer.com/chapter/10.1007/8415{_}2010{_}23

[61] A. C. Dunn, J. A. Cobb, A. N. Kantzios, S. J. Lee, M. Sarntinoranont, R. Tran-Son-Tay, and W. G. Sawyer, "Friction coefficient measurement of hydrogel materials on living epithelial cells," *Tribology Letters*, vol. 30, no. 1, p. 13–19, apr 2008. [Online]. Available: https://link.springer.com/article/10.1007/s11249-008-9306-5

[62] L. Capron and P. Bruneval, "Influence of applied stress on mitotic response of arteries to injury with a balloon catheter: Quantitative study in rat thoracic aorta," p. 941–948, 1989. [Online]. Available: https://academic.oup.com/cardiovascres/article/23/11/941/307714

[63] S. Vad, A. Eskinazi, T. Corbett, T. McGloughlin, and J. P. Vande Geest, "Determination of coefficient of friction for self-expanding stent-grafts," *Journal of Biomechanical Engineering*, vol. 132, no. 12, nov 2010.

[64] P. Prokopovich and S. Perni, "Prediction of the frictional behavior of mammalian tissues against biomaterials," *Acta Biomaterialia*, vol. 6, no. 10, p. 4052–4059, oct 2010.

[65] ——, "Contact interactions of aorta against PVC catheters," *Tribology International*, vol. 66, p. 157–164, oct 2013.

[66] S. Nagaoka and R. Akashi, "Low Friction Hydrophilic Surface for Medical Devices," *Journal of Bioactive and Compatible Polymers*, vol. 5, no. 2, p. 212–226, jul 1990. [Online]. Available: https://journals.sagepub.com/doi/abs/10.1177/088391159000500205?journalCode=jbca

[67] K. H. Dellimore, A. R. Helyer, and S. E. Franklin, "A scoping review of important urinary catheter induced complications," *Journal of Materials Science: Materials in Medicine*, vol. 24, no. 8, p. 1825–1835, 2013. [Online]. Available: http://eprints.whiterose.ac.uk/112508/

[68] K. H. Dellimore, S. E. Franklin, and A. R. Helyer, "A Review of Catheter Related Complications During Minimally Invasive Transcatheter Cardiovascular Intervention with Implications for Catheter Design," p. 217–232, 2014.

[69] D. Graiver, R. L. Durall, and T. Okada, “Surface morphology and friction coefficient of various types of Foley catheter,” *Biomaterials*, vol. 14, no. 6, p. 465–469, may 1993.

[70] A. Niemczyk, M. El Fray, and S. E. Franklin, “Friction behaviour of hydrophilic lubricious coatings for medical device applications,” *Tribology International*, vol. 89, p. 54–61, sep 2015. [Online]. Available: https://www.sciencedirect.com/science/article/pii/S0301679X15000481

[71] D. Weiss, A. Gefen, and S. Einav, “Modelling catheter–vein biomechanical interactions during an intravenous procedure,” *Computer Methods in Biomechanics and Biomedical Engineering*, vol. 19, no. 3, p. 330–339, feb 2016. [Online]. Available: https://pubmed.ncbi.nlm.nih.gov/25853223/

[72] A. Panadero, G. Iohom, J. Taj, N. Mackay, and G. Shorten, “A dedicated intravenous cannula for postoperative use: Effect on incidence and severity of phlebitis,” *Anaesthesia*, vol. 57, no. 9, p. 921–925, sep 2002. [Online]. Available: https://associationofanaesthetists-publications.onlinelibrary.wiley.com/doi/full/10.1046/j.1365-2044.2002.02786.xhttps://associationofanaesthetists-publications.onlinelibrary.wiley.com/doi/abs/10.1046/j.1365-2044.2002.02786.xhttps://associationofanaesthetists-publications.onlinelibrary.wiley.com/doi/10.1046/j.1365-2044.2002.02786.x

[73] J. Stensballe, D. Looms, P. N. Nielsen, and M. Tvede, “Hydrophilic-coated catheters for intermittent catheterisation reduce urethral micro trauma: A prospective, randomised, participant-blinded, crossover study of three different types of catheters,” *European Urology*, vol. 48, no. 6, p. 978–983, dec 2005. [Online]. Available: https://pubmed.ncbi.nlm.nih.gov/16126331/

[74] C. Lin, H. Wan, H. J. Kaper, and P. K. Sharma, “A hyaluronic acid based lubricious coating for cardiovascular catheters,” *Tribology International*, vol. 151, nov 2020. [Online]. Available: http://creativecommons.org/licenses/by/4.0/

[75] P. Sobolewski and M. El Fray, “Cardiac catheterization: Consequences for the endothelium and potential for nanomedicine,” *Wiley Interdisciplinary Reviews: Nanomedicine and Nanobiotechnology*, vol. 7, no. 3, p. 458–473, 2015.

[76] K. H. Dellimore, A. J. Mank, J. Wojnowski, C. Noble, and S. E. Franklin, “Evaluation of catheter-induced tribological damage to porcine aorta using infra-red spectroscopy,” *Biotribology*, vol. 7, p. 11–21, 2016.

[77] R. Franke, R. Fuhrmann, A. Krüger, and F. Jung, "Reaction of arterial endothelial cells to stent impression: In vitro study using a model of the human artery wall," *Journal of Cellular Biotechnology*, vol. 1, no. 1, p. 119–130, jul 2015.

[78] A. C. Dunn, T. D. Zaveri, B. G. Keselowsky, and W. G. Sawyer, "Macroscopic friction coefficient measurements on living endothelial cells," *Tribology Letters*, vol. 27, no. 2, p. 233–238, 2007.

[79] T. Chen, M. Lancaster, D. S. Lin, M. G. Doyle, T. L. Forbes, and C. H. Amon, "Measurement of Frictional Properties of Aortic Stent Grafts and Their Delivery Systems," *Journal of Medical Devices, Transactions of the ASME*, vol. 13, no. 2, jun 2019.

[80] O. M. McGee, W. Sun, and L. M. McNamara, "An in vitro model quantifying the effect of calcification on the tissue–stent interaction in a stenosed aortic root," *Journal of Biomechanics*, vol. 82, p. 109–115, jan 2019. [Online]. Available: https://pubmed.ncbi.nlm.nih.gov/30381157/

[81] D. Dean, J. Hemmer, A. Vertegel, and M. LaBerge, "Frictional behavior of individual vascular smooth muscle cells assessed by lateral force microscopy," *Materials*, vol. 3, no. 9, p. 4668–4680, 2010. [Online]. Available: /pmc/articles/PMC3113676//pmc/articles/PMC3113676/?report=abstracthttps://www.ncbi.nlm.nih.gov/pmc/articles/PMC3113676/

[82] K. Liffman, M. M. Lawrence-Brown, J. B. Semmens, A. Bui, M. Rudman, and D. E. Hartley, "Analytical modeling and numerical simulation of forces in an endoluminal graft," *Journal of Endovascular Therapy*, vol. 8, no. 4, p. 358–371, 2001. [Online]. Available: https://www.researchgate.net/publication/11794431

[83] G. A. Holzapfel, M. Stadler, and T. C. Gasser, "Changes in the mechanical environment of stenotic arteries during interaction with stents: Computational assessment of parametric stent designs," *Journal of Biomechanical Engineering*, vol. 127, no. 1, p. 166–180, feb 2005. [Online]. Available: https://pubmed.ncbi.nlm.nih.gov/15868799/

[84] D. L. Burris and W. G. Sawyer, "Addressing practical challenges of low friction coefficient measurements," *Tribology Letters*, vol. 35, no. 1, p. 17–23, 2009. [Online]. Available: https://www.researchgate.net/publication/225859873

[85] A. Schütte, M. Mack, H. Behler, M. Ruland, C. Weiß, and M. L. Schwarz, "Tribometer for measuring coefficients of friction of uneven surfaces like articular cartilage," *Review of Scientific Instruments*, vol. 91, no. 3, p. 034102, mar 2020. [Online]. Available: http://aip.scitation.org/doi/10.1063/1.5124006

[86] T. L. Schmitz, J. E. Action, J. C. Ziegert, and W. G. Sawyer, "The difficulty of measuring low friction: Uncertainty analysis for friction coefficient measurements," *Journal of Tribology*, vol. 127, no. 3, p. 673–678, jul 2005.

[87] C. T. McKee, J. A. Last, P. Russell, and C. J. Murphy, "Indentation versus tensile measurements of young's modulus for soft biological tissues," *Tissue Engineering - Part B: Reviews*, vol. 17, no. 3, p. 155–164, jun 2011. [Online]. Available: /pmc/articles/PMC3099446//pmc/articles/PMC3099446/?report=abstracthttps://www.ncbi.nlm.nih.gov/pmc/articles/PMC3099446/

[88] H. Yoshie, N. Koushki, R. Kaviani, M. Tabatabaei, K. Rajendran, Q. Dang, A. Husain, S. Yao, C. Li, J. K. Sullivan, M. Saint-Geniez, R. Krishnan, and A. J. Ehrlicher, "Traction force screening enabled by compliant pdms elastomers," *Biophysical Journal*, vol. 114, no. 9, pp. 2194–2199, 2018. [Online]. Available: https://www.sciencedirect.com/science/article/pii/S0006349518304399

[89] X. Y. Wang, C. Fillafer, C. Pichl, S. Deinhammer, R. Hofer-Warbinek, M. Wirth, and F. Gabor, "A multichannel acoustically driven microfluidic chip to study particle-cell interactions," *Biomicrofluidics*, vol. 7, no. 4, 2013. [Online]. Available: http://dx.doi.org/10.1063/1.4819273]

[90] J. H. Kim, P. Chhai, and K. Rhee, "Development and characterization of viscoelastic polydimethylsiloxane phantoms for simulating arterial wall motion," *Medical Engineering & Physics*, vol. 91, pp. 12–18, 2021. [Online]. Available: https://www.sciencedirect.com/science/article/pii/S1350453321000278

[91] S. Deguchi, J. Hotta, S. Yokoyama, and T. S. Matsui, "Viscoelastic and optical properties of four different PDMS polymers," *Journal of Micromechanics and Microengineering*, vol. 25, no. 9, 2015.

[92] S.-S. D. Carter, A.-R. Atif, S. Kadekar, I. Lanekoff, H. Engqvist, O. P. Varghese, M. Tenje, and G. Mestres, "PDMS leaching and its implications for on-chip studies focusing on bone regeneration applications," *Organs-on-a-Chip*, vol. 2, p. 100004, 2020.

[93] K. J. Regehr, M. Domenech, J. T. Koepsel, K. C. Carver, S. J. Ellison-Zelski, W. L. Murphy, L. A. Schuler, E. T. Alarid, and D. J. Beebe, "Biological implications of polydimethylsiloxane-based microfluidic cell culture," p. 2132–2139, 2009. [Online]. Available: www.rsc.org/loc

[94] M. W. Toepke and D. J. Beebe, "PDMS absorption of small molecules and consequences in microfluidic applications," p. 1484–1486, 2006. [Online]. Available: www.rsc.org/loc

[95] B. J. van Meer, H. de Vries, K. S. Firth, J. van Weerd, L. G. Tertoolen, H. B. Karperien, P. Jonkheijm, C. Denning, A. P. IJzerman, and C. L. Mummery, "Small molecule absorption by PDMS in the context of drug response bioassays," *Biochemical and Biophysical Research Communications*, vol. 482, no. 2, p. 323–328, 2017. [Online]. Available: http://creativecommons.org/licenses/by/4.0/

[96] J. N. Lee, C. Park, and G. M. Whitesides, "Solvent Compatibility of Poly(dimethylsiloxane)-Based Microfluidic Devices," *Analytical Chemistry*, vol. 75, no. 23, p. 6544–6554, 2003. [Online]. Available: https://pubs.acs.org/sharingguidelines

[97] K. Raman, T. R. Srinivasa Murthy, and G. M. Hegde, "Fabrication of refractive index tunable Polydimethylsiloxane photonic crystal for biosensor application," in *Physics Procedia*, vol. 19. Elsevier, jan 2011, p. 146–151.

[98] C. Smart and E. Willis, "Determination of refractive indices of polystyrene latices by light scattering," *Journal of Colloid And Interface Science*, vol. 25, no. 4, p. 577–583, 1967.

[99] H. Zeng and J. R. Sanes, "Neuronal cell-type classification: Challenges, opportunities and the path forward," p. 530–546, 2017. [Online]. Available: www.nature.com/nrn

[100] L. Bacakova, M. Travnickova, E. Filova, R. Matějka, J. Stepanovska, J. Musilkova, J. Zarubova, and M. Molitor, "The Role of Vascular Smooth Muscle Cells in the Physiology and Pathophysiology of Blood Vessels," in *Muscle Cell and Tissue - Current Status of Research Field*. IntechOpen, oct 2018. [Online]. Available: https://www.intechopen.com/chapters/61602

[101] B. B. Hafen and B. Burns, *Physiology, Smooth Muscle*. StatPearls Publishing, aug 2019. [Online]. Available: https://www.ncbi.nlm.nih.gov/books/NBK526125/http://www.ncbi.nlm.nih.gov/pubmed/30252381

[102] M. KGaA, "MG-63 Cell Line human." [Online]. Available: https://www.sigmaaldrich.com/GB/en/product/sigma/cb{_}86051601

[103] E. M. Conway and P. Carmeliet, "The diversity of endothelial cells: A challenge for therapeutic angiogenesis," *Genome Biology*, vol. 5, no. 2, p. 1–5, jan 2004. [Online]. Available: https://genomebiology.biomedcentral.com/articles/10.1186/gb-2004-5-2-207

[104] I. Lang, M. A. Pabst, U. Hiden, A. Blaschitz, G. Dohr, T. Hahn, and G. Desoye, "Heterogeneity of microvascular endothelial cells isolated from human term placenta and macrovascular umbilical vein endothelial cells," *European Journal of Cell Biology*, vol. 82, no. 4, p. 163–173, apr 2003.

[105] M. Otto, F. Bittinger, J. Kriegsmann, and C. J. Kirkpatrick, "Differential adhesion of polymorphous neutrophilic granulocytes to macro- and microvascular endothelial cells under flow conditions," *Pathobiology*, vol. 69, no. 3, p. 159–171, 2001. [Online]. Available: https://www.karger.com/Article/FullText/48771https://www.karger.com/Article/Abstract/48771

[106] CoolLED, "pE-300lite." [Online]. Available: https://www.coolled.com/products/pe-300lite/

[107] C. McQuin, A. Goodman, V. Chernyshev, L. Kamentsky, B. A. Cimini, K. W. Karhohs, M. Doan, L. Ding, S. M. Rafelski, D. Thirstrup, W. Wiegraebe, S. Singh, T. Becker, J. C. Caicedo, and A. E. Carpenter, "CellProfiler 3.0: Next-generation image processing for biology," *PLoS Biology*, vol. 16, no. 7, p. e2005970, jul 2018.

[108] E. Kilinc and R. J. Hand, "Mechanical properties of soda-lime-silica glasses with varying alkaline earth contents," *Journal of Non-Crystalline Solids*, vol. 429, p. 190–197, 2015. [Online]. Available: http://eprints.whiterose.ac.uk/95393/

[109] Schott_AG, "Chemical Composition." [Online]. Available: https://www.schott.com/d/tubing/9a0f5126-6e35-43bd-bf2a-349912caf9f2/schott-algae-brochure-borosilicate.pdf

[110] MatWeb LLC, "AK STeel 316 Austenitic Stainless Steel," 2015. [Online]. Available: http://www.matweb.com/search/DataSheet.aspx?MatGUID=9e9ab696974044cab4a7fd83687934eb{&}ckck=1

[111] J. E. Mark, D. L. Kerbow, A. C. M. Kuo, and Z. Pu, "Polymer data handbook, 2nd ed," *Journal of the American Chemical Society*, vol. 131, no. 44, p. 16330–16330, 2009.

[112] P. J. Rae and E. N. Brown, "The properties of poly(tetrafluoroethylene) (PTFE) in tension," *Polymer*, vol. 46, no. 19 SPEC. ISS., p. 8128–8140, sep 2005.

[113] F. E. Grubbs, "Sample Criteria for Testing Outlying Observations," *The Annals of Mathematical Statistics*, vol. 21, no. 1, p. 27–58, mar 1950. [Online]. Available: https://projecteuclid.org/journals/annals-of-mathematical-statistics/volume-21/issue-1/Sample-Criteria-for-Testing-Outlying-Observations/10.1214/aoms/1177729885.fullhttps://projecteuclid.org/journals/annals-of-mathematical-statistics/volume-21/issue-1/Sample-Criteria-for-Testing-Outlying-Observations/10.1214/aoms/1177729885.short

[114] NIST, "1.3.5.17. Detection of Outliers," p. 1–5, 2013. [Online]. Available: https://www.itl.nist.gov/div898/handbook/eda/section3/eda35h.htmhttp://www.itl.nist.gov/div898/handbook/eda/section3/eda35h.htm

[115] S. S. Shapiro and M. B. Wilk, "An Analysis of Variance Test for Normality (Complete Samples)," *Biometrika*, vol. 52, no. 3/4, p. 591, 1965.

[116] W. Feneberg, M. Aepfelbacher, and E. Sackmann, "Microviscoelasticity of the apical cell surface of human umbilical vein endothelial cells (HUVEC) within confluent monolayers," *Biophysical Journal*, vol. 87, no. 2, p. 1338–1350, aug 2004. [Online]. Available: http://www.cell.com/article/S0006349504736139/fulltexthttp://www.cell.com/article/S0006349504736139/abstracthttps://www.cell.com/biophysj/abstract/S0006-3495(04)73613-9

[117] H. Sato, N. Kataoka, F. Kajiya, M. Katano, T. Takigawa, and T. Masuda, "Kinetic study on the elastic change of vascular endothelial cells on collagen matrices by atomic force microscopy," *Colloids and Surfaces B: Biointerfaces*, vol. 34, no. 2, pp. 141–146, 2004. [Online]. Available: https://www.sciencedirect.com/science/article/pii/S0927776503003114

[118] A. Krüger-Genge, A. Blocki, R. P. Franke, and F. Jung, "Vascular endothelial cell biology: An update," sep 2019. [Online]. Available: /pmc/articles/PMC6769656//pmc/articles/PMC6769656/?report=abstracthttps://www.ncbi.nlm.nih.gov/pmc/articles/PMC6769656/

[119] F. M, *The Endothelium: Part 1: Multiple Functions of the Endothelial Cells—Focus on Endothelium-Derived Vasoactive Mediators*. Morgan & Claypool Publishers LLC, jun 2011, vol. 3. [Online]. Available: https://pubmed.ncbi.nlm.nih.gov/21850763/

[120] S. M. Zehnder, M. Suaris, M. M. Bellaire, and T. E. Angelini, "Cell volume fluctuations in MDCK monolayers," *Biophysical Journal*, vol. 108, no. 2, p. 247–250, 2015. [Online]. Available: http://dx.doi.org/10.1016/j.bpj.2014.11.1856

[121] M. Takahashi, E. L. Petry, P. R. Lurie, S. E. Kirkpatrick, and R. E. Stanton, "Percutaneous heart catheterization in infants and children. I. Catheter placement and manipulation with guide wires." *Circulation*, vol. 42, no. 6, p. 1037–1048, 1970. [Online]. Available: https://www.ahajournals.org/doi/abs/10.1161/01.CIR.42.6.1037

[122] S. E. Kirkpatrick, M. Takahashi, E. L. Petry, R. E. Stanton, and P. R. Lurie, "Percutaneous heart catheterization in infants and children. II. Prospective study of results and complications in 127 consecutive cases." *Circulation*, vol. 42, no. 6, p. 1049–1056, 1970. [Online]. Available: https://www.ahajournals.org/doi/abs/10.1161/01.cir.42.6.1049

[123] S. medical, "Jelco® Seriva™ IV Catheters, Peripheral IV Catheters | Smiths Medical." [Online]. Available: https://www.smiths-medical.com/products/peripheral-iv-catheters/conventional-iv-catheters/jelco-seriva-iv-catheters

[124] M. Fineschi, T. Gori, G. Sinicropi, and A. Bravi, "Polytetrafluoroethylene (PTFE) covered stents for the treatment of coronary artery aneurysms," *Heart*, vol. 90, no. 5, p. 490, may 2004. [Online]. Available: https://heart.bmj.com/content/90/5/490https://heart.bmj.com/content/90/5/490.abstract

[125] S. Neupane and K. Dass, "Use of polytetrafluoroethylene (PTFE)-covered stent in treatment of RCA aneurysm," p. 144, 2014. [Online]. Available: /pmc/articles/PMC4832776/https://www.ncbi.nlm.nih.gov/pmc/articles/PMC4832776/

[126] Johannes Vermehren, “PTFE Stents for Treatment of Malignant Biliary Strictures,” *https://clinicaltrials.gov/show/NCT03763214*, 2018. [Online]. Available: https://www.cochranelibrary.com/central/doi/10.1002/central/CN-01918538/full

[127] A. Plastics, “Teflon Coated Guidewire Solutions | PTFE Nitinol Tube | Applied Plastics.” [Online]. Available: https://appliedplastics.com/about/news/ptfe-coated-nitinol-tube-for-ptca-guide-wires-catheters-and-needles/

[128] Medica-Europe, “PTFE Coated Guidewires - Boston Scientific.” [Online]. Available: https://www.medica-europe.com/products-en/cardiologyradiology/guidewires/ptfe-coated-guidewires

[129] C. Feng and X. Huang, “Polymer Brushes: Efficient Synthesis and Applications,” *Accounts of Chemical Research*, vol. 51, no. 9, p. 2314–2323, sep 2018. [Online]. Available: https://pubs.acs.org/doi/abs/10.1021/acs.accounts.8b00307

[130] L. Möckl, “The Emerging Role of the Mammalian Glycocalyx in Functional Membrane Organization and Immune System Regulation,” p. 253, apr 2020.

[131] J. Klein, “Hydration lubrication,” *Friction*, vol. 1, no. 1, p. 1–23, 2013.

[132] I. Rosenhek-Goldian, N. Kampf, and J. Klein, “Trapped Aqueous Films Lubricate Highly Hydrophobic Surfaces,” *ACS Nano*, 2018. [Online]. Available: https://pubs.acs.org/doi/pdf/10.1021/acsnano.8b04735

[133] J. T. Black and R. A. Kohser, *DeGarmo’s Materials and Processes in Manufacturing*, 11th ed. Wiley, 2011.

[134] P. M. Mcguiggan, J. S. Wallace, D. T. Smith, I. Sridhar, Z. W. Zheng, and K. L. Johnson, “Contact mechanics of layered elastic materials: experiment and theory,” *J. Phys. D: Appl. Phys*, vol. 40, p. 5984–5994, 2007.

[135] Y. M. Efremov, S. L. Kotova, and P. S. Timashev, “Viscoelasticity in simple indentation-cycle experiments: a computational study,” *Scientific Reports*, vol. 10, no. 1, p. 13302, 2020.

[136] S. K. Rhee, “Surface energies of silicate glasses calculated from their wettability data,” *Journal of Materials Science*, vol. 12, no. 4, p. 823–824, 1977. [Online]. Available: https://doi.org/10.1007/BF00548176

[137] M. Kłonica and J. Kuczmaszewski, "Determining the value of surface free energy on the basis of the contact angle," *Advances in Science and Technology Research Journal*, vol. 11, no. 1, p. 66–74, 2017. [Online]. Available: https://doi.org/10.12913/22998624/68800

[138] A. J. Kinloch and A. J. Kinloch, *Adhesion and adhesives: science and technology*. Springer Science & Business Media, 1987.

[139] A. J. Kirtane and G. W. Stone, "How to minimize stent thrombosis," *Circulation*, vol. 124, no. 11, p. 1283–1287, sep 2011. [Online]. Available: https://www.ahajournals.org/doi/abs/10.1161/CIRCULATIONAHA.110.976829

[140] M. J. Lim, "10 - complications of percutaneous coronary interventions," in *The Interventional Cardiac Catheterization Handbook (Fourth Edition)*, 4th ed., M. J. Kern, P. Sorajja, and M. J. Lim, Eds. Elsevier, 2018, pp. 261–285. [Online]. Available: https://www.sciencedirect.com/science/article/pii/B9780323476713000107

[141] P. W. Serruys, P. de Jaegere, F. Kiemeneij, C. Macaya, W. Rutsch, G. Heyndrickx, H. Emanuelsson, J. Marco, V. Legrand, P. Materne, J. Belardi, U. Sigwart, A. Colombo, J. J. Goy, P. van den Heuvel, J. Delcan, and M.-a. Morel, "A Comparison of Balloon-Expandable-Stent Implantation with Balloon Angioplasty in Patients with Coronary Artery Disease," *New England Journal of Medicine*, vol. 331, no. 8, p. 489–495, jan 1994. [Online]. Available: https://www.nejm.org/doi/full/10.1056/nejm199408253310801

[142] D. L. Fischman, M. B. Leon, D. S. Baim, R. A. Schatz, M. P. Savage, I. Penn, K. Detre, L. Veltri, D. Ricci, M. Nobuyoshi, M. Cleman, R. Heuser, D. Almond, P. S. Teirstein, R. D. Fish, A. Colombo, J. Brinker, J. Moses, A. Shaknovich, J. Hirshfeld, S. Bailey, S. Ellis, R. Rake, and S. Goldberg, "A Randomized Comparison of Coronary-Stent Placement and Balloon Angioplasty in the Treatment of Coronary Artery Disease," *New England Journal of Medicine*, vol. 331, no. 8, p. 496–501, aug 1994. [Online]. Available: https://pubmed.ncbi.nlm.nih.gov/8041414/

[143] M. Moussavian, P. J. Casterella, and P. S. Teirstein, "Restenosis after Angioplasty," *Current treatment options in cardiovascular medicine*, vol. 3, no. 2, p. 103–113, apr 2001. [Online]. Available: https://pubmed.ncbi.nlm.nih.gov/11242557/

[144] A. W. Chan, S. R. Ramee, T. Collins, H. Quintana, and C. J. White, "Rotaglide-facilitated stent delivery: Mission accomplished," *Catheterization and Cardiovascular Interventions*, vol. 59, no. 4, p. 477–481, aug 2003. [Online]. Available: https://pubmed.ncbi.nlm.nih.gov/12891612/

[145] A. Singh, M. Awar, A. Ahmed, D. L. Fischman, P. Walinsky, and M. P. Savage, "Facilitated stent delivery using applied topical lubrication," *Catheterization and Cardiovascular Interventions*, vol. 69, no. 2, p. 218–222, feb 2007.

[146] S. Elmore, "Apoptosis: A Review of Programmed Cell Death," p. 495–516, 2007. [Online]. Available: /pmc/articles/PMC2117903//pmc/articles/PMC2117903/?report=abstracthttps://www.ncbi.nlm.nih.gov/pmc/articles/PMC2117903/

[147] S. M. Hart, G. D. Degen, J. M. Urueña, P. P. Levings, W. G. Sawyer, and A. A. Pitenis, "Friction-Induced Apoptosis," *Tribology Letters*, vol. 67, no. 3, p. 82, 2019. [Online]. Available: https://doi.org/10.1007/s11249-019-1197-0

[148] J. Zhang, X. Wang, W. Cui, W. Wang, H. Zhang, L. Liu, Z. Zhang, Z. Li, G. Ying, N. Zhang, and B. Li, "Visualization of caspase-3-like activity in cells using a genetically encoded fluorescent biosensor activated by protein cleavage," *Nature Communications*, vol. 4, no. 1, p. 1–13, jul 2013. [Online]. Available: https://www.nature.com/articles/ncomms3157

[149] Z. Zhang, J. Dequidt, J. Back, H. Liu, and C. Duriez, "Motion Control of Cable-Driven Continuum Catheter Robot Through Contacts," *IEEE Robotics and Automation Letters*, vol. 4, no. 2, p. 1852–1859, 2019. [Online]. Available: https://hal.archives-ouvertes.fr/hal-02052637

[150] R. D. Brewer, "Improving Peripheral IV Catheterization Through Robotics: from Simple Assistive Devices to a Fully-Autonomous System," Ph.D. dissertation, STANFORD UNIVERSITY, 2015. [Online]. Available: http://purl.stanford.edu/qh215qd3853https://search.proquest.com/dissertations-theses/improving-peripheral-iv-catheterization-through/docview/2501173397/se-2?accountid=13042{%}0Ahttp://oxfordsfx.hosted.exlibrisgroup.com/oxford?url{_}ver=Z39.88-2004{&}rft{_}val{_}fm

[151] Y. Okumura, S. B. Johnson, T. J. Bunch, B. D. Henz, C. J. O'Brien, and D. L. Packer, "A systematical analysis of in vivo contact forces on virtual catheter tip/tissue surface contact during cardiac mapping and intervention," *Journal of Cardiovascular Electrophysiology*, vol. 19, no. 6, p. 632–640, jun 2008.

[152] A. B. Haymet, N. Bartnikowski, E. S. Wood, M. P. Vallely, A. McBride, S. Yacoub, S. B. Biering, E. Harris, J. Y. Suen, and J. F. Fraser, "Studying the Endothelial Glycocalyx in vitro: What Is Missing?" *Frontiers in Cardiovascular Medicine*, vol. 8, p. 280, apr 2021.

[153] D. Chappell, M. Jacob, O. Paul, M. Rehm, U. Welsch, M. Stoeckelhuber, P. Conzen, and B. F. Becker, "The glycocalyx of the human umbilical vein endothelial cell: An impressive structure ex vivo but not in culture," p. 1313–1317, jun 2009. [Online]. Available: http://circres.ahajournals.org

[154] D. Tsvirkun, A. Grichine, A. Duperray, C. Misbah, and L. Bureau, "Microvasculature on a chip: Study of the Endothelial Surface Layer and the flow structure of Red Blood Cells," *Scientific Reports*, vol. 7, no. 1, p. 1–11, mar 2017. [Online]. Available: https://www.nature.com/articles/srep45036

[155] A. Ueda, M. Shimomura, M. Ikeda, R. Yamaguchi, and K. Tanishita, "Effect of glycocalyx on shear-dependent albumin uptake in endothelial cells," *American Journal of Physiology - Heart and Circulatory Physiology*, vol. 287, no. 5 56-5, p. 2287–2294, nov 2004. [Online]. Available: https://journals.physiology.org/doi/abs/10.1152/ajpheart.00808.2003

[156] S. N. Bhatia and D. E. Ingber, "Microfluidic organs-on-chips," p. 760–772, aug 2014. [Online]. Available: https://www.nature.com/articles/nbt.2989

[157] E. Berthier, E. W. Young, and D. Beebe, "Engineers are from PDMS-land, biologists are from polystyrenia," p. 1224–1237, mar 2012. [Online]. Available: https://pubs.rsc.org/en/content/articlehtml/2012/lc/c2lc20982ahttps://pubs.rsc.org/en/content/articlelanding/2012/lc/c2lc20982a

[158] E. K. Sackmann, A. L. Fulton, and D. J. Beebe, "The present and future role of microfluidics in biomedical research," p. 181–189, 2014.

[159] S. Varma and J. Voldman, "Caring for cells in microsystems: principles and practices of cell-safe device design and operation," *Lab on a Chip*, vol. 18, no. 22, p. 3333–3352, nov 2018. [Online]. Available: https://pubs.rsc.org/en/content/articlehtml/2018/lc/c8lc00746bhttps://pubs.rsc.org/en/content/articlelanding/2018/lc/c8lc00746b

[160] S. K. Sia and G. M. Whitesides, “Microfluidic devices fabricated in poly(dimethylsiloxane) for biological studies,” *Electrophoresis*, vol. 24, no. 21, p. 3563–3576, nov 2003.

[161] E. Jastrzebska, A. Zuchowska, S. Flis, P. Sokolowska, M. Bulka, A. Dybko, and Z. Brzozka, “Biological characterization of the modified poly(dimethylsiloxane) surfaces based on cell attachment and toxicity assays,” *Biomicrofluidics*, vol. 12, no. 4, 2018. [Online]. Available: https://doi.org/10.1063/1.5035176

[162] A. Gokaltun, M. L. Yarmush, A. Asatekin, and O. B. Usta, “Recent advances in nonbiofouling PDMS surface modification strategies applicable to microfluidic technology,” *TECHNOLOGY*, vol. 05, no. 01, p. 1–12, mar 2017. [Online]. Available: /pmc/articles/PMC5501164//pmc/articles/PMC5501164/?report=abstracthttps://www.ncbi.nlm.nih.gov/pmc/articles/PMC5501164/

[163] C. Kühlbach, S. da Luz, F. Baganz, V. C. Hass, and M. M. Mueller, “A microfluidic system for the investigation of tumor cell extravasation,” *Bioengineering*, vol. 5, no. 2, jun 2018. [Online]. Available: /pmc/articles/PMC6027408//pmc/articles/PMC6027408/?report=abstracthttps://www.ncbi.nlm.nih.gov/pmc/articles/PMC6027408/

[164] P. G. Gezer, S. Brodsky, A. Hsiao, G. L. Liu, and J. L. Kokini, “Modification of the hydrophilic/hydrophobic characteristic of zein film surfaces by contact with oxygen plasma treated PDMS and oleic acid content,” *Colloids and Surfaces B: Biointerfaces*, vol. 135, p. 433–440, nov 2015.

[165] F. Akther, S. B. Yakob, N. T. Nguyen, and H. T. Ta, “Surface Modification Techniques for Endothelial Cell Seeding in PDMS Microfluidic Devices,” p. 182, nov 2020. [Online]. Available: https://www.mdpi.com/2079-6374/10/11/182/htmhttps://www.mdpi.com/2079-6374/10/11/182

[166] M. J. Owen and P. J. Smith, “Plasma treatment of polydimethylsiloxane,” *Journal of Adhesion Science and Technology*, vol. 8, no. 10, p. 1063–1075, 1994. [Online]. Available: https://www.tandfonline.com/doi/abs/10.1163/156856194X00942

[167] H. Hillborg and U. Gedde, “Hydrophobicity changes in silicone rubbers,” *IEEE Transactions on Dielectrics and Electrical Insulation*, vol. 6, no. 5, p. 703–717, dec 1999.

[168] D. T. Eddington, J. P. Puccinelli, and D. J. Beebe, “Thermal aging and reduced hydrophobic recovery of polydimethylsiloxane,” *Sensors and Actuators, B: Chemical*, vol. 114, no. 1, p. 170–172, mar 2006.

[169] J. Alipal, N. A. Mohd Pu’ad, T. C. Lee, N. H. Nayan, N. Sahari, H. Basri, M. I. Idris, and H. Z. Abdullah, “A review of gelatin: Properties, sources, process, applications, and commercialisation,” in *Materials Today: Proceedings*, vol. 42, 2019, p. 240–250. [Online]. Available: https://doi.org/10.1016/j.matpr.2020.12.922

[170] X.-Y. Wang, Z.-H. Jin, B.-W. Gan, S.-W. Lv, M. Xie, and W.-H. Huang, “Engineering interconnected 3D vascular networks in hydrogels using molded sodium alginate lattice as the sacrificial templates,” in *Lab Chip*, vol. 00, 2014, p. 1–8. [Online]. Available: www.rsc.org/

[171] J. W. Nichol, S. T. Koshy, H. Bae, C. M. Hwang, S. Yamanlar, and A. Khademhosseini, “Cell-laden microengineered gelatin methacrylate hydrogels,” *Biomaterials*, vol. 31, no. 21, p. 5536–5544, jul 2010.

[172] C. G. Cornelissen, M. Dietrich, K. Gromann, J. Frese, S. Krueger, J. S. Sachweh, and S. Jockenhoevel, “Fibronectin coating of oxygenator membranes enhances endothelial cell attachment.” *Biomedical engineering online*, vol. 12, p. 7, jan 2013.

Appendix A

Scripts

A.1 Image Stitcher

```
classdef imageStitcherv2 < handle
    properties
        initialised = false;
        imageLoaded = false;
        figuresInitialised = false;
        originalImages
        originalImage_red
        originalImage_blue
        originalImage_bf
        originalImage_combined
        BCAdjustedImage_red
        BCAdjustedImage_blue
        BCAdjustedImage_bf
        BCAdjustedImage_combined
        oldXLim = [0 1];
        oldYLim = [0 1];
        manipulatedImage
        myInstanceControlFigure
        myInstanceImageFigure
        loadedFromPath = {pwd}
        lTopVal = 1
        lBotVal = 1
        lRigVal = 1
        lLefVal = 1
        rotAngVal = 0
        lTopUI
        lBotUI
        lRigUI
        lLefUI
        red_gain_inputBox
        blue_gain_inputBox
        bf_gain_inputBox
        red_min_inputBox
```

```
34          blue_min_inputBox
35          bf_min_inputBox
36          red_max_inputBox
37          blue_max_inputBox
38          bf_max_inputBox
39          red_gain = 50
40          blue_gain = 120
41          bf_gain = 1
42          red_min = 0
43          blue_min = 0
44          bf_min = 0
45          red_max = 65535
46          blue_max = 65535
47          bf_max = 65535
48          rotAngUI
49          consoleUI
50          originalImageAxes_red
51          originalImageAxes_blue
52          originalImageAxes_combined
53          histogramAxes_red
54          histogramAxes_blue
55          histogramAxes_bf
56          manipulatedImageAxes
57          eventHistory
58          imageAxes
59          guessed_target_filename
60      end
61
62      methods
63          function obj = imageStitcherv2()
64              obj.myInstanceControlFigure = figureFullscreen(1);
65              set(obj.myInstanceControlFigure, 'units','normalized');
66              obj.myInstanceImageFigure= figureFullscreen(3);
67              set(obj.myInstanceImageFigure, 'units','normalized');
68              obj.eventHistory = {'created.'};
69              obj.plotMyFigure();
70          end
71
72          function addHistoryEntry(this, text)
73              this.eventHistory = [text, this.eventHistory];
74          end
75
76          function load(this, scr, event)
77              [this.originalImages, this.loadedFromPath,...
78                  this.guessed_target_filename] =...
79                  overlapImages(this.loadedFromPath{1});
80              this.originalImage_red = this.originalImages{1};
81              this.originalImage_blue = this.originalImages{2};
82              this.originalImage_bf = this.originalImages{3};
83              this.originalImage_combined = cat(3, ...
                    this.originalImage_red,...
84                  this.originalImage_red.*0, this.originalImage_blue);
85              this.addHistoryEntry(strcat('Loaded from Path ',...
86                  this.loadedFromPath{1}, ' the Red Images.'));
```

```
87              this.addHistoryEntry(strcat('Loaded from Path ',...
88                  this.loadedFromPath{2}, ' the Blue Images.'));
89              this.addHistoryEntry(strcat('Loaded from Path ',...
90                  this.loadedFromPath{3}, ' the BF Images.'));
91              this.figuresInitialised = false;
92              this.imageLoaded = true;
93              this.plotMyFigure();
94          end
95
96          function save(this, scr, event)
97              this.plotMyFigure();
98              [file,path] = ...
                    uiputfile(strcat(this.loadedFromPath{1},'/',...
99                  this.guessed_target_filename,'.MAT'));
100             this.addHistoryEntry(strcat('Saved Image to Location ...
                    ',...
101                 path, file, '.'));
102             imwrite(this.originalImage_red, strcat(path, ...
                    file(1:end-4),...
103                 '_originalImage_red.TIF'));
104             imwrite(this.originalImage_blue, strcat(path, ...
                    file(1:end-4),...
105                 '_originalImage_blue.TIF'));
106             imwrite(this.originalImage_bf, strcat(path, ...
                    file(1:end-4), ...
107                 '_originalImage_bf.TIF'));
108             imwrite(this.originalImage_combined, strcat(path,...
109                 file(1:end-4), '_originalImage_combined.TIF'));
110             imwrite(this.BCAdjustedImage_red, strcat(path,...
111                 file(1:end-4), '_BCAdjustedImage_red.TIF'));
112             imwrite(this.BCAdjustedImage_blue, strcat(path,...
113                 file(1:end-4), '_BCAdjustedImage_blue.TIF'));
114             imwrite(this.BCAdjustedImage_bf, strcat(path,...
115                 file(1:end-4), '_BCAdjustedImage_bf.TIF'));
116             imwrite(this.BCAdjustedImage_combined, strcat(path,...
117                 file(1:end-4), '_BCAdjustedImage_combined.TIF'));
118             f = fopen(strcat(path, file(1:end-4),...
119                 '_BCAdjustConfig.txt'), 'w');
120             fprintf(f,'1 %f\n',this.red_gain);
121             fprintf(f,'2 %f\n',this.red_min);
122             fprintf(f,'3 %f\n',this.red_max);
123             fprintf(f,'4 %f\n',this.blue_gain);
124             fprintf(f,'5 %f\n',this.blue_min);
125             fprintf(f,'6 %f\n',this.blue_max);
126             fprintf(f,'7 %f\n',this.bf_gain);
127             fprintf(f,'8 %f\n',this.bf_min);
128             fprintf(f,'9 %f\n',this.bf_max);
129             fclose(f);
130             this.plotMyFigure();
131
132         end
133
134         function plotMyFigure(this, ¬, ¬)
```

```
135             %first check if figure has been initialised. If so, ...
                    save values
136             if this.figuresInitialised
137                 this.red_gain = ...
                        str2double(this.red_gain_inputBox.String)
138                 this.blue_gain = ...
                        str2double(this.blue_gain_inputBox.String)
139                 this.bf_gain = ...
                        str2double(this.bf_gain_inputBox.String)
140                 this.red_min = ...
                        str2double(this.red_min_inputBox.String)
141                 this.blue_min = ...
                        str2double(this.blue_min_inputBox.String)
142                 this.bf_min = str2double(this.bf_min_inputBox.String)
143                 this.red_max = ...
                        str2double(this.red_max_inputBox.String)
144                 this.blue_max = ...
                        str2double(this.blue_max_inputBox.String)
145                 this.bf_max = str2double(this.bf_max_inputBox.String)
146                 this.lTopVal = str2double(this.lTopUI.String);
147                 this.lBotVal = str2double(this.lBotUI.String);
148                 this.lLefVal = str2double(this.lLefUI.String);
149                 this.lRigVal = str2double(this.lRigUI.String);
150                 this.rotAngVal = str2double(this.rotAngUI.String);
151                 this.oldXLim = this.imageAxes(4).XLim;
152                 this.oldYLim = this.imageAxes(4).YLim;
153              else
154                  this.oldXLim = [0  1];
155                  this.oldYLim = [0  1];
156             end
157             if this.lLefVal < 1
158                 this.lLefVal = 1;
159             end
160             if this.lTopVal <1
161                 this.lTopVal = 1;
162             end
163
164             this.BCAdjustImages();
165             this.originalImage_combined = cat(3,...
166                 this.originalImage_red,...
167                 this.originalImage_red*0,...
168                 this.originalImage_blue);
169             this.BCAdjustedImage_combined = cat(3,...
170                 this.BCAdjustedImage_red,...
171                 this.BCAdjustedImage_red*0,...
172                 this.BCAdjustedImage_blue);
173             % now clear the figure
174             clf(this.myInstanceControlFigure)
175             clf(this.myInstanceImageFigure)
176
177             % select figure that carries all the control elements
178             figure(this.myInstanceControlFigure)
179             % add gui elements to control figure
180             this.drawControlFigure()
```

```
181             imageHeigth = size(this.originalImage_red, 1);
182             imageWidth  = size(this.originalImage_red, 2);
183             figure(this.myInstanceImageFigure)
184             this.imageAxes = generateAxes(2,4,0.051,0.051);
185             linkaxes(this.imageAxes, 'xy');
186             [X,Y]=meshgrid(1:200:imageWidth+199, ...
                    1:200:imageHeigth+199);
187             axes(this.imageAxes(4));imshow(this.originalImage_red);
188             axis on;hold on;plot(X,Y,'g');plot(X',Y','g');
189             axes(this.imageAxes(3));imshow(this.originalImage_blue);
190             axis on;hold on;plot(X,Y,'g');plot(X',Y','g');
191             axes(this.imageAxes(2));
192             imshow(this.originalImage_combined);
193             axis on;hold on;plot(X,Y,'g');plot(X',Y','g');
194             axes(this.imageAxes(1));imshow(this.originalImage_bf);
195             axis on;hold on;plot(X,Y,'g');plot(X',Y','g');
196             axes(this.imageAxes(8));imshow(this.BCAdjustedImage_red);
197             axis on;hold on;plot(X,Y,'g');plot(X',Y','g');
198             axes(this.imageAxes(7));imshow(this.BCAdjustedImage_blue);
199             axis on;hold on;plot(X,Y,'g');plot(X',Y','g');
200             axes(this.imageAxes(6));
201             imshow(this.BCAdjustedImage_combined);
202             axis on;hold on;plot(X,Y,'g');plot(X',Y','g');
203             axes(this.imageAxes(5));imshow(this.BCAdjustedImage_bf);
204             axis on;hold on;plot(X,Y,'g');plot(X',Y','g');
205             if this.figuresInitialised
206                 this.imageAxes(4).XLim= this.oldXLim;
207                 this.imageAxes(4).YLim= this.oldYLim;
208             else
209                 this.figuresInitialised = true;
210             end
211             set(this.myInstanceControlFigure,'KeyPressFcn',...
212                 @this.registerKeys);
213             if ¬isequal(this.oldXLim, [0 1])
214                 this.originalImageAxes_red.XLim = this.oldXLim;
215             end
216             if ¬isequal(this.oldYLim, [0 1])
217                 this.originalImageAxes_red.YLim = this.oldYLim;
218             end
219         end
220         function BCAdjustImages(this, acr, event)
221             this.BCAdjustedImage_red=this.originalImage_red;
222             this.BCAdjustedImage_red(this.BCAdjustedImage_red<...
223                 this.red_min) = 0;
224             this.BCAdjustedImage_red(this.BCAdjustedImage_red>...
225                 this.red_max) = this.red_max;
226             this.BCAdjustedImage_red = this.BCAdjustedImage_red...
227                 *this.red_gain;
228             this.BCAdjustedImage_blue=this.originalImage_blue;
229             this.BCAdjustedImage_blue(this.BCAdjustedImage_blue<...
230                 this.blue_min) = 0;
231             this.BCAdjustedImage_blue(this.BCAdjustedImage_blue>...
232                 this.blue_max) = this.blue_max;
233             this.BCAdjustedImage_blue = this.BCAdjustedImage_blue...
```

```
234                 *this.blue_gain;
235             this.BCAdjustedImage_bf=this.originalImage_bf;
236             this.BCAdjustedImage_bf(this.BCAdjustedImage_bf<...
237                 this.bf_min) = 0;
238             this.BCAdjustedImage_bf(this.BCAdjustedImage_bf>...
239                 this.bf_max) = this.bf_max;
240             this.BCAdjustedImage_bf = this.BCAdjustedImage_bf...
241                 *this.bf_gain;
242         end
243         function drawControlFigure(this, scr, event)
244             annotation('textbox', 'Units', 'normalized', ...
                    'Position',...
245                 [0.02 0.5  , 0.03 0.03], 'String', "Red")
246             annotation('textbox', 'Units', 'normalized', ...
                    'Position',...
247                 [0.02 0.46 , 0.03 0.03], 'String', "Blue")
248             annotation('textbox', 'Units', 'normalized', ...
                    'Position',...
249                 [0.02 0.42 , 0.03 0.03], 'String', "BF")
250             annotation('textbox', 'Units', 'normalized', ...
                    'Position',...
251                 [0.06 0.54 , 0.03 0.03], 'String', "gain ")
252             annotation('textbox', 'Units', 'normalized', ...
                    'Position',...
253                 [0.10 0.54 , 0.03 0.03], 'String', "min")
254             annotation('textbox', 'Units', 'normalized', ...
                    'Position',...
255                 [0.14 0.54 , 0.03 0.03], 'String', "max")
256             this.red_gain_inputBox  = uicontrol('Style', 'edit',...
257                 'Units', 'normalized', 'Position',...
258                 [0.06 0.5 , 0.03 0.03], 'String', this.red_gain);
259             this.blue_gain_inputBox = uicontrol('Style', 'edit',...
260                 'Units', 'normalized', 'Position',...
261                 [0.06 0.46, 0.03 0.03], 'String', this.blue_gain);
262             this.bf_gain_inputBox   = uicontrol('Style', 'edit',...
263                 'Units', 'normalized', 'Position',...
264                 [0.06 0.42, 0.03 0.03], 'String', this.bf_gain);
265             this.red_min_inputBox   = uicontrol('Style', 'edit',...
266                 'Units', 'normalized', 'Position',...
267                 [0.10 0.5 , 0.03 0.03], 'String', this.red_min);
268             this.blue_min_inputBox  = uicontrol('Style', 'edit',...
269                 'Units', 'normalized', 'Position',...
270                 [0.10 0.46, 0.03 0.03], 'String', this.blue_min);
271             this.bf_min_inputBox    = uicontrol('Style', 'edit',...
272                 'Units', 'normalized', 'Position',...
273                 [0.10 0.42, 0.03 0.03], 'String', this.bf_min);
274             this.red_max_inputBox   = uicontrol('Style', 'edit',...
275                 'Units', 'normalized', 'Position',...
276                 [0.14 0.5 , 0.03 0.03], 'String', this.red_max);
277             this.blue_max_inputBox  = uicontrol('Style', 'edit',...
278                 'Units', 'normalized', 'Position',...
279                 [0.14 0.46, 0.03 0.03], 'String', this.blue_max);
280             this.bf_max_inputBox    = uicontrol('Style', 'edit',...
281                 'Units', 'normalized', 'Position',...
```

```
282                 [0.14 0.42, 0.03 0.03], 'String', this.bf_max);
283             this.lTopUI    = uicontrol('Style', 'edit', 'Units',...
284                 'normalized', 'Position', [0.06, 0.7 , 0.05, ...
                        0.03],...
285                 'String', this.lTopVal);
286             this.lBotUI    = uicontrol('Style', 'edit', 'Units',...
287                 'normalized', 'Position', [0.06, 0.64, 0.05, ...
                        0.03],...
288                 'String', this.lBotVal);
289             this.lLefUI    = uicontrol('Style', 'edit', 'Units',...
290                 'normalized', 'Position', [0.01, 0.67, 0.05, ...
                        0.03],...
291                 'String', this.lLefVal);
292             this.lRigUI    = uicontrol('Style', 'edit', 'Units',...
293                 'normalized', 'Position', [0.11, 0.67, 0.05, ...
                        0.03],...
294                 'String', this.lRigVal);
295             this.rotAngUI  = uicontrol('Style', 'edit', 'Units',...
296                 'normalized', 'Position', [0.06, 0.67, 0.05, ...
                        0.03],...
297                 'String', this.rotAngVal);
298             this.consoleUI = uicontrol('Style', 'listbox', ...
                    'Units',...
299                 'normalized', 'Position', [0.01, 0.01, 0.98, ...
                        0.07],...
300                 'String', this.eventHistory);
301
302             c = uicontrol('Units', 'normalized', 'Position',...
303                 [0.01 0.92, 0.09 0.06]);
304             c.String = 'Update Image';
305             c.Callback = @this.plotMyFigure;
306             l = uicontrol('Units', 'normalized', 'Position',...
307                 [0.01 0.85, 0.09 0.06]);
308             l.String = 'Load';
309             l.Callback = @this.load;
310             l = uicontrol('Units', 'normalized', 'Position',...
311                 [0.01 0.78, 0.09 0.06]);
312             l.String = 'Save';
313             l.Callback = @this.save;
314
315             this.histogramAxes_red  = axes('Units', 'normalized',...
316                 'Position', [0.2 0.7  , 0.14 0.24]);
317             histogram(this.originalImage_red(:))
318             %xlim([0,65535])
319             this.histogramAxes_blue = axes('Units', 'normalized',...
320                 'Position', [0.2 0.4  , 0.14 0.24]);
321             histogram(this.originalImage_blue(:))
322             %xlim([0,65535])
323             BCAdjustedHistogramAxes_red  = axes('Units', ...
                    'normalized',...
324                 'Position', [0.39 0.7  , 0.14 0.24]);
325             histogram(this.BCAdjustedImage_red(:))
326             xlim([0,65535])
```

```
327             BCAdjustedHistogramAxes_blue = axes('Units', ...
                    'normalized',...
328                 'Position', [0.39 0.4 , 0.14 0.24]);
329             histogram(this.BCAdjustedImage_blue(:))
330             xlim([0,65535])
331         end
332
333         function updateImages(this, scr, event)
334             axes(this.originalImageAxes_red);
335             imshow(this.originalImage_red*str2double(...
336                 this.red_gain_inputBox.String));
337             axes(this.originalImageAxes_blue);
338             imshow(this.originalImage_red*str2double(...
339                 this.blue_gain_inputBox.String));
340         end
341
342
343         function registerKeys(this, scr, event)
344             %this
345             %scr
346             %event
347             disp(['key pressed: ' event.Key])
348             if strcmp(event.Key, 'c')
349                 disp('select range');
350                 this.rotAngUI.String = -this.getRange()
351             end
352         end
353
354         function mAngle = getRange(this)
355             c = ginput(2);
356             x1 = c(1, 1);
357             x2 = c(2, 1);
358             y1 = c(1, 2);
359             y2 = c(2, 2);
360             mAngle = 180/pi*atan2((x2-x1),(y2-y1))-90;
361         end
362
363     end
364 end
365
366 function [img, loadpath, sampleOutputNameGuessed] = ...
    overlapImages(lastPath)
367
368     % fx = 2305/1500; %pixels/um
369     % fy = -71/1500;  %pixels/um
370
371
372     % transformation matrix for 10x without tube
373     % M = 1/750 * [   -1150      -35    ;
374     %                   35    -1155    ];
375
376     % transformation matrix for 4x with tube
377     M =  [ -0.92725      -0.028    ;
378               0.028    -0.92725    ];
```

```
379     [file,path] = uigetfile(strcat(lastPath, ...
            '/*.tif'),'MultiSelect',...
380                 'on','Select Brightfield Images');
381     file_bf = file
382     loadpath_bf = path;
383     if isequal(file,0)
384        disp('User selected Cancel');
385     end
386     if(iscell(file))
387         imageName=file{1};
388         l = split(imageName(1:end-4), '_s');
389         imageNumberSelected = uint16(str2double(l{2}));
390         scratchNumberGuessed = 1;
391         if imageNumberSelected==7 | imageNumberSelected==8 |...
392                 imageNumberSelected==9
393             scratchNumberGuessed = 2;
394         elseif imageNumberSelected==13 | imageNumberSelected==14 |...
395                 imageNumberSelected==15
396             scratchNumberGuessed = 3;
397         end
398         l2 = split(imageName(1:end-4), '_');
399         sampleIdentifier = strcat(l2(1,:),'_',l2(2,:));
400         sampleOutputNameGuessed = strcat(sampleIdentifier{1}, '_',...
401                 num2str(scratchNumberGuessed));
402         for i = 1:1:size(file, 2)
403             %file_name = strcat(fileNames(i, :), '.tif');
404             file_name = fullfile(path,file{i});
405             imgData(i).img_bf = Tiff(file_name).read();
406             imgData(i).info_bf = imfinfo(file_name);
407             imgData(i).x_pos_bf = str2double(parseTiffDescription...
408                 (imgData(i).info_bf, 'stage-position-x'));
409             imgData(i).y_pos_bf = -str2double(parseTiffDescription...
410                 (imgData(i).info_bf, 'stage-position-y'));
411         end
412     else
413         file_name = fullfile(path,file);
414         i = 1;
415         imgData(i).img_bf = Tiff(file_name).read();
416         imgData(i).info_bf = imfinfo(file_name);
417         imgData(i).x_pos_bf = str2double(parseTiffDescription(...
418                 imgData(i).info_bf, 'stage-position-x'));
419         imgData(i).y_pos_bf = -str2double(parseTiffDescription(...
420                 imgData(i).info_bf, 'stage-position-y'));
421     end
422     file = strrep(file_bf,'w1Brightfield','w2Blue')
423     loadpath_blue = path;
424     if isequal(file,0)
425        disp('User selected Cancel');
426     end
427     disp(file)
428     if(iscell(file))
429         for i = 1:1:size(file, 2)
430             %file_name = strcat(fileNames(i, :), '.tif');
431             file_name = fullfile(path,file{i})
```

```
432             imgData(i).img_blue = Tiff(file_name).read();
433             imgData(i).info_blue = imfinfo(file_name);
434             imgData(i).x_pos_blue = ...
                    str2double(parseTiffDescription(...
435                 imgData(i).info_blue, 'stage-position-x'));
436             imgData(i).y_pos_blue = ...
                    -str2double(parseTiffDescription(...
437                 imgData(i).info_blue, 'stage-position-y'));
438         end
439     else
440         file_name = fullfile(path,file);
441         imgData(i).img_blue = Tiff(file_name).read();
442         imgData(i).info_blue = imfinfo(file_name);
443         imgData(i).x_pos_blue = str2double(parseTiffDescription(...
444                 imgData(i).info_blue, 'stage-position-x'));
445         imgData(i).y_pos_blue = -str2double(parseTiffDescription(...
446                 imgData(i).info_blue, 'stage-position-y'));
447     end
448     file = strrep(file_bf,'w1Brightfield','w3Red')
449     loadpath_red = path;
450     if isequal(file,0)
451        disp('User selected Cancel');
452     end
453     disp(file)
454     if(iscell(file))
455         for i = 1:1:size(file, 2)
456             %file_name = strcat(fileNames(i, :), '.tif');
457             file_name = fullfile(path,file{i})
458             imgData(i).img_red = Tiff(file_name).read();
459             imgData(i).info_red = imfinfo(file_name);
460             imgData(i).x_pos_red = ...
                    str2double(parseTiffDescription(...
461                 imgData(i).info_red, 'stage-position-x'));
462             imgData(i).y_pos_red = ...
                    -str2double(parseTiffDescription(...
463                 imgData(i).info_red, 'stage-position-y'));
464         end
465     else
466         file_name = fullfile(path,file);
467         imgData(i).img_red = Tiff(file_name).read();
468         imgData(i).info_red = imfinfo(file_name);
469         imgData(i).x_pos_red = str2double(parseTiffDescription(...
470                 imgData(i).info_red, 'stage-position-x'));
471         imgData(i).y_pos_red = -str2double(parseTiffDescription(...
472                 imgData(i).info_red, 'stage-position-y'));
473     end
474     % check if image data seems to make sense
475     % - check if coordinates match
476     counter = 0;
477     for i = imgData
478         counter = counter + 1;
479         if((i.x_pos_red == i.x_pos_blue) & (i.x_pos_red == ...
                i.x_pos_bf))
480             disp(strcat("image set ", num2str(counter),...
```

```
481                 "x coordinates match"));
482         else
483             disp(strcat("image set ", num2str(counter),...
484                 "x coordinates DO NOT match"));
485             error(strcat("image set ", num2str(counter),...
486                 "x coordinates DO NOT match"));
487         end
488         if((i.y_pos_red == i.y_pos_blue) & (i.y_pos_red == ...
                i.y_pos_bf))
489             disp(strcat("image set ", num2str(counter),...
490                 "y coordinates match"));
491         else
492             disp(strcat("image set ", num2str(counter),...
493                 "y coordinates DO NOT match"));
494             error(strcat("image set ", num2str(counter),...
495                 "y coordinates DO NOT match"));
496         end
497     end
498     %#####################   LOADING AND CHECKING DONE   ...
            ######################
499     % - now stitch it together
500     % - check how wide one image is first
501     imageWidth  = size(imgData(1).img_red, 2);
502     imageHeigth = size(imgData(1).img_red, 1);
503
504     % first image at pixel position (1|1)
505     zeroX = 1;
506     zeroY = 1;
507
508     % calculate position respective position of all images relative ...
            to
509     % image furthest left (min(x)) and furthest up (min(y)). We ...
            will use
510     % red image coordinates from now on (should be the same to blue ...
            and bf
511     % image coordinates, though).
512     for i = 1:length(imgData)
513         imgData(i).posum = [imgData(i).x_pos_red-min(...
514                 [imgData(:).x_pos_red]); imgData(i).y_pos_red...
515                 -min([imgData(:).y_pos_red])];
516     end
517     % transform relative positions using transformation matrix M.
518     % M must be determined by stitching images manually.
519
520     %       posB = position vector in the image, unit = pixel
521     %       posM = position vector of the microscope stage when ...
            taking the
522     %       picture, unit = micrometre
523     %       M = transformation matrix, unit = pixel/micrometre
524     %
525     %       posB = M*posM
526     %
527     %
528     %       x, pixel      m,xx    m, xy    x, microns
```

```
529     %  =>              =                    *
530     %         y, pixel       m,yx    m, yy     y, microns
531     %
532
533     for i = 1:length(imgData)
534         imgData(i).pospx = round([zeroX; zeroY]+M*imgData(i).posum);
535     end
536     pospx = [imgData.pospx];
537
538     % For the transition areas, where two or more images overlap, ...
            we will
539     % generate a mask. That means that if
540     % two images overlap, pixels in this region will get the ...
            average of the
541     % pixel values. Can be turned of with mask = false;
542     mask = true;
543
544     img_mask = ...
            double(zeros(max(pospx(2,:))-min(pospx(2,:))+imageHeigth,...
545                 max(pospx(1,:))-min(pospx(1,:))+imageWidth));
546     for i = 1:length(imgData)
547         imgPosX = imgData(i).pospx(1)-min(pospx(1,:))+1;
548         imgPosY = imgData(i).pospx(2)-min(pospx(2,:))+1;
549         img_mask(imgPosY:imgPosY+imageHeigth-1, imgPosX:imgPosX+...
550                 imageWidth-1) = ...
                        img_mask(imgPosY:imgPosY+imageHeigth-1,...
551                 imgPosX:imgPosX+imageWidth-1)+1;
552     end
553     img_mask(img_mask==0) = 1;
554     % if there was no image at a pixel location, set mask to 1
555     % to avoid getting infinite values in the next line
556     img_mask = 1./img_mask;
557
558     % create empty images that will fit the finished stitched image
559     % we need a red, a brightfield and a blue one
560     img_red = ...
            uint16(zeros(max(pospx(2,:))-min(pospx(2,:))+imageHeigth,...
561                 max(pospx(1,:))-min(pospx(1,:))+imageWidth));
562     img_bf = ...
            uint16(zeros(max(pospx(2,:))-min(pospx(2,:))+imageHeigth,...
563                 max(pospx(1,:))-min(pospx(1,:))+imageWidth));
564     img_blue = ...
            uint16(zeros(max(pospx(2,:))-min(pospx(2,:))+imageHeigth,...
565                 max(pospx(1,:))-min(pospx(1,:))+imageWidth));
566     % stitch the images together by writing the respective image ...
            data at
567     % the position calculated using M
568     for i = 1:length(imgData)
569         imgPosX = imgData(i).pospx(1)-min(pospx(1,:))+1;
570         imgPosY = imgData(i).pospx(2)-min(pospx(2,:))+1;
571         if mask == true
572             img_red(imgPosY:imgPosY+imageHeigth-1, ...
                    imgPosX:imgPosX+...
```

```
573                     imageWidth-1) = ...
                            img_red(imgPosY:imgPosY+imageHeigth-1,...
574                     imgPosX:imgPosX+imageWidth-1)+uint16(double(imgData(i)...
575                     .img_red).*img_mask(imgPosY:imgPosY+imageHeigth-1,...
576                     imgPosX:imgPosX+imageWidth-1));
577                 img_bf(imgPosY:imgPosY+imageHeigth-1, imgPosX:imgPosX+...
578                     imageWidth-1) = ...
                            img_bf(imgPosY:imgPosY+imageHeigth-1,...
579                     imgPosX:imgPosX+imageWidth-1)+uint16(double(imgData(i)...
580                     .img_bf).*img_mask(imgPosY:imgPosY+imageHeigth-1,...
581                     imgPosX:imgPosX+imageWidth-1));
582                 img_blue(imgPosY:imgPosY+imageHeigth-1, ...
                        imgPosX:imgPosX+...
583                     imageWidth-1) = ...
                            img_blue(imgPosY:imgPosY+imageHeigth-1,...
584                     imgPosX:imgPosX+imageWidth-1)+uint16(double(imgData(i)...
585                     .img_blue).*img_mask(imgPosY:imgPosY+imageHeigth-1,...
586                     imgPosX:imgPosX+imageWidth-1));
587             else
588                 img_red(imgPosY:imgPosY+imageHeigth-1,...
589                     imgPosX:imgPosX+imageWidth-1) = imgData(i).img_red;
590                 img_bf(imgPosY:imgPosY+imageHeigth-1,...
591                     imgPosX:imgPosX+imageWidth-1) = imgData(i).img_red;
592                 img_blue(imgPosY:imgPosY+imageHeigth-1,...
593                     imgPosX:imgPosX+imageWidth-1) = imgData(i).img_red;
594             end
595         end
596         img = {img_red, img_blue, img_bf, img_mask};
597         loadpath = {loadpath_red, loadpath_blue, loadpath_bf};
598     end
599
600
601
602
603         function val = parseTiffDescription(imgInfo, prop_id)
604             prop_id = strcat('"', prop_id, '"');
605             str = imgInfo.ImageDescription;
606             z = strsplit(str, prop_id);
607             y = strsplit(z{2}, 'value="');
608             x = strsplit(y{2}, '"');
609             val = x{1};
610         end
611
612     function fig = figureFullscreen(monitorN)
613         MP=get(0,'MonitorPositions');
614         fig=figure;
615         if monitorN<=size(MP,1)
616             pause(0.01);
617             set(fig,'Position',[MP(monitorN,1:2)+MP(monitorN,3:4)/4 ...
618                     MP(monitorN,3:4)/2]);
619             pause(0.01);
620             set(fig,'WindowState','maximized');
621         else
```

```
622         disp(strcat("attempted to create fullscreen figure on ...
                monitor ",...
623         string(monitorN),...
624         " but not enough monitors were detected.",...
625         "Figure was not set to fullscreen."));
626     end
627 end
628
629
630 function a = generateAxes(nx, ny, dx, dy)
631     imgAxPos = zeros(nx*ny,4);
632     sizex = (1-dx)/nx;
633     sizey = (1-dy)/ny;
634     for x = 1:nx
635         for y = 1:ny
636             currentAx = (x-1)*ny+y;
637             posx = dx/(nx+1)*x+sizex*(x-1);
638             posy = dy/(ny+1)*y+sizey*(y-1);
639             imgAxPos(currentAx,1:4) = [posx, posy, sizex, sizey];
640         end
641     end
642     for i =1:size(imgAxPos,1)
643         a(i) = axes('Units', 'normalized', 'Position', ...
                imgAxPos(i,:));
644     end
645 end
```

A.2 Image Cropper

```
1  classdef imageCropper < handle
2      properties
3          myInstanceControlFigure
4          myInstanceImageFigure
5          eventHistory
6          initialised = false;
7          imageLoaded = false;
8          figuresInitialised = false;
9          originalImage_red
10         originalImage_blue
11         originalImage_bf
12         originalImage_combined
13         BCAdjustedImage_red
14         BCAdjustedImage_blue
15         BCAdjustedImage_bf
16         BCAdjustedImage_combined
17         originalImage_manipulated_red
18         originalImage_manipulated_blue
19         originalImage_manipulated_bf
20         originalImage_manipulated_combined
```

```
21          BCAdjustedImage_manipulated_red
22          BCAdjustedImage_manipulated_blue
23          BCAdjustedImage_manipulated_bf
24          BCAdjustedImage_manipulated_combined
25          oldXLim = [0  1];
26          oldYLim = [0  1];
27          manipulatedImage
28          loadedFromPath = pwd
29          loadedFromBaseName
30          lTopVal = 1
31          lBotVal = 1
32          lRigVal = 1
33          lLefVal = 1
34          rotAngVal = 0
35          UIs
36          consoleUI
37          imageAxes
38          scratchX = 329;
39          scratchY = 283;
40          scratchW = 1500;
41          scratchL = 10680;
42      end
43
44      methods
45          function obj = imageCropper()
46              obj.myInstanceControlFigure = figureFullscreen(1);
47              set(obj.myInstanceControlFigure, 'units','normalized');
48              obj.myInstanceImageFigure= figureFullscreen(3);
49              set(obj.myInstanceImageFigure, 'units','normalized');
50              obj.eventHistory = {'created.'};
51              obj.plotMyFigure();
52          end
53
54
55
56          function addHistoryEntry(this, text)
57              this.eventHistory = [text, this.eventHistory];
58          end
59
60          function load(this, scr, event)
61              [file,path] = uigetfile(strcat('pwd', ...
                    '/*.tif'),'MultiSelect','off','Select an Image');
62              if isequal(file,0)
63                 disp('User selected Cancel');
64              else
65                 disp(['User selected ', fullfile(path,file)]);
66              end
67              file_name = fullfile(path,file)
68              if contains(file_name, 'BCAdjustedImage')
69                  base_name = split(file_name, 'BCAdjustedImage');
70                  base_name = base_name{1};
71              elseif contains(file_name, 'originalImage')
72                  base_name = split(file_name, 'originalImage');
73                  base_name = base_name{1};
```

```
74              end
75              this.loadedFromPath = path;
76              this.loadedFromBaseName = base_name;
77              this.originalImage_red = Tiff(strcat(base_name, ...
                    'originalImage_red.TIF')).read();
78              this.originalImage_blue = Tiff(strcat(base_name, ...
                    'originalImage_blue.TIF')).read();
79              this.originalImage_bf = Tiff(strcat(base_name, ...
                    'originalImage_bf.TIF')).read();
80              this.originalImage_combined = Tiff(strcat(base_name, ...
                    'originalImage_combined.TIF')).read();
81              this.BCAdjustedImage_red = Tiff(strcat(base_name, ...
                    'BCAdjustedImage_red.TIF')).read();
82              this.BCAdjustedImage_blue = Tiff(strcat(base_name, ...
                    'BCAdjustedImage_blue.TIF')).read();
83              this.BCAdjustedImage_bf = Tiff(strcat(base_name, ...
                    'BCAdjustedImage_bf.TIF')).read();
84              this.BCAdjustedImage_combined = Tiff(strcat(base_name, ...
                    'BCAdjustedImage_combined.TIF')).read();
85
86              this.addHistoryEntry(strcat("Loaded Images from Base ...
                    Name ", base_name));
87              this.figuresInitialised = false;
88              this.imageLoaded = true;
89              this.lTopVal = 1;
90              this.lBotVal = 0;
91              this.lLefVal = 40;
92              this.lRigVal = 40;
93              this.plotMyFigure();
94          end
95
96          function plotMyFigure(this, ¬, ¬)
97              % plotMyFigure(this, scr, event), scr and event not ...
                    used, so set = ¬
98              % first check if figure has been initialised. If so, ...
                    save values.
99              if this.figuresInitialised
100                 this.scratchX = str2double(this.UIs{1}.String);
101                 this.scratchY = str2double(this.UIs{2}.String);
102                 this.scratchW = str2double(this.UIs{3}.String);
103                 this.scratchL = str2double(this.UIs{4}.String);
104                 this.lTopVal  = str2double(this.UIs{5}.String);
105                 this.lBotVal  = str2double(this.UIs{6}.String);
106                 this.lLefVal  = str2double(this.UIs{7}.String);
107                 this.lRigVal  = str2double(this.UIs{8}.String);
108                 this.rotAngVal = str2double(this.UIs{9}.String);
109                 this.oldXLim = this.imageAxes(end).XLim;
110                 this.oldYLim = this.imageAxes(end).YLim;
111             else
112                  this.oldXLim = [0 1];
113                  this.oldYLim = [0 1];
114             end
115             if this.lLefVal < 1
116                 this.lLefVal = 1;
```

```
117             end
118             if this.lTopVal < 1
119                 this.lTopVal = 1;
120             end
121             if this.lRigVal > size(this.BCAdjustedImage_red, 2)
122                 this.lRigVal = size(this.BCAdjustedImage_red, 2);
123                 disp("Right crop value too large");
124             end
125             if this.lBotVal > size(this.BCAdjustedImage_red, 1)
126                 this.lBotVal = size(this.BCAdjustedImage_red, 1);
127                 disp("Bottom crop value too large");
128             end
129 
130             %rotate and crop images
131             this.updateImages();
132 
133             % now clear the figure
134             clf(this.myInstanceControlFigure)
135             clf(this.myInstanceImageFigure)
136 
137             set(this.myInstanceControlFigure,'KeyPressFcn',...
138                 @this.registerKeys);
139             set(this.myInstanceImageFigure,'KeyPressFcn',...
140                 @this.registerKeys);
141 
142             % select figure that carries all the control elements
143             figure(this.myInstanceControlFigure)
144             % add gui elements to control figure
145             this.drawControlFigure();
146             figure(this.myInstanceImageFigure)
147             this.drawImageFigure();
148 
149         end
150 
151         function drawImageFigure(this, ¬, ¬)
152             this.imageAxes = generateAxes(1,2,0.051,0.051);
153             linkaxes(this.imageAxes(1:2), 'xy');
154             axes(this.imageAxes(2));
155             imshow(this.BCAdjustedImage_manipulated_red);
156             axis on
157             hold on
158             this.drawScratchOutlines();
159             axes(this.imageAxes(1));
160             imshow(this.BCAdjustedImage_manipulated_blue);
161             axis on;
162             hold on;
163             this.drawScratchOutlines();
164             if this.figuresInitialised
165             else
166                 this.figuresInitialised = true;
167             end
168         end
169 
170         function drawScratchOutlines(this, ¬, ¬)
```

```
171             imageHeigth = size(this.originalImage_manipulated_red, ...
                    1);
172             imageWidth  = size(this.originalImage_manipulated_red, ...
                    2);
173             di = 20;
174             do = 50;
175             compareLeft = this.scratchX-di;
176             compareRight = ...
                    imageWidth-(this.scratchX+this.scratchL)-di;
177             compareTop = this.scratchY-di;
178             compareBot = ...
                    imageHeigth-(this.scratchY+this.scratchW)-di;
179             scratchEdgeColor = 'white';
180             scratchFaceColor = 'blue';
181             scratchFaceAlpha = 0.2';
182             compareFaceAlpha = 0.2;
183             scratchPosX = [this.scratchX, this.scratchX, ...
184                 this.scratchX+this.scratchL, ...
                        this.scratchX+this.scratchL];
185             scratchPosY = [this.scratchY, ...
                    this.scratchY+this.scratchW,...
186                 this.scratchY+this.scratchW, this.scratchY];
187             scratchPos = [scratchPosX',scratchPosY'];
188             patch('Faces', 1:size(scratchPos, 1), ...
                    'Vertices',scratchPos,...
189                 'FaceColor','red','FaceAlpha', 0.0, 'EdgeColor', ...
                        'white')
190             indentPosX = [this.scratchX,this.scratchX,...
191                 this.scratchX+this.scratchW, ...
                        this.scratchX+this.scratchW];
192             indentPosY = [this.scratchY, ...
                    this.scratchY+this.scratchW,...
193                 this.scratchY+this.scratchW, this.scratchY];
194             indentPos = [indentPosX',indentPosY'];
195             patch('Faces', 1:size(indentPos, 1), 'Vertices', ...
                    indentPos,...
196                 'FaceColor','blue','FaceAlpha', 0.0, 'EdgeColor', ...
                        'white')
197             compareLeftPosX = [this.scratchX-compareLeft,...
198                 this.scratchX-compareLeft, this.scratchX-do, ...
                        this.scratchX-do];
199             compareLeftPosY = [this.scratchY,...
200                 this.scratchY+this.scratchW,...
201                 this.scratchY+this.scratchW, this.scratchY];
202             compareLeftPos = [compareLeftPosX',compareLeftPosY'];
203             patch('Faces', 1:size(compareLeftPos, 1), 'Vertices',...
204                 compareLeftPos,'FaceColor','green','FaceAlpha',...
205                 compareFaceAlpha, 'EdgeColor', 'white')
206             compareRightPosX = [this.scratchX+this.scratchL+do,...
207                 this.scratchX+this.scratchL+do,...
208                 this.scratchX+this.scratchL+compareRight,...
209                 this.scratchX+this.scratchL+compareRight];
210             compareRightPosY = [this.scratchY,...
211                 this.scratchY+this.scratchW,...
```

```
212             this.scratchY+this.scratchW, this.scratchY];
213         compareRightPos = [compareRightPosX',compareRightPosY'];
214         patch('Faces', 1:size(compareRightPos, 1), 'Vertices',...
215             compareRightPos,'FaceColor','green','FaceAlpha',...
216             compareFaceAlpha, 'EdgeColor', 'white')
217         compareTopPosX = [this.scratchX,this.scratchX,...
218             this.scratchX+this.scratchL, ...
                    this.scratchX+this.scratchL];
219         compareTopPosY = [this.scratchY-compareTop,...
220             this.scratchY-do, this.scratchY-do,...
221             this.scratchY-compareTop];
222         compareTopPos = [compareTopPosX',compareTopPosY'];
223         patch('Faces', 1:size(compareTopPos, 1), 'Vertices',...
224             compareTopPos,'FaceColor','green','FaceAlpha',...
225             compareFaceAlpha, 'EdgeColor', 'white')
226         compareBotPosX = [this.scratchX,this.scratchX,...
227             this.scratchX+this.scratchL, ...
                    this.scratchX+this.scratchL];
228         compareBotPosY = [this.scratchY+this.scratchW+do,...
229             this.scratchY+this.scratchW+compareBot,...
230             this.scratchY+this.scratchW+compareBot,...
231             this.scratchY+this.scratchW+do];
232         compareBotPos = [compareBotPosX',compareBotPosY'];
233         patch('Faces', 1:size(compareBotPos, 1), 'Vertices',...
234             compareBotPos,'FaceColor','green','FaceAlpha',...
235             compareFaceAlpha, 'EdgeColor', 'white')
236         circleB(this.scratchX+this.scratchW/2,...
237             this.scratchY+this.scratchW/2, this.scratchW/2, ...
                    1/2*pi,...
238             3/2*pi, 'white', 0, scratchFaceColor, ...
                    scratchFaceAlpha);
239         circleB(this.scratchX+this.scratchL-this.scratchW/2,...
240             this.scratchY+this.scratchW/2, this.scratchW/2, ...
                    -1/2*pi,...
241             1/2*pi, 'white', 0, scratchFaceColor, ...
                    scratchFaceAlpha);
242         patchPos = [this.scratchX+this.scratchW/2, ...
                this.scratchY;...
243             this.scratchX+this.scratchL-this.scratchW/2,...
244             this.scratchY;...
245             this.scratchX+this.scratchL-this.scratchW/2,...
246             this.scratchY+this.scratchW;...
247             this.scratchX+this.scratchW/2,...
248             this.scratchY+this.scratchW];
249         patch('Faces', 1:size(patchPos, 1), 'Vertices',...
250             patchPos,'FaceColor',scratchFaceColor,'FaceAlpha',...
251             scratchFaceAlpha, 'EdgeColor', 'white', ...
                    'EdgeAlpha', 0)
252         circleA(this.scratchX+this.scratchW/2,...
253             this.scratchY+this.scratchW/2, this.scratchW/2, 0, ...
                    2*pi,...
254             scratchEdgeColor);
255         circleA(this.scratchX+this.scratchL-this.scratchW/2,...
```

```
256                 this.scratchY+this.scratchW/2, this.scratchW/2, ...
                        -pi/2,...
257                 1/2*pi, scratchEdgeColor);
258             end
259
260             function updateImages(this, scr, event)
261                 this.BCAdjustedImage_manipulated_red = rotCropImage(...
262                     this.BCAdjustedImage_red, this.lLefVal, ...
                            this.lRigVal,...
263                     this.lTopVal, this.lBotVal, this.rotAngVal);
264                 this.BCAdjustedImage_manipulated_blue = rotCropImage(...
265                     this.BCAdjustedImage_blue, this.lLefVal, ...
                            this.lRigVal,...
266                     this.lTopVal, this.lBotVal, this.rotAngVal);
267                 this.BCAdjustedImage_manipulated_bf = rotCropImage(...
268                     this.BCAdjustedImage_bf, this.lLefVal, ...
                            this.lRigVal,...
269                     this.lTopVal, this.lBotVal, this.rotAngVal);
270                 this.BCAdjustedImage_manipulated_combined = ...
                        rotCropImage(...
271                     this.BCAdjustedImage_combined, this.lLefVal,...
272                      this.lRigVal, this.lTopVal, this.lBotVal, ...
                            this.rotAngVal);
273                 this.originalImage_manipulated_red = rotCropImage(...
274                     this.originalImage_red, this.lLefVal,...
275                      this.lRigVal, this.lTopVal, this.lBotVal, ...
                            this.rotAngVal);
276                 this.originalImage_manipulated_blue = rotCropImage(...
277                     this.originalImage_blue, this.lLefVal,...
278                      this.lRigVal, this.lTopVal, this.lBotVal, ...
                            this.rotAngVal);
279                 this.originalImage_manipulated_bf = rotCropImage(...
280                     this.originalImage_bf, this.lLefVal,...
281                      this.lRigVal, this.lTopVal, this.lBotVal, ...
                            this.rotAngVal);
282                 this.originalImage_manipulated_combined = ...
                        rotCropImage(...
283                     this.originalImage_combined, this.lLefVal,...
284                      this.lRigVal, this.lTopVal, this.lBotVal, ...
                            this.rotAngVal);
285             end
286
287             function drawControlFigure(this, scr, event)
288                 blackPixelCounter_red = annotation('textbox', 'Units',...
289                     'normalized', 'BackgroundColor','red', 'Color', ...
                            'black',...
290                     'Position', [0.52 0.95 , 0.13 0.03], 'String', ...
291                     strcat("Black pixels on red image: ",...
292                     num2str(sum(sum(...
293                     this.originalImage_manipulated_red == 0)))))
294                 blackPixelCounter_blue  = annotation('textbox', ...
                        'Units', 'normalized', 'BackgroundColor','red', ...
                        'Color', 'black', 'Position', [0.52 0.91 , 0.13 ...
                        0.03], 'String', strcat("Black pixels on blue ...
```

```
            image: ...
            ",num2str(sum(sum(this.originalImage_manipulated_blue ...
            == 0)))))
295         blackPixelCounter_bf  = annotation('textbox', 'Units', ...
            'normalized', 'BackgroundColor','red', 'Color', ...
            'black', 'Position',  [0.52 0.87  , 0.13 0.03], ...
            'String', strcat("Black pixels on bf image: ...
            ",num2str(sum(sum(this.originalImage_manipulated_bf ...
            == 0)))))
296         if sum(sum(this.originalImage_manipulated_red == 0)) == ...
            0; blackPixelCounter_red.BackgroundColor = 'green'; ...
            end
297         if sum(sum(this.originalImage_manipulated_blue == 0)) ...
            == 0; blackPixelCounter_blue.BackgroundColor = ...
            'green'; end
298         if sum(sum(this.originalImage_manipulated_bf == 0)) == ...
            0; blackPixelCounter_bf.BackgroundColor = 'green'; end
299         disp(strcat("Number of completely black pixels on red : ...
            ", ...
            num2str(sum(sum(this.originalImage_manipulated_red ...
            == 0)))));
300         annotation('textbox', 'Units', 'normalized', ...
            'BackgroundColor','white', 'Color', 'black', ...
            'Position',  [0.01, 0.7  , 0.05, 0.03], 'String', ...
            strcat("slide X"))
301         annotation('textbox', 'Units', 'normalized', ...
            'BackgroundColor','white', 'Color', 'black', ...
            'Position',  [0.01, 0.67 , 0.05, 0.03], 'String', ...
            strcat("slide Y"))
302         annotation('textbox', 'Units', 'normalized', ...
            'BackgroundColor','white', 'Color', 'black', ...
            'Position',  [0.01, 0.64 , 0.05, 0.03], 'String', ...
            strcat("slide Width"))
303         annotation('textbox', 'Units', 'normalized', ...
            'BackgroundColor','white', 'Color', 'black', ...
            'Position',  [0.01, 0.61 , 0.05, 0.03], 'String', ...
            strcat("slide Length"))
304         this.UIs{1} = uicontrol('Style', 'edit',    'Units', ...
            'normalized', 'Position', [0.06, 0.7 , 0.05, 0.03], ...
            'String', this.scratchX);
305         this.UIs{2} = uicontrol('Style', 'edit',    'Units', ...
            'normalized', 'Position', [0.06, 0.67, 0.05, 0.03], ...
            'String', this.scratchY);
306         this.UIs{3} = uicontrol('Style', 'edit',    'Units', ...
            'normalized', 'Position', [0.06, 0.64, 0.05, 0.03], ...
            'String', this.scratchW);
307         this.UIs{4} = uicontrol('Style', 'edit',    'Units', ...
            'normalized', 'Position', [0.06, 0.61, 0.05, 0.03], ...
            'String', this.scratchL);
308         annotation('textbox', 'Units', 'normalized', ...
            'BackgroundColor','white', 'Color', 'black', ...
            'Position',  [0.46, 0.73 , 0.05, 0.03], 'String', ...
            strcat("crop top"))
```

```
309             annotation('textbox', 'Units', 'normalized', ...
                    'BackgroundColor','white', 'Color', 'black', ...
                    'Position', [0.36, 0.67 , 0.05, 0.03], 'String', ...
                    strcat("crop left"))
310             annotation('textbox', 'Units', 'normalized', ...
                    'BackgroundColor','white', 'Color', 'black', ...
                    'Position', [0.46, 0.61 , 0.05, 0.03], 'String', ...
                    strcat("crop bot"))
311             annotation('textbox', 'Units', 'normalized', ...
                    'BackgroundColor','white', 'Color', 'black', ...
                    'Position', [0.56, 0.67 , 0.05, 0.03], 'String', ...
                    strcat("crop right"))
312             this.UIs{5} = uicontrol('Style', 'edit',    'Units', ...
                    'normalized', 'Position', [0.46, 0.7 , 0.05, 0.03], ...
                    'String', this.lTopVal);    % top
313             this.UIs{6} = uicontrol('Style', 'edit',    'Units', ...
                    'normalized', 'Position', [0.46, 0.64, 0.05, 0.03], ...
                    'String', this.lBotVal);    % bot
314             this.UIs{7} = uicontrol('Style', 'edit',    'Units', ...
                    'normalized', 'Position', [0.41, 0.67, 0.05, 0.03], ...
                    'String', this.lLefVal);    % left
315             this.UIs{8} = uicontrol('Style', 'edit',    'Units', ...
                    'normalized', 'Position', [0.51, 0.67, 0.05, 0.03], ...
                    'String', this.lRigVal);    % right
316             this.UIs{9} = uicontrol('Style', 'edit',    'Units', ...
                    'normalized', 'Position', [0.47, 0.67, 0.04, 0.03], ...
                    'String', this.rotAngVal);    % rot
317             annotation('textbox', 'Units', 'normalized', ...
                    'BackgroundColor','white', 'Color', 'black', ...
                    'Position', [0.46, 0.67 , 0.01, 0.03], 'String', ...
                    strcat(""))
318             this.consoleUI = uicontrol('Style', 'listbox', 'Units', ...
                    'normalized', 'Position', [0.01, 0.5, 0.6, 0.07], ...
                    'String', this.eventHistory);
319
320             c = uicontrol('Units', 'normalized', 'Position', [0.01 ...
                    0.92, 0.09 0.06]);
321             c.String = 'Update Image';
322             c.Callback = @this.plotMyFigure;
323             l = uicontrol('Units', 'normalized', 'Position', [0.01 ...
                    0.85, 0.09 0.06]);
324             l.String = 'Load';
325             l.Callback = @this.load;
326             l = uicontrol('Units', 'normalized', ...
                    'BackgroundColor','red', 'Position', [0.01 0.78, ...
                    0.09 0.06]);
327             l.String = 'Save';
328             l.Callback = @this.save;
329             if sum(sum(this.originalImage_manipulated_red == 0)) == ...
                    0; l.BackgroundColor = 'green'; end
330         end
331
332         function save(this, ~, ~)
333             this.updateImages()
```

```
334             imwrite(this.originalImage_manipulated_red, ...
                    strcat(this.loadedFromBaseName, ...
                    'cropped_originalImage_red.TIF'));
335             imwrite(this.originalImage_manipulated_blue, ...
                    strcat(this.loadedFromBaseName, ...
                    'cropped_originalImage_blue.TIF'));
336             imwrite(this.originalImage_manipulated_bf, ...
                    strcat(this.loadedFromBaseName, ...
                    'cropped_originalImage_bf.TIF'));
337             imwrite(this.originalImage_manipulated_combined, ...
                    strcat(this.loadedFromBaseName, ...
                    'cropped_originalImage_combined.TIF'));
338             imwrite(this.BCAdjustedImage_manipulated_red, ...
                    strcat(this.loadedFromBaseName, ...
                    'cropped_BCAdjustedImage_red.TIF'));
339             imwrite(this.BCAdjustedImage_manipulated_blue, ...
                    strcat(this.loadedFromBaseName, ...
                    'cropped_BCAdjustedImage_blue.TIF'));
340             imwrite(this.BCAdjustedImage_manipulated_bf, ...
                    strcat(this.loadedFromBaseName, ...
                    'cropped_BCAdjustedImage_bf.TIF'));
341             imwrite(this.BCAdjustedImage_manipulated_combined, ...
                    strcat(this.loadedFromBaseName, ...
                    'cropped_BCAdjustedImage_combined.TIF'));
342             imageHeigth = size(this.originalImage_manipulated_red, ...
                    1);
343             imageWidth  = size(this.originalImage_manipulated_red, ...
                    2);
344             f = fopen(strcat(this.loadedFromBaseName, ...
                    'crop_config.txt'), 'w');
345             for i = 1:size(this.UIs, 2)
346                 fprintf(f,strcat(num2str(i), ' ...
                        %f\n'),str2double(this.UIs{i}.String));
347             end
348             fprintf(f,strcat(num2str(10), ' %f\n'),imageHeigth);
349             fprintf(f,strcat(num2str(11), ' %f\n'),imageWidth);
350             fclose(f);
351             this.addHistoryEntry(strcat('Saved Image to Base Name ...
                    ', this.loadedFromBaseName, '.'));
352             this.plotMyFigure();
353         end
354
355         function registerKeys(this, ~, event)
356             disp(['key pressed: ' event.Key])
357             if strcmp(event.Key, 'c')
358                 disp('select scratch angle');
359                 c = ginputWhite(2);
360                 x1 = c(1, 1);
361                 x2 = c(2, 1);
362                 y1 = c(1, 2);
363                 y2 = c(2, 2);
364                 mAngle = 180/pi*atan2((x2-x1),(y2-y1))-90;
365                 this.UIs{9}.String = ...
                        str2double(this.UIs{9}.String)-mAngle;
```

```
366                 this.plotMyFigure();
367             end
368             if strcmp(event.Key, 'w')
369                 disp('select scratch start Y');
370                 c = ginputWhite(1);
371                 this.UIs{2}.String = round(c(2));
372                 this.plotMyFigure();
373             end
374             if strcmp(event.Key, 'a')
375                 disp('select scratch start X');
376                 c = ginputWhite(1);
377                 this.UIs{1}.String = round(c(1));
378                 this.plotMyFigure();
379             end
380             if strcmp(event.Key, 's')
381                 disp('select scratch Width');
382                 c = ginputWhite(1);
383                 this.UIs{3}.String = ...
                        round(c(2)-str2double(this.UIs{2}.String));
384                 this.plotMyFigure();
385             end
386             if strcmp(event.Key, 'd')
387                 disp('select scratch Length');
388                 c = ginputWhite(1);
389                 this.UIs{4}.String = ...
                        round(c(1)-str2double(this.UIs{1}.String));
390                 this.plotMyFigure();
391             end
392             if strcmp(event.Key, 't')
393                 disp('select cutoff Top');
394                 c = ginputWhite(1);
395                 this.UIs{5}.String = ...
                        round(c(2)+str2double(this.UIs{5}.String));
396                 this.plotMyFigure();
397             end
398             if strcmp(event.Key, 'f')
399                 disp('select cutoff Left');
400                 c = ginputWhite(1);
401                 this.UIs{7}.String = ...
                        round(c(1)+str2double(this.UIs{7}.String));
402                 this.plotMyFigure();
403             end
404             if strcmp(event.Key, 'g')
405                 disp('select cutoff Bottom');
406                 c = ginputWhite(1);
407                 this.UIs{6}.String = ...
                        round(size(this.BCAdjustedImage_red, ...
                        1)-(c(2)+str2double(this.UIs{5}.String)));
408                 this.plotMyFigure();
409             end
410             if strcmp(event.Key, 'h')
411                 disp('select cutoff Right');
412                 c = ginputWhite(1);
```

```
413                     this.UIs{8}.String = ...
                            round(size(this.BCAdjustedImage_red, ...
                            2)-(c(1)+str2double(this.UIs{7}.String)));
414                     this.plotMyFigure();
415                 end
416             end
417
418         end
419     end
420
421     function h = circleA(x,y,r,a1,a2,lineColour)
422     hold on
423     th = a1:pi/50:a2;
424     xunit = r * cos(th) + x;
425     yunit = r * sin(th) + y;
426     h = plot(xunit, yunit, 'color', lineColour);
427     hold off
428     end
429
430     function h = circleB(x,y,r,a1,a2,lineColour, lineAlpha, areaColour, ...
            areaAlpha)
431     hold on
432     th = a1:pi/50:a2;
433     xunit = r * cos(th) + x;
434     yunit = r * sin(th) + y;
435     h = patch('Faces', 1:size(xunit, 2), 'Vertices', [xunit', ...
            yunit'],'FaceColor',areaColour,'FaceAlpha', areaAlpha, ...
            'EdgeColor', lineColour, 'EdgeAlpha', lineAlpha);
436     hold off
437     end
438
439     function fig = figureFullscreen(monitorN)
440         MP=get(0,'MonitorPositions');
441         fig=figure;
442         if monitorN<=size(MP,1)
443             pause(0.01); % this seems sometimes necessary on a Mac
444             set(fig,'Position',[MP(monitorN,1:2)+MP(monitorN,3:4)/4 ...
                    MP(monitorN,3:4)/2]);
445             pause(0.01); % this seems sometimes necessary on a Mac
446             set(fig,'WindowState','maximized');
447             %figure('units','normalized','outerposition',[0 0 1 1], ...
                    'WindowState','maximized');
448         else
449             disp(strcat("attempted to create fullscreen figure on ...
                    monitor ", string(monitorN), " but not enough monitors ...
                    were detected. Figure was not set to fullscreen."));
450         end
451     end
452
453     function outImg = rotCropImage(inImg, leftCrop, rightCrop, topCrop, ...
            botCrop, rotAng)
454         imageHeigth = size(inImg, 1);
455         imageWidth  = size(inImg, 2);
456         crpArea = round([topCrop, leftCrop, botCrop, rightCrop]);
```

```
457         if rotAng ~= 0
458             outImg = imrotate(inImg, rotAng, 'bilinear','crop');
459         else
460             outImg = inImg;
461             disp("not rotating image")
462         end
463         if isequal(crpArea, [1 1 0 0])
464             disp("not cropping image")
465         else
466             outImg = outImg(crpArea(1):imageHeigth-crpArea(3), ...
                    crpArea(2):imageWidth-crpArea(4), :);
467         end
468     end
469
470     function a = generateAxes(nx, ny, dx, dy)
471         imgAxPos = zeros(nx*ny,4);
472         sizex = (1-dx)/nx;
473         sizey = (1-dy)/ny;
474         for x = 1:nx
475             for y = 1:ny
476                 currentAx = (x-1)*ny+y;
477                 posx = dx/(nx+1)*x+sizex*(x-1);
478                 posy = dy/(ny+1)*y+sizey*(y-1);
479                 imgAxPos(currentAx,1:4) = [posx, posy, sizex, sizey];
480             end
481         end
482         for i =1:size(imgAxPos,1)
483             a(i) = axes('Units', 'normalized', 'Position', ...
                    imgAxPos(i,:));
484         end
485     end
```

A.3 Nuclei Loader

```
1
2   function retVals = nucleiLoader(sampleID, slideN, verbose)
3       % verbose = false; % verbose = true ^= show pictures.
4
5       configName = strcat(sampleID, "/slide_", slideN, "/", sampleID, ...
            "_", slideN, "_crop_config.txt");
6       nucleifileName_blue = strcat(sampleID, "/slide_", slideN, ...
            "/hoechst_stained_nuclei.csv");
7       nucleifileName_red = strcat(sampleID, "/slide_", slideN, ...
            "/pi_stained_nuclei.csv");
8
9       if verbose == true
10          imageName_blue = strcat(sampleID, "/slide_", slideN, "/", ...
                sampleID, "_", slideN, ...
                "_cropped_BCAdjustedImage_blue.TIF");
```

```
11          imageName_red = strcat(sampleID, "/slide_", slideN, "/", ...
                sampleID, "_", slideN, ...
                "_cropped_BCAdjustedImage_red.TIF");
12      end
13
14
15      formatSpec = '%f,%f,%f,%f,%f,%f\n';
16      sizeA = [6 Inf];
17
18
19
20
21      f=fopen(nucleifileName_blue, 'r');
22      fgetl(f);;
23      Ab =fscanf(f,formatSpec, sizeA);
24      fclose(f);
25      f=fopen(nucleifileName_red, 'r');
26      fgetl(f);;
27      Ar =fscanf(f,formatSpec, sizeA);
28      fclose(f);
29
30      f = fopen(configName, 'r');
31      params =fscanf(f,'%d %f', [2 Inf]);
32      fclose(f);
33      scratchX = params(2,params(1,:)==1);
34      scratchY = params(2,params(1,:)==2);
35      scratchW = params(2,params(1,:)==3);
36      scratchL = params(2,params(1,:)==4);
37      cutoffTop = params(2,params(1,:)==5);
38      cutoffBot = params(2,params(1,:)==6);
39      cutoffLeft = params(2,params(1,:)==7);
40      cutoffRight = params(2,params(1,:)==8);
41      rotAng = params(2,params(1,:)==9);
42      imageHeigth = params(2,params(1,:)==10);
43      imageWidth  = params(2,params(1,:)==11);
44      di = 20;
45      do = 50;
46
47      if verbose == true
48          b = Tiff(strcat(imageName_blue)).read();
49          r = Tiff(strcat(imageName_red)).read();
50      end
51
52
53      %r = rotCropImage(r, cutoffLeft, cutoffRight, cutoffTop, ...
            cutoffBot, rotAng);
54      %b = rotCropImage(b, cutoffLeft, cutoffRight, cutoffTop, ...
            cutoffBot, rotAng);
55      if verbose == true
56          imageHeigth = size(r, 1);
57          imageWidth  = size(r, 2);
58
59  %     this part is to save image height and width into crop config ...
        file.
```

```
60  %
61          f = fopen(configName, 'w');
62          for i = 1:9
63              fprintf(f,strcat(num2str(i), ' ...
                    %f\n'),params(2,params(1,:)==i));
64          end
65          fprintf(f,strcat(num2str(10), ' %f\n'),imageHeigth);
66          fprintf(f,strcat(num2str(11), ' %f\n'),imageWidth);
67          fclose(f);
68      end
69
70
71
72      compareLeft = scratchX-di;
73      compareRight = imageWidth-(scratchX+scratchL)-di;
74      compareTop = scratchY-di;
75      compareBot = imageHeigth-(scratchY+scratchW)-di;
76
77      cellsSlide_red = Ar(:,Ar(3,:)>scratchX+scratchW & ...
            Ar(3,:)<scratchX+scratchL-scratchW & Ar(4,:)>scratchY & ...
            Ar(4,:)<scratchY+scratchW);
78      cellsCompareTop_red = Ar(:,Ar(3,:)>scratchX+scratchW & ...
            Ar(3,:)<scratchX+scratchL-scratchW & ...
            Ar(4,:)>scratchY-compareTop & Ar(4,:)<scratchY-do);
79      cellsCompareBot_red = Ar(:,Ar(3,:)>scratchX+scratchW & ...
            Ar(3,:)<scratchX+scratchL-scratchW & ...
            Ar(4,:)>scratchY+scratchW+do & ...
            Ar(4,:)<scratchY+scratchW+compareBot);
80      cellsCompareLeft_red = Ar(:,Ar(3,:)>scratchX-compareLeft & ...
            Ar(3,:)<scratchX-do & Ar(4,:)>scratchY & ...
            Ar(4,:)<scratchY+scratchW);
81      cellsCompareRight_red = Ar(:,Ar(3,:)>scratchX+scratchL+do & ...
            Ar(3,:)<scratchX+scratchL+compareRight & Ar(4,:)>scratchY & ...
            Ar(4,:)<scratchY+scratchW);
82      cellsCompareTotal_red = [cellsCompareTop_red, ...
            cellsCompareBot_red, cellsCompareLeft_red, ...
            cellsCompareRight_red];
83
84      cellsSlide_blue = Ab(:,Ab(3,:)>scratchX+scratchW & ...
            Ab(3,:)<scratchX+scratchL-scratchW & Ab(4,:)>scratchY & ...
            Ab(4,:)<scratchY+scratchW);
85      cellsCompareTop_blue = Ab(:,Ab(3,:)>scratchX+scratchW & ...
            Ab(3,:)<scratchX+scratchL-scratchW & ...
            Ab(4,:)>scratchY-compareTop & Ab(4,:)<scratchY-do);
86      cellsCompareBot_blue = Ab(:,Ab(3,:)>scratchX+scratchW & ...
            Ab(3,:)<scratchX+scratchL-scratchW & ...
            Ab(4,:)>scratchY+scratchW+do & ...
            Ab(4,:)<scratchY+scratchW+compareBot);
87      cellsCompareLeft_blue = Ab(:,Ab(3,:)>scratchX-compareLeft & ...
            Ab(3,:)<scratchX-do & Ab(4,:)>scratchY & ...
            Ab(4,:)<scratchY+scratchW);
88      cellsCompareRight_blue = Ab(:,Ab(3,:)>scratchX+scratchL+do & ...
            Ab(3,:)<scratchX+scratchL+compareRight & Ab(4,:)>scratchY & ...
            Ab(4,:)<scratchY+scratchW);
```

```
89      cellsCompareTotal_blue = [cellsCompareTop_blue, ...
            cellsCompareBot_blue, cellsCompareLeft_blue, ...
            cellsCompareRight_blue];
90
91
92
93      if verbose == true
94          f = figureFullscreen(3);
95          a = generateAxes(1, 2, 0.05, 0.05);
96          axes(a(2))
97          imshow(r)
98          hold on
99          plot(Ar(3,:), Ar(4,:), 'x', 'Color', 'white')
100         plot(cellsSlide_red(3,:), cellsSlide_red(4,:), 'o', ...
                'Color', 'c')
101         plot(cellsCompareTop_red(3,:), cellsCompareTop_red(4,:), ...
                'o', 'Color', 'r')
102         plot(cellsCompareBot_red(3,:), cellsCompareBot_red(4,:), ...
                'o', 'Color', 'r')
103         plot(cellsCompareLeft_red(3,:), cellsCompareLeft_red(4,:), ...
                'o', 'Color', 'r')
104         plot(cellsCompareRight_red(3,:), ...
                cellsCompareRight_red(4,:), 'o', 'Color', 'r')
105         drawScratchOutlines(configName, r);
106         axes(a(1));
107         imshow(b)
108         hold on
109         plot(Ab(3,:), Ab(4,:), 'x', 'Color', 'white')
110         plot(cellsSlide_blue(3,:), cellsSlide_blue(4,:), 'o', ...
                'Color', 'c')
111         plot(cellsCompareTop_blue(3,:), cellsCompareTop_blue(4,:), ...
                'o', 'Color', 'r')
112         plot(cellsCompareBot_blue(3,:), cellsCompareBot_blue(4,:), ...
                'o', 'Color', 'r')
113         plot(cellsCompareLeft_blue(3,:), ...
                cellsCompareLeft_blue(4,:), 'o', 'Color', 'r')
114         plot(cellsCompareRight_blue(3,:), ...
                cellsCompareRight_blue(4,:), 'o', 'Color', 'r')
115         drawScratchOutlines(configName, b);
116     end
117
118     ASlide = scratchW*(scratchL-2*scratchW);
119     ACompareTop = (compareTop-do)*(scratchL-2*scratchW);
120     ACompareBot = (compareBot-do)*(scratchL-2*scratchW);
121     ACompareLeft = (compareLeft-do)*(scratchW);
122     ACompareRight = (compareRight-do)*(scratchW);
123     ACompareTotal = ...
            ACompareTop+ACompareBot+ACompareLeft+ACompareRight;
124
125
126     rhoSlide_red = size(cellsSlide_red, 2)/ASlide*10000;
127     rhoCompareTop_red = size(cellsCompareTop_red, ...
            2)/ACompareTop*10000;
```

```
128     rhoCompareBot_red = size(cellsCompareBot_red, ...
            2)/ACompareBot*10000;
129     rhoCompareLeft_red = size(cellsCompareLeft_red, ...
            2)/ACompareLeft*10000;
130     rhoCompareRight_red = size(cellsCompareRight_red, ...
            2)/ACompareRight*10000;
131     rhoCompareTotal_red = size(cellsCompareTotal_red, ...
            2)/ACompareTotal*10000;
132
133
134
135     rhoSlide_blue = size(cellsSlide_blue, 2)/ASlide*10000;
136     rhoCompareTop_blue = size(cellsCompareTop_blue, ...
            2)/ACompareTop*10000;
137     rhoCompareBot_blue = size(cellsCompareBot_blue, ...
            2)/ACompareBot*10000;
138     rhoCompareLeft_blue = size(cellsCompareLeft_blue, ...
            2)/ACompareLeft*10000;
139     rhoCompareRight_blue = size(cellsCompareRight_blue, ...
            2)/ACompareRight*10000;
140     rhoCompareTotal_blue = size(cellsCompareTotal_blue, ...
            2)/ACompareTotal*10000;
141
142     X = categorical({'Top','Bot','Left','Right', 'Total Compare', ...
            'Slide'});
143     X = reordercats(X,{'Top','Bot','Left','Right', 'Total Compare', ...
            'Slide'});
144
145     if verbose == true
146         f2 = figureFullscreen(1);
147         figure(f2)
148         a2 = generateAxes(2,1,0.1, 0.1);
149         axes(a2(2));
150         bar(X, [rhoCompareTop_blue, rhoCompareBot_blue, ...
                rhoCompareLeft_blue, rhoCompareRight_blue, ...
                rhoCompareTotal_blue, rhoSlide_blue], 'blue');
151         title('blue nuclei densities')
152
153         axes(a2(1));
154         bar(X, [rhoCompareTop_red, rhoCompareBot_red, ...
                rhoCompareLeft_red, rhoCompareRight_red, ...
                rhoCompareTotal_red, rhoSlide_red], 'red');
155
156         title('red nuclei densities')
157     end
158
159     retVals.slideIdentifier = strcat(sampleID, "_", slideN);
160     retVals.rhoCompareTop_red = rhoCompareTop_red;
161     retVals.rhoCompareBot_red = rhoCompareBot_red;
162     retVals.rhoCompareLeft_red = rhoCompareLeft_red;
163     retVals.rhoCompareRight_red = rhoCompareRight_red;
164     retVals.rhoCompareTotal_red = rhoCompareTotal_red;
165     retVals.rhoSlide_red = rhoSlide_red;
166     retVals.rhoCompareTop_blue = rhoCompareTop_blue;
```

```
167     retVals.rhoCompareBot_blue = rhoCompareBot_blue;
168     retVals.rhoCompareLeft_blue = rhoCompareLeft_blue;
169     retVals.rhoCompareRight_blue = rhoCompareRight_blue;
170     retVals.rhoCompareTotal_blue = rhoCompareTotal_blue;
171     retVals.rhoSlide_blue = rhoSlide_blue;
172
173 end
174
175 %AComp =
176
177
178 function drawScratchOutlines(configFile, image)
179     f2 = fopen(configFile, 'r');
180     params =fscanf(f2,'%d %f', [2 Inf]);
181     fclose(f2);
182     imageHeigth = size(image, 1);
183     imageWidth  = size(image, 2);
184     di = 20;
185     do = 50;
186     scratchX = params(2,params(1,:)==1);
187     scratchY = params(2,params(1,:)==2);
188     scratchW = params(2,params(1,:)==3);
189     scratchL = params(2,params(1,:)==4);
190     compareLeft = scratchX-di;
191     compareRight = imageWidth-(scratchX+scratchL)-di;
192     compareTop = scratchY-di;
193     compareBot = imageHeigth-(scratchY+scratchW)-di;
194     scratchEdgeColor = 'g';
195     scratchFaceColor = 'blue';
196     scratchFaceAlpha = 0.2';
197     compareFaceAlpha = 0.2;
198     scratchPosX = [scratchX,scratchX, scratchX+scratchL, ...
            scratchX+scratchL];
199     scratchPosY = [scratchY, scratchY+scratchW, scratchY+scratchW, ...
            scratchY];
200     scratchPos = [scratchPosX',scratchPosY'];
201     patch('Faces', 1:size(scratchPos, 1), 'Vertices', ...
            scratchPos,'FaceColor','red','FaceAlpha', 0.0, 'EdgeColor', ...
            'white')
202     compareLeftPosX = [scratchX-compareLeft,scratchX-compareLeft, ...
            scratchX-do, scratchX-do];
203     compareLeftPosY = [scratchY, scratchY+scratchW, ...
            scratchY+scratchW, scratchY];
204     compareLeftPos = [compareLeftPosX',compareLeftPosY'];
205     patch('Faces', 1:size(compareLeftPos, 1), 'Vertices', ...
            compareLeftPos,'FaceColor','green','FaceAlpha', ...
            compareFaceAlpha, 'EdgeColor', 'white')
206     compareRightPosX = [scratchX+scratchL+do,scratchX+scratchL+do, ...
            scratchX+scratchL+compareRight, ...
            scratchX+scratchL+compareRight];
207     compareRightPosY = [scratchY, scratchY+scratchW, ...
            scratchY+scratchW, scratchY];
208     compareRightPos = [compareRightPosX',compareRightPosY'];
```

```
209     patch('Faces', 1:size(compareRightPos, 1), 'Vertices', ...
            compareRightPos,'FaceColor','green','FaceAlpha', ...
            compareFaceAlpha, 'EdgeColor', 'white')
210     compareTopPosX = [scratchX+scratchW,scratchX+scratchW, ...
            scratchX+scratchL-scratchW, scratchX+scratchL-scratchW];
211     compareTopPosY = [scratchY-compareTop, scratchY-do, ...
            scratchY-do, scratchY-compareTop];
212     compareTopPos = [compareTopPosX',compareTopPosY'];
213     patch('Faces', 1:size(compareTopPos, 1), 'Vertices', ...
            compareTopPos,'FaceColor','green','FaceAlpha', ...
            compareFaceAlpha, 'EdgeColor', 'white')
214     compareBotPosX = [scratchX+scratchW,scratchX+scratchW, ...
            scratchX+scratchL-scratchW, scratchX+scratchL-scratchW];
215     compareBotPosY = [scratchY+scratchW+do, ...
            scratchY+scratchW+compareBot, scratchY+scratchW+compareBot, ...
            scratchY+scratchW+do];
216     compareBotPos = [compareBotPosX',compareBotPosY'];
217     patch('Faces', 1:size(compareBotPos, 1), 'Vertices', ...
            compareBotPos,'FaceColor','green','FaceAlpha', ...
            compareFaceAlpha, 'EdgeColor', 'white')
218     indentPosX = [scratchX,scratchX, scratchX+scratchW, ...
            scratchX+scratchW];
219     indentPosY = [scratchY, scratchY+scratchW, scratchY+scratchW, ...
            scratchY];
220     indentPos = [indentPosX',indentPosY'];
221     patch('Faces', 1:size(indentPos, 1), 'Vertices', ...
            indentPos,'FaceColor','blue','FaceAlpha', 0.0, 'EdgeColor', ...
            'blue')
222     compareBotPosX = [scratchX+scratchW,scratchX+scratchL-scratchW, ...
            scratchX+scratchL-scratchW, scratchX+scratchW];
223     compareBotPosY = [scratchY, scratchY, scratchY+scratchW, ...
            scratchY+scratchW];
224     compareBotPos = [compareBotPosX',compareBotPosY'];
225     patch('Faces', 1:size(compareBotPos, 1), 'Vertices', ...
            compareBotPos,'FaceColor','green','FaceAlpha', 0.3, ...
            'EdgeColor', 'white')
226
227     circleB(scratchX+scratchW/2, scratchY+scratchW/2, scratchW/2, ...
            1/2*pi, 3/2*pi, 'white', 0, scratchFaceColor, ...
            scratchFaceAlpha);
228     circleB(scratchX+scratchL-scratchW/2, scratchY+scratchW/2, ...
            scratchW/2, -1/2*pi, 1/2*pi, 'white', 0, scratchFaceColor, ...
            scratchFaceAlpha);
229     scratchMarkPos = [scratchX+scratchW/2, scratchY; ...
            scratchX+scratchL-scratchW/2, scratchY; ...
            scratchX+scratchL-scratchW/2, scratchY+scratchW; ...
            scratchX+scratchW/2, scratchY+scratchW];
230     patch('Faces', 1:size(scratchMarkPos, 1), 'Vertices', ...
            scratchMarkPos,'FaceColor',scratchFaceColor,'FaceAlpha', ...
            scratchFaceAlpha, 'EdgeColor', 'white', 'EdgeAlpha', 0)
231     scratchSlidePos = [scratchX+scratchW, scratchY; ...
            scratchX+scratchL-scratchW, scratchY; ...
            scratchX+scratchL-scratchW, scratchY+scratchW; ...
            scratchX+scratchW, scratchY+scratchW];
```

```
232     patch('Faces', 1:size(scratchSlidePos, 1), 'Vertices', ...
            scratchSlidePos,'FaceColor',scratchFaceColor,'FaceAlpha', ...
            0.0, 'EdgeColor', 'red', 'EdgeAlpha', 1.0)
233     circleA(scratchX+scratchW/2, scratchY+scratchW/2, scratchW/2, ...
            0, 2*pi, scratchEdgeColor);
234     circleA(scratchX+scratchL-scratchW/2, scratchY+scratchW/2, ...
            scratchW/2, 0, 2*pi, scratchEdgeColor);
235 end
236
237 function h = circleA(x,y,r,a1,a2,lineColour)
238 hold on
239 th = a1:pi/50:a2;
240 xunit = r * cos(th) + x;
241 yunit = r * sin(th) + y;
242 h = plot(xunit, yunit, 'color', lineColour);
243 hold off
244 end
245
246 function h = circleB(x,y,r,a1,a2,lineColour, lineAlpha, areaColour, ...
        areaAlpha)
247 hold on
248 th = a1:pi/50:a2;
249 xunit = r * cos(th) + x;
250 yunit = r * sin(th) + y;
251 h = patch('Faces', 1:size(xunit, 2), 'Vertices', [xunit', ...
        yunit'],'FaceColor',areaColour,'FaceAlpha', areaAlpha, ...
        'EdgeColor', lineColour, 'EdgeAlpha', lineAlpha);
252 hold off
253 end
254
255 function a = generateAxes(nx, ny, dx, dy)
256     imgAxPos = zeros(nx*ny,4);
257     sizex = (1-dx)/nx;
258     sizey = (1-dy)/ny;
259     for x = 1:nx
260         for y = 1:ny
261             currentAx = (x-1)*ny+y;
262             posx = dx/(nx+1)*x+sizex*(x-1);
263             posy = dy/(ny+1)*y+sizey*(y-1);
264             imgAxPos(currentAx,1:4) = [posx, posy, sizex, sizey];
265         end
266     end
267     for i =1:size(imgAxPos,1)
268         a(i) = axes('Units', 'normalized', 'Position', ...
                imgAxPos(i,:));
269     end
270 end
271
272 function fig = figureFullscreen(monitorN)
273     MP=get(0,'MonitorPositions');
274     fig=figure;
275     if monitorN<=size(MP,1)
276         pause(0.01); % this seems sometimes necessary on a Mac
```

```
277             set(fig,'Position',[MP(monitorN,1:2)+MP(monitorN,3:4)/4 ...
                    MP(monitorN,3:4)/2]);
278             pause(0.01); % this seems sometimes necessary on a Mac
279             set(fig,'WindowState','maximized');
280             %figure('units','normalized','outerposition',[0 0 1 1], ...
                    'WindowState','maximized');
281         else
282             disp(strcat("attempted to create fullscreen figure on ...
                    monitor ", string(monitorN), " but not enough monitors ...
                    were detected. Figure was not set to fullscreen."));
283         end
284     end
```

A.4 Friction Analysis

```
1  close all
2  clear all
3
4  [file,path] = uigetfile('.csv')
5  frictionDataPath = strcat(path, file);
6
7  %file = 'asdf'
8  %frictionDataPath = ...
       'S201111_1\slide_1\data_friction\S201111_1_scratch1_sliding.csv';
9
10 dataTemp = readUMTDataMatlab(frictionDataPath);
11
12 t = dataTemp.slides.t;
13 cof = -dataTemp.slides.force_x./dataTemp.slides.force_z;
14 x = -dataTemp.slides.Δ_x;
15 Fz = dataTemp.slides.force_z;
16 Fx = -dataTemp.slides.force_x;
17 Δz = dataTemp.slides.Δ_z;
18
19 tMax = 11;
20 allowedTVals = (t≤tMax);
21
22 % sliding range is 0.1 mm > x > max(x) - 0.1 mm
23 xStart = 0.1;
24 xEnd = max(x)-0.1;
25 x_slideRange = x(xStart<x & x<xEnd);
26 t_slideRange = t(xStart<x & x<xEnd);
27 Δz_slideRange = Δz(xStart<x & x<xEnd);
28
29 p = polyfit(x_slideRange, Δz_slideRange, 5);
30 Δz_polynomial = polyval(p, x_slideRange);
31 pdX = polyder(p);
32 ΔzdX_polynomial = polyval(pdX, x_slideRange);
33
```

```
34
35 % figure 1: space domain
36
37 % f2 = figureFullscreen(3);
38 % figure(f2)
39 % a = axes();
40 % yyaxis right;
41 % p = plot(x(allowedTVals), Fx(allowedTVals), 'xg');
42 % yyaxis left;
43 % hold on
44 % plot(x_slideRange, ΔzdX_slideRange, 'r');
45 % plot(x_slideRange, Δz_slideRange, 'b');
46 %% polynomial approximation:
47 % plot(x_slideRange, ΔzdX_polynomial, '.r', 'LineWidth',2);
48 % plot(x_slideRange, Δz_polynomial, '.b', 'LineWidth',2);
49 % xlim([0, xEnd+1]);
50 % grid on
51
52
53 % figure 2 test time domain
54
55 f = figureFullscreen(1);
56 figure(f)
57 a = axes();
58 yyaxis right;
59 p = plot(t, Fx, '-xblue');
60 ax = gca; set(ax, 'YColor', 'blue');
61 xlim(xlim-[1, 0]);
62 xlimbef = a.XLim;
63 ylimbef = a.YLim;
64 ylabel('Force in x-direction F_X [mN]');
65 yyaxis left;
66 line([-2,15],[0, 0], 'LineWidth', 1, 'Color', [0 0 0], ...
      'HandleVisibility', 'off')
67 hold on
68 Δz_plot = plot(t, Δz, ':black');
69 %p2 = plot(t(1:end-k), ΔzdX, ':r');
70 %p4 = plot(t_slideRange, Δz_slideRange, '--b');
71 Δz_polynomial_plot = plot(t_slideRange, Δz_polynomial, '-black', ...
      'LineWidth',2);
72 ΔzdX_polynomial_plot = plot(t_slideRange, ΔzdX_polynomial, '-', ...
      'LineWidth',2, 'Color', [0.5 0.5 0.5]);
73 ax = gca; set(ax, 'YColor', 'black');
74 grid on
75 set(gca,'fontsize', 24);
76 ylabel('Height of probe [{\mu}m] / slope [{\mu}m/mm] ...
      ','FontSize',28);
77 yyaxis right;
78 xlabel('Time [s]','FontSize',28);
79 title('UMT Stage Friction and Position Data','FontSize',32)
80
81
82
83 % figure 2: time domain
```

```
84
85 % backup 1
86 % f = figureFullscreen(1);
87 % figure(f)
88 % a = axes();
89 % yyaxis right;
90 % p = plot(t(allowedTVals), Fx(allowedTVals), 'x');
91 % hold on
92 % yyaxis left;
93 % p3 = plot(t(allowedTVals), ΔZ(allowedTVals), '-');
94 % grid on
95 % yyaxis left;
96
97 % f = figureFullscreen(3);
98 % a = axes();
99 % yyaxis left;
100 % p = plot(t(allowedTVals), Fx(allowedTVals), 'x');
101 % hold on
102 % yyaxis right;
103 % p2 = plot(t(allowedTVals), x(allowedTVals)*100, '-');
104 % p3 = plot(t(allowedTVals), ΔZ(allowedTVals), '-');
105 % yyaxis left;
106
107
108
109
110
111
112
113 c = ginput(8);
114 %c = [-0.0783    0.4553
115 %       0.0528    0.4492
116 %       0.0877    0.4471
117 %       0.2100    0.4471
118 %       1.1099    0.4288
119 %       2.2107    0.3962
120 %       3.1193    0.4268
121 %       4.0104  -27.1847
122 %       8.5010  -20.3822
123 %       9.1300  -20.6115];
124
125
126 measure_FF_before_motion_x1 = c(1,1);
127 measure_FF_before_motion_x2 = c(2,1);
128 measure_FF_static_x1 = c(3,1);
129 measure_FF_static_x2 = c(4,1);
130 measure_FF_initial_motion_x1 = c(5,1);
131 measure_FF_initial_motion_x2 = c(6,1);
132 measure_FF_zero_slope_x1 = c(7,1);
133 measure_FF_zero_slope_x2 = c(8,1);
134
135
136 rectangle('Position', [measure_FF_before_motion_x1, a.YLim(1), ...
      measure_FF_before_motion_x2-measure_FF_before_motion_x1, ...
```

```
        a.YLim(2)-a.YLim(1)], 'EdgeColor', 'none', 'FaceColor', [1 0 0 ...
        0.3]);
137 rectangle('Position', [measure_FF_static_x1, a.YLim(1), ...
        measure_FF_static_x2-measure_FF_static_x1, ...
        a.YLim(2)-a.YLim(1)], 'EdgeColor', 'none', 'FaceColor', [0 1 0 ...
        0.3]);
138 rectangle('Position', [measure_FF_initial_motion_x1, a.YLim(1), ...
        measure_FF_initial_motion_x2-measure_FF_initial_motion_x1, ...
        a.YLim(2)-a.YLim(1)], 'EdgeColor', 'none', 'FaceColor', [0 0 1 ...
        0.3]);
139 rectangle('Position', [measure_FF_zero_slope_x1, a.YLim(1), ...
        measure_FF_zero_slope_x2-measure_FF_zero_slope_x1, ...
        a.YLim(2)-a.YLim(1)], 'EdgeColor', 'none', 'FaceColor', [0 0 0 ...
        0.3]);
140
141
142
143 a.XLim = xlimbef;
144 a.YLim = ylimbef;
145
146 FF_before_motion = mean( ...
        Fx(t>measure_FF_before_motion_x1&t<measure_FF_before_motion_x2) )
147 FF_static = max( Fx(t>measure_FF_static_x1&t<measure_FF_static_x2) )
148 maxFxFz = Fz( Fx==FF_static )
149 FF_initial_motion = mean( ...
        Fx(t>measure_FF_initial_motion_x1&t<measure_FF_initial_motion_x2) ...
        );
150 FF_zero_slope = mean( ...
        Fx(t>measure_FF_zero_slope_x1&t<measure_FF_zero_slope_x2) );
151
152 plot([a.XLim(2), measure_FF_before_motion_x1], [FF_before_motion, ...
        FF_before_motion], ':black', 'LineWidth', 2);
153 plot([a.XLim(2), measure_FF_static_x1], [FF_static, FF_static], ...
        ':blue', 'LineWidth', 2);
154 plot([a.XLim(2), measure_FF_initial_motion_x1], [FF_initial_motion, ...
        FF_initial_motion], ':green', 'LineWidth', 2);
155 plot([a.XLim(2), measure_FF_zero_slope_x1], [FF_zero_slope, ...
        FF_zero_slope], ':red', 'LineWidth', 2);
156
157
158 legend('h_m(t) probe height measured',...
159        'h_p(t) probe height polynomial',...
160        '\partial_x h_p(t) slope polynomial',...
161        'F_X',...
162        'F_X before motion',...
163        'F_X static',...
164        'F_X sliding initial',...
165        'F_X zero slope');
166
167 a.YTick = sort([a.YTick, FF_before_motion, FF_static, ...
        FF_initial_motion, FF_zero_slope]);
168
169
170
```

```
171 f_clipboard(file, [FF_before_motion, FF_static, maxFxFz(1), ...
        FF_initial_motion, FF_zero_slope]);
172
173 %pause(2);
174
175 %close(f)
176
177
178
179 function outputData = readUMTDataMatlab(filename)
180 fid = fopen(filename);
181 nSlides = 0;
182 currentSlidingDirection = 1;
183 % dataCounter = 0;
184 % lineCounter = 0;
185 frictionData = newFrictionData();
186 slides = struct([]);
187 while(feof(fid) == false)
188     %     old method (slower)
189     %     l = fgetl(fid);
190     %     lineCounter = lineCounter + 1;
191     %     if(isempty(l) == false)
192     %         ln = textscan(l, '%f,%f,%f,%f,%f,%f,%f,%f,%f,%f,%f');
193     %         if(isempty(ln{1}) == false)
194     %             dataCounter = dataCounter + 1;
195     %             frictionData(dataCounter, :) = [ln{:}];
196     %
197     %         end
198     %     end
199
200     %     new method (faster)
201     ln = textscan(fid, '%f,%f,%f,%f,%f,%f,%f,%f,%f,%f,%f');
202     if(isempty(ln{1}) == false)
203         nSlides = nSlides + 1;
204         slides(nSlides).direction = currentSlidingDirection;
205         currentSlidingDirection = -currentSlidingDirection;
206         slides(nSlides).force_x = [ln{:,1}];
207         slides(nSlides).force_z = -[ln{:,2}];
208         slides(nSlides).pos_z = [ln{:,3}];
209         slides(nSlides).pos_y = [ln{:,4}];
210         slides(nSlides).pos_x = [ln{:,5}];
211         slides(nSlides).vel_1 = [ln{:,6}];
212         slides(nSlides).vel_2 = [ln{:,7}];
213         slides(nSlides).vel_3 = [ln{:,8}];
214         slides(nSlides).t = [ln{:,9}];
215         slides(nSlides).force_f = [ln{:,10}];
216         slides(nSlides).CoF = [ln{:,11}];
217         slides(nSlides).delta_x=slides(nSlides).pos_x-slides(1).pos_x(1);
218         % difference in x (sliding distance) [mm]
219         slides(nSlides).delta_z=...
220             -(slides(nSlides).pos_z-slides(1).pos_z(1))*1000;
221         % difference in z (height difference to starting point) [µm].
222         % Negative because that is the coordinate system of the UMT ...
              machine.
```

```
223
224         frictionData.force_x = [frictionData.force_x; ...
                slides(nSlides).force_x];
225         frictionData.force_z = [frictionData.force_z; ...
                slides(nSlides).force_z];
226         frictionData.pos_z = [frictionData.pos_z; ...
                slides(nSlides).pos_z];
227         frictionData.pos_y = [frictionData.pos_y; ...
                slides(nSlides).pos_y];
228         frictionData.pos_x = [frictionData.pos_x; ...
                slides(nSlides).pos_x];
229         frictionData.vel_1 = [frictionData.vel_1; ...
                slides(nSlides).vel_1];
230         frictionData.vel_2 = [frictionData.vel_2; ...
                slides(nSlides).vel_2];
231         frictionData.vel_3 = [frictionData.vel_3; ...
                slides(nSlides).vel_3];
232         frictionData.t = [frictionData.t; slides(nSlides).t];
233         frictionData.force_f = [frictionData.force_f; ...
                slides(nSlides).force_f];
234         frictionData.CoF = [frictionData.CoF; slides(nSlides).CoF];
235         frictionData.Δ_x = [frictionData.Δ_x; slides(nSlides).Δ_x];
236         frictionData.Δ_z = [frictionData.Δ_z; slides(nSlides).Δ_z];
237     end
238     outputData.frictionData = frictionData;
239     outputData.slides = slides;
240     outputData.nSlides = nSlides;
241     fgetl(fid);
242 end
243 fclose(fid);
244 frictionData.slides = slides;
245 end
246
247 function frictionData = newFrictionData()
248 frictionData = struct;
249 frictionData.force_x = [];
250 frictionData.force_z = [];
251 frictionData.pos_z = [];
252 frictionData.pos_y = [];
253 frictionData.pos_x = [];
254 frictionData.vel_1 = [];
255 frictionData.vel_2 = [];
256 frictionData.vel_3 = [];
257 frictionData.t = [];
258 frictionData.force_f = [];
259 frictionData.CoF = [];
260 frictionData.Δ_x = [];
261 frictionData.Δ_z = [];
262 end
263
264 function fig = figureFullscreen(monitorN)
265     MP=get(0,'MonitorPositions');
266     fig=figure;
267     if monitorN≤size(MP,1)
```

```
268             pause(0.01); % this seems sometimes necessary on a Mac
269             set(fig,'Position',[MP(monitorN,1:2)+MP(monitorN,3:4)/4 ...
                    MP(monitorN,3:4)/2]);
270             pause(0.01); % this seems sometimes necessary on a Mac
271             set(fig,'WindowState','maximized');
272             %figure('units','normalized','outerposition',[0 0 1 1], ...
                    'WindowState','maximized');
273         else
274             disp(strcat("attempted to create fullscreen figure on ...
                    monitor ", string(monitorN), " but not enough monitors ...
                    were detected. Figure was not set to fullscreen."));
275         end
276     end
```

Appendix B

Experiments on Cell Adhesion

Cell adhesion is an important factor in cell culture and it is important to make sure that the cells are well adhered on the substrate. Cell culture vessels are commonly made out of PS or glass because both of those materials offer biocompatible surfaces for cells that permit good cell attachment. These substrates are also very hard (3.25 GPa and 63 GPa, respectively), which does not reflect the *in vivo* situation (125 kPa [87]). For this reason, PDMS was used as a soft substrate. PDMS, however, immediately after curing, is not an attractive surface for cells to attach to and grow on. Due to its strong hydrophobicity, it is difficult to cover the whole area with water-based solutions, such as medium with suspended cells [160], and cell attachment can vary with the cell type [161]. This issue required attention in order to make a substrate that reflects the *in vivo* situation appropriately, both mechanically and in favouring cell adhesion, which is topic of this chapter.

B.1 Background

Three ways were identified and tested to make the PDMS more suitable for cells. The first option was to apply plasma treatment in air on the PDMS after curing. When plasma treating the surface, dissociated gases like oxygen, hydrogen and argon react with the PDMS surface, forming functional groups [162]. This is beneficial for cell adhesion [163] and decreases hydrophobicity significantly [164], however is temporary [165][166][167][168]. The second method trialled to improve cell adhesion was gelatin coating. Gelatin is part of the ECM and derived from the protein collagen [169] and has been shown to possess the ability to help HUVECs to attach [170][171]. Thirdly, coating with fibronectin was trialled. Fibronectin also belongs to the family of ECM proteins and microfluidic experiments have shown that it is one of the best suited ECM proteins for growing endothelial monolayers [89].

B.2 Objectives

The objective of this experiment was to determine the best way of making the soft PDMS suitable for cell culture, especially for HUVEC, by means of surface treatment, coating or a combination of the two. This was assessed qualitatively based on cell atttachment quality and the attached cells ability to proliferate.

B.3 Methods

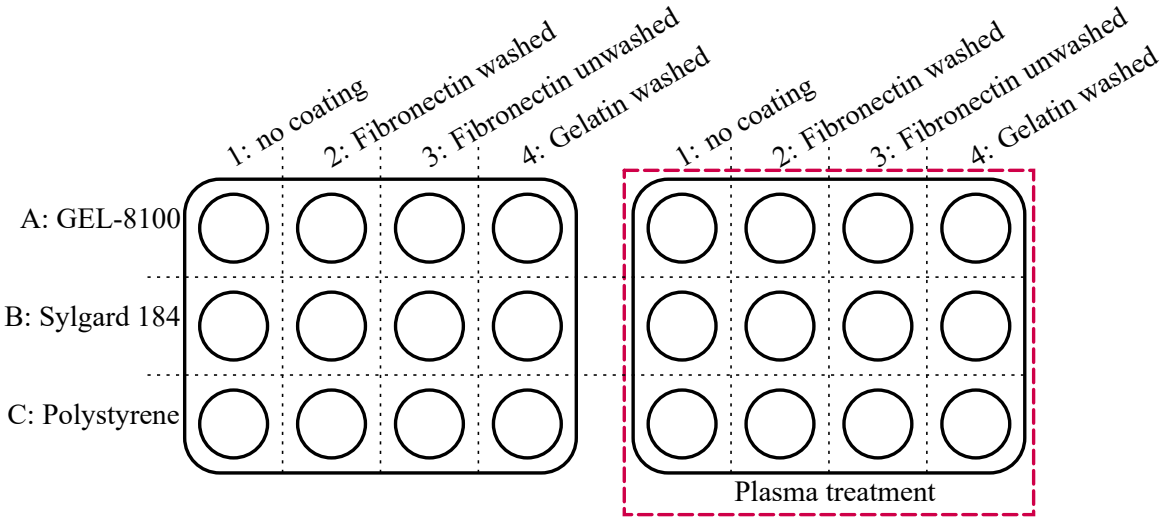

Figure B.1: Well plate layout for cell adhesion experiment. Row A was filled with GEL-8100 and row B was filled with Sylgard 184, while row C was left empty. Two well plates were manufactured like this and one of them was plasma treated. In each well plate, wells in column 1 were not coated, wells in column 2 were coated with fibronectin and washed 3 times with PBS, wells in column 3 were coated with fibronectin and not washed and wells in column 4 were coated with gelatin and washed.

The purpose of this experiment was to compare different types of surface treatment on different types of PDMS and standard cell culture material (PS). Two types of PDMS were compared with cell culture grade PS. For this, a standard cell culture 12 well plate, as seen in Figure B.2b, made from PS was used as a graft. Wells on a 12 well plate are arranged in rows A to C and columns 1 to 4 as seen in Figure B.1. For each well plate, the respective top row A was filled with GEL-8100 and row B was filled with Sylgard 184. Row C was left empty to retain the polystyrene surface. The three substrates were used uncoated, with fibronectin (washed), fibronectin (unwashed) and gelatin coating. Furthermore, the influence of plasma treatment was investigated. For this, a second well plate was prepared with the same substrates and coatings, however, before coating, the substrate was plasma treated. As one of the earliest in this work, this experiment was conducted using MG-63

cells because they are a very robust starter cell line. The experiment was then repeated with HUVEC. In total, the experiment was conducted twice for each cell type.

Sample Creation

Two types of PDMS were used. Sylgard 184 from DOWSIL, which is one of the most common and most readily available PDMS products. Hence it acted as a control to ensure the detaching did not only happen due to the soft PDMS. PS was used as a second control and baseline because it is the most common cell culture substrate and cells usually attach to it even without additional surface treatment in the lab. The second PDMS, GEL-8100 from NuSil with 1 % added Sylgard 184 crosslinker was used because it is softer and closer to the mechanical properties of blood vessel tissue values. The methodology to manufacture GEL-8100 substrates is described in Section 3.4.

Sylgard 184 was manufactured according to the manufacturers guidance by mixing 10 parts polymer with 1 part curing agent. The mixture was desiccated before curing. Both polymers were cured at 65°C for 8 h as in Section 3.4.

Plasma Treatment

For plasma treatment of the second 12 well plate, a ZEPTO 8 plasma machine by Diener electronics was used. The plasma machine set-up can be seen in Figure B.2a. First, the well plate was inserted into the chamber. Then, the lid was closed and a vaccum was generated by turning the vacuum pump on. The pressure was monitored with the pressure gauge and when the pressure in the chamber approached 0.2 mbar, dial 2 was used to keep it at a constant 0.2 mbar. Once the pressure stabilised at this value, the generator was turned on, ionising the air within the chamber, starting the plasma treatment. The pump was left on during that process. While the generator was turned on, the air inside the chamber glowed. This glow is electromagnetic radiation emitted from the gas atoms that undergo an energy jump and is (similar to fluorescence) specific to the gas(es) in the chamber due to discrete energy levels of the atoms. As air was used for plasma treatment, the gas within the chamber glowed purple, as seen in Figure B.2c. The gases ions functionalise the PDMS surface. When the air was ionised, the pressure increased, hence dial 2 had to be adjusted in order to keep the chamber at a constant pressure level of 0.2 mbar. The generator ran for 60 s. After the generator turned off automatically, dial 2 was closed, then the vacuum pump was turned off. Afterwards, the ventilation was initiated and when the pressure within the chamnber was restored, the lid came off the chamber and the plate was taken out.

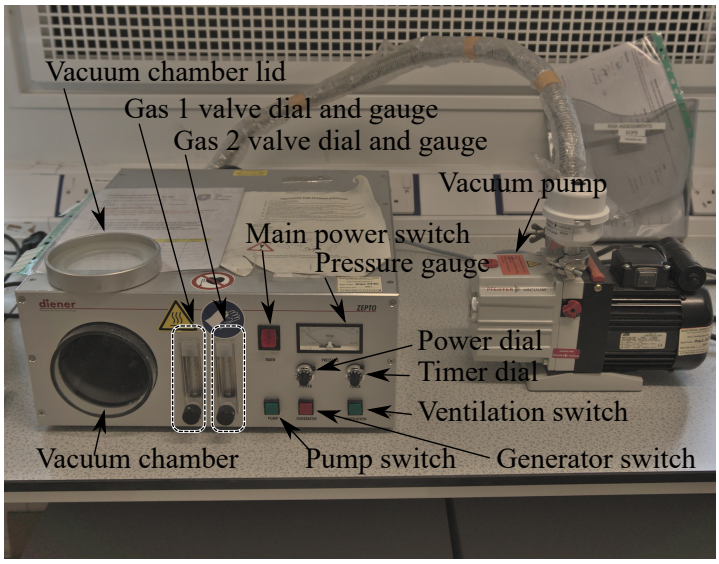

(a) Plasma machine

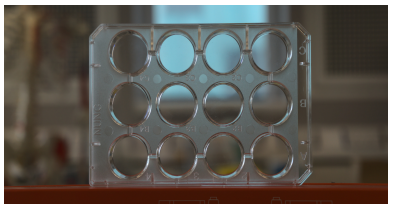

(b) 12 well plate

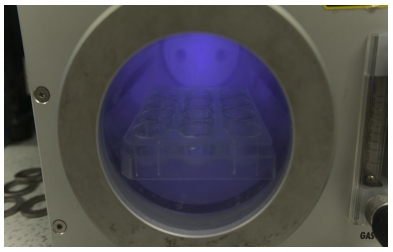

(c) Plasma treating

Figure B.2: **(a)** Photo of plasma machine with main parts annotated **(b)** Photo of a 12 well plate. **(c)** Photo of plasma treatment process of a 12 well plate

To check whether plasma treatment worked as intended, a small amount of water was put on the PDMS surface. The plasma treated PDMS was significantly less hydrophobic than the untreated one resulting in a higher wettability and a smaller contact angle. Only a small amount of water was required to cover the whole plasma treated well exhibiting small contact angles, while water droplets on the untreated well showed a much bigger contact angle and a high amount of water was required to cover the whole dish. The effect was not quantified in terms of contact angle, but only used as a qualitative observation to determine whether plasma treatment worked. The qualitative observation matched what is widely reported in the literature and hence no quantitative assessment has been made in this regard. Both plates were sterilised with 70 % IMS and transferred into the cell culture hood. Inside the cell culture hood, all wells were washed 3 times with PBS.

Fibronectin and Gelatin Coating

Column 1 of each well plate was not coated. Fibronectin coating was conducted as described in Section 3.5 for column 2 of the well plates and similarly for column 3, with the slight modification that wells in column 3 were not washed after fibronectin coating. This was to investigate whether the fibronectin was strongly coated and resistant to washing.

Column 4 was coated with gelatin as per the following protocol. 0.1 w/v% (weight per volume) gelatine coating solution was prepared in quantities of 500 mL. For this, 0.5 g of gelatin were weighed and transferred into a borosilicate glass bottle. 500 mL of DH_2O were

added. At this stage, the gelatin did not fully dissolve. The lid was closed loosely, but not fully tightened to avoid a pressure build up within the bottle during the next step. Next, the solution was autoclaved at 130°C at 1.2 bar for 30 minutes, which sterilsied the solution and caused full dissolving of the gelatin. The solution was stored at 4°C in the fridge and was left to warm up to room temperature before use.

Each well that was to be coated with gelatin was filled with 3.5 mL of gelatine coating solution. The solution was left for 30 minutes to incubate at room temperature. After the incubation period, the wells were washed three times with PBS and were ready for cell seeding.

Cell Culture

As this experiment was conducted early in the PhD, MG-63 cells and HUVEC were used. HUVEC culture methods are described extensively in Section D.2. MG-63s were cultured in a similar fashion, however, an appropriate cell culture medium was used. The protocol for preparing this medium can be found in Section D.1.1. In short, 89 parts of Lonza α-MEM (catalog #: BE12-002F) were mixed with 10 parts fetal bovine serum (FBS) and 1 part penicillin streptomycin (P/S) = L-glutamine. Media refreshes, splitting and seeding were carried out similar to how they were with HUVECs, but with MG-63 medium. However, MG-63 were seeded with a density of 20 000 cells/cm^2.

Imaging

The well plates were imaged on day 1, day 3 and day 5 (The day of cell seeding marked day 0). For imaging, the fluorescence microscope in standard light microscopy mode was used (see Subsection 3.10.5).

B.4 Results

The images taken on day 1 and day 3 were examined and classed qualitatively by degree of cell attachment as per the observations in Table B.1. The results are shown in Figure B.4. On day 1, cells grew well in all PS-based wells (Category A: Good attachment). Cells had also attached and been growing well to both PDMS surfaces that were not plasma treated and coated with fibronectin. There were no apparent differences between washed and unwashed fibronectin coatings, and between GEL-8100 and Sylgard 184. The cells attached in all four plasma treated, fibronectin coated PDMS wells, but did not spread out as much nor grow as well (category B: Adequate attachment) as they did when the PDMS was not plasma

Category	Observations
A	Fully confluent monolayer
B	Surface significantly less densely populated compared to control (PS)
C	Only individual cells attaching
D	no attachment or atypical behaviour

Table B.1: Categories of cell attachment and growth and respective characteristic observations.

treated. Cell attachment in the gelatin coated, plasma treated well was poor and the cells did not seem to grow well (Category C: poor attachment). Cells did not attach in the gelatin coated, not plasma treated well (Category D: No attachment). The cells also did not attach to any PDMS that did not receive a coating, neither plasma treated, nor untreated. As the cells were not fully confluent, the experiment was continued.

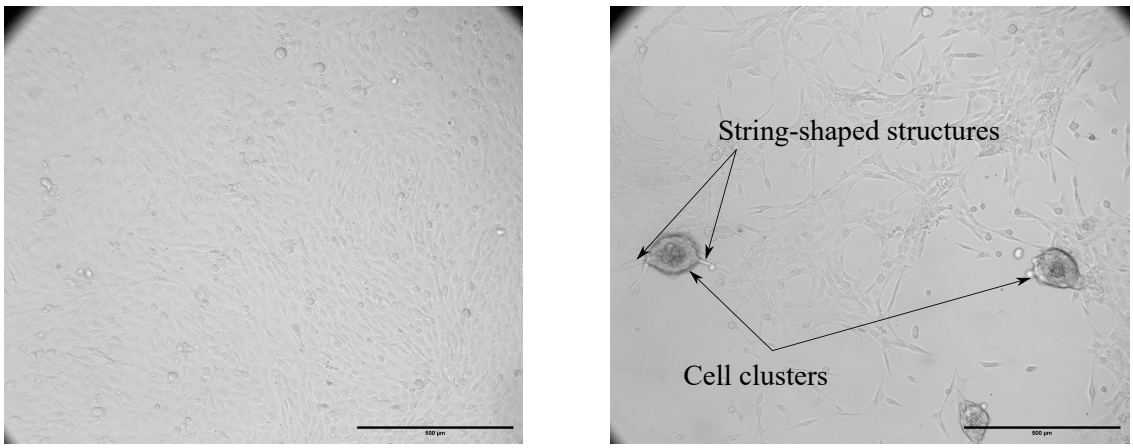

(a) Well A2, untreated

(b) Well A2, plasma treated

Figure B.3: (a) Image of MG-63 on untreated, fibronectin coated GEL-8100. **(b)** Image of MG-63 on plasma treated, fibronectin coated GEL-8100. On plasma treated GEL-8100, MG-63 detached and formed clusters that were only connected to the substrate by string-shaped structures.

On day 3, in the wells with no attachment on day 1, no cells were present anymore as they were washed out during media refreshes. The only exception to that was plasma treated Sylgard 184 without coating (well B1, on plasma treated plate), where some cells survived. However, attachment was very poor. In the wells with plasma treated PDMS coated with fibronectin (wells A2, A3, B2 and B3, on plasma treated plate) which initially had adequate attachment, cells had detached from the PDMS surface and had formed clumps that were only connected to the surface by string-shaped structures (see Figure B.3b), just as observed earlier. There were still cells attached, however, many were misshaped or formed atypical clusters. On the same surface, but not plasma treated, the cells formed a confluent

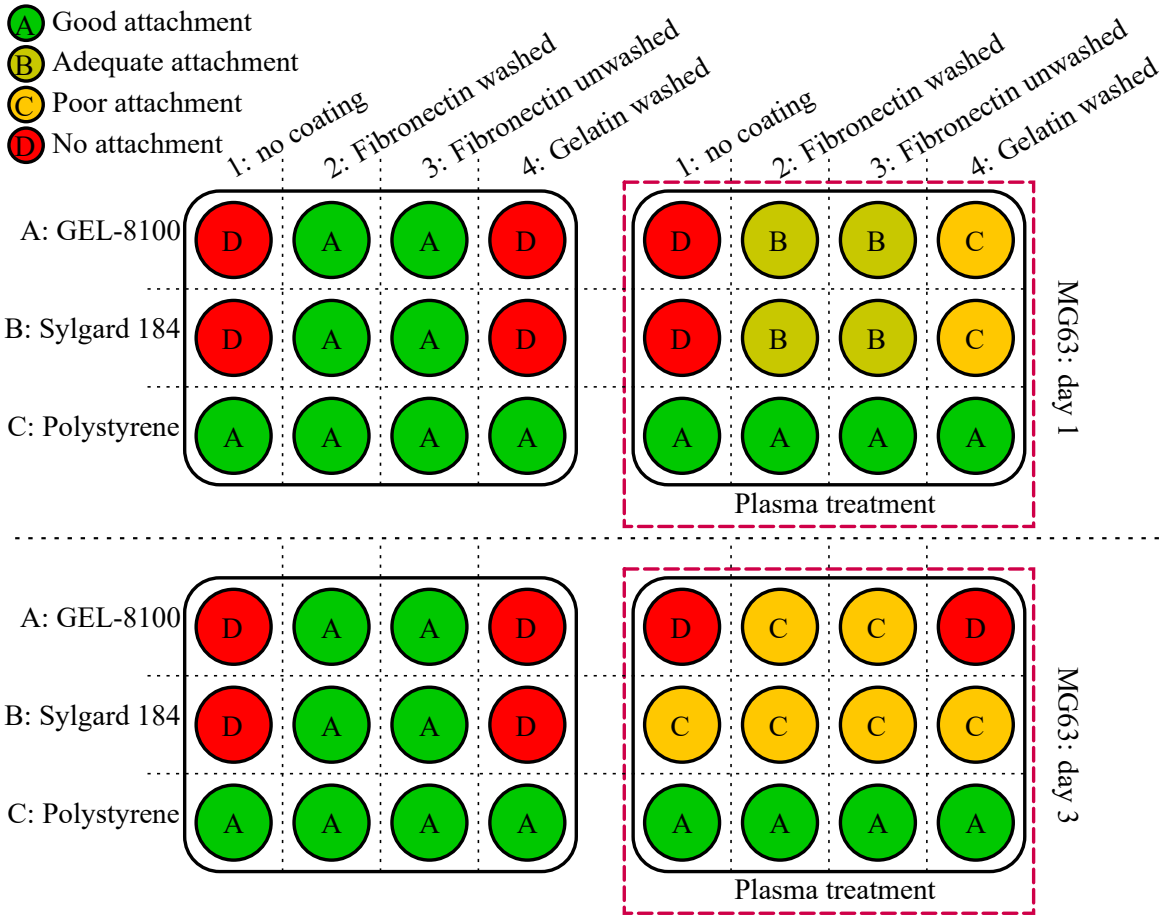

Figure B.4: Cell adhesion results for MG-63 on day 1 and day 3 of cell culture. Wells were classed by attachment and proliferation quality "A" to "D" and color-coded. "A" meant good attachment or proliferation, "B" is adequate attachment or proliferation, "C" is poor attachment or proliferation and "D" means no attachment and proliferation.

monolayer as seen in Figure B.3a. In all PS-based wells, cells still proliferated as expected with good attachment. The only PDMS surfaces with good attachment were ones that were fibronectin coated (both washed and unwashed) and not plasma treated. At this point, the cells were either fully confluent (all category A wells), stagnated in proliferation or behaved atypically with cells clustering up. Media changes were continued, but no change could be determined after day 3.

The experiment was repeated with HUVEC and the results are shown in Figure B.5. In wells with no plasma treatment, on uncoated GEL-8100, HUVEC were found to attach in patches, but proliferated poorly. They attached slightly better on plasma treated and uncoated GEL-8100 and proliferated better. On fibronectin (both, washed and unwashed) and gelatin coated GEL-8100, HUVEC attached and proliferated very well, for untreated and plasma treated surfaces. HUVEC did not attach to untreated, uncoated Sylgard 184 PDMS. They managed to attach to and proliferate on uncoated Sylgard 184, when it was

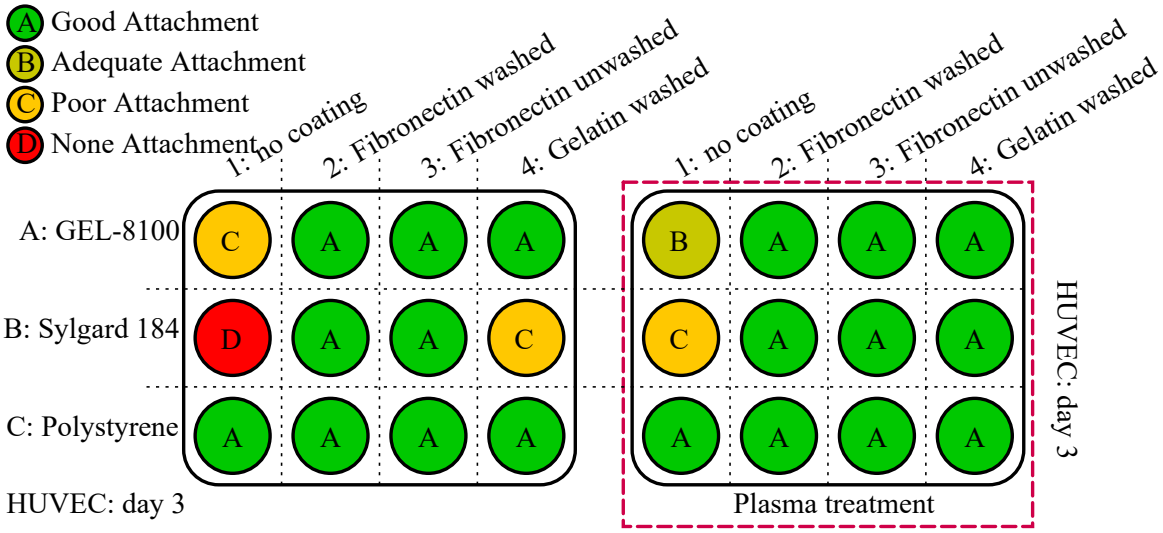

Figure B.5: Cell adhesion results for HUVEC on day 3 of cell culture. Wells were classed by attachment and proliferation quality "A" to "D" and color-coded like the MG-63 results.

plasma treated, but many cells were misshaped. When fibronectin coated, Sylgard 184 always offered a good surface for cell attachment and proliferation. Gelatin coated Sylgard 184 worked well, when it was plasma treated, but when it was not, HUVEC attached in patches and proliferated poorly. In all wells without PDMS, HUVEC attached and grew well. The experiment was continued until day 5, at which point cells in all wells had either reached full confluency or stagnated. No significant changes in cell attachment quality and proliferation could be determined on day 5 compared to day 3. In general, HUVEC attached better than MG-63 and did not show the behaviour of forming clusters like MG-63 did.

B.5 Discussion and Conclusions

In this experiment, the attachment and proliferation quality of MG-63 cells and HUVEC for different substrates was qualitatively assessed. In general, HUVEC managed to attach and proliferate better. This is likely due to the natural phenotype of these cells: HUVEC are designed to serve as vessel linings and as such have to attach strongly to withstand fluid shear stress, while MG63 are derived from bone cells. HUVEC attached well to both PDMS types if they were coated with fibronectin or gelatin. Whether they were plasma treated did not seem to influence this for HUVEC attachment. The only exception was untreated Sylgard 184 with a gelatin coating which HUVEC did not attach to very well.

In the rest of this work, HUVEC were used, and therefore, the aim of this experiment was to assess primarily HUVEC attachment, however, the MG-63 tests showed cells detaching from day 1 to day 3, which indicates that the surface was changing during that time. Indeed,

PDMS has been reported to be able to recover its hydrophobic properties fully as quickly as within 24 h in air [165][166][167][168] because the polymer chains of low molecular weight migrate to the surface [164]. This could be the reason why MG-63 managed to attach to begin with. However, as the surface became more and more hydrophobic, they detached one by one and formed clumps. HUVEC seem to be less influenced by this effect, which is supported by the fact that they managed to attach to untreated PDMS - which is strongly hydrophobic from the beginning - when MG-63 could not.

Cells live and do not behave in exactly the same way every time, which means that sometimes it takes longer for them to proliferate and become fully confluent. Further, the PDMS surface properties cannot be measured under the cell layer before testing. To avoid variations in the PDMS surface at the time of testing due to differences in how long it takes for samples to become fully confluent, it was decided to conduct future experiments without plasma treatment for consistency. Fibronectin was chosen for coating in following experiments because, while gelatin worked on untreated GEL-8100, cells struggled to attach to untreated Sylgard 184 with gelatin coating. Additionally, fibronectin has been reported to be the most suitable coating for growth of HUVEC monolayers [89]. Some studies suggest that fibronectin coating is not appropriate for long-term culture of all endothelial cell types [165][172]. However, this could not be confirmed for HUVEC in this experiment, as the cells reached full confluency on all fibronectin coated materials. While no effect of washing the surface after coating was observed in this experiment, in future experiments, washing with PBS after fibronectin coating was conducted to remove any excess fibronectin for consistency.

Appendix C

Original Blue/Red Channel Images

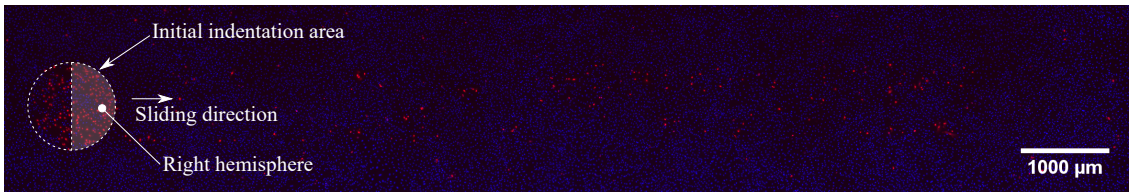

(a) 10 mN

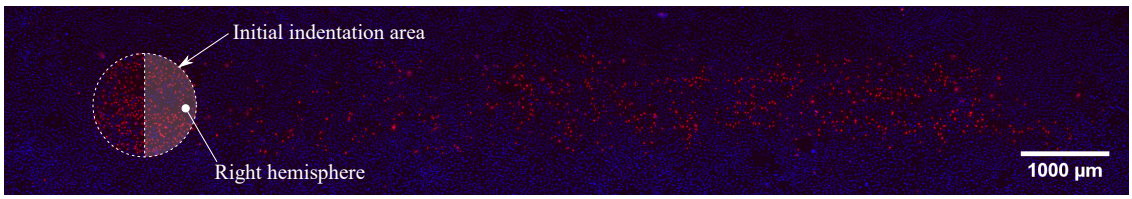

(b) 20 mN

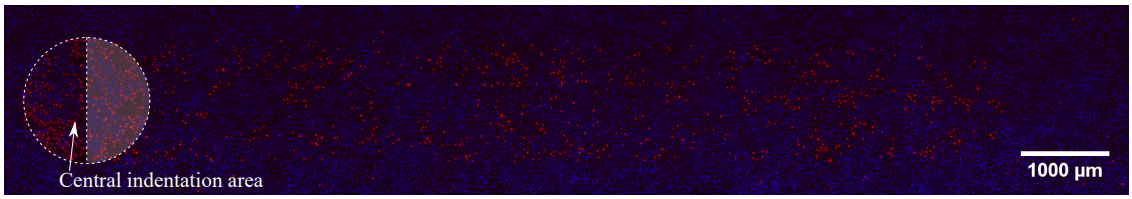

(c) 40 mN

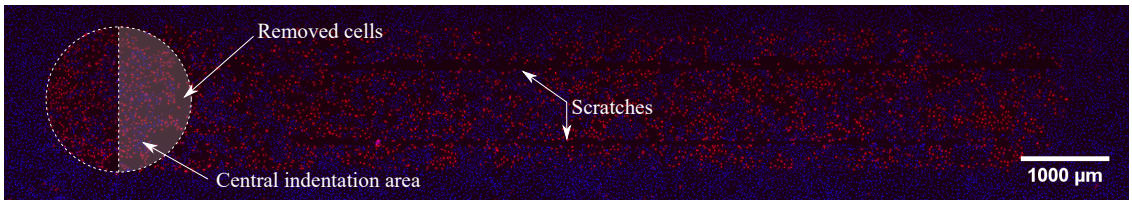

(d) 80 mN

Figure C.1: Blue/red channel version of Figure 4.15.

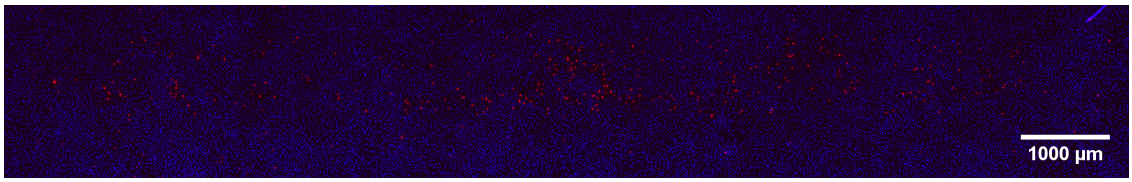

(a) 10 mN

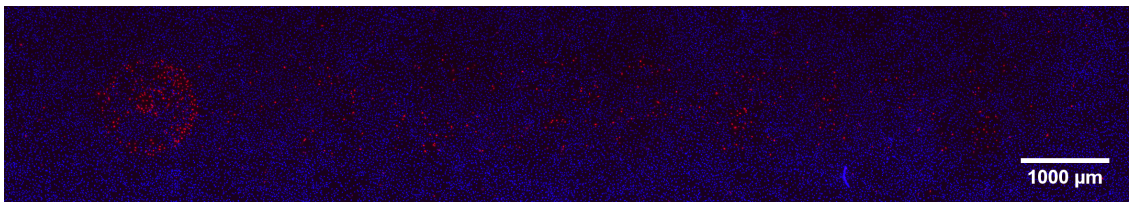

(b) 20 mN

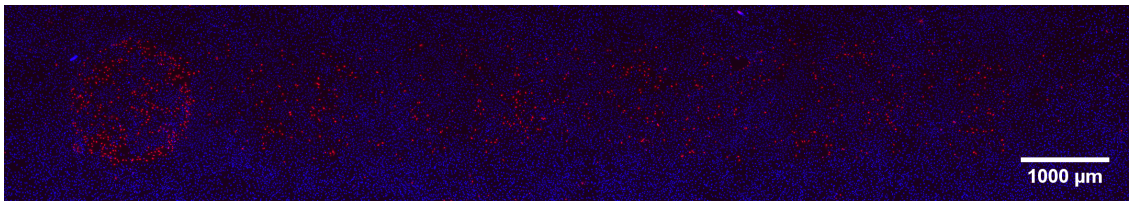

(c) 40 mN

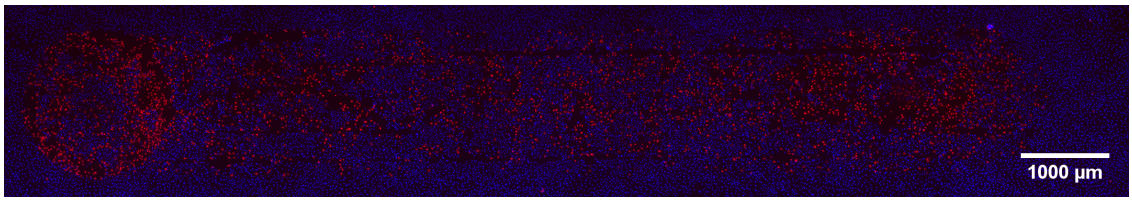

(d) 80 mN

Figure C.2: Blue/red channel version of Figure 4.17.

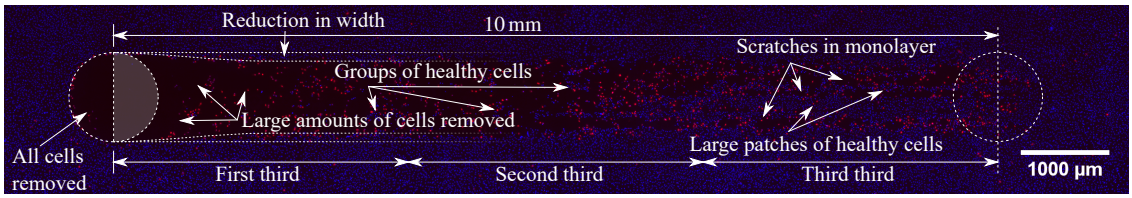

(a) 10 mN

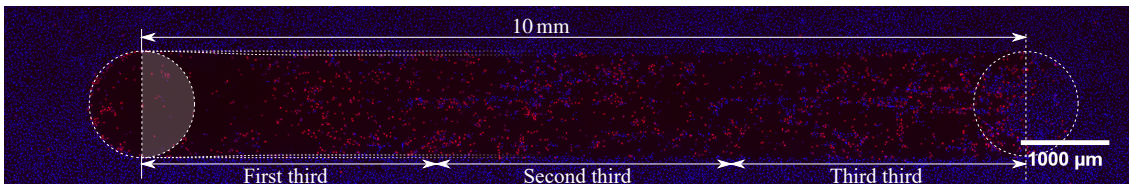

(b) 20 mN

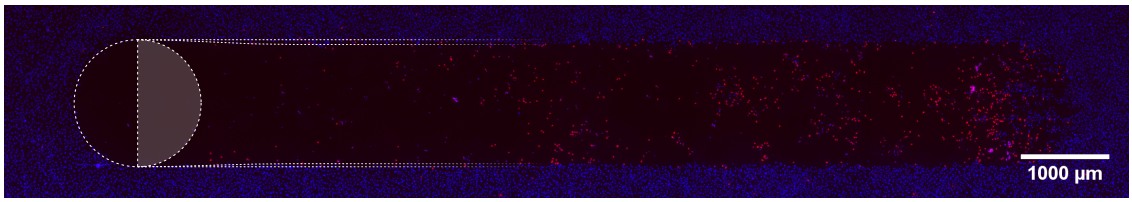

(c) 40 mN

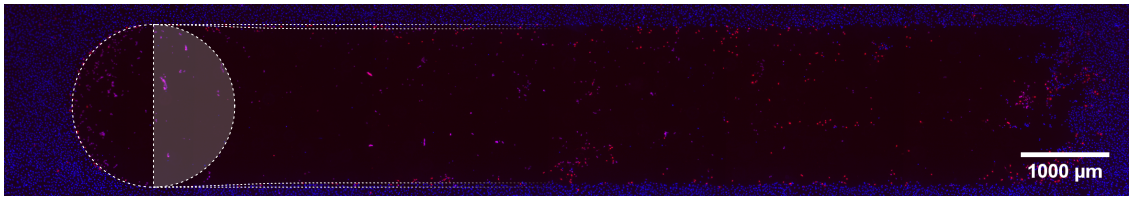

(d) 80 mN

Figure C.3: Blue/red channel version of Figure 4.19.

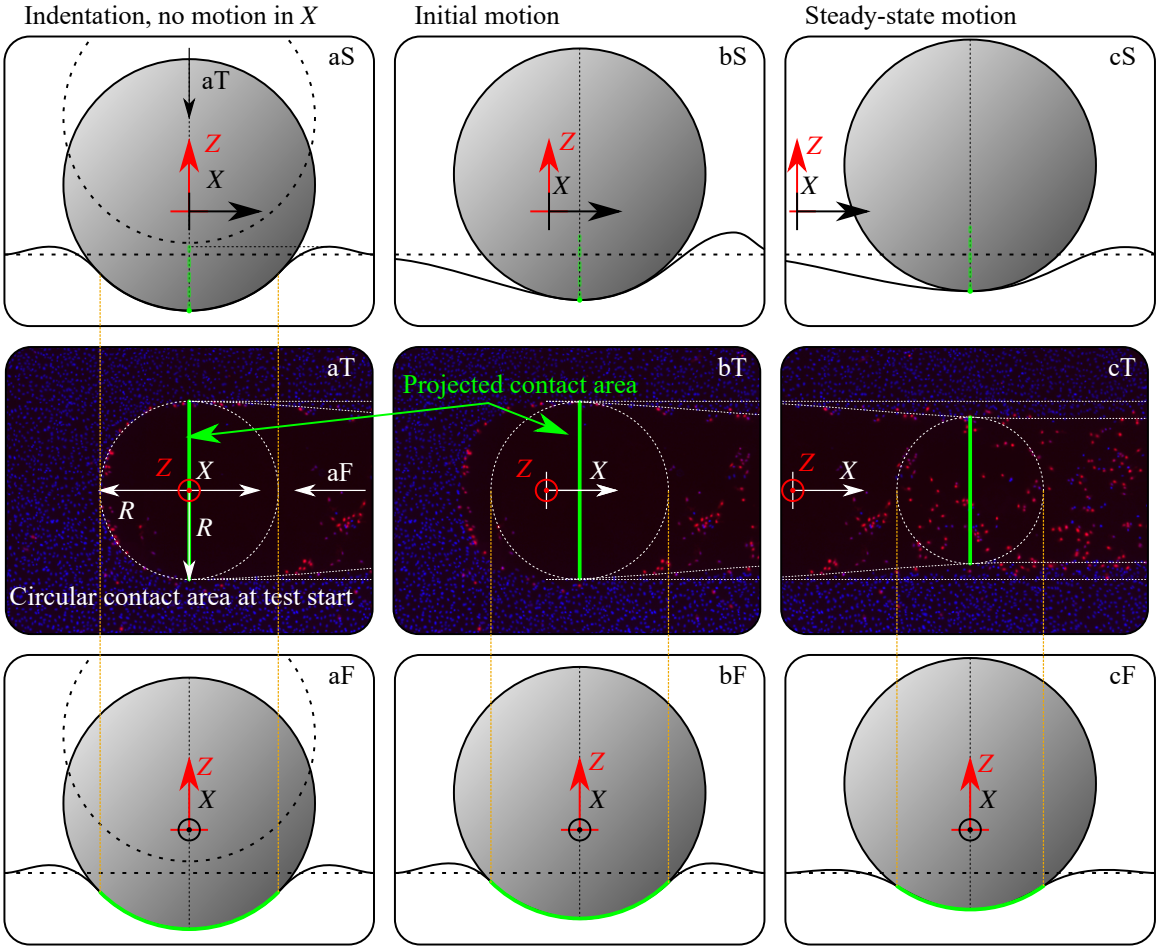

Figure C.4: Version with blue/red channels of Figure 4.28.

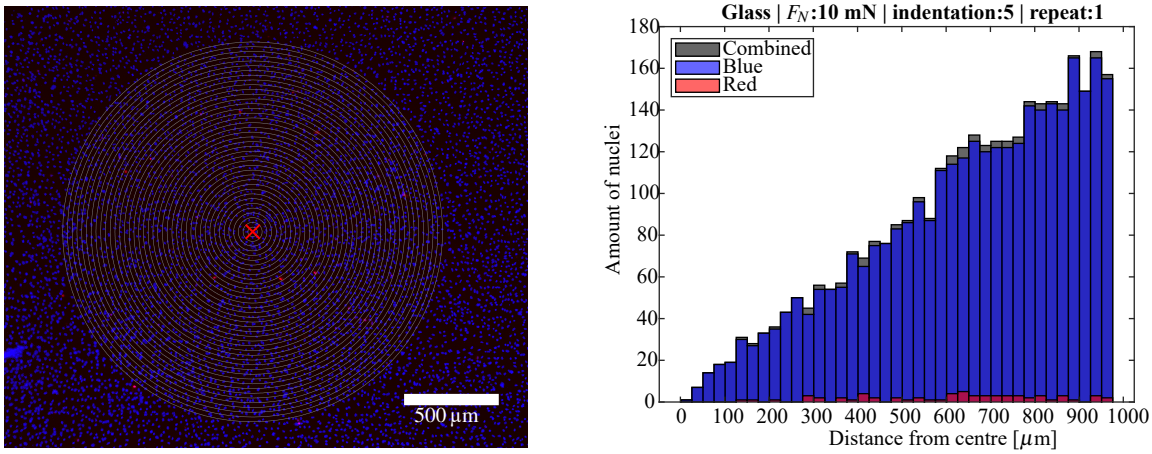

(a) Red and blue channel images

(b) Histogram

Figure C.5: Version with blue/red channels of Figure 5.4.

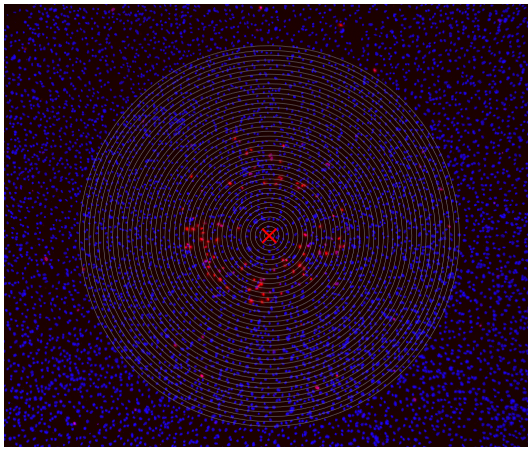

(a) Red and blue channel images

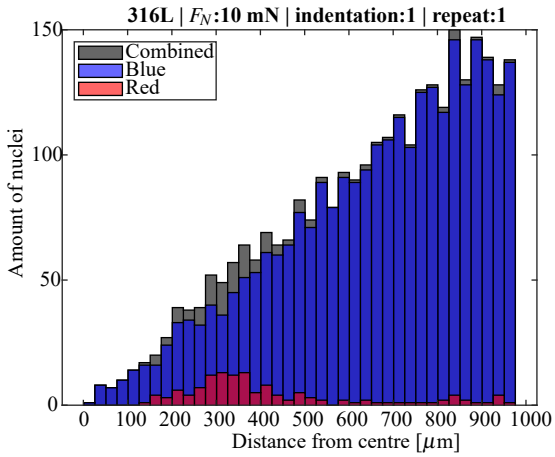

(b) Histogram

Figure C.6: Version with blue/red channels of Figure 5.5.

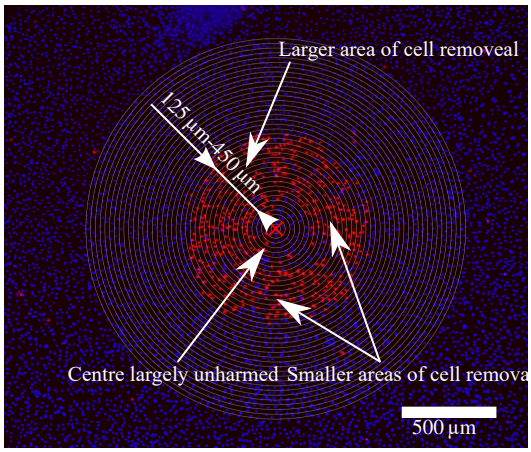

(a) Red and blue channel images

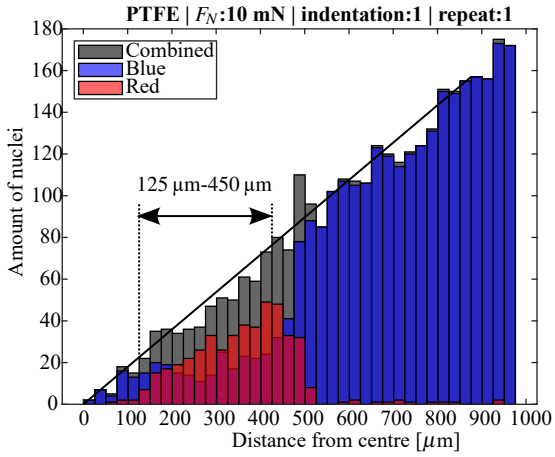

(b) Histogram

Figure C.7: Version with blue/red channels of Figure 5.6.

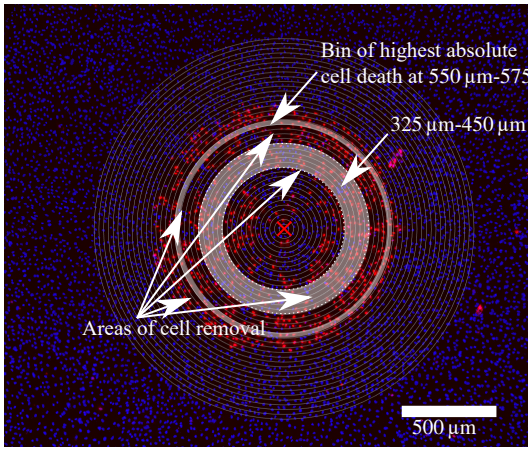

(a) Red and blue channel images

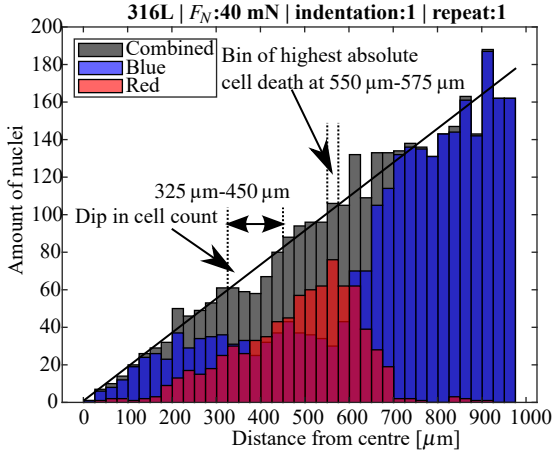

(b) Histogram

Figure C.8: Version with blue/red channels of Figure 5.7.

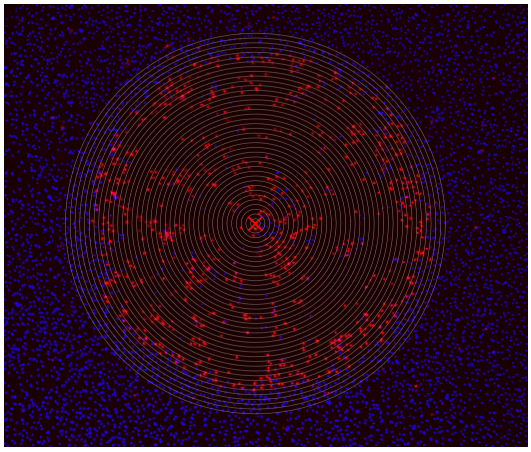

(a) Red and blue channel images

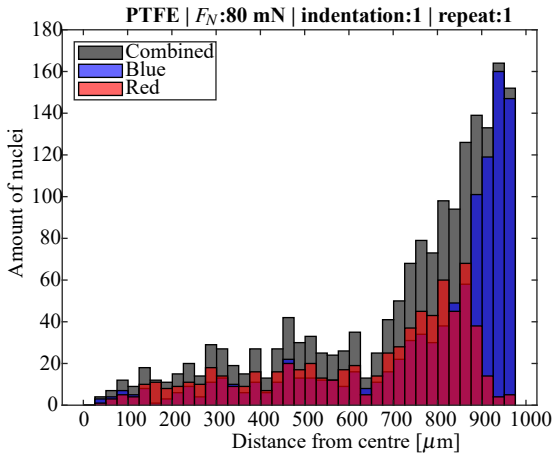

(b) Histogram

Figure C.9: Version with blue/red channels of Figure 5.8.

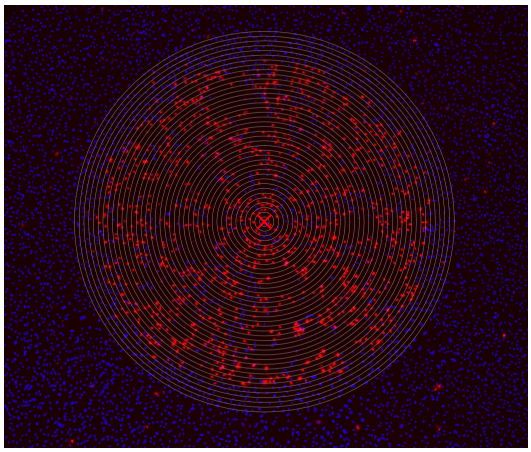

(a) Red and blue channel images

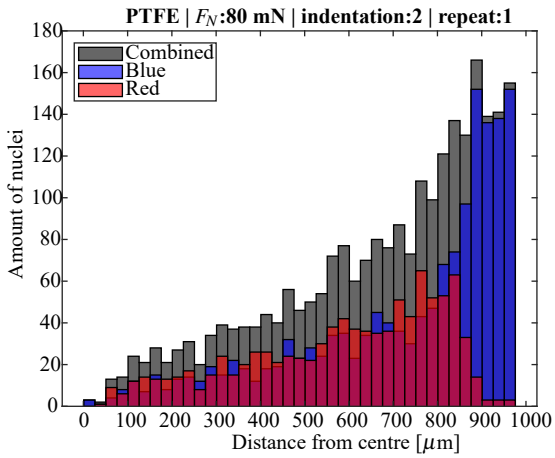

(b) Histogram

Figure C.10: Version with blue/red channels of Figure 5.9.

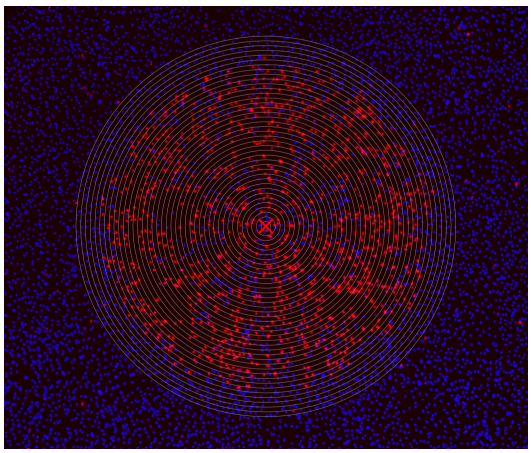

(a) Red and blue channel images

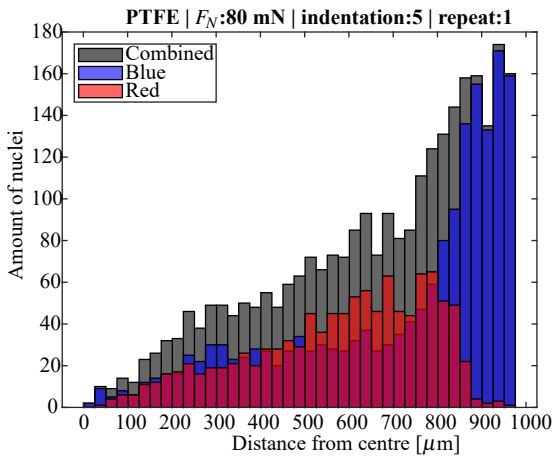

(b) Histogram

Figure C.11: Version with blue/red channels of Figure 5.10.

Appendix D

Standard Cell Culture Procedurses

D.1 Media Preparation

As described in Section 3.6, different cell lines have different requirements for nutrients and growth factors which must be reflected in the appropriate medium composition. Some cells need a very special type of medium, while others can be cultured with an all purpose one. This section explains how the appropriate medium for each cell type used in this work was prepared.

D.1.1 MG63 Medium

MG63s are very resilient and easy to culture. Hence, a standard culture medium is used in the laboratory for this cell type. First, a bottle of α-MEM (minimum essential medium) from Lonza (catalog #: BE12-002F) was taken from the fridge and transferred into a cell culture hood. 55 mL of the α-MEM were discarded. Then, a previously defrosted 50 mL aliquot (a smaller portion of a larger whole) FBS was transferred into the α-MEM bottle. After that, a previously defrosted 5 mL aliquot of P/S + L-glutamine, containing 10 000 units penicillin, 10 mg/mL streptomycin, and 200 mmol L-glutamine, was added to the bottle. These amounts of ingredients produce standard concentrations of penecillin, streptomycin and L-glutamine used for cell culture. Penecillin and streptomycin are antibiotics used to prevent bacterial infections. L-glutamine is an amino acid additive used in cell culture. Afterwards, the medium was aliquoted into smaller portions and stored in the fridge.

D.1.2 HUVEC Growth Medium

EC growth medium for HUVEC was purchased as a kit from Promocell (catalog #: C-22010) and pepared according to the manufacturers guidance. The basal medium bottle was transferred from the fridge into the cell culture hood. Then, the contents of the supplement vial were added to it. Additionally, P/S mix was added to the medium to prevent infections in the same concentrations as it was for MG63 medium. No L-glutamine was added because the supplement vial already contains the appropriate amount of nutrients as intended by the manufacturer. Once prepared, the HUVEC medium was aliquoted into smaller portions and stored in the fridge.

D.2 Cell Culture and Seeding

Cell culture is the process of keeping cells alive and letting them proliferate. The cells can be steered to develop a certain direction by manipulating factors. This is useful to study the effect of drugs, observe cell reactions to changes in their mechanical environment (e.g. shear stress), or develop artificial organs. There are standard cell culture techniques used in this work which are laid out in this section.

Good cell culture practice is required to avoid cross-contamination (transfer of non-desired bacteria into the cell culture which then proliferate there and supersede or affect the desired cell culture, changing the outcome of the experiment). For this, a sterile environment is of paramount importance. Therefore, all cell culture work was conducted in a cell culture hood, when sterility was a priority. Such a cell culture hood as used in this work is shown in Figure D.1. Cell culture hoods work in a similar fashion to fume cupboards, however, their purpose is to protect the contents of the hood, rather than the user. Therefore, the laminar flow, which is created inside the hood, is directed out of the cupboard so that any bacteria or microorganisms that could contaminate a cell culture vesssel are blown out. This laminar flow comes through the vents in the working surface as indicated in Figure D.1. The worktop is typically made from stainless steel.

D.2.1 Standard Cell Culture Techniques

Standard cell culture techniques ensure that samples and cell culture vessels are kept sterile and cells are exposed to appropriate environmental conditions. As such, they lay the foundation for all repeatable and meaningful experiments involving cells. Some of the most common cell culture devices and consumables are shown in Figure D.2.

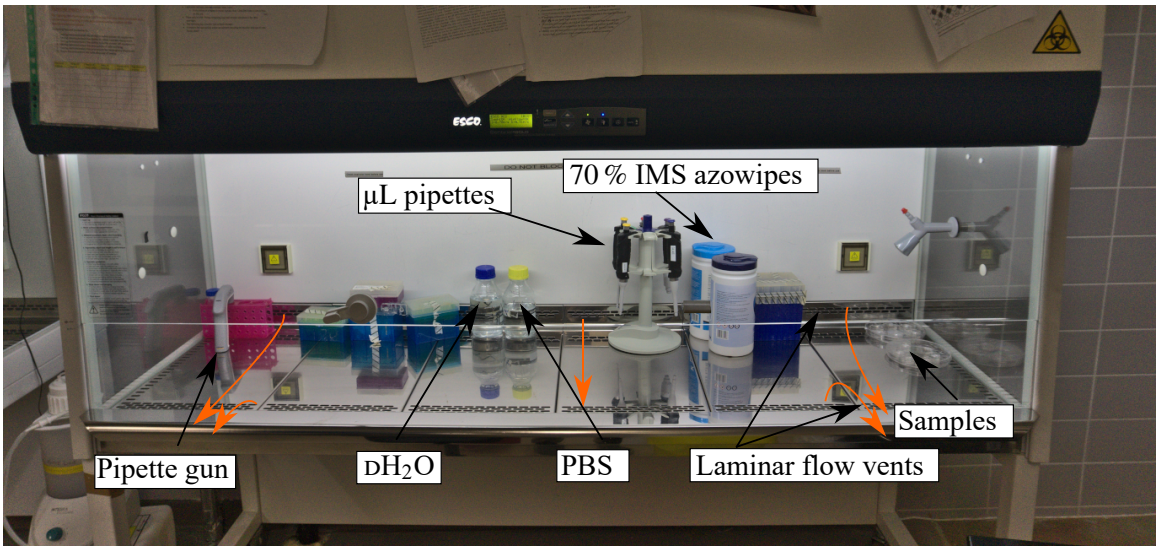

Figure D.1: Cell culture hood used in this work for media preparation, passaging, seeding and media refreshing. The hood contains common cell culture tools and substances such as pipette gun, µL pipettes and Azowipes and PBS and water. There are also some samples in the hood being coated with fibronectin overnight. A laminar flow indicated by the orange arrows is generated through the vents in the stainless steel working plates and helps preventing infections of the cell cultures.

Often in cell culture volumes of liquids have to be measured and mixed to gain a certain concentration of ingredients, for example when making cell culture medium. For this, in the interest of best possible precision and repeatability, pipettes are used. There are two main types of pipettes. The first type are serological pipettes, which are used with a pipette gun and allow the user to read the volume from a scale. The second type are µL litre-pipettes which, as the name suggests, can measure volumes of µL dimension and they can do that with sub µL precision. This makes them ideal for lower volumes, for example, when a small amount of liquid needs to be examined (e.g. cell counting), or when only a low concentration is required (e.g. cell staining with dyes).

In life sciences, cells are usually cultured in square-shaped flasks, which are defined by the size of the area they provide for the cells to grow on. A T75 (A = 75 cm) and a T25 (A = 25 cm) flask are shown in Figure D.2. Petri dishes are another fairly common cell culture vessel, although nowadays, usually well plates are used which are principally shaped like several Petri dishes (wells) next to each other. In this work, the smaller size of Petri dishes with a surface area A of 8.8 cm^2 was used for sample creation, because using a large well plate would have meant that the cells in the wells that were tested later would have been out of the incubator for a long time before they were tested. Hence, using only an individual dish was better.

As the small Petri dishes with cells are flimsy and difficult to handle, they were stored within the larger Petri dishes in the incubator. The larger Petri dishes also provided an

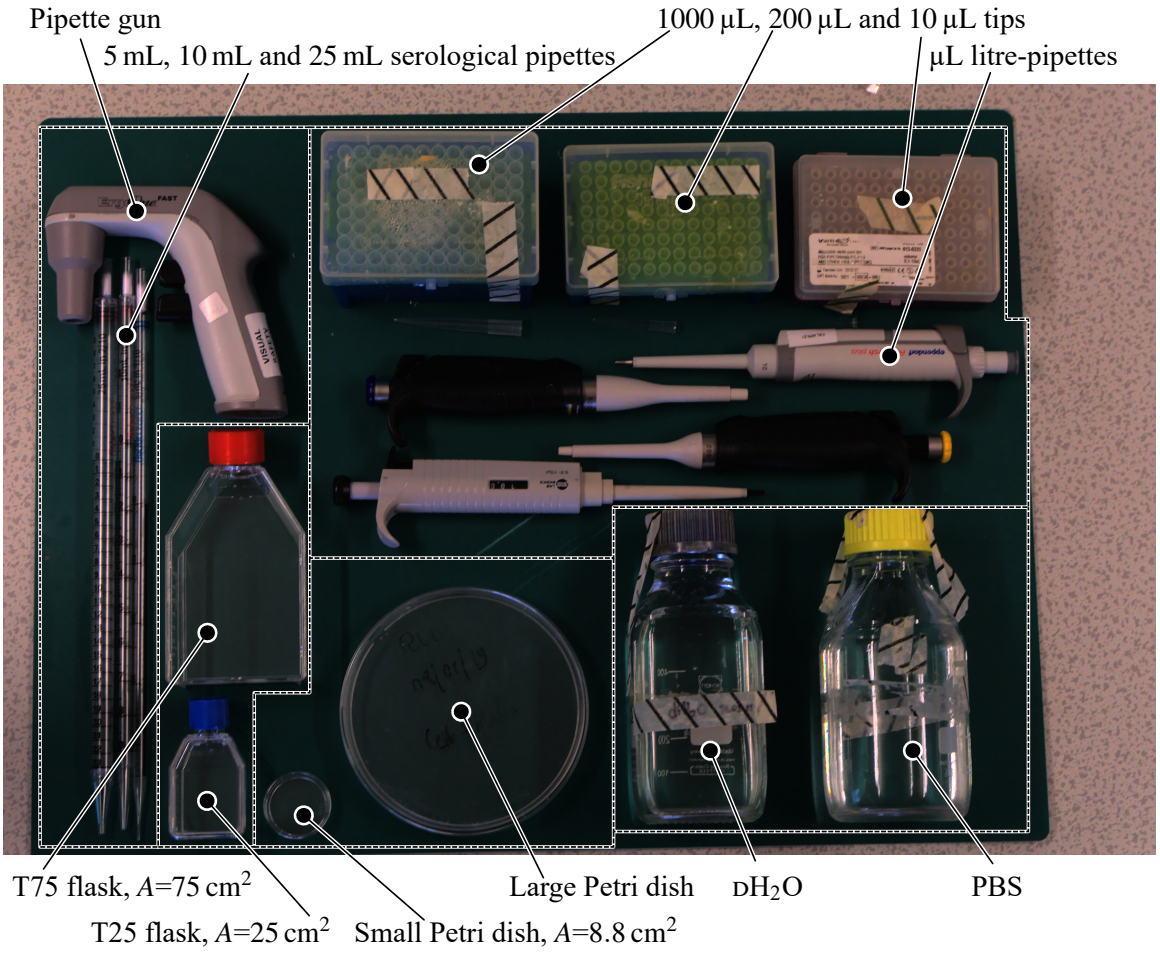

Figure D.2: Cell culture equipment and consumables commonly used in life science labs. Pipette guns with appropriate serological pipettes are used to transfer and measure large amounts of liquid (up to 25 mL), while µL pipettes with fitting tips are used to measure smaller amounts of liquid with sub-µL precision. Two sizes of standard cell culture vessels, a T75 and a T25 flask, with respective surface areas A of 75 cm^2 and 25 cm^2 are shown. Two sizes of Petri dishes are displayed. Dishes of the smaller size were used to create soft PDMS samples and the larger ones were used to store said samples in the incubator. Two important cell culture reagents are in the picture too: deionised water and phosphate buffered saline, a phosphate-based pH buffer.

additional layer of protection from harmful bacteria. Cells need to be washed frequently during cell culture with PBS. It is a phosphate-based buffer solution to keep the pH at a level appropriate for cells. For the preparation or resuspension of dyes or proteins, DH_2O is necessary. Those two cell reagents are also highlighted in the picture.

Most of those devices, consumables and reagents are generally arranged within the cell culture hood as shown in Figure D.1 for sterile application. Anything that is transferred into the cell culture hood is sterilised beforehand, either by autoclaving (heating to 130°C at 1.2 bar for 30 minutes), or by spraying with 70 % IMS. When sterility is not required, for example when working with fixed cells (cells that have been killed and preserved with a reagent like formaldehyde), those devices were used outside of the cell culture hood.

Apart from the cell culture hood, two important pieces of equipment are the incubator and the aspirator which are shown in Figure D.3. The incubator, shown in Figure D.3a is a sealed box withthe ability to control carbon dioxide (CO_2) content, humidity and temperature of its contents. A rubber seal is mounted around the opening against which the glass door presses when closed, providing a proper seal. The incubator has a CO_2 sensor (which cannot be seen in the figure) and a gas inlet connected to a valve, behind which a CO_2 cylinder sits. This allows the incubator to control the CO_2 concentration within it by closing and opening the valve. It also has a fan, which is constantly spinning to ensure the CO_2 concentration is homogeneous throughout the incubator. The water reservoir at the bottom of the incubator ensures that the air is saturated with water, preventing media in cell culture vessels from evaporating. Finally, the temperature is controlled electronically, however, the temperature sensor and heating elements cannot be seen. The temperature inside the incubator is always maintained at 37°C, because normal animal processes work the best at that temperature. The incubator contains T25 and T75 flasks and well plates, which were mentioned earlier. On the bottom shelf, there is a large Petri dish containing samples with cells which were proliferating at the time this picture was taken. The shelves and walls are made from copper, which has antibacterial properties.

Figure D.3b shows an aspirator. The aspirator has a vacuum pump in its base and a tank to hold the aspirated liquid. The tank has several inlets and outlets that connect to tubes. On the front of the base, there is a control interface through which the aspirator can be turned on and its suction strength can be changed. The vaccum pump is connected to the tank so that, when turned on, it creates a lower pressure in the tank than the atmospheric pressure. One of the other tubes that are connected to the aspirator has an aspiration tip which is usually inside of the cell culture hoods. As the pressure at the aspiration tip is the same as in the tank, i.e. smaller than atmospheric pressure, when the tip is submerged in a liquid it sucks the liquid into the tank. The aspirator was used to remove medium from Petri dishes and well plates because it provides a constant, adjustable flowrate, ensuring that the cells are not detached from the surface. It is also a lot quicker than aspirating by hand.

Furthermore, for cell culture, a centrifuge and a waterbath are required. The centrifuge can be seen in Figure D.4a. It has a control interface through which the spinning frequency and time can be set. When the lid is closed, the rotor spins with the specified frequency. Centrifuging is applied when separation of two phases in a suspension is desired. In cell culture, more often than not, this is a cell suspension in a tube. After centrifuging, the cells form a pellet at the bottom of the tube which can be collected with ease. For this work, cells were centrifuged at 1000 rpm for 3 min, unless otherwise stated.

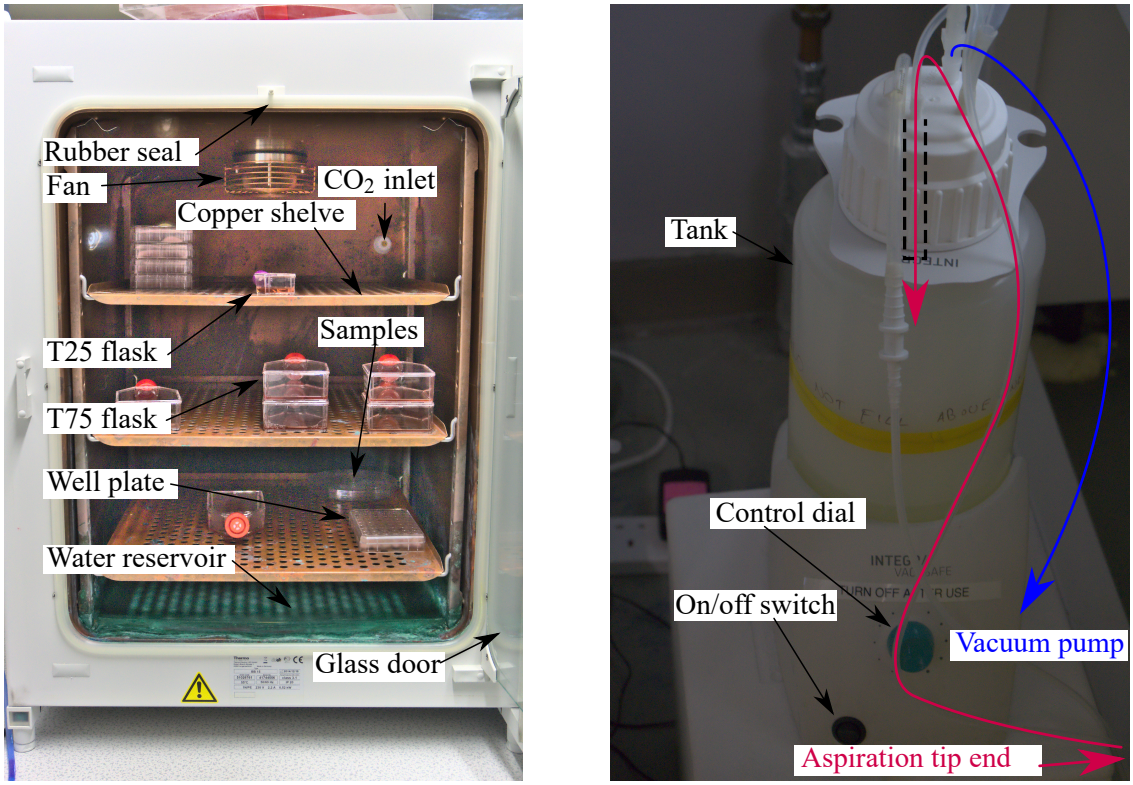

(a) Cell culture incubator

(b) Aspirator

Figure D.3: **(a)** A Standard copper cell incubator. Rubber seal, fan, copper shelve, CO_2 connector and water reservoir are labelled. In the incubator there are T25 and T75 flasks, well plates and a large Petri dish containing samples. **(b)** An Aspirator. The control interface allows the user to turn the machine on and adjust its aspiration power. The vacuum pump in the base pumps air from the tank as indicated, generating a lower pressure than is in the atmosphere, which causes any fluid at the aspiration tip end (which is usually in a cell culture hood) to be sucked in.

The waterbath (Figure D.4b) is necessary to bring the medium and other reagents to the appropriate temperature (37°C) for cell culture. It has a control interface to set the temperature, however, it should always be at 37°C. The lid helps to keep the heat in.

It is also important to have a microscope that can be used spontaneously in the laboratory. Figure D.5a shows a simple light microscope. This microscope was used for checking cell confluency (percentage of area covered with cells) and cell counting. The microscope used to collect results from experiments is a much larger, more advanced, fluorescence-enabled microscope which is presented later, in Section 3.10.5.

For cell counting, a hemocytometer is required, which is shown in Figure D.5b. It creates a cavity of a defined depth d (0.1 mm) between the bottom and the cover glass and has a small, square pattern etched in the bottom glass, as seen in the figure. By counting the number of cells in the square, knowing the surface area A and depth of the cavity, the cell concentration per unit volume is determined, which is done by multiplying the number

of cells with 10000/mL. In the figure, there are 6 cells, meaning that the cell concentration would be 6 cells $\times$ 10000 cells/mL = 60000 cells/mL

In Figure D.5c, a 15 mL and a 50 mL centrifuge tube are shown, which are used for centrifuging cell suspensions, in order to separate the cells from the medium, storing aliquots of reagents, or mixing chemicals.

D.2.2 Cell Passaging

HUVEC (Catalogue number C-12253) were acquired from Promocell, Germany, and cultured using the appropriate culture medium (Catalogue number C-22010) from the same manufacturer in T25 or T75 flasks. The cell culture flasks were stored in an incubator at 37°C, 95 % relative humidity and 5 % CO_2 with media changes carried out every 2 to 3 days. These are ideal conditions for mammalian cells and therefore they grow and multiply

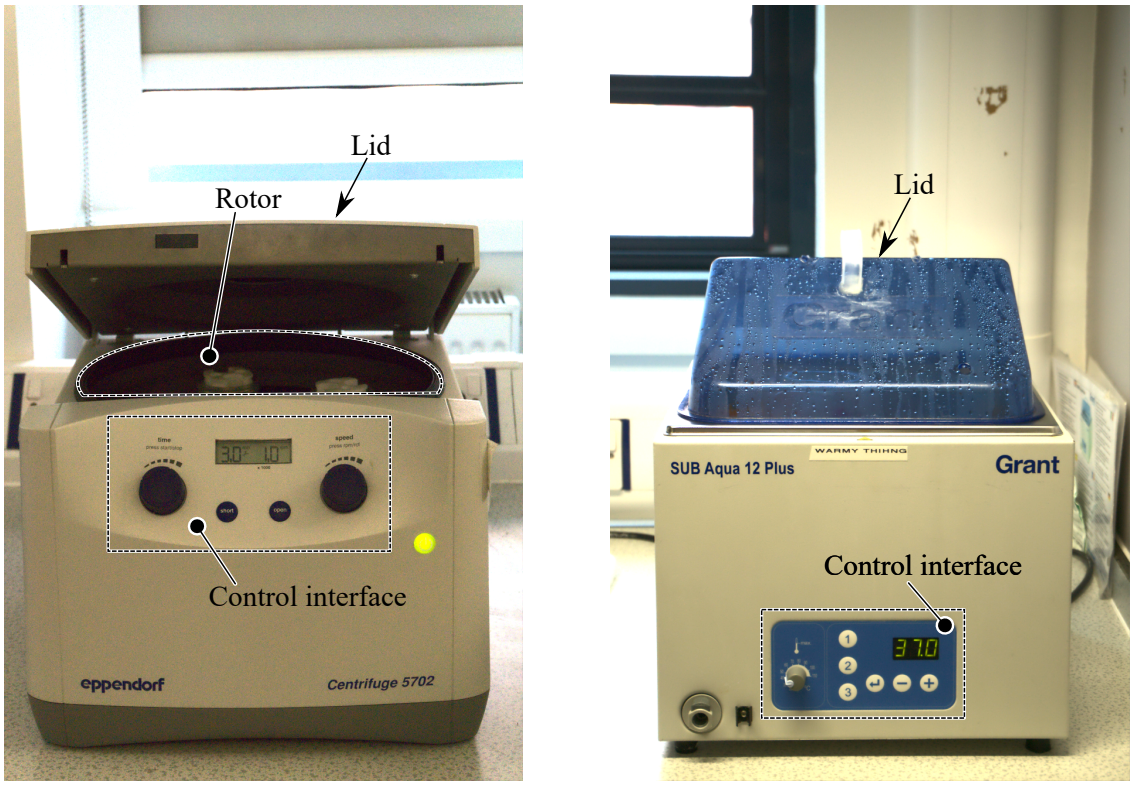

(a) Centrifuge **(b)** Waterbath

Figure D.4: (a) A Centrifuge. When the lid is closed for protection, the rotor spins with the desired frequency (set to 1000 rpm in the picture) for the specified amount of time (3 min in the picture). These are standard settings that were used for cell work throughout this work, unless otherwise stated. **(b)** A waterbath. A set temperature is specified through the control interface which the waterbath maintains when turned on. The lid helps to keep the bath warm. Similar to the incubator, it is always set to 37°C because that is the optimal temperature for normal cell processes.

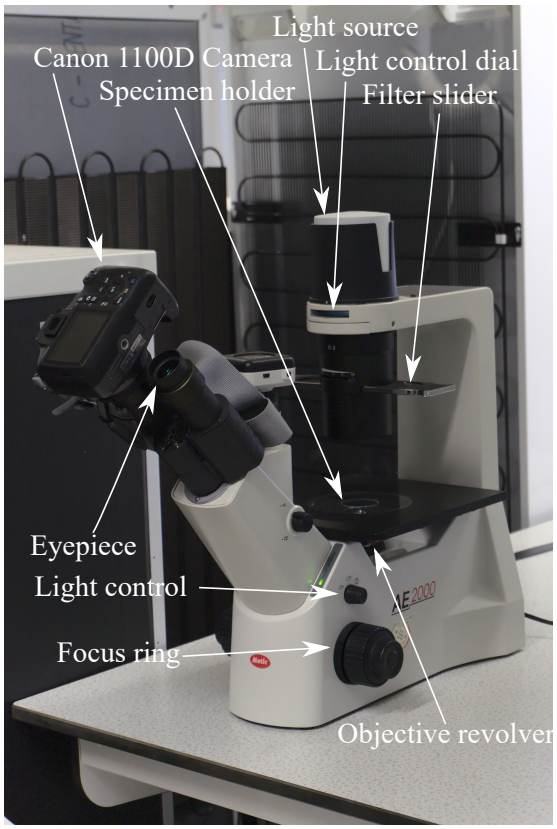

(a) Microscope

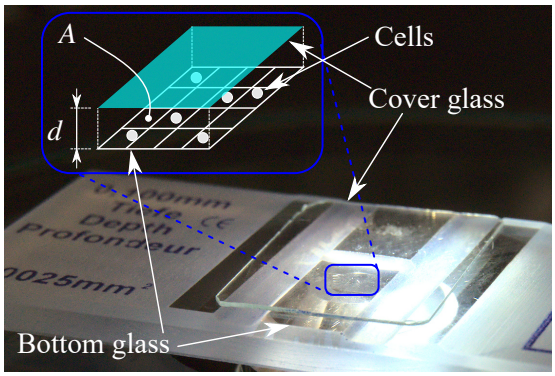

(b) Hemocytometer

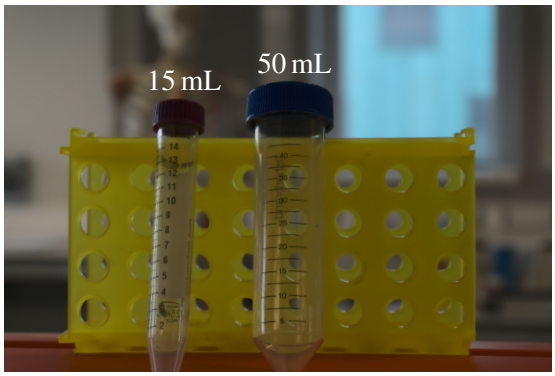

(c) 15 mL and 50 mL centrifuge tubes

Figure D.5: (a) General purpose light microscope used for cell counting and determining how confluent cells were in a flask or on a sample. The light is generated by the light source and its intensity can be controlled with the light control dial. It travels through the filter to the specimen which rests on the specimen holder. The specimen holders height is adjusted with the focus ring to bring the specimen in focus. From there the light goes through the objective and is guided to the eyepiece. The camera can be used to take pictures. **(b)** A hemocytometer and schematic on the microscope. It provides a defined test volume $V = A \times d$ that is filled with a cell suspension and allows counting of cells. From there, the cell concentration in cells/mL is determined. **(c)** 15 mL and 50 mL centrifuge tubes, used to separate cells from the medium they are suspended in. Apart from that, they are used for storing and mixing media and reagents.

in the flasks, covering more and more area. However, a flask can only provide a limited amount of growth area and most cell lines only grow as a monolayer. The ratio of the area that is covered with cells to the whole area is called confluency. A monolayer is a cell layer that is one cell thick, meaning that there are not really any cells on top of each other (there may be very slight overlapping of cells at the junctions between them, but this is due to their shape; they do not grow on each other). This is even more the case for EC lines like HUVEC, which are used in this work because even naturally, they do not grow in a 3D pattern, but only as a monolayer. This means that at some point the cells in a flask will run out of space because they have covered the whole available area, at which point the flask is called fully confluent. From there, the cells may detach because there are just too many of

them and they cannot hold on to the surface anymore. This should be avoided at all costs.

Therefore, when the cells in the flasks were about 90 %-100 % confluent, the cells were ready for detaching and seeding on samples. As cells were cultured in regular Petri dishes and friction tests were conducted in a non-sterile environment, sterility could not be fully guaranteed. Hence, despite all efforts were made to keep the dishes sterile during every step of the methodology before testing, the Petri dishes could be infected by bacteria or fungi (which happened several times before antibiotics were added to the medium). To avoid infections, cell culture was conducted with a standard dose of P/S added to the culture medium.

Cells were detached by washing with PBS and adding trypsin. For a T75 flask, 1.5 mL of trypsin was used; for a T25 flask, 0.5 mL of trypsin was used. A vial of a trypsin aliquot can be seen in Figure D.6a. Trypsin is an enzyme that decomposes proteins of the ECM. This causes the cells to start detaching and roll up. The process of detaching cells with trypsin is called trypsinisation. Once the cells had rolled up, the flask was gently tapped to fully detach all cells. The cells were then counted with a hemocytometer (see Figure D.5b) on the microscope. Healthy cells rolled up to spheres, while cells that were damaged in the process or died a natural death could not roll up and thus showed up misshaped. By adding Trypan Blue, which is a blue dye of watery viscosity (see Figure D.7), to the cell suspension, damaged cells were also stained blue, which made it easier to identify them. Figure D.6b shows the hemocytometer containing a cell suspension stained with Trypan Blue imaged through a light microscope. Only healthy cells were counted. For passaging on cells, a sixth to a quarter of the population was kept, while the rest were seeded on a sample or frozen and any unused cells were discarded.

PBS was made according to the manufacturers guidance by diluting two PBS tablets (see Figure D.7) in 400 mL $\mathrm{dH_2O}$. Once the tablets had fully dissolved, the PBS was transfered into the autoclave and sterilised by heating to 130°C at 1.2 bar for 30 minutes.

D.2.3 Cell Seeding

To seed cells on a sample, the aforementioned steps to detach cells were executed. Then, the detached cells were collected with a pipette. After centrifuging, the cell pellet was diluted in appropriate medium and the cells were counted with a hemocytometer.

A recommended seeding density of 5000 cells/$\mathrm{cm^2}$-10 000 cells/$\mathrm{cm^2}$ is specified in the manual issued by Promocell. Cell culture vessels with a PS bottom did not have to be coated, however, PDMS surfaces were coated with fibronectin before seeding as described in Section 3.5. HUVEC were always seeded with a density of 10 000 cells/$\mathrm{cm^2}$, which resulted in a total number of 88 000 cells/dish for the small Petri dishes. For this, the appropriate

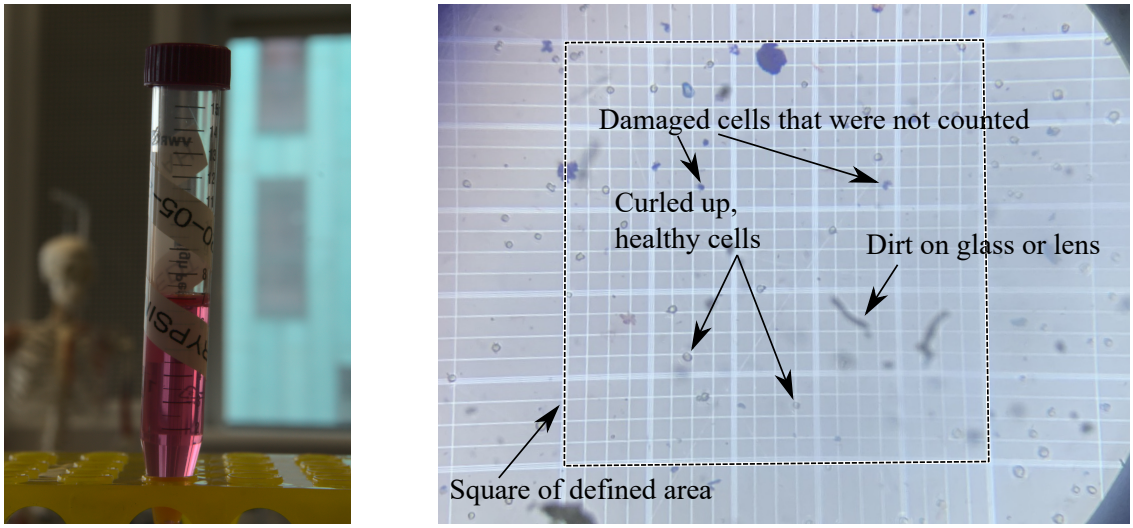

(a) Centrifuge tube with trypsin

(b) Hemocytometer under the microscope

Figure D.6: (a) An aliquot of trypsin in a 15 mL centrifuge tube. **(b)** View on hemocytometer through microscope. Healthy cells are showing up as spheres, while damaged cells are misshaped and were not counted.

amount of cells was taken by calculating the cell suspension equivalent; i.e. if the cell suspension before contained 1.5×10^6 cells/mL, in order to obtain 88 000 cells for one dish, the necessary amount of cell suspension was $\frac{88\,000\,\text{cells}}{1.5\times10^6\,\text{cells/mL}} = 58.67\,\mu\text{L}$. That volume was then diluted in 3.5 mL cell culture medium and this cell suspension was transferred onto the sample.

Similar to the culture flasks, cultured samples were stored in an incubator at 37°C, 95 % relative humidity and 5 % CO_2 with media changes carried out every 2 to 3 days. The culture medium was changed every 2 to 3 days until confluency was reached after between 7 and 10 days and, as such, the sample was ready for tribological testing. The cells were tested deliberately at full confluency and not after a fixed time as the target was for the sample to represent the usual state of an artery *in vivo*.

D.2.4 Cryopreservation and Thawing

Cells were ordered once, split into multiple flasks and cryopreserved so that these cells could be stored and used later. Aside from the financial benefits, this also meant that cell populations originating from the same batch are compared with each other. To cryopreserve cells, they were detached and centrifuged according to the protocol outlined previously. After, they were counted and suspended to a concentration of 1 000 000 cells/mL in the appropriate medium containing 10 % FBS and 10 % dimethyl sulfoxide (DMSO). This suspension is the cell freezing suspension. DMSO is a transparent liquid that is more viscous than water

Figure D.7: Reagents for cell counting and freezing. Triton-X100 is a strong surfactant. DMSO prevents crystallisation during freezing which helps to keep cells alive. PBS is used for washing cells and prepared by diluting the tablet in $\mathrm{DH_2O}$. With Trypan Blue, dead cells are stained blue, making them easily distinguishable from live ones.

(see Figure D.7). While DMSO itself is odourless, cell culture grade DMSO has a strong odour originating from residual dimethyl sulfide. DMSO is required to reduce crystallisation during freezing, which is required to allow cells to survive freezing. Additional FBS also helps the survival rate of cells by providing enough nutrients right after the strenuous freezing and thawing cycle.

The cell freezing suspension is aliquoted (split into smaller portions) into 1 mL cryovials and frozen down using Mr. Frosty, Sigma, UK. Mr. Frosty is a container with a holder to hold the cryovials. It is filled with isopropanol. Once placed into the $-80°\mathrm{C}$ freezer, Mr. Frosty ensures a steady $-1°\mathrm{C/min}$ freezing rate of the cell suspension. After freezing the cells overnight in Mr. Frosty, they were ready to be transferred into liquid nitrogen ($\mathrm{LN_2}$), where they could be stored long term.

For thawing, a 1 mL cryovial was warmed up in the 37°C waterbath. Once around 70 % of the contents of the vial were thawed, the vial was sprayed with 70 % IMS and transferred into the cell culture hood. The 1 mL of cell freezing suspension was mixed with 4 mL of regular culture medium and centrifuged at 1000 rpm for 3 min in a 50 mL centrifuge tube. After sterilising the outside of the tube by spraying it with 70 % IMS, it was transferred

back into the cell culture hood and the medium was carefully discarded, ensuring that the cell pellet at the bottom of the tube was not detached. After resuspending the cell pellet with 15 mL medium, the cell suspension was transferred to a flask and the cell passaging techniques described previously were applied.